REGIONAL GEOTHERMAL CHARACTERIZATION OF NORTHERN KENYA RIFT FROM RESISTIVITY AND GRAVITY

Charles Muturia Lichoro

Faculty of Earth Sciences
University of Iceland
2019

REGIONAL GEOTHERMAL CHARACTERISATION OF NORTHERN KENYA RIFT FROM RESISTIVITY AND GRAVITY

Charles Muturia Lichoro

Dissertation submitted in partial fulfillment of a
Philosophiae Doctor degree in Geophysics

PhD Committee
Knútur Árnason, ISOR Iceland GeoSurvey,
William Cumming, Cumming Geoscience, USA,
Bryndís Brandsdóttir, University of Iceland
Andri Stefansson, University of Iceland
Lúðvík S. Georgsson, UNU-GTP, Orkustofnun

Opponents
Prof. Egidio Armadillo
Dr. Peter Omenda

Faculty of Earth Sciences
School of Engineering and Natural Sciences
University of Iceland
Reykjavik, December 2019

Regional geothermal characterization of northern Kenya rift from resistivity and gravity
Dissertation submitted in partial fulfillment of a *Philosophiae Doctor* degree in Geophysics

Faculty of Earth Sciences
School of Engineering and Natural Sciences
University of Iceland
Öskju, Sturlugötu 7
101, Reykjavik
Iceland

Telephone: +354 525 4000

Bibliographic information:
Charles M. Lichoro, 2019, *Regional geothermal characterization of northern Kenya rift from resistivity and gravity*, PhD dissertation, Faculty of Earth Sciences, University of Iceland, 169 pp.

ISBN: 978-9935-9412-4-4

Printing: Háskólaprent
Reykjavik, Iceland, December 2019

Abstract

An extensive geophysical survey comprising over 400 MT and 515 gravity stations on the Korosi, Paka and Silali volcanoes in the northern Kenya rift was conducted in order to assess the occurrence of geothermal resources in the context of the geophysics of the major volcanic centers. Additional study has also included speculation of magma detectability below the volcanoes.

Resistivity data has been interpreted using 1D joint inversion of magnetotelluric (MT) and co-located transient electromagnetic (TEM) which has revealed a resistivity pattern consistent with the existence of several geothermal systems within the study area. Each geothermal system is characterized by a relatively resistive 100 Ωm surficial layer overlying a ~ 10 Ωm low resistivity zone interpreted as the hydrothermally altered clay cap of the system. Low resistivity is also correlated with clay-rich volcanoclastics deposited on the margins of the rift adjacent to the volcanoes. The cap overlies a higher resistivity zone of about 60 Ωm with a top at about 1000 m depth, interpreted as a potential high temperature alteration zone. The trend of moderate high resistivity at the depth of the potential reservoir corresponds to the zone of intense faulting and fracturing as imaged on the surface.

Gravity data has been analysed through estimation of shallow density by testing the correlation of measured gravity with topography, reviewing results of earlier density measurements of surface rocks in the Kenya Rift, comparison to regional gravity surveys that constrained larger scale deeper density contrasts and 2D gravity modeling correlated with the MT resistivity pattern. Gravity models reveal a dominant 10 to 15 km wide gravity high of 8 mGal amplitude striking NNE along the inner rift corresponding to high resistivity outlined at 2 km depth by recent MT studies. Gravity lows due to structures shallower than 2 km depth at the Paka and Korosi volcanoes have been interpreted as low density bodies within their edifices, likely to consist of either unaltered near-surface pyroclastics or deeper tuffs altered at 60 to 180°C to hydrothermal smectite clay. The high resistivity, low density near-surface rocks on the flanks are interpreted to represent unaltered pyroclastics above the water table, whereas low resistivity, low density bodies underneath the Paka and Korosi volcanos indicate low density tuffs, hydrothermally altered to hydrated smectite clay. Away from the volcanoes on both East and West low density and low resistivity anomalies flanks the central gravity high. The deeper high density zone below the volcanic inner rift is likely to be a combination of higher temperature, low porosity alteration associated with geothermal reservoirs and/or denser rocks related to intrusions.

Surface fissure swarm correlates with both high gravity and resistivity south of Paka volcano but northwards between Paka and Silali volcanoes, there appears inconsistency where the fissure swarm strikes NE but both gravity and resistivity shows a feature west of the currently active fissure zone. This suggests that the rift has recently moved eastwards.

A preliminary review of geoscientific data has been made to evaluate the developed geothermal systems within the Kenya rift and use them as analogs for the geothermal prospects. The comparisons are based on thermal features, geological structures, gravity anomalies and resistivity signatures. Further, 2D synthetic modelling was performed to speculate on the size and depth of magma beneath the volcanoes and demonstrate what can be resolved at depth and what cannot. This has also been used to illustrate the limitations of 1D inversion and test the depth and size of magma that can be detected.

Útdráttur

Umfangsmiklar jarðeðlisfræðilegar mælingar, yfir 150 Magnetotelluric (MT) mælingar og þyngdarmælingar á 515 mælistöðum, hafa verið gerðar við eldstöðvakerfin Korosi, Paka og Silali í norður hluta sigdalsins mikla í Kenía til að meta jarðhitaauðlindir. Samtúlkun MT-mælinganna við Transient ElectroMagnetic (TEM) mælingar á sama stað sýnir viðnámsskipan sem bendir til nokkurra jarðhitakerfa innan rannsóknasvæðisins. Öll jarðhitakerfin hafa viðnámsskipan sem samanstendur af yfirborðslagi með háu eðlisviðnámi (~ 100 Ωm), ofan lágviðnámslags (~ 10 Ωm), sem er túlkað sem ummyndunarleirkápa og þakberg yfir jarðhitakerfinu. Neðan lágviðnámskápunnar er háviðnámskjarni með hærra eðlisviðnámi (~60 Ωm). Þar sem grynnst er á kjarnann er hann á um 1000 m dýpi. Háviðnámskjarninn er talinn sýna berg með háhitaummyndun. Háviðnámskjarnarnir eru undir brotasvæðum, þar sem fjölmargar sprungur og misgengi eru sjáanlegar á yfirborði.

Í þyngdargögnunum er ráðandi 10 til 15 km breið þyngdarhæð (um 8 mGal) eftir innri sigdalnum með norðnorðaustlæga stefnu, sem fellur vel saman við hátt eðlisviðnám neðan 2 km dýpis. Þyngdarlægðir ofan 2 km dýpis í Paka og Korosi eldstöðvunum eru taldar endurspegla bergskrokka með litla eðlisþyngd innan eldstöðvanna. Þeir eru líklega annað hvort úr lausum gosefnum eða dýpra túff með smektít-ummyndun við 60 til 180 °C hita. Líkön byggð á MT-mælingum voru notuð til að skorða tvívíð eðlisþyngdarlíkön. Eðlislétt jarðlög með hátt eðlisviðnám til hliðar eru talin vera óummynduð laus gosefni ofan grunnvatnsborðs, meðan eðlislétt jarðlög með lágt eðlisviðnám undir Paka og Korosi eldstöðvunum eru talin vera eðlislétt túff, ummyndað í vatnaðan smektít leir. Dýpri eðlisþung jarðlög undir eldfjöllunum í innri hluta sigdalsins eru talin vera berg með lágan poruhluta og háhitaumyndun og/eða eðlisþung innskot.

Sunnan Paka er gott samræmi milli kortlagðra brota, þyngdarfrávika og djúps háviðnáms, en þar fyrir norðan, milli Paka og Silali eldstöðvanna, sést misræmi þar sem sprungureinin sýnir ákveðna norðaustlæga stefnu, en bæði eðlisviðnám og þyngdarmæligögn sýna frávik vestan við sprungureinina. Þetta bendir til þess að gliðnun hafi nýlega færst til austurs á þessu svæði.

Með samanburði á jarðvísindalegum gögnum er gerð tilraun til að draga fram hliðstæður milli jarðhitasvæða. Samanburðurinn tekur til jarðhita á yfirborði, jarðfræði, þyngdargagna og viðnámsskipanar, og nær yfir 7 eldfjalla-/jarðhitakerfi. Þá eru gerðir tvívíðir líkanreikningar til að reyna að meta umfang og dýpi kviku undir eldstöðvunum, til að fá tilfinningu fyrir því hvað hægt sé að greina með viðnámsmælingum og hvað ekki. Líkanreikningarnir eru einnig notaðir til að sýna takmarkanir einvíðrar túlkunar viðnámsmælinga, og til að kanna dýpi og stærð kvikuinnskota sem greina má.

Preface

Resistivity and gravity methods were applied to geothermal areas in the northern Kenya Rift, aimed at defining geothermal and structural characteristics of the study area. Further analysis of developed geothermal fields in other segments of the rift have been used as analogs for the undeveloped prospects so as to predict their likely character. The results of this work are summarized in three scientific papers, two of which have been published in Geothermics and the other was submitted to peer-reviewed scientific journals respectively:

I. Lichoro, C.M., Árnason, K., Cumming, W., 2017. Resistivity imaging of geothermal resources in northern Kenya Rift by joint 1D inversion of MT and TEM data. *Geothermics 68, 20–32.* https://doi.org/10.1016/j.geothermics.2017.02.006

II. Lichoro, C.M., Árnason, K., Cumming, W., 2019. Joint interpretation of gravity and resistivity data from the Northern Kenya volcanic rift zone: Structural and geothermal significance. *Geothermics 77, 139–150.* https://doi.org/10.1016/j.geothermics.2018.09.006

III. Lichoro, C.M., Cumming, W., Árnason, K., 2019. A review and comparison of developed and undeveloped geothermal systems in the Kenya Rift based on resistivity, gravity studies and geological structure. Submitted to *Journal of Volcanology and Geothermal Research.*

Table of Contents

List of Figures

List of Tables

Abbreviations

1D	One-Dimensional
2D	Two-Dimensional
3D	Three-Dimensional
ANT	Ambient noise tomography
ASTER	Advanced Spaceborne Thermal Emission and Reflection Radiometer
BOC	Base of clay cap
BP	Before present
CKR	Central Kenya Rift
DEM	Digital Elevation Model
DGPS	Differential Global Positioning System
E	Electric field
EARS	East African Rift System
EDI	Electronic Data Interchange
EM	Electromagnetic
GDC	Geothermal Development Company
GDP	Geophysical Data Processor
GMT	Generic Mapping Tools
GPS	Global Positioning System
H	Magnetic field
IDDP	Iceland Deep Drilling Program
INSAR	Synthetic Aperture Radar Interferograms
ISOR	Iceland GeoSurvey
ka	Thousand year in geological notation

KENGEN	Kenya Electricity Generating Company
km	Kilometre
KPS	Korosi-Paka-Silali
KRISP	Kenya Rift International Seismic Project
m a.s.l	Metres above sea level
m b.s.l	Metres below sea level
Ma	Million year in geological notation
MEQ	Micro-Earthquake
mGal	Milligal
MT	Magnetotelluric
MTU-5A	Magnetotelluric data acquisition system
MWe	Megawatt electric
NKR	Northern Kenya Rift
SHmin	Minimum horizontal stress
SKR	South Kenya Rift
SRTM	The Shuttle Radar Topography Mission
TE	Transverse Electric
TEM	Transient Electromagnetic
TEMTD	A software for inversion of MT and TEM data
TM	Transverse Magnetic
TVA	Tectono-Volcanic Axis
UNU-GTP	United Nation University-Geothermal Training Programme
UTM	Universal Transverse Mercator
WGS	World Geodetic System
Ωm	Ohm-metre

Acknowledgements

As I take responsibility for this piece of work I recognize that many even greater minds have contributed to its success: many of who have taught me and shaped my vision. I am deeply humbled.

This journey was initiated during the 2013 UNU geothermal short course in Kenya when I had a discussion with Knútur Árnason about some interesting geophysical anomalies that occur adjacent to some volcanoes within the Kenya rift valley. This discussion subsequently led to an application for scholarship to study geophysics of the rift in a more regional sense. In the end I was granted the scholarship by the United Nations University–Geothermal Training Programme (UNU-GTP) courtesy of the UNU-GTP director, Lúðvík Georgsson who was privy to the discussion that preceded. I am indeed indebted to the two gentlemen for believing in me even when I didn't believe in myself, I believe this is what mentors are there for. Thank you once more for granting me this scholarship. It has been my pleasure being your student.

My sincere gratitude goes to my employer the Geothermal Development Company Limited (GDC) for granting me leave of absence to pursue my studies in Iceland and allowing use of data for my PhD research and financing additional fieldwork later in my studies. I am indeed grateful to the government of Iceland through the UNU-GTP for awarding me this scholarship and all the support I have had over the period. I thank the University of Iceland for availing all the resources I needed and the lecturers at the faculty of Earth sciences for instilling knowledge and shaping my research focus. The Geothermal Energy Research Group of Iceland (GEORG), University of Iceland graduate travel fund and the UNU-GTP are much appreciated for funding conference attendance in the course of this study.

I take this opportunity to thank my PhD study committee comprising of Knútur Árnason (Iceland GeoSurvey), Bill Cumming (Cumming Geoscience) Andri Stefansson and Bryndís Brandsdóttir (University of Iceland) and Lúðvík Georgsson (UNU-GTP director) for many ideas, suggestions and comments that greatly enhanced the scientific content of this thesis. I appreciate your patience with me even when things didn't work out the way we planned.

Once more Knútur Árnason is thanked for providing his TEMTD program, for Joint inversion of MT and TEM, Ingvar Magnusson for the use of his Gravos program to process gravity data, Wolfgang Soyer of CGG for offering to invert part of my MT data using their Geotools 3D inversion code and GDC Co. Ltd for availing Winglink Dongle for inversion of both MT and gravity. This research was financially supported by both GDC and UNU-GTP.

I want to recognize the invaluable support from the staff of UNU-GTP for facilitating my studies all the way; Lúðvík Georgsson (director), Ingimar Haraldsson, Málfrídur Ómarsdóttir, Thórhildur Ísberg (Tori) and Markús Wilde. My sincere thanks to you all. A special mention goes to Tori for managing my application process, organizing my accommodation on arrival and scheduling my itinerary whenever I needed to travel. The

computer staff Jóhann Kristjánsson – am grateful for your support, in particular managing my many computer problems and software support. The librarian, M/s Rósa Jónsdóttir played a key role: availing the required research papers and books promptly whenever I need them even from outside libraries.

During my studies I made numerous friends both from the UNU fellows and at University of Iceland who left a mark in my life, I cannot name all but am indeed grateful to you all. However, I cannot fail to mention a few of them, we shared office together: TingTing, Gift, Maureen, Jack, Lilian, Moneer and Daniel; Am grateful for the encouragement and many jokes that we shared together.

I cannot pen off this piece without mention many key resource persons that made this work a success: From ISOR Ingvar Magnusson for the help with gravity data modelling and availing his programs to manipulate the data, Kristjan Agustsson and Palmi Erlendsson for assistance with configurations for Seiscomp software and Gunnlaugur Einarsson for inducting me on Arcgis and manipulation of maps. Olafur Gudmundsson of Uppsala University is greatly appreciated for his kindness and understanding and for finding time when in Iceland to assist me with ambient noise data analysis and for answering my many queries on email. We also thank Ezer Patlan formerly at University of Texas at El paso for his assistance in provision of initial programs to process raw seismic noise data. I appreciate you for answering my many questions about use of python programs and being available for numerous skype discussions over time. Am greatly indebted to you all for your kindness and many fruitful discussions we had.

Back at the GDC geophysics office, I want to recognize the support you have given me over the years and all the effort you put to collect quality data in the field. I cannot fail to mention those of you who have dedicated your time for several years to collect data: Wamalwa, Raymond, Noor, Gichira, Deflorah, Mukiri, Omondi, Ogada, Basweti, Kiama, Rose, Magdaline and Kamau. This work is a product of your effort. Ammon at KenGen is greatly acknowledged for all the support and information on geophysics of Olkaria.

To my wife Joyce, sons Arnold, Emmanuel, Trevis and daughter Precious, thank you for your patience, prayers, encouragement and understanding during my prolonged stay out of the country. Without your moral support I certainly could never have completed this thesis, or even started it. I will surely find time to make up for the long absence. To my mother thank you so much for your unceasing prayers, they were surely answered.

Above all glory and honour is to the almighty God for his loving care and protection and for this far he has brought me.

Joyce, Arnold, Emmanuel, Trevis and Precious this work is dedicated to you.

1 Introduction

The purpose of this introduction is to give a brief overview of the geophysical methods as applied in mapping of geological structures that are important in geothermal exploration especially in the context of the magmatically-heated systems of the eastern branch of the EARS. The main subjects of the papers are summarized, and the results highlighted with an attempt to give perspective on the contribution of the overall work. The work involves application of both resistivity and gravity methods in the characterization of geothermal systems hosted in northern Kenya volcanic province. This involves delineating the clay cap above and adjacent to the geothermal reservoir and speculate on the probable geometry of the magma where it exists. Further the character of already developed geothermal fields to the undeveloped geothermal prospects is compared so as to use the known geothermal areas as analogs for unexploited geothermal areas. This way I can characterize the volcanoes as potential geothermal prospects in the context of the rift.

1.1 Research Background

For centuries geothermal resources have been known to exist in different settings worldwide; mainly occurring in areas of high heat flow normally characterized by volcanoes, fumaroles, geysers, hot springs and other geological phenomena. These Geothermal reservoirs are buried in the earth and sometimes do not express themselves on the surface. The most productive geothermal resources are found along major tectonic plate boundaries typically associated with occurrence of earthquakes and volcanoes. One such tectonic feature known to host commercial geothermal resources is the East African Rift System (EARS). This is an intra-continental rift stretching over a distance of more than 3000 km from the Red Sea in the north to Mozambique in the south. The EARS branches into two to form eastern and western rift basins comprised of subsiding grabens and uplifted shoulders. The Kenyan rift lies on the eastern branch where this study is focused.

Previous geophysical studies of the Rift have been regional in scope and focused on understanding the deeper crust; these have included determining the seismogenic layer thickness at the base of the crust (Ebinger, 2005), the rifting process driven by asthenospheric upwelling (Keller et al., 1991; Chorowicz, 2005), crustal thickness variations (KRISP Working Group, 1991; Mechie et al., 1994) and melt accumulation at the base of the crust (Pointing and Maguire, 1990). The most detailed regional review of geothermal prospects in the Kenyan Rift has been done by Dunkley et al. (1993). To date no resistivity study has been done to characterize the conductivity structure of the entire Kenyan Rift.

1.2 Research Prospects

Geophysical surface exploration provides information used to characterize geological attributes that influence the flow of geothermal fluids. The methods applied, indirectly determine the physical parameters that define geothermal systems. Geophysical methods can be used to deduce properties of the geothermal reservoirs like temperature, permeability, fracture density, system cap, fluid saturation and reservoir boundaries among others. The main geophysical methods applied in geothermal exploration include resistivity, gravity and microseismics. The MT method is the most effective technique used to image the 3D geometry of the low resistivity smectite clay that caps permeable geothermal reservoirs associated with volcanoes. The gravity method on the other hand detects lateral changes in subsurface density that may be associated with a variety of geologic patterns commonly found in volcano-hosted geothermal systems including: density contrasts where rock properties differ across faults; hydrothermal alteration that preserves porosity in low temperature hydrated clays or reduces porosity in higher temperature propylitic alteration and lateral variation in the proportion of low density ash versus high density lava with respect to vent areas. The "microseismic" studies use the pattern of hypocenters, the pattern of seismic velocity from tomography, and earthquake focal mechanisms to infer the presence of magma and the geometry and stress state of active structures before development. Detailed geophysical exploration studies have been conducted for some individual volcanoes in the study area but these have not been linked in a more general interpretation of the Northern Kenyan Rift.

In my opinion, the main contribution of this thesis is the interpretation of low resistivity zones on the volcanic flanks by inferring their petrological properties from gravity, and the clear delineation of the high resistivity alignment with the fissure zone particularly the offset inferred in the segment between Paka and Silali volcanoes where geological mapping has not been able to detected lithologic variation revealed in this work suggesting a shift in the axis of the fissure zone.

1.3 Aims of this study

The purpose of this thesis is to investigate causes for the anomalously low resistivity, thick segment observed on the flanks of most volcanoes on the Kenyan Rift zone. In some areas this has been assumed to host geothermal resources and has been erroneously interpreted to represent geothermal alteration or higher permeability. Further work involved comparison of surface geophysics of undrilled geothermal prospects to the surface geophysics and the subsurface geology of the drilled fields in the Kenyan Rift and speculate on the likelihood of existence of magma bodies.

Further primary objectives of this study are:

1. To evaluate the resistivity characteristics of the different sectors of the northern Kenya Rift in order to define prospective areas for future geothermal development.

2. To identify geological structural trends and correlate them with both MT resistivity and gravity density models.

3. To compare the surface geophysics of undrilled prospects in the Northern Rift to the surface geophysics, subsurface geology and thermodynamic conditions of the drilled fields in the South and Central Rift.

4. To analyze MT resistivity and gravity results for Northern Kenyan volcanic centers, interpret them in a manner that appropriately distinguishes near-surface (<500 m depth) and deeper (500 to 3000 m depth) geologic elements that are reliably constrained by the data, and correlate these models with the rift-wide regional interpretations and more local prospect interpretations previously completed for this study area.

1.4 Geophysical prospecting

The Earth's interior has undergone geological deformation in the past and continues to deform at present. These changes have modified the physical properties of the earth and can be monitored and measured indirectly by geophysical means from the surface. If detected the properties can be used to explain the nature of the earth and processes that have taken place. In order to characterize these properties different geophysical methods are used to map them in terms of size, geometry and depth of occurrence. The reliability of detection and subsequent interpretation is key issue in geophysical exploration. Although there have been advances in instrumentation, computer codes, processing and interpretation techniques to model the earth, progress has been much slower in effectively characterizing the uncertainty of these models. Resistivity and passive seismic (earthquake) methods are currently the most used geophysical techniques in the exploration of volcano-hosted geothermal systems. The MT particularly when used in conjunction with TEM in a multidimensional approach can delineate the sub-surface resistivity structure from near surface to depths of tens of km. The gravity method on the other hand can detect lateral changes in subsurface density that may be associated with a variety of geologic patterns commonly found in volcano-hosted geothermal systems such as: density contrasts where rock properties differ across faults; hydrothermal alteration that preserves porosity in low temperature hydrated clays or reduces porosity in higher temperature propylitic alteration; and lateral variation in the proportion of low density ash versus high density lava with respect to vent areas. Likewise, micro-earthquake applications use the pattern of hypocenters and seismic velocity from tomography, and earthquake focal mechanisms to infer the presence of magma and the geometry and stress state of active structures. When applied together they can help gain enormous information about the earth. However, other geophysical techniques offer important additional information including ground magnetics, DC resistivity and active seismic. When integrated with geology and geochemistry support the development of resource conceptual models used to better understand the sub-surface. Below I present a short overview of the methods applied in this study.

1.4.1 Magnetotelluric method

The theory of the magnetotelluric method as applied in resistivity studies is based on Maxwell's equations which relate electric and magnetic fields. For derivation of the equations applied in magnetotelluric methods the reader is referred to (Ward and Hohmann, 1988; Simpson and Bahr, 2005). The magnetotelluric is a passive source electromagnetic method that utilizes Earth's electromagnetic fields to investigate the

electrical properties of the subsurface. The MT method can be used to probe the earth from depths of tens of metres to tens of kilometres. The MT signal originates from two sources; high frequency (10^4 Hz to 1 Hz) from worldwide lightning activity and low frequencies (1 Hz to 10^{-4} Hz) from the variations in the magnetic field due to solar activity. When the MT signals, modeled as coupled electric and magnetic fields traveling as EM waves in free space, penetrate the Earth's surface, electrical currents induced by the electric field in conductive materials dissipate the electric field so that EM propagation below the surface is governed by a diffusion rather than a wave equation (Vozoff, 1991). The MT measures only the horizontal components of the resulting electric (Ex, Ey) and three magnetic (Hx, Hy, Hz) fields.

Most of our MT recording used pairs of non-polarizing porous potentiometer electrodes (e.g. Pb-$PbCl_2$) to measure perpendicular electric fields (by measuring potential difference), magnetic induction sensors to measure magnetic field and a recording unit for timing and recording the data as shown in Fig. 1.1(a). The standard MT installation in Kenya include electrode separation of about 50-100 m long with the electrode pairs installed in the ground in magnetic north-south and east-west directions.

For the MT method, measurement uncertainties mainly result from; static shift distortion (Ledo et al., 1998), departure from flat earth assumption (in case measurements are taken in extreme topography), departure from plane-wave assumption of the source field (Jiracek, 1990), cultural noise, layout or human errors and environmental disturbances e.g by wild animals among others. The static shift problem is inherent to all methods that use dipoles to measure the electric field, including MT, and is caused by local near-surface resistivity inhomogeneities close to the sounding site (Sternberg et al., 1988; Árnason, 2008). Static shift in MT can in most cases be corrected by taking a TEM measurement at the same site and jointly inverting both data sets (Fig. 1.1c) to correct for the distortion (Sternberg et al., 1988; Pellerin and Hohmann, 1990; Meju, 1996). This is based on the fact that TEM measures magnetic field instead of electric field (and so does not use the electrodes that produce polarization and static distortion effects) and hence it is not affected by static shift which affects MT. However, this method assumes the structure in the shallow common depth for MT and time-domain soundings is one-dimension. The dimensional distortion can be addressed by correctly interpreting MT data for the appropriate dimensionality in the MT responses. The author recognizes that the earth is most likely three-dimensional (3D) especially at depth. However, many geothermal fields have been reliably imaged using appropriately limited 1D methods to the crucial transition at the base of the clay cap.

The MT information is contained in the impedance tensor whose elements depend on the conductivity distribution in the subsurface (Simpson and Bahr, 2005). The conductivity information of MT is derived from the impedance tensor which relates the measured electric and magnetic fields whose field components are related as follows:

$$\begin{pmatrix} E_x \\ E_y \end{pmatrix} = \begin{pmatrix} Z_{xx} & Z_{xy} \\ Z_{yx} & Z_{yy} \end{pmatrix} \begin{pmatrix} H_x \\ H_y \end{pmatrix} \quad (1)$$

The electric field attenuation is frequency dependent such that high frequency attenuates at shallow depth and hence provides information about the near-surface while low frequency sample the deepest part of the earth. The Impedance tensor is complex due to phase differences between the electric and magnetic fields. The off-diagonal components as a

function of angular frequency of the impedance tensor are used for calculating the apparent resistivity and phase for the two orthogonal components as follows:

$$\rho_{xy} = \frac{1}{\omega\mu_0}\left|Z_{xy}\right|^2 \qquad \& \qquad \phi_{xy} = arctan\left(\frac{ImZ_{xy}}{ReZ_{xy}}\right)$$

$$\rho_{yx} = \frac{1}{\omega\mu_0}\left|Z_{yx}\right|^2 \qquad \& \qquad \phi_{yx} = arctan\left(\frac{ImZ_{yx}}{ReZ_{yx}}\right) \tag{2}$$

where, ω is the angular frequency and μ_o is the magnetic permeability of vacuum. The depth of investigation is dependent on the period of the EM wave and the resistivity of the medium in which the EM wave propagates. Therefore, apparent resistivity of the earth for different periods can be approximated using the approximate Cagniad formula as follows:

$$RhoApp_{xy} = 0.2T * \left|\frac{E_{xy}}{H_{yx}}\right|^2 \tag{3}$$

where $RhoApp$ is apparent resistivity in Ωm, T is period (sec), E_{xy} is electric field in mV/km, H_{yx} is magnetic field in nT in the *xy* and *yx* polarizations respectively. For a given subsurface resistivity the depth of penetration (skin depth) increases with the square root of medium's resistivity and period.

Thus, skin depth $\delta(\omega) \approx 0.5\sqrt{\rho T}$ [km] (4)

Therefore, in order to realize deeper penetration, data should be acquired at sufficiently longer periods. The skin depth explains the limitations of the EM technique, particularly the decreasing resolution with increasing depth of penetration.

MT dimensionality indicators

Before interpreting MT data, a clear analysis of dimensionality in the data is required so as to know the mode of inversion to apply and understand the limitations of models in case the correct dimensionality is not addressed. We recognize that dimensionality is frequency dependent (Simpson and Bahr, 2005), such that the MT response at lower frequencies are affected by both deeper and most distant changes in resistivity and so the dimensionality of the data becomes more complex at lower frequency. Some important parameters that are evaluated to measure dimensionality during MT data interpretation include skew, ellipticity, MT polarization (polar diagrams) and phase tensor analysis. The most effective modern dimensionality indicators are the $AppRho_{xx}$ and $AppRho_{yy}$ spectra plotted in direct comparison to the xy and yx spectra.

The skew (S) is a dimensionless parameter that indicates how the data vary from an ideal 2-D model as defined by Swift (1967) and is expressed as follows.

$$S = \frac{\left|Z_{xx} + Z_{yy}\right|}{\left|Z_{xy} - Z_{yx}\right|} \tag{5}$$

When Skew is <0.2, it indicates that the resistivity geometry is likely to be 1-D or 2-D, whereas Skew >0.2 indicates 3D resistivity geometry (Reddy et al., 1977). A more direct 3D illustration can be reliably demonstrated by comparison of xx and yy amplitude to xy and yx amplitude on an apparent resistivity vs frequency plot.

Ellipticity (*E*) on the other hand relates to the ratio of magnitude of the difference of rotated diagonal elements to the sum of the rotated off-diagonal elements of the rotated impedance tensor as defined by (Ranganayaki, 1984) as shown below. If *E* is < 0.1 the underlying structure is 1D.

$$E = \frac{\left|Z_{xx}^{'} - Z^{'}_{yy}\right|}{\left|Z_{xy}^{'} + Z^{'}_{yx}\right|} \tag{6}$$

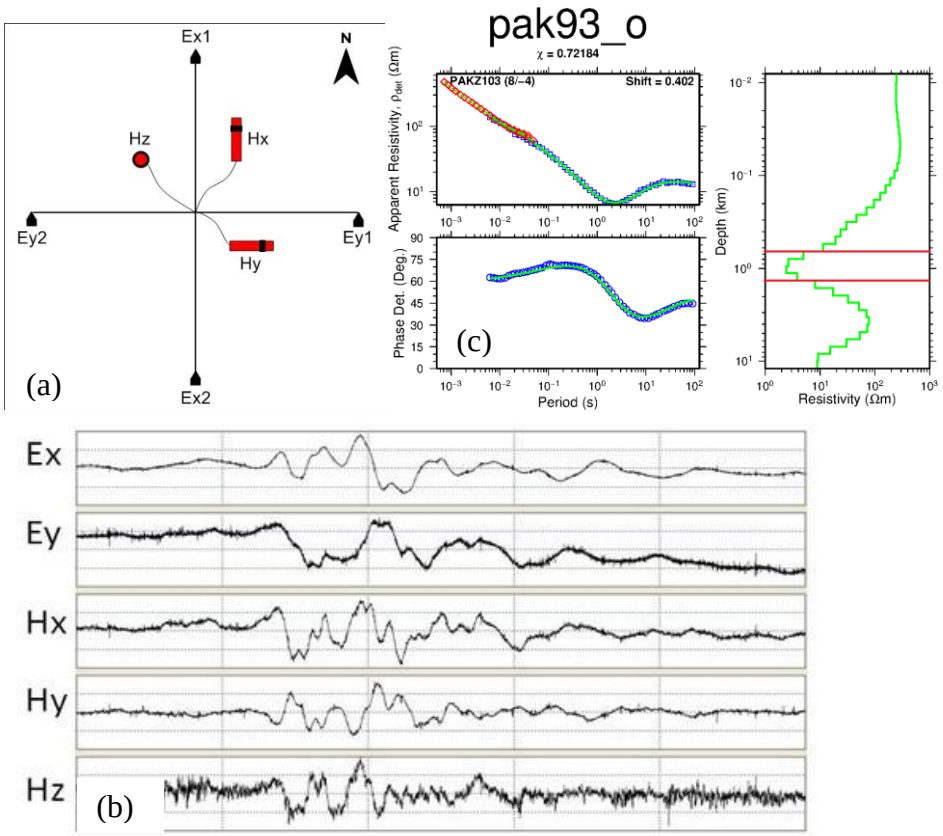

Figure 1.1: (a) MT field layout (b) MT time series data and (c) On the left panel, Joint inversion of MT (blue) and TEM (red) data; On the right panel is the resultant 1D inversion model. The red lines mark the inferred low resistivity clay cap.

Phase tensor on the other hand expresses how the phase relationships change with polarization in the general case where the conductivity structure is 3-D. This method does not take into consideration the dimensionality of the underlying structure. The Phase tensor can be shown graphically as an ellipse, such that the major and minor axes represent the principal axes of the tensor (Caldwell et al., 2004). The advantage of the phase tensor is that it is independent of the static distortion that affects the impedance tensor. The Phase tensor can be denoted as an ellipse with principal phase values of the tensor represented by

major and minor axes of the ellipse respectively and the skew angle (β), which is a dimensional indicator. When the difference between principal phase values and the phases for TE and TM are small and the skew angle is zero, then the conductivity structure is taken to be 2D. On the other hand when a big difference arises between the principal phase values and the two polarization phase values in addition to a large skew angle then 3D structure is implied. To visually assess the dimensionality of the resistivity structures over a given area, a map of the phase tensor ellipses is shown for representative area at Paka volcano (See Appendix C).

1.4.2 Transient Electromagnetic (TEM) method

The TEM method is a geophysical method which provides subsurface resistivity information. The method is based upon the fact that a magnetic field that varies in time, according to the Maxwell equations, will induce an electrical current in the ground. Usually a transmitter loop of wire is placed on the ground and driven by a time varying current that creates a primary magnetic field. The transmitter current is abruptly terminated generating eddy currents, which flow in such a way as to preserve the magnetic field that existed before the current was withdrawn and further generates a secondary magnetic field. This secondary magnetic field decays with time and induces a voltage in a receiver coil. The magnitude of the secondary field depends upon the type and distribution of conductive material in the subsurface.

Measuring the current in the receiver coil will therefore give information about the resistivity as a function of depth. Just after the current in the transmitter loop is turned off, the current in the ground will be close to the surface, and the measured signal reflects primarily the resistivity of the top layers. At later decay-times the current has diffused deeper into the ground, and the measured signal then contains information about the resistivity of the deeper earth layers. The depth of exploration depends primarily on the transmitter moment (product of the current and the area of the loop) and the conductivity structure of the earth. Basic foundations of TEM method can be found in Árnason (1989); Spies and Frischknecht (1991); Ward and Hohmann (1987) or McNeill (1994).

The TEM method used in this study was the central loop which employs a square transmitter loop and an inductive receiver coil which couples to the logging unit. The frequency of transmission is regulated by a controller unit that ensures switching on and off current into the loop. The receiver measures the decaying voltage after the transmitter is turned off ensuring that small secondary voltages are measured since there is no primary field when the current is off. Distortions in TEM measurements may result from; cultural noise, instrumental noise from electronics, natural electromagnetic noise or due to dimensional distortion, especially related to topography (Stark et al., 2013). Some of these distortions can be reduced by careful site selection and repetative stacking of measurements for every frequency and taking averages. The TEM method is well suited for 1D layered earth model since it is downward focused. It is particularly useful when resolving the near-surface conductivity structure because it has better resolution compared to the MT. Therefore, TEM data acquired at same site as MT soundings often provides an effective means to correct for the MT static shift (Pellerin and Hohmann, 1990; Sternberg et al., 1988).

1.4.3 Resistivity methods applied in geothermal exploration in Kenya

Electromagnetic methods, particularly MT combined with TEM to correct MT static distortion, have been extensively used in geothermal exploration to inverstigate deep resistivity pattern in the earth. This is because, unlike other practical resistivity methods, MT has sufficient depth of investigation to image resistivity to the depth of typical geothermal reservoir. In particular MT and TEM plays an important role in imaging the 3D resistivity geometry of crucial conceptual elements of volcano-hosted geothermal reservoirs including the low resistivity smectite clay that forms the impermeable cap, the transition to the higher resistivity propylitic alteration of a >200°C permeable reservoir and, in special cases, the low resistivity magma heat source. The first case of MT application in geothermal exploration in Kenya dates back to the 1980s but the outcome did not prove promising as the results were never used for any geothermal development. Being a new method in Kenya back then, there was lack of knowledge in proper data collection, modelling and misleading interpretation due to the erroneous assumption that the geothermal reservoirs should be imaged as a low resistivity zone. This assumption was born out of some older resistivity methods that had limited depth of investigation that could only image the shallow low resistivity and the expectation that geothermal reservoirs were low resistivity. Later in the early 2000s the method gained wider application and has become the method of choice in geothermal exploration in Kenya. Internationally combined MT and TEM has been used in many geothermal fields with great success when delineating geothermal reservoirs and for well targeting. Specifically the method has been used to resolve the hydrothermal clay alteration overlaying numerous geothermal reservoirs (Árnason et al., 2000; Cumming et al., 2000; Muñoz, 2014).

1.4.4 Resistivity of geothermal reservoir

Geothermal reservoirs are characterized by numerous properties that affect resistivity variation in the rocks. Most resistivity variation, especially in volcano-hosted geothermal systems, is associated with the the low resistivity smectite clay alteration of the cap and the transition to high resistivity chlorite/illite clay alteration of the reservoir, followed by porosity, water saturation, temperature and salinity (Ussher et al., 2000). Brine has high concentrations of dissolved ions that form conductive electrolytes within the rock matrix. This electrolyte when subjected to high temperature can result in large reduction in the bulk resistivity. The resulting resistivity can greatly be reduced if clay minerals are present. It has been demonstrated (Flovenz et al., 2005) that the variation in cation exchange capacity of the smectite clay content is the main factor that determines resistivity variation in geothermal systems. In a typical high temperature hydrothermal system, the lowest resistivity corresponds to the smectite clay cap overlying the geothermal reservoir, in which case the resistivity of the reservoir itself may be much higher.

The dominant clay type in the low temperature part of the clay cap is smectite but, because smectite is unstable at temperature higher than 70°C, it alters to chlorite (in the case of basaltic rocks) or illite (for andesite and rhyolite rocks). The ratio of chlorite or illite to smectite increases with temperature from 70 to 180 °C, causing low temperature minerals such as zeolites and smectite to disappear at about 220 °C so that only rare traces of dehydrated high resistivity smectite are found at temperatures above 240 °C where chlorite/illite are dominant. The low resistivity imaged above the smectite-illite transition

zone in many high-temperature geothermal reservoirs is associated with much higher cation exchange capacity in smectite than in the alteration minerals below. In this way, the use of MT to image variations in clay alteration is considered to be the most important geophysical tool used to characterize the geometry of hydrothermal reservoirs and, in combination with geology and geochemistry to constrain geothermal resource conceptual models used to target wells. This relationship has also enabled interpretation of resistivity pattern in terms of temperature, subject to temperature equilibration with the dominant clay alteration (Árnason et al., 2000). The low resistivity smectite found in the cap is plastic and so inhibits permeability while the chlorite and illite at higher temperature are more brittle and permissive of permeability at a much higher clay fraction than smectite. Therefore, as long as the chlorite and illite content are above 50% or so, stressed fractures are likely to form open space permeability.

Case histories have shown that fossil hydrothermal pattern have similar resistivity as active geothermal systems. In some cases, the low resistivity geothermal cap and the high resistivity core may not have enough contrast to be mapped out. Parts of reservoirs that have a non-smectite cap such as chlorite will be harder to to delineate, but this is part of the risk assessment. The most common examples of non-smectite caps are the moderate resistivity mixed-layer smectite-illite/chlorite clay cap (e.g. Pellerin et al., 1996) or higher resistivity phyllic (illitic) zones (Melosh et al., 2012) that act as a transition beneath some smectite caps, or bordering part of a reservoir. For example, the Namora-I-Langit field shown in Cumming (2000) has a high resistivity chlorite-illite cap on its SW edge, making the interpretation of that edge more ambiguous. However, these issues can be considered in the integrated risk assessment, for example, at Silali. Similarly, a thick layer of volcanic ash and clastics weathered to clay might give a similar conductive structure as a geothermal clay cap. To avoid misinterpretation, the resistivity imaging should be integrated with gas and water geochemistry of fumaroles and hot springs, geology including both deposition and erosion reconstruction, alteration mapping, structural geology, hydrology, relevant supplementary geophysics such as gravity and seismic monitoring, and the constraints of thermodynamics to build the resource conceptual models used to support risk assessments of geothermal resource capacity and target wells. The gravity and seismic monitoring methods are not generally prudent for all geothermal targets but they are generally recommended for geothermal prospects in the Kenya Rift.

1.4.5 Gravity method

Gravity prospecting involves measurements of variations in the earth's gravitational field, which are caused by the variable mass distribution in the earth related to variations in rock density. In practical gravity surveys, the magnitude of the gravity variation depends on the following five factors: latitude, elevation, topography of the surrounding terrain, earth tides, and density variations in the subsurface. For this study gravity patterns due to density variations are of interest and so gravity effects by the other factors were removed. However, density variations occur at different depths in the earth and need to be separated in terms of regional and residual anomalies due to more local density variations. The long wavelength features are associated with deeper sources whereas short wavelengths are associated with near-surface sources. The major challenge in gravity interpretation is separating anomalies of interest from the overlapping effects of other features, hence the need to remove the regional field so as to emphasize the residual anomalies. This can be done in a wide variety of ways including trend surface analysis (fitting and subtracting a

low order polynomial surface to the observed data) and low-pass filtering. In the current study trend surface analysis was used.

Gravity interpretation is non-unique, due to the presence of data errors and the inherent source ambiguity of the gravity potential. Hence an infinite number of bodies can give rise to a specified anomaly. Therefore, supplementary geological, geophysical, and other sub-surface constraints are essential to minimize the ambiguity.

A detailed review of gravity technique is found in Telford et al. (1990) and Hinze et al. (2013). The Bouguer residual gravity pattern is then compared to computed gravity from a model of subsurface density contrasts to constrain a density distribution that would explain the anomalies in terms of gravity variation in amplitude and geometry. Rock densities in the shallow subsurface range from about 0.8 g/cm^3 to 3.0 g/cm^3 and are dependent on porosity, mineral composition and water saturation which, in turn, depend on rock type, burial and temperature history among others. Previous gravity surveys in the east African rift have been either more regional, extending 100s of km outside the EARS and focused on the deep lithoshere or more local, investigating a specific geothermal prospect.

At the base of the reservoir intrusion of dense material in the crystalline basement could potentially produce a gravity high but recent intrusions are likely to be less dense than the Precambrian. When liquid magma intrudes into the basement low density anomalies are generated. Although these processes occur, they are not the main themes of geothermal density variation related to gravity interpretation.

Density of rocks

In gravity exploration the quantity sought for is the local lateral variation in density. The density of the rocks used in interpreting gravity is typically infered from the borehole logging, drill cores samples or estimated from seismic velocity. Density variations depend on the rock types, porosity, saturation state, age, depth of burial and mineral composition. Aside from dense carbonate rocks, sedimentary rock density is primarily affected by its porosity. Volcanic rocks have a similar range of density but tend to be denser where lavas predominate over tuff. Intrusive rocks tend to be denser than sediments and shallow volcanics because of their lower porosity. However, high grade metamorphic rocks tend to contain many heavier minerals in their matrix and have lower porosity, so they tend to be the most dense. Density will also vary depending on levels of fragmentation, weathering or dehydrations due to high temperature alteration.

Geothermal systems can as well have varying gravity anomalies depending on the level of mineral precipitation especially in low density within high porosity host rocks (Allis, 1990). However, densification of porous rocks may occur for instance due to calcite, silica or epidote deposition resulting in increased density. On the other hand, if dense rocks are fractured, they create open space which slightly reduce density, albeit probably not at a detectable level. Geothermal alteration in fractured and presumably permeable rocks will not be smectite (or there would be no open fractures). Alteration at higher temperature usually decreases porosity and increases density. Chemical leaching tends to involve relatively minor volumes of surface acid leaching and deeper zones in unprospective vapor cores causing density decrease.

Density estimation

Because of the ambiguity of gravity interpretation, the density values used in gravity models are constrained in a wide variety of ways; these include in situ laboratory measurements of rock densities sampled from the area of study, density measurements in boreholes, correlative measurements from seismic velocity and theoretical estimation by Nettleton and Parasnis methods. Laboratory density measurements are subject to a number of short-comings resulting in unrepresentative densities caused by obtaining weathered rock samples, making measurements on unconsolidated samples and measuring the density of rocks with high porosity. Terrain density of near-surface rocks can be estimated by taking a series of gravity measurements over a topographic feature using the Nettleton density profile method (Nettleton, 1939). The density which gives the least correlation between the calculated gravity and the topography is assumed to be the density of the surface material forming the topography. The Parasnis technique on the other hand assumes that subsurface density variations will not be correlated with topography, therefore terms in the Bouguer reduction formula independent of density (G_{obs}–G_n+0.3086*h) are plotted as a function of the terms multiplying density (0.04191*h-Tc) giving a straight line with a slope equal to the estimated density. In calculation of Bouguer anomalies, errors may however arise due to the assumed density of material in the near-subsurface.

Gravity data processing and interpretation

There are two stages of processing employed in this study; 1) data reduction from field measurements to Bouguer gravity, and 2) modeling and comparison between the gravity predicted from the model and the measured gravity. Gravity observations include effects caused by temporal and spatial variations that must be removed before the data can be interpreted in terms of density variations. These variations arise from instrumentation, terrain, rotation of the Earth, the tidal effects due to the Moon and Sun, the variation in radial distance from stations to the Earth's center, and the Earth's average gravity field.

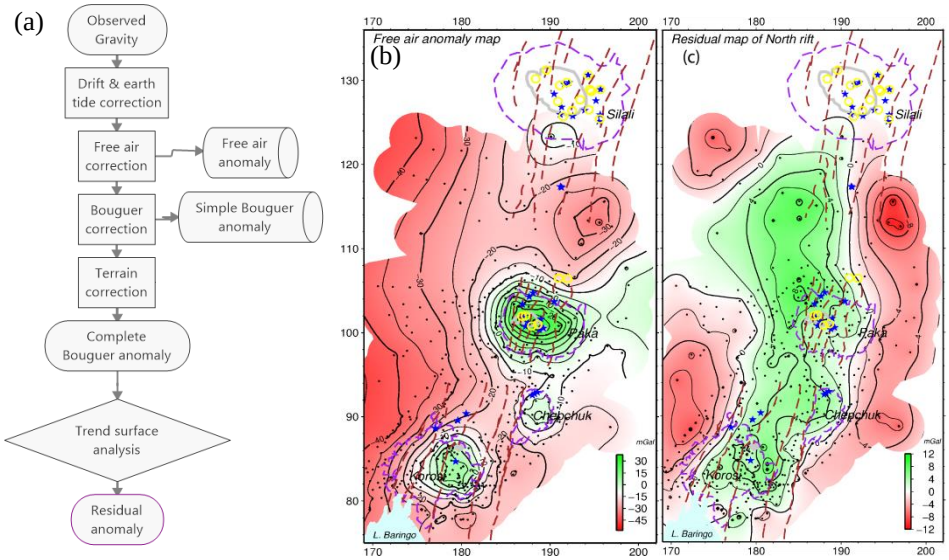

Figure 1.2: (a) Workflow for generating gravity residual anomalies. (b) Map of free-air-anomaly; shows high gravity on the volcanoes. (c) Residual Bouguer anomaly map; shows the final gravity anomaly after all corrections have been done.

Figure 1.2 shows steps involved in gravity data reduction in order to obtain residual anomaly. Gravity data interpretation involves qualitatively and quantitatively analyzing the reduced data in order to infer an earth "structure". A common approach to inferring subsurface structure based on gravity data is to use trial-and-error modeling. In this approach, a geometric model for variations in density in the subsurface is proposed, the gravity response of the proposed model is computed, the computed gravity is compared to the observed gravity, and the model is adjusted to improve the fit in a manner consistent with other geophysical and geological constraints. By iteration the parameters of the presumed subsurface model are adjusted until a close match is achieved between the observed and estimated values. The final interpreted models obtained have to be transformed into appropriate physical parameters of geological significance.

1.4.6 Use of developed geothermal fields as analogs for undeveloped prospects

Knowledge gained in exploration and development of one geothermal field can be applied to other similar undeveloped geothermal prospects. In the Kenyan rift only three geothermal fields have been developed out of seventeen identified prospects. The developed geothermal fields are in south and central rift while all prospects in north rift remain undeveloped. Comparisons based on thermal features, geological structures, gravity anomalies and resistivity signatures for developed geothermal fields in the Kenya Rift can be used to get a better understanding of how these are likely to constrain geothermal resources in the other undeveloped prospects and characterize what additional data would provide the most effective constraints on resource conceptual models being developed for resource likelihood, capacity and well target assessment. The approach is to use geophysical results for southern and central Kenya geothermal fields as analogs for the undeveloped geothermal fields in the northern Kenya rift. The Olkaria geothermal complex and Menengai are the areas with the largest expected geothermal power developments in the south and central Kenya rift respectively.

The known surface geological and geophysical features and subsurface reservoir properties of analogous developed reservoirs can be compared to similar surface data and models from the undrilled prospects in order to assess the limitations of resource characterization based on the MT and gravity data and to identify what additional geophysical data sets would most improve the integration with gas and water geochemistry analyses of hot springs and fumaroles, hydrologic modeling and structural geology and supporting geoscience to produce thermodynamically consistent resource conceptual models. To achieve this, the elevation of clay cap was mapped by MT to help approximate the top of the underlying reservoir.

The intensity of smectite clay alteration in the volcanoes is indicative of the character of the underlying reservoir, whether liquid or steam dominated. The low intensity especially at Suswa caldera (albeit with minimal MT coverage at the inner caldera), Silali caldera and at the apex of Paka caldera might point at possible underlying boiling zones.

1.5 Present study

1.5.1 Study area

The survey area is located within the EARS (Fig. 1.3), covering mainly the Northern volcanic zone (Korosi, Paka and Silali) and the Southern volcanic zone (Olkaria, Longonot and Suswa). The Central rift zone where Menengai volcano is located has been used in the comparisons where applicable. The first part of the study (Paper I), covers the resistivity study of the northern rift zone while the second part (Paper II) covers the gravity application in the same area. The final part of the study (Paper III) compares geothermal systems developed in the southern and central rift and applies them as analogs for the geothermal prospects which are yet to be developed in the other sectors of the rift.

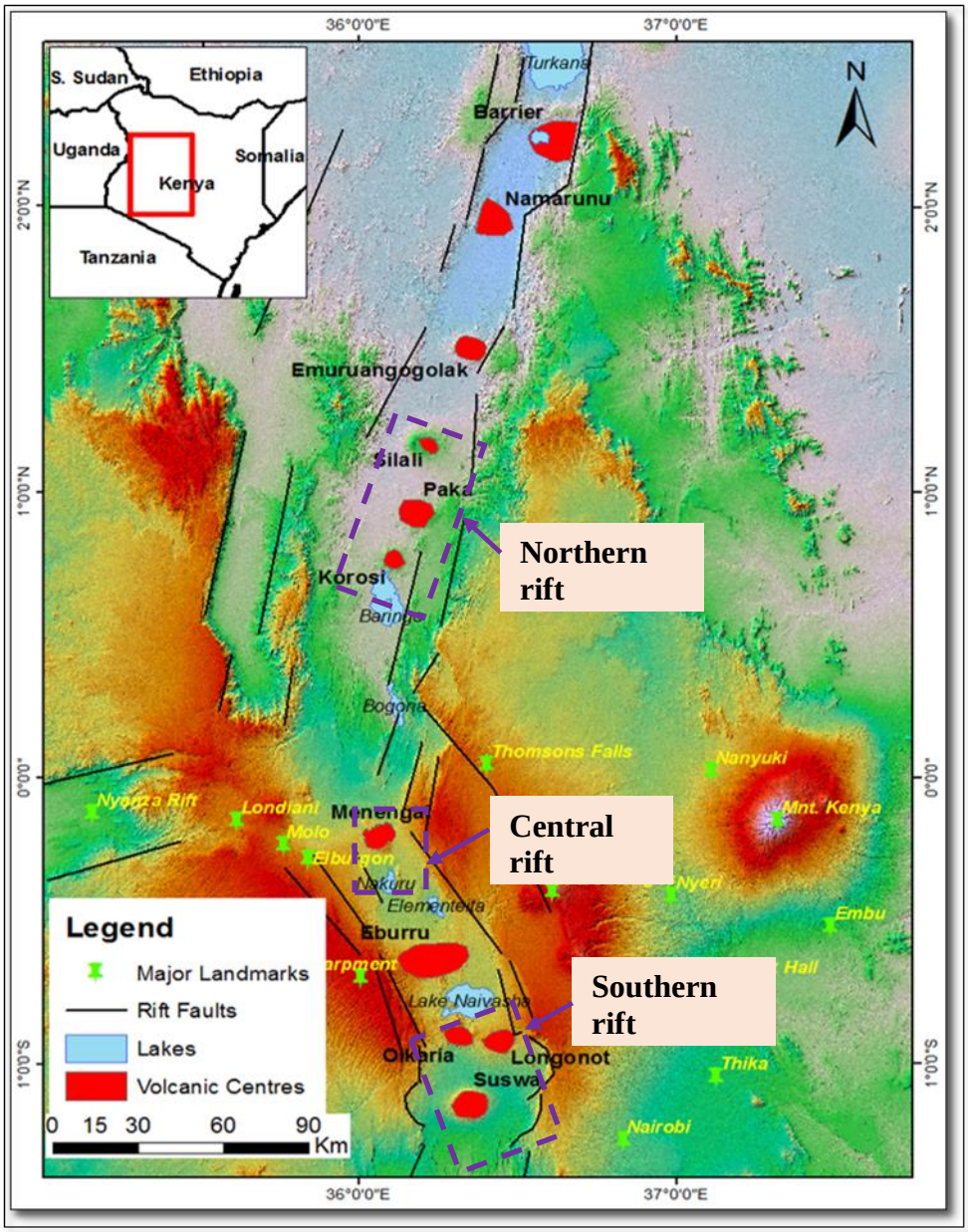

Figure 1.3: Map showing geothermal areas in the Kenya Rift. The dashed-purple rectangles represent the areas considered in this study. Coordinates are UTM km Zone 37 WGS84.

Methods used in the study

The occurrence of volcanic centers and geothermal systems within the EARS has allowed to focus this study in order to gain information and help infer hydrothermal systems and associated structural features.

This study involves analysis and interpretation of three data sets namely, MT and TEM resistivity and gravity and synthetic MT computed from 2D models to test 2D modelling resolution. This approach is aimed at integrating all the datasets to come up with a geophysical interpretation that is consistent with all the datasets. The MT and TEM have been jointly interpreted so as to correct for static shift in MT and recover the resistivity pattern. Although 3D inversion is a standard best practice for most geothermal MT data sets, this approach was used for only one area in this study because of large gaps in data coverage and poorer data quality at the lower MT frequencies that would be best analyzed using 3D inversion. The one 3D inversion was used to test the 1D MT inversion used for a profile across Paka volcanic center. However the author acknowledge the advantages of 3D MT inversion and recommend extending it to the prospects in the northern Kenya rift as data coverage improves.

Gravity aims at delineating density contrast in the subsurface and due to its inherent ambiguity, it has been jointly interpreted using MT resistivity cross-sections as constraints on likely bodies with contrasting density. Synthetic MT data was computed from 2D models to test whether the 1D inversions used in this paper could reliably detect a magna body below the volcanoes. The combined resistivity and density data were interpreted with context of the volcanic geology of the Kenyan Rift.

This thesis consists of six chapters; Chapter 1 introduces the methods and the geological aspects of the study area. Chapter 2 summarizes the resistivity structure of the Northern Kenya volcanic zone as detailed in the published Paper I. In the paper, over 400 MT and TEM data points were analyzed through joint inversion to come up with resistivity models. Chapter 3 describes the integration of gravity and resistivity data of the study area leading to modelling of subsurface density structure as illustrated in the published Paper II. It encompasses about 515 gravity data points covering the northern Kenya rift province from where 2D gravity models have been jointly interpreted with MT resistivity cross-sections. Chapter 4 compares geophysical and geological properties of developed geothermal systems in the Kenya Rift and applies them as analogs to undeveloped geothermal prospects and hence predict the likely character of the undeveloped fields as described in Paper III. Overall, the compared geothermal fields points at the limitations of resistivity and gravity to delineate magma under the volcanic systems. Chapter 5 covers general conclusions and discussions from the previous chapters. Lastly Chapter 6 discusses the way forward with regards to further research.

2 PAPER I: Resistivity Imaging of Northern Kenya rift

2.1 Summary

The search for geothermal resources in the Kenya Rift has intensified since 2000. This has focused on the volcanoes that align with the rift. Geophysical and supporting geoscience exploration has been carried out on a number of volcanoes with promising results indicating resource potential. Resistivity is the most diagnostic geophysical parameter in the characterization of volcano-hosted geothermal resource capacity and well targets. The resistivity structure in this case is typically interpreted in terms of alteration mineralogy where the low resistivity smectite clay cap transitions to high resistivity illite/chlorite in a potential reservoir (Árnason et al., 2000; Gunderson et al., 2000; Ussher et al., 2000). These clay transitions are controlled by both temperature and kinetics (Essene and Peacor, 1995). According to Gunderson et al. (2000), as smectite-bearing rocks are compacted and indurated, smectite becomes more dehydrated as it transitions to mixed layer smectite-chlorite/illite, and also gradually increases in resistivity. As a result, temperature at the base of a low to moderate resistivity smectite and mixed layer clay cap can vary widely. Alteration of precursor minerals to smectite can begin at 60 or 70 °C and the transition from the smectite to chlorite and illite takes place over a wide range of temperature up to 240 °C (Ussher et al., 2000). Low resistivity smectite (Cumming 2016) is also found in altered rocks adjacent to geothermal systems and is commonly found as one component of the clays in sedimentary shales and weathered volcanic lahar and ash deposits commonly found in basins adjacent to volcanoes.

Previous resistivity studies in the Kenya Rift were focused on individual volcanoes most of which revealed low resistivity segments on the flanks of the volcanoes that have sometimes been erroneously interpreted as hosting geothermal resource. This prompted a regional-wide study of several volcanoes together to better understand this phenomenon. For this purpose, we have resolved the cause of these deep and conductive segments and identified promising areas likely to host the geothermal resources. This was achieved by jointly inverting MT invariant and TEM data to recover the resistivity structure of the volcanic zone and followed up in Paper II by modeling this feature together with the gravity data.

Case studies of many geothermal fields have indicated that 1D inversion of MT data is usually good enough to characterize the overall resistivity geometry of a geothermal clay cap but may not be sufficient to resolve variations in resistivity below it, particularly when higher dimensions are involved (Anderson et al., 2000; Árnason et al., 2000; Cumming et al., 2000). In this study smooth 1D joint inversion of invariant MT and TEM data were computed, ensuring good fit between MT and TEM. The resulting inversion models are stitched to form resistivity cross-sections along interpreted profiles (Fig. 2.1). We reckon

that the resolution deteriorates beneath the clay cap, making details of resistivity at reservoir depths uncertain, but with careful modelling, the resistivity pattern can be reliably interpreted in a conventional geothermal context.

2.2 Main highlights

The resistivity results were determined using one-dimensional joint-inversion of MT and TEM data to characterize the resistivity pattern of volcanoes as follows:

- A resistive top layer from about 200 m to 500 m depth along the rift overlies a very conductive layer (~10 Ωm) in the Paka-Silali segment and a moderate resistivity layer (about 30 Ωm) beneath Korosi. Both are underlain by a higher resistivity core (~60 Ωm) which domes beneath the volcanoes. The resistive surface layer is associated with recent, well-drained tuffs and lavas. The second layer is low resistivity, reflecting hydrothermal alteration with resistivity dictated by the amount of smectite in the layer. The third layer is higher resistivity, potentially corresponding to a geothermal reservoir with upwelling zones represented by the higher resistivity doming beneath a low resistivity cap associated with thermal manifestations on individual volcanoes.

- Flanking the volcanoes are very thick and deep conductors, which have been interpreted as volcanoclastic sediments.

- The trend of the resistivity at sea level is aligned with the strike of the exposed faults, consistent with the distribution of lava and pyroclastics related to fissure eruptions along the rift axis as well as eruptions associated with the volcanic centers. However, between Paka and Silali volcanoes the resistivity trend is offset to the west. This break and the accompanying offset indicates a possible eastwards shift of the axis of the rift alignment between Paka and Silali volcanoes.

- The lack of a well-developed low resistivity cap in some parts of the volcano edifices could be related to lack of geothermal activity or to lower production of smectite in trachyte. This is because trachyte is lower in magnesium than in basalt therefore magnesium must be added to trachyte by groundwater to form smectite (Cumming, 2016).

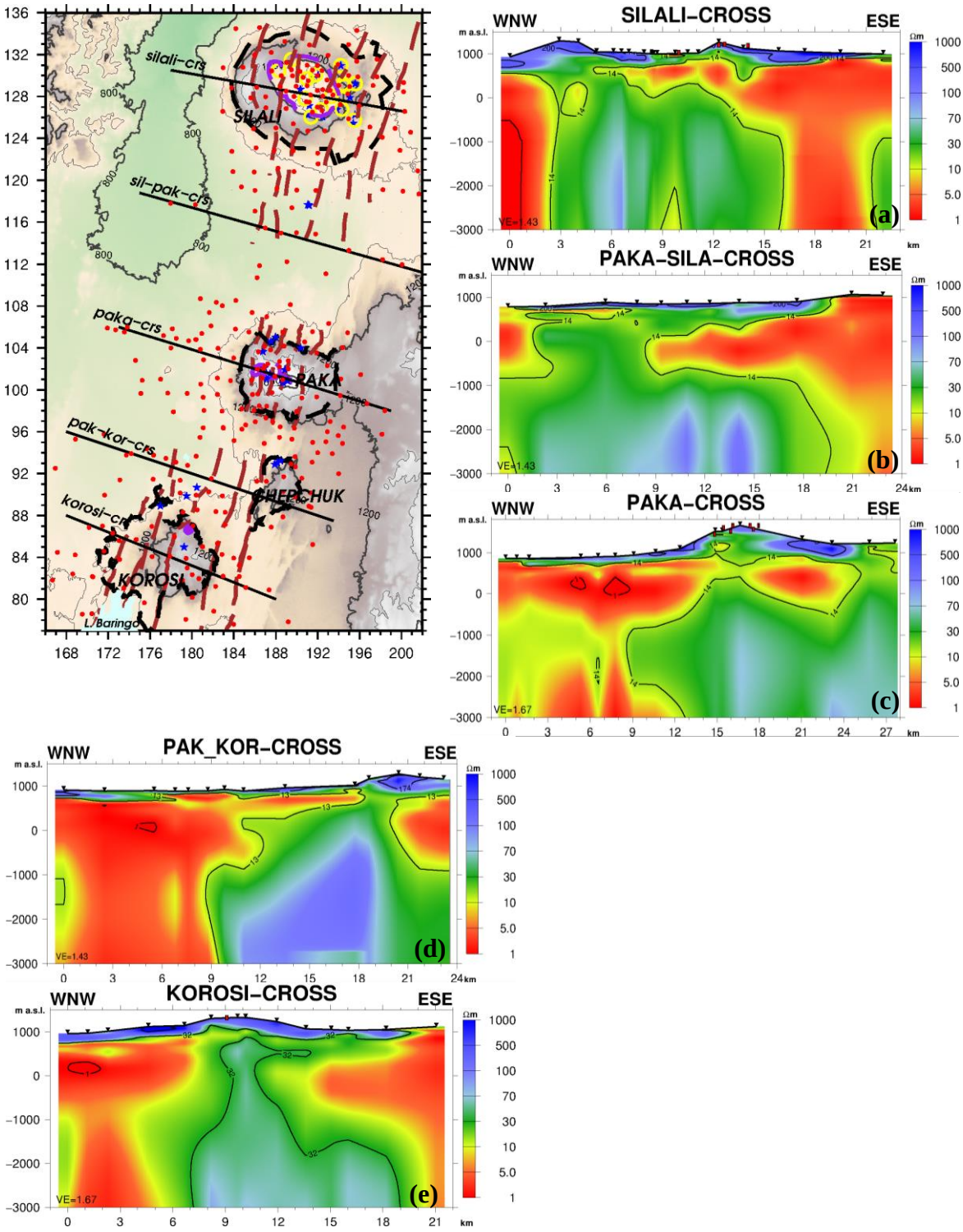

Figure 2.1: Resistivity cross-sections across Korosi, Paka and Silali based on 1D joint inversion of MT and TEM data: From top; (a) across Silali; (b) between Paka and Silali; (c) Paka; (d) Chepchuk and (e) Korosi volcanoes as shown on the location map to the left. Inverted triangles are MT stations and Red symbols on cross-sections *are fumaroles. Volcanoes are shown in broken black lines and craters in purple. Blue stars and yellow rings: geothermal surface manifestations.*

3 PAPER II: Joint modelling of Gravity and resistivity of Northern Kenya rift

3.1 Summary

Gravity studies in the northern Kenya rift segment have been carried out on a regional scale and therefore have focused on large rift structures with >70 km depth extent and >200 km width. This implies that structures that are of local importance have been given little attention and few gravity models at the scale of the volcanoes extending along the North Kenyan rift have been studied. With this realization, this study acquired data in an area (30 km wide by 55 km long) covering Korosi, Paka and Silali volcanoes in order to detect density features at the scales of the individual volcanoes, and extended to examine variation along the rift axis. Since the areal extent of the current survey is smaller than the regional surveys, the larger regional trends were removed in the regional-residual separation in order to allow modelling of smaller residual features as shown in Fig. 3.1 (a-c). Therefore, the current data set is adequate to model the details of the central gravity high and the immediate gravity low flanking inner rift axis but not the outer edge of the rift or the deeper roots of the rift below 5 km depth.

Models deeper than (~5 km) could not be supported by the more limited gravity data distribution (20 to 30 km wide). This disadvantage was offset by reducing the model ambiguity in several ways, including jointly interpreting the gravity model with MT resistivity imaging, by correlating the gravity with local geology (Dunkley et al., 1993), by using measured densities (Cantini et al., 1990) from other EAR volcanoes, and by considering the petrophysical properties from boreholes in roughly analogous areas. Based on these considerations, the pattern of the gravity could be fit using models to a depth of only 3 km.

This allowed us to model gravity in conformity with MT resistivity and geological structures as mapped on the surface. Rock samples from a geologically comparable area at Suswa volcano (Cantini et al., 1990) showed that a wide range of densities are expected in the study area. Trachyte and basalt lavas have a typical density of 2.55 g/cm^3 at most depths and alteration states. In contrast, trachytic pyroclastics have a density ranging from 1.2 to 2.5 g/cm^3, depending on whether they are dry or wet, altered to smectite clay and still hydrated with low density, altered at higher temperature to more crystalline chlorite-illite clay of much higher density; or buried to greater depth and so more compacted to higher density. Volcanoclastic sediments have a similar density range of 1.8 to 2.5 g/cm^3, with similar sources of the variation. The metamorphic rocks that outcrop adjacent to the rift and are expected to floor the rift are likely to have a density of over 2.8 g/cm^3.

3.2 Main highlights

- Residual Bouguer maps show a clear NNE-SSW positive gravity anomaly extending through the inner rift segments. The gravity processing and modelling illustrate how the overall gravity trend correlates with the mapped fissures of the axis of the rift.

- Gravity results are in agreement with the westward offset in high resistivity seen in the Silali sector north of Paka volcano (Fig. 3.1d). This pattern has been interpreted as a possible buried structural step-over in the rift alignment between Paka and Silali volcanoes. Both studies suggest that Silali volcano lies west of the currently active rift zone, which has gradually moved eastwards (based on younger eruption centers) to align with the Paka volcanic axis.

- Combined resistivity and 2D gravity models reveal three density categories, from shallowest to deepest: 1) a high resistivity surface layer modelled as intermediate density and consisting of low density tuffs and high density lavas; 2) a low resistivity smectite clay cap modelled as low density altered tuffs; and 3) a resistive layer modelled as high density volcanic, intrusive and Precambrian metamorphic rocks.

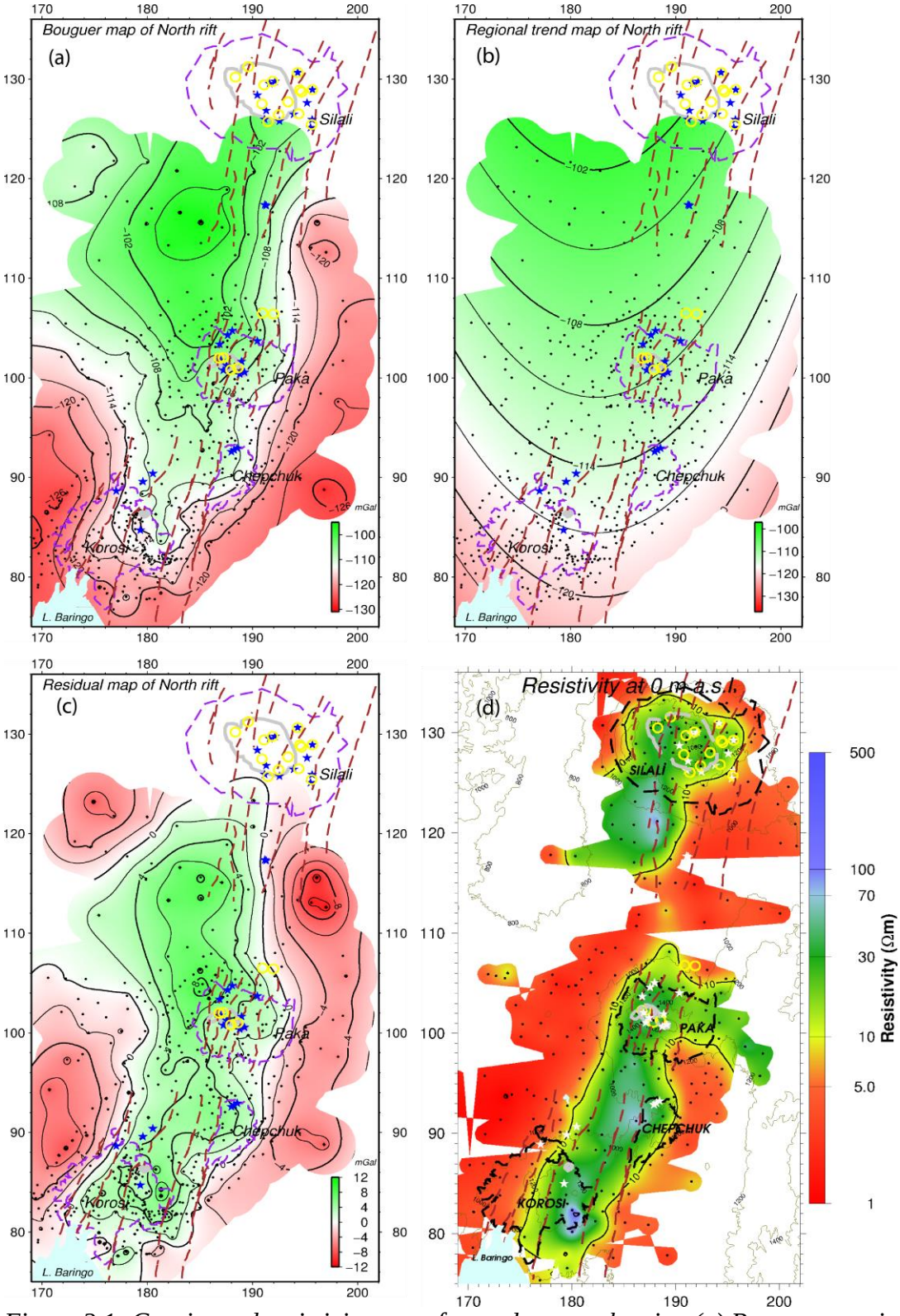

Figure 3.1: Gravity and resistivity maps for study area, showing (a) Bouguer gravity (b) Regional gravity (c) Residual gravity and (d) Resistivity at sea level. Stars and yellow rings are geothermal surface manifestations, purple and black dashed line outline the boundaries of the volcanoes, and brown dashed lines show fissure swarm. Coordinates are in UTM in km zone 37 (WGS84).

4 PAPER III: A review and comparison of developed and undeveloped geothermal systems in the Kenya Rift based on resistivity, gravity studies and geological structure.

4.1 Summary

In this study, a choice of 7 volcanoes aligned with the axis of the Kenya Rift are considered, two of which host developed geothermal fields and the rest are at exploration stage. These developed fields can be used as analogs in the investigation of similar undrilled geothermal prospects in the North Rift. Based on resistivity and drilling results at both the Olkaria and Menengai developed fields, the overall reservoir at Olkaria has much larger area, much deeper and possibly thicker than at Menengai. Shallow resistivity at Menengai show a thin low intensity smectite cap especially at the centre of the caldera where majority of productive wells have been drilled. Away from the central summit area thicker moderate resistivity dominates and the wells drilled there have not been so productive. The depth at the base of Menengai reservoir is constrained by intrusions. Similarly, by comparing results from other undeveloped geothermal systems we can draw comparisons with these two developed areas. To aid in comparisons we review the resistivity responses for each area including system capping and volcanic systems relative to rift activity.

In the usual case for volcano-hosted reservoirs, low resistivity smectite clays form at temperatures from about 50 to 90°C and are gradually converted to chlorite and/or illite as temperatures increase (Árnason et al., 2000) until hydrated smectite has entirely disappeared by about 220 °C. In the most typical geothermal cases, a map of the base of the clay cap (BOC) marks the transition from low temperature cap to high temperature reservoir if the transition takes place over a geothermal reservoir and if the alteration mineralogy reflects current temperature. In this case, the BOC was estimated by determining the elevation of the base of the <10 Ωm from the 1D models for each MT station and then contouring the data (Anderson et al., 2000). This is a risky approach especially for liquid dominated reservoirs and in areas where low resistivity smectite (Cumming 2016) is found in altered rocks adjacent to geothermal systems or as a result of the clays in sedimentary shales, weathered volcanic lahar and ash deposits commonly found in basins adjacent to volcanoes. The Map of BOC shows that the transition occurs at elevation of above 1000 m in the areas south of Longonot, Olkaria-domes and Olkaria NE

but appear to be deeper below the Suswa caldera and Olkaria-west. Similarly, BOC elevation have been contoured for the Korosi, Paka and Silali volcanic zones showing a consistent elevation along the fractured rift zone between the volcanoes while getting shallower beneath the volcanic edifices. On the margins of the volcanoes a thick low resistivity (<10 ohm-m) dominates on either side of the studied northern Kenya volcanoes, Fig 4.1(a-c) and to the western-most margin at Olkaria complex (Fig 4.1e).

Some areas also lack conductive cap especially those underlain by trachyte or more recent unaltered eruption vents and therefore may act as potential places where cold water could penetrate the broken clay cap. Due to tectonic movements crack may form through the older clay cap cooling the reservoir substantially especially from the margins. At both Olkaria and Menengai, MT does not detect either cooling in the reservoir or breakages in the clay cap; these express themselves as temperature reversals in the wells and where they have been drilled into fossil alteration the wells have turned out to be non-productive. To alleviate these challenges, a detailed assessment that includes geology, geochemistry and hydrology need to be incorporated in a conceptual model.

To test whether magma can be detected beneath the volcanoes, we designed a 2-D mesh for the Paka volcano and generated synthetic data through forward modelling. Synthetic model studies are useful because the true models are known, and therefore the 1D inversions used in this study can be tested for its ability to recover the known structure. Models tested in this study were done by setting known clay cap dimensions in a resistive half space and imposing deeper conductors corresponding to magma bodies of different dimensions and then compute the MT responses to a range of magma body sizes and then test the ability of 1D inversion to detect the body using synthetic 2D MT data. This was used to demonstrate what can be reliably resolved at depth using 1D inversion and what cannot. For cases where the near-surface layer is very conductive and thick and the magma body has a resistivity of 3 ohm-m embedded in 100 ohm-m rock, then resolution of deeper magma is not easily resolvable. Magma can only be resolved below the clay cap if its resistivity is low and lateral dimensions are larger than their depth.

4.2 Main highlights

- From the resistivity patterns (Fig. 4.1) and the modelled magma depths this study suggests that Suswa and Silali volcanic systems might resemble Olkaria and are therefore likely to host much large (thicker) resource. However, resistivity at Suswa has a tabular 2 km thick moderate resistivity slab surrounding it with only a very thin low resistivity cap but lacks MT data over the inner caldera. On the other hand, Paka and Longonot geothermal systems might be close to Menengai and likely to host a thin resource on top of the heat source.

- The evaluation of geothermal prospects especially the undeveloped-fields based on base of the clay cap is an essential approach in well targeting.

- Resistivity can effectively reveal sub-surface geothermal properties even in areas lacking both thermal and geological structural features.

- A full 3D inversion of the MT tensor gives results that are comparable to the 1D joint inversion of MT and TEM data across a selected cross-section through the summit area of Paka volcano in the top 2 km. The resolution of the resistivity structure beneath the clay cap is fairly consistent between the two models which gives us confidence to extend the 1D inversion beyond the clay cap though with potential limitations.

- The occurrence of shallow seismicity in the upper crust is an indication that the base of seismicity will be at the brittle-ductile transition especially when consistent with dike intrusions. This could as well be potentially a consequence of cooling in the shallow reservoir where cold-water flow interacts with hot rocks. On the other hand, lack of seismicity as in the case of Silali might point at the uniform stress state of the crust with respect to the deeper magma chamber.

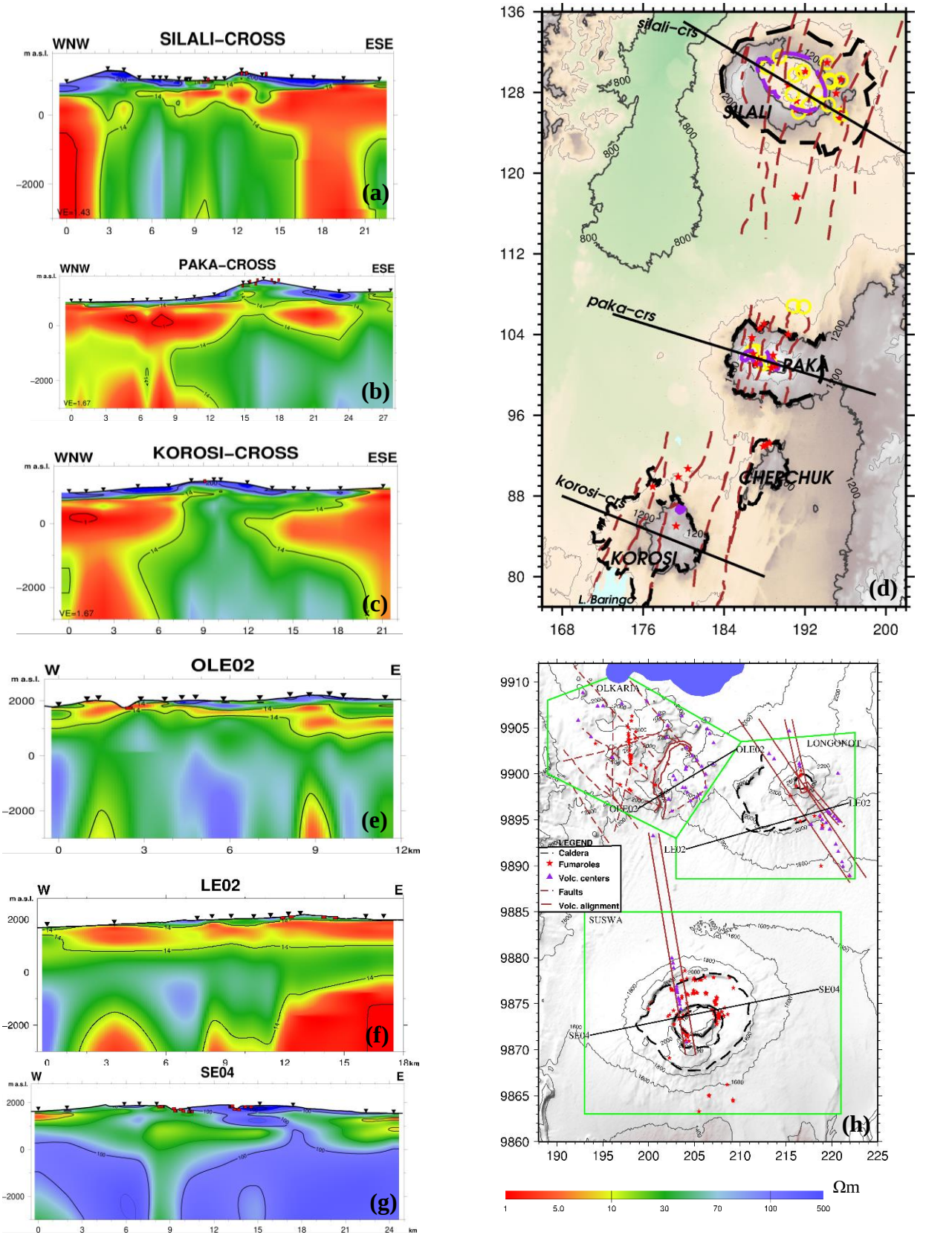

Figure 4.1: Resistivity cross-sections through the volcanoes in the north and south rift segments (a) Silali (b) Paka (c) Korosi (d) N. rift location map (e) Olkaria (f) Longonot (g) Suswa and (h) S. rift location map. Inverted triangles are MT stations, red rectangles are fumaroles on-profile. On the location maps volcanoes/calderas are marked by broken-black lines, broken-brown lines are faults and fissures, stars are fumaroles, yellow rings are altered surfaces, purple triangles are volcanic centres, brown lines mark volcanic alignments and green boxes show geothermal prospect boundaries in south rift.

5 General Conclusions

This dissertation presents the use of electromagnetic and gravity methods to characterize geothermal systems hosted in volcanic zones of the Kenya rift. The two methods have been able to consistently reveal the pattern of hydrothermal systems occurrence and related them with the known surficial structures. A major finding of this study is the delineation of a buried trend not discernible from geological surface mapping and interpreted it as an older buried rift trend north of Paka volcano. This trend is consistently mapped by both resistivity and gravity and implies that the rift could have moved eastwards in the recent past. This is supported by occurrence of more active thermal manifestations eastwards.

This study was focused on a regional-wide analysis of several volcanoes so as to examine the overall geophysical pattern in the entire volcanic zone. Some earlier isolated studies identified low resistivity zones on the flanks of the volcanoes which could not be clearly interpreted. These low resistivity zones have been delineated in this study both by resistivity and concluded that these zones are very unlikely to be prospective for geothermal development. They result from deposition of low resistivity and low density volcanoclastics and sediments that have been weathered or altered where they are below the water table, as is common for such clastics. They however align along the edges of the high temperature hydrothermal systems identified in the study area.

The study has identified a resistivity pattern typical of a volcano-hosted geothermal systems with a generally high resistivity unaltered surface formations, likely host for cooler meteoric aquifers; overlaying a low resistivity clay cap typically characterized by very conductive smectite clays. However the clay caps in trachytic volcanics are sometimes not as conductive as in basalts, possibly due to lower content of magnesium in trachyte compared to basalt, which has to be added to trachyte by groundwater to create abundant smectite. The higher resistivity zone beneath the clay cap may be associated with the propylitic alteration of a high temperature geothermal reservoir. If resolvable, localized zones of low resistivity below the resistive reservoir might be associated with magma that forms the heat source for the geothermal system.

To test the size of magma body that can be resolved, synthetic MT data was computed from 2D resistivity models derived from the same profiles as the real data. Drilling has intercepted magma at Menengai but MT data has not been able to resolve it which implies that the magma is too small to be imaged. Modelled synthetic data confirms that the dimension of magma at Menengai needs to be atleast 4 km wide for it to be identified by 1D inversions of MT. Synthetic model studies are useful because the true models are known, and therefore the 1D and 2D inversion can be tested for its ability to recover the known structure. The resolvable size of magma is subject to the conductivity and thickness of the near surface layer in which case magma can only be resolved below the clay cap using 1D inversion (of noiseless data) if its lateral dimensions are larger than the depth to the top of the body.

Considering both the resistivity pattern and the modelled magma depths this study suggests that Suswa and Silali volcanic systems might somehow resemble Olkaria and are therefore likely to host much large (thicker) resource. On the other hand, Paka and Longonot geothermal systems might be close in resemblance to Menengai and likely to host a thin resource.

Mapping of clay cap geometry is aimed at inferring locations where clay alteration occurs at shallow depth and can be roughly used to approximate potential areas where reservoir is shallowest hence suggest upflow zones. This approach however, has many pitfalls, most commonly, drilling an outflow rather than the reservoir. Areas where the resistivity pattern indicates deep base of the smectite zone are riskier for geothermal well targeting. The Map of BOC shows the transition occurs at elevation of above 1000 m a.s.l in the areas south of Longonot, Olkaria-domes and Olkaria NE but appear to be deeper below the Suswa caldera and Olkaria-west. Similarly, BOC elevation of about sea level have been contoured for Korosi, Paka and Silali zone.

6 Further research

At the heart of the analysis of this MT data is the realization of the importance of MT remote reference; This however was not applied in the current study. I acknowledge that this approach could have improved the quality of data and probably the modeled output. I have however initiated a plan of establishing locations that could serve as good remote sites for future MT data acquisition. With on-going drilling and installation of power lines within and close to the geothermal fields in the EARS low quality data will continue to be acquired and the setting up of remote reference site for use by most MT practitioners in the East Africa region will go a long way in alleviating the MT data quality issues.

A detailed full tensor 3D MT inversion is recommended once a good quality MT data is collected for the entire volcanic segment under study; this will aid in development of a detailed conceptual model of the area. In addition, a 3D inversion code either MoDEM or CGG code should be availed to carry out the inversion. To better define and characterize density structure of the segment studied here an extensive gravity survey is proposed to cover the entire Silali volcano to the north and extending to the rift margins on either side of the volcanic area under this study.

Further studies to address the lack of seismicity at Silali volcano and understand the rift dynamics would benefit from the on-going studies by the author on the ambient noise tomography (ANT). This is effective especially when applied in conjunction with the earthquake tomography since ANT can resolve shallow velocity structure particularly in the rift setting like the EARS where teleseismic/local events recorded by the network cannot resolve small dimensions relative to the wavelength of the low velocity bodies. Preliminary ambient noise study in the northern Kenya rift show that it has capability to constrain the upper velocity structure. Since depth is the most inaccurate parameter in microearthquake hypocenter analyses and the fact that earthquakes do not normally occur near the surface then ambient noise is a means of further constraining earthquake depths.Microseismic monitoring surveys are arguably the best practice for developed geothermal fields where produced water will be injected into rocks below 1 km depth that are >50°C hotter than the injection fluid or for undeveloped geothermal prospects where shallow magma may be present. After a limited initial survey has established that sufficient seismicity exists to warrant a larger scale survey, we recommend that seismic arrays be installed with capabilities suitable for magma detection at all seismically active prospects. For example, on-going microearthquake monitoring in the NKR volcanic zone has detected shallow seismicity at Paka volcano but not at Silali volcano, justifying a more detailed seismic monitoring survey at Paka. To monitor temporal changes, ground deformation monitoring by INSAR should also be regularly used to give important information on subsurface changes and magma movements.

References

Allis, R.., 1990. Geophysical anomalies over epithermal systems. J. Geochem. Explor. 36, 339–374.

Anderson, E., Crosby, D., Ussher, G., Zealand, N., 2000. Bulls-Eye ! - Simple Resistivity Imaging To Reliably Locate the Geothermal Reservoir. World Geotherm. Congr. 909–914.

Árnason, K., 2008. The MT static shift problem. GeoSurvey Rep. ÍSOR/08088; Reykjavik; Iceland; 17 pp.

Árnason, K., 1989. Central loop transient electromagnetic sounding over a horizontally layered earth (No. OS-89032/JHD-06). Reykjavik: Orkustofnun.

Árnason, K., Karlsdottir, R., Eysteinsson, H., Flóvenz, Ó.G., Thor, S., 2000. The Resistivity Structure of High-Temperature Geothermal Systems in Iceland. Proc. World Geotherm. Congr. 2000 923–928.

Caldwell, T.G., Bibby, H.M., Brown, C., 2004. The magnetotelluric phase tensor 457–469. doi:10.1111/j.1365-246X.2004.02281.x

Cantini, P., Cataldi, A., Pinna, E., 1990. Gravity study of the structure of Suswa volcano and basement in the Kenya Rift. Geothermics 19, 367–384. doi:10.1016/0375-6505(90)90039-E

Chorowicz, J., 2005. The East African rift system. J. African Earth Sci. 43, 379–410. doi:10.1016/j.jafrearsci.2005.07.019

Cumming, W., 2016. Resource Conceptual Models of Volcano-Hosted Geothermal Reservoirs for Exploration Well Targeting and Resource Capacity Assessment: Construction, Pitfalls and Challenges. Geothermal Resources Council Transactions. Geotherm. Resour. Counc. Trans. 40, 623–638.

Cumming, W.B., Nordquist, G.A., Astra, D., 2000. Geophysical Exploration for Geothermal Resources – An Application of Combined MT-TDEM, vol.19. Society of Exploration Geophysics, pp. 1071 – 1074 (extended abstracts).

Dunkley, P.N., Smith, M., Allen, D.J., Darling, W.G., 1993. The geothermal activity and geology of the northern sector of the Kenya Rift Valley, British Geological Survey Research Report.

Ebinger, C., 2005. Continental break-up: The East African perspective. Astron. Geophys. 46, 2.16–2.21.

Essene, E.., Peacor, D.., 1995. Clay Mineral T hermometry: A critical perspective. Clays Clay Miner. vol 43, 540–553.

Flovenz, O., Spangenberg, E., Kulenkampff, J., Arnason, K., Karlsdottir, R., Huenges, E., 2005. The role of Electrical conduction in geothermal exploration. Paper presented at

the World Geothermal Congress, Antalya, Turkey.

Gunderson, R., Cumming, W., Astra, D., Harvey, C., Ussher, G., Harvey, C., Johnstone, R., Anderson, E., Zealand, N., 2000. Analysis of smectite clays in geothermal drill cuttings by the methylene blue method : for well site geothermometry and resistivity sounding correlation. Proc. World Geotherm. Congr. 1175–1181.

Hinze, W.J., Frese, V.R.R., Saad, A.H., 2013. Gravity and Magnetic Exploration: Principles, Practices, and Applications. Cambridge University Press 2013.

Jiracek, G., 1990. Near-surface and topographic distortions in electromagnetic induction. Surv. Geophys., 11,163-203.

Keller, R., Wendlandt, R.F., Prodehl, C., Baldridge, W.S., Olsen, K.H., Prodehl, C., Braile, L.W., 1991. A comparative study of the Rio Grande and Kenya rifts A comparative study of the Rio Grande and Kenya rifts. Tectonophysics 197. doi:10.1016/0040-1951(91)90050-3

KRISP Working Group, 1991. A compilation of data from the 1990 Kenya Rift International Seismic Project KRISP 90 seismic refraction-wide angle reflection experiment. Open-File Report 91-1, Univ. Karlsruhe, 80 pp.

Ledo, J., Queralt, P., Pous, J., 1998. three-dimensional regional structure 295–301.

McNeill, 1994. Principle and application of time domain electromagnetic techniques for resistivity sounding . Geonics Ltd., Ontario, technical note TN 27, 15 pp.

Mechie, J., Keller, G.R., Prodehl, C., Gaciri, S., Braile, L.W., Mooney, W.D., Gajewski, D., Sandmeier, K., 1994. Crustal structure beneath the Kenya Rift from axial profile data 236, 179–200.

Meju, M. a., 1996. Joint inversion of TEM and distorted MT soundings: Some effective practical considerations. Geophysics 61, 56. doi:10.1190/1.1443956

Melosh, G., Moore, J., Stacey, R., 2012. Natural Reservoir Evolution in the Tolhuaca Geothermal Field, Southern Chile. Proc. Work. Geotherm. Reserv. Eng. 37, 217–223.

Muñoz, G., 2014. Exploring for Geothermal Resources with Electromagnetic Methods. Surv. Geophys. 35, 101–122. https://doi.org/10.1007/s10712-013-9236-0

Nettleton, L.L., 1939. Determination of Density for Reduction of Gravimeter Observations. Geophysics 4, 176–183. doi:10.1190/1.1437088

Pellerin, L., Hohmann, G.W., 1990. Transient electromagnetic inversion: A remedy for magnetotelluric static shifts. Geophysics 55, 1242. doi:10.1190/1.1442940

Pellerin, L., Johnston, J.., Hohmann, G.., 1996. A numerical evaluation of electromagnetic methods in geothermal exploration. Geophysics 61, 121 – 130 61, 121–130.

Pointing, A.J., Maguire, P.K.H., 1990. A seismic velocity model for the Upper Mantle in Northern Kenya derived from teleseismic earthquake data. J. African Earth Sd~nces, Vol. 11, 391–399.

Ranganayaki, R., 1984. An interpretative analysis of magnetotelluric data. Geophsics 49, 1730–1748.

Reddy, I.K., Rankin, D., Phillips, R.J., 1977. Three-dimensional modelling in magnetotelluric and magnetic variational sounding. Geophys. J. R. Astr. Soc. 51: 313

– 325.

Simpson, F., Bahr, K., 2005. Practical Magnetotellurics, First publ. ed, Cambridge University Press. London.

Spies, B.R., Frischknecht, F.C., 1991. Electromagnetic sounding, in Nabighian, M. N., ed., Electromagnetic methods in applied geophysics, v. 2: Society of Exploration Geophysicists, p. 285 – 425.

Sternberg, B.K., Washburne, J.C., Pellerin, L., 1988. Correction for the static shift in magnetotellurics using transient electromagnetic soundings. Geophysics 53, 1459–1468. doi:10.1190/1.1442426

Swift, C.M., 1967. A magnetotelluric investigation of electrical conductivity anomaly in the southern United States. PhD Thesis. Massachusetts Institute of Technology, Cambridge, MA.

Telford, W.M., Geldart, L.P., Sherif, R.E., 1990. Telford, W. M., L. P. Geldart, and R. E. Sheriff, 1990, Applied geophysics: Cambridge University Press. 1990.

Ussher, G., Harvey, C., Johnstone, R., Anderson, E., Zealand, N., 2000. Understanding the Resistivities Observed in Geothermal Systems. Proc. World Geotherm. Congr. 1915–1920.

Vozoff, K., 1991. The Magnetotelluric Method, in Electromagnetic method in applied geophysics, 2B, edited by M.N. Nabighian, soc Explor. Geophys, Tulsa Okla, 641-711.

Ward, S., Hohmann, G., 1988. Electromagnetic theory for geophysical applications (Vol. 1): Society of Exploration Geophysicists. 1.

Ward, S.H., Hohmann, G.W., 1987. Electromagnetic Theory for Geophysical Applications. In: Nabighian, M.N., Ed., Electromagnetic Methods in Applied Geophysics, Vol. 1, Society of Exploration Geophysicists, 131-311. 1.

Paper I

Resistivity imaging of geothermal resources in northern Kenya rift by joint 1D inversion of MT and TEM data

Charles Muturia Lichoro, Knútur Árnason, William Cumming
Journal of Geothermics, 68 (2017) 20–32

Geothermics 68 (2017) 20–32

Contents lists available at ScienceDirect

Geothermics

journal homepage: www.elsevier.com/locate/geothermics

Resistivity imaging of geothermal resources in northern Kenya rift by joint 1D inversion of MT and TEM data

Charles Muturia Lichoro [a,d,e,*], Knútur Árnason [b], William Cumming [c]

[a] Geothermal Development Company Ltd., P.O. Box: 17700-20100, Polo House, Nakuru, Kenya
[b] ISOR Iceland GeoSurvey, Grensasvegur 9, 108 Reykjavik, Iceland
[c] Cumming Geoscience,4728 Shade Tree Lane, Santa Rosa, CA 95405, USA
[d] University of Iceland, Sæmundargata2, 101, Reykjavík, Iceland
[e] UNU-GTP, Orkustofnun, Grensásvegi 9, IS-108 Reykjavík, Iceland

ARTICLE INFO

Article history:
Received 16 December 2016
Received in revised form 11 February 2017
Accepted 13 February 2017

Keywords:
Geothermal exploration
Resistivity structure
Hydrothermal alteration
Joint inversion

ABSTRACT

An extensive electromagnetic (EM) survey comprising over 400 sites on the Korosi, Paka and Silali volcanoes in the northern volcanic province in Kenya was conducted in order to assess the occurrence of geothermal resources in the context of the geophysics of the major volcanic centers of the north Kenyan East African Rift System (EARS). This area lies within the (EARS) where active extension is currently taking place. A joint inversion of magnetotelluric (MT) and co-located Transient electromagnetic (TEM) has revealed a resistivity pattern consistent with the existence of several geothermal systems within the study area. Each geothermal system is characterized by a relatively resistive 100 Ω m surficial layer overlying a ~ 10 Ω m low resistivity zone interpreted as the hydrothermally altered clay cap of the system. The cap overlies a higher resistivity zone of about 60 Ω m with a top at about 1000 m depth, interpreted as a potential high temperature alteration zone. The trend of moderate high resistivity at the depth of the potential reservoir corresponds to the zone of intense faulting and fracturing as imaged on the surface. Similarly the moderate high resistivity at sea level mimics the trend of the rift with a break in between Paka and Silali volcanoes where the resistivity trend is offset to the west. This break and the accompanying offset maps a possible westward shift of the axis of the rift in the rift alignment between Paka and Silali volcanoes. Although the 1000–2000 m thick low resistivity zones imaged on the flanks of the Korosi, Paka and Silali volcanoes have been tentatively interpreted as volcanoclastic sediments, elsewhere in the Kenyan EARS, low resistivity zones adjacent to volcanoes have been interpreted differently. To address this ambiguity, these thick low resistivity zones will be further investigated, principally using gravity surveys.

1. Introduction

Active geothermal systems are characterized by the presence of a reservoir with geothermal fluids sustained by a heat source. Hydrothermally altered rocks are commonly present in and around the reservoir. The change in physical properties caused by hydrothermal alteration can be detected by various geophysical methods including a variety of resistivity methods as well as passive seismic, magnetic and gravity surveys. Resistivity methods, particularly magnetotelluric (MT) and transient electromagnetic (TEM) methods have played dominant role in imaging the geometry of geothermal reservoirs (Ussher et al., 2000; Rosenkjaer et al., 2015; Árnason et al., 2010).

Using a joint inversion of MT and co-located TEM data this study was aimed at imaging volcano-hosted geothermal systems within three volcanic areas in the northern Kenya Rift; Korosi, Paka and Silali, in order to infer their geothermal potential. Geothermal exploration effort in this region has been intermittent from the 1980s until 2010 when it was intensified after the formation of the Geothermal Development Company (GDC). Early studies included structural/petrological mapping (Macdonald et al., 1995; Smith et al., 1995; Williams et al., 1984; Dunkley et al., 1993), geochemical studies (Darling, 1998) and upper crustal seismic investigation (Maguire et al., 1994; Keller et al., 1994a). The earliest comprehensive account of geothermal exploration in the region is given by (Dunkley et al., 1993). The results indicated geothermal systems at shallow levels within volcanic centers with young trachytic activ-

* Corresponding author at: Geothermal Development Company Ltd, P.O. Box: 17700-20100, Polo House, Nakuru, Kenya.
E-mail address: cmuturia@gmail.com (C.M. Lichoro).

http://dx.doi.org/10.1016/j.geothermics.2017.02.006
0375-6505/

ity. Later studies have focused on the individual volcanic centers aimed at understanding different aspects of the resources, but a comprehensive geothermal resource assessment has thus far only been completed at Silali volcano (Melosh et al., 2014) while an assessment is in progress at Paka volcano.

MT resistivity surveys, combined with collocated TEM stations to address MT static distortions (Sternberg et al., 1988; Pellerin, 1990; Árnason et al., 2010; Manzella et al., 2004), are routinely used to resolve four conceptual elements of volcano-hosted geothermal systems (Cumming, 2016), enumerated here from shallowest to deepest. 1) The generally high resistivity unaltered surface formations typically host cooler meteoric aquifers that may be sources for cold water intrusion into a geothermal aquifer system if a cold aquifer at high elevation penetrates the reservoir cap. 2) The low resistivity clay cap is typically characterized by very conductive smectite clays, although clay caps in trachytic volcanics are sometimes not as conductive as in basalts. It has been hypothesized that this is because trachyte is lower in magnesium than basalt and that magnesium must be added to trachyte or phonolite by groundwater to make abundant smectite (Cumming, 2016). 3) The higher resistivity zone beneath the clay cap may be associated with the propylitic alteration of a high temperature geothermal reservoir, but this is ambiguous. The higher resistivity may be associated with lower temperature outflow, relict alteration zones, or hot but impermeable metamorphosed crystalline rocks. 4) Local zones of low resistivity below the resistive reservoir might be associated with magma that sometimes floors basalt or trachyte hosted geothermal reservoirs. The uncertainty in the interpretation of the third element, the resistive geothermal reservoir, can be significantly reduced by combining the resistivity images with the results of geochemistry, geology, structure and supporting geophysical surveys in a consistent range of geothermal resource conceptual models (Cumming, 2016).

Volcanoes built within subsiding basins are commonly surrounded by a thick zone of low resistivity volcanoclastic rocks underlain by resistive older volcanics or much older crystalline metamorphic and intrusive rocks. When a geothermal field below the flank of a volcano is located adjacent to such a basin, the volcanoclastics may have particularly low resistivity if smectite clay from the geothermal cap erodes into the basin or a moderate temperature hydrothermal outflow extends into the basin. However, particularly thick and deep low resistivity zones in the rift near the Olkaria geothermal field have been attributed to a more direct magmatic association, raising the possibility of an alternative interpretation for the zones adjacent to the Korosi, Paka and Silali volcanoes.

Previous studies of the geothermal system of Silali volcano (Wamalwa and Serpa, 2013; Lichoro, 2013; Cumming, 2014) showed very thick low resistivity zones imaged at 500–2000 m depth below the flanks of the volcano interpreted by Cumming (2014) to consist of clay-rich volcanoclastics and altered ash deposited on the margins of the current and former eruptive axes of the rift. A zone of high resistivity embedded within N-S aligned conductors on the southwestern flank of Silali, has been interpreted (Melosh et al., 2014) as an older rift zone dominated by fissure eruptions and now buried by lavas, the more recent volcanism near Silali has shifted to fissure eruptions within the present rift east and north of the caldera.

In this paper we correlate the resistivity structure of the Northern Kenya rift (including the Korosi, Paka and Silali volcanoes) with the surface geology, gas and water geochemistry (Marini, 2014) so as to provide a coherent inference of geothermal potential in the area. Using joint 1D inversion of MT and co-located TEM data, we model the resistivity distribution within the rift to support the development of geothermal resource conceptual models, for example, where a high temperature geothermal system is evidenced below the flank of a volcano by up doming of high resistivity at the base of the clay cap near fumaroles with gas geochemistry consistent with an underlying high temperature geothermal reservoir. Although Silali and Paka have been separately investigated using 1D and 3D MT-TEM resistivity imaging, this is the first integrated geophysical assessment of the geothermal resource potential of the Northern Kenyan rift as a whole. The ongoing research program includes a plan to acquire a more extensive series of gravity profiles across several segments of the Northern Kenyan Rift and integrate these with available geophysical and geoscience data to further develop the geological model for the large volcanoes and their intervening segmented rift fissures and basins. A series of resistivity cross-sections through the volcanic centers illustrate the initial interpretation and highlight ambiguities that ongoing gravity surveys and microearthquake monitoring are expected to resolve.

2. Evolution, geological and structural setting of the northern Kenya volcanic centres

The Kenyan Rift is part of the greater East African Rift System (EARS) which runs from the Red Sea in the north to Mozambique in the south, a distance of about 3000 km. The Kenya Rift is at an advanced stage of evolution having formed at about 30 Ma ago (MacDonald, 2003). Rifting developed as a result of initiation of mantle plume activity beneath east Africa forming two distinct eastern and western segments as it propagated from north to south, as evidenced from gravity and refraction seismic surveys (Ebinger et al., 1989; Nyblade et al., 1990; Achauer, 1992). The Kenyan Rift is a part of the eastern branch of the EARS, which is characterized by much thicker section of recent volcanic rocks and shallower magma accumulation than in the western branch of the EARS. Refraction seismic studies have also shown crustal thinning northwards from 35 km depth beneath Lake Baringo in the center of the Kenyan Rift to 20 km thickness in the Lake Turkana area at the north end (Fig. 1), spanning the study area (Maguire et al., 1994; Keller et al., 1994a; Mechie et al., 1997). Ebinger (2005) postulated this crustal thinning to be probably a combination of crustal extension and plume-related thermal erosion (Ring et al., 2014; Corti, 2009). Volcanism in this sector of the rift commenced about 23 Ma and continued until about 2 Ma forming half graben structures (Keller et al., 1991) that was subsequently infilled by volcanism within the rift. Volcanism continued through the Quaternary focused within the 10 km wide area around an axis along the Suguta Trough, north of Silali (MacDonald, 2003) which led to construction of a series of large shield volcanoes including Korosi, Paka and Silali. From south to north, Korosi, Paka and Silali are the largest central volcanoes in the northern Kenyan Rift. The area is located immediately north of the Lake Baringo and extends 60 km northwards (Fig. 1). It is within the inner trough of the Kenya rift which is bisected by an 8–10 km wide area of intense faulting and fracturing, extending N10°E, from L. Baringo to north of Silali Volcano. The MT and TEM survey area lies within this sector extending from the Korosi volcano in the south to Silali volcano in the north (Fig. 1). The geology of the survey area is mainly dominated by trachytes but with significant occurrences of basalts and pyroclastic deposits.

2.1. Geology and structure of Korosi

Korosi volcanic shield mainly consists of a trachyte lava pile of about 500 m thickness above the rift floor. Volcanic activity dates back to 0.5 Ma with alternating sequences of trachyte and basalt eruptions as seen in the stratigraphy. The volcano is bisected by a fracture zone of NNE-trending faults which steps progressively eastwards across the volcanic complex between the two major bounding faults within which numerous geothermal surface man-

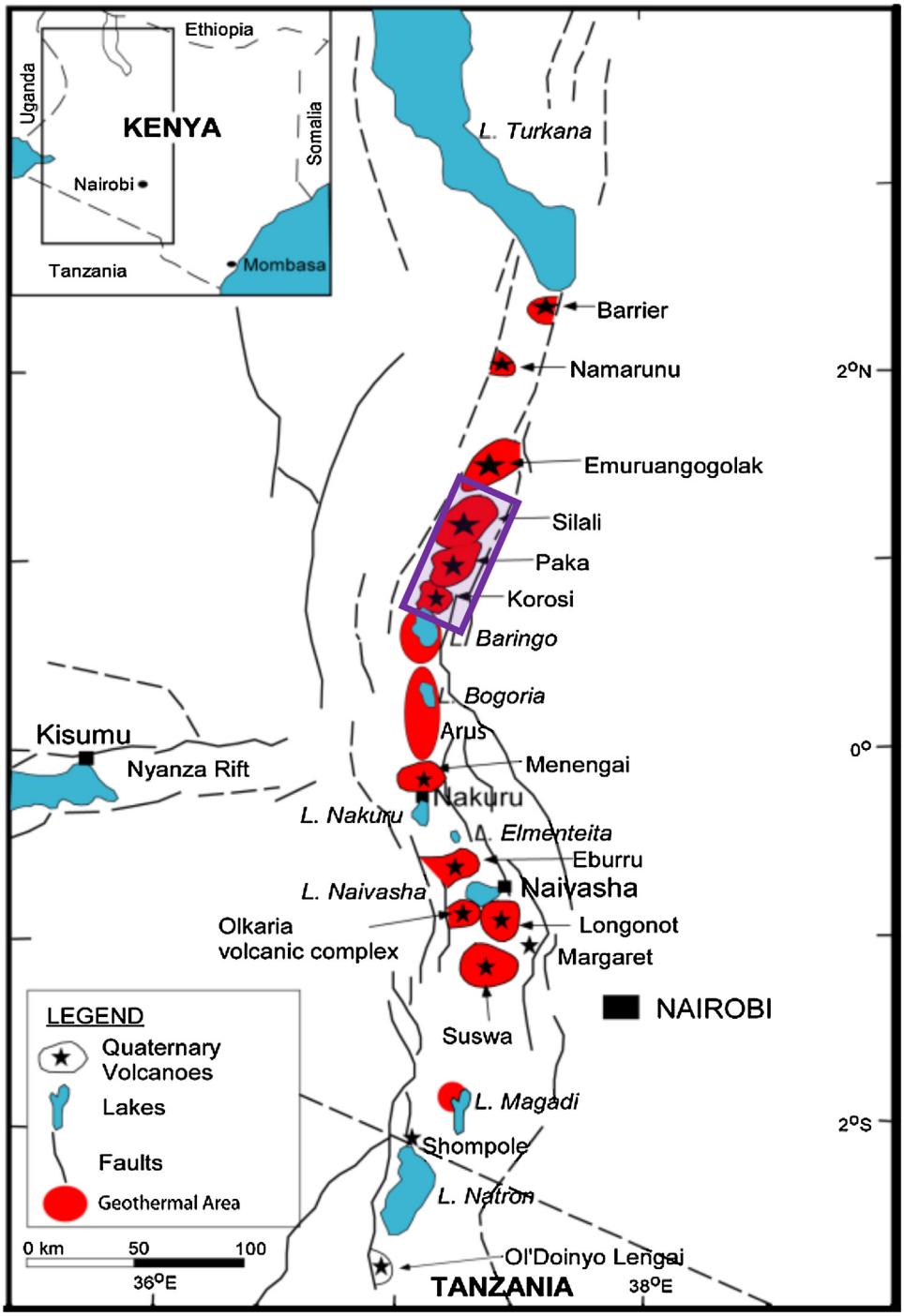

Fig. 1. A simplified tectonic map showing geothermal prospects in Kenya. The rectangular box shows the volcanoes under study.

ifestations occur (Dunkley et al., 1993). Pit craters formed at the summit of the volcano and are thought to be associated with lateral drainage of magma.

Surface manifestations include hot ground, steaming ground and fumaroles and cover an area of about 33 km^2 (see Fig. 2). Most manifestations are closely associated with NNE faults within a zone of generally intense fracturing to the east of the main boundary fault running along the western margin of the Korosi volcano. Temperatures in excess of 95 °C have been recorded in the area. Sinter is found at the locations of former hot springs, indicative of a higher local water table in the recent past.

2.2. Geology and structure of Paka

The Paka rift zone is bounded by the eastern and western boundary faults which constrain the geothermal activity in the area. Tectonically, Paka is dominated by a zone of intense normal faulting and fissuring both on the eastern and northeastern flanks (Dunkley et al., 1993). The buildup of the Paka shield was initiated by eruption of the Lower Trachyte formation at about 380 ka which was followed by a period of faulting and basaltic volcanism before the next sequence of trachytic eruptions began (Dunkley et al., 1993; Sceal, 1974). Later alternating sequences of trachyte and basalt eruptions followed before the eventual eruption of pyroclastic deposits at

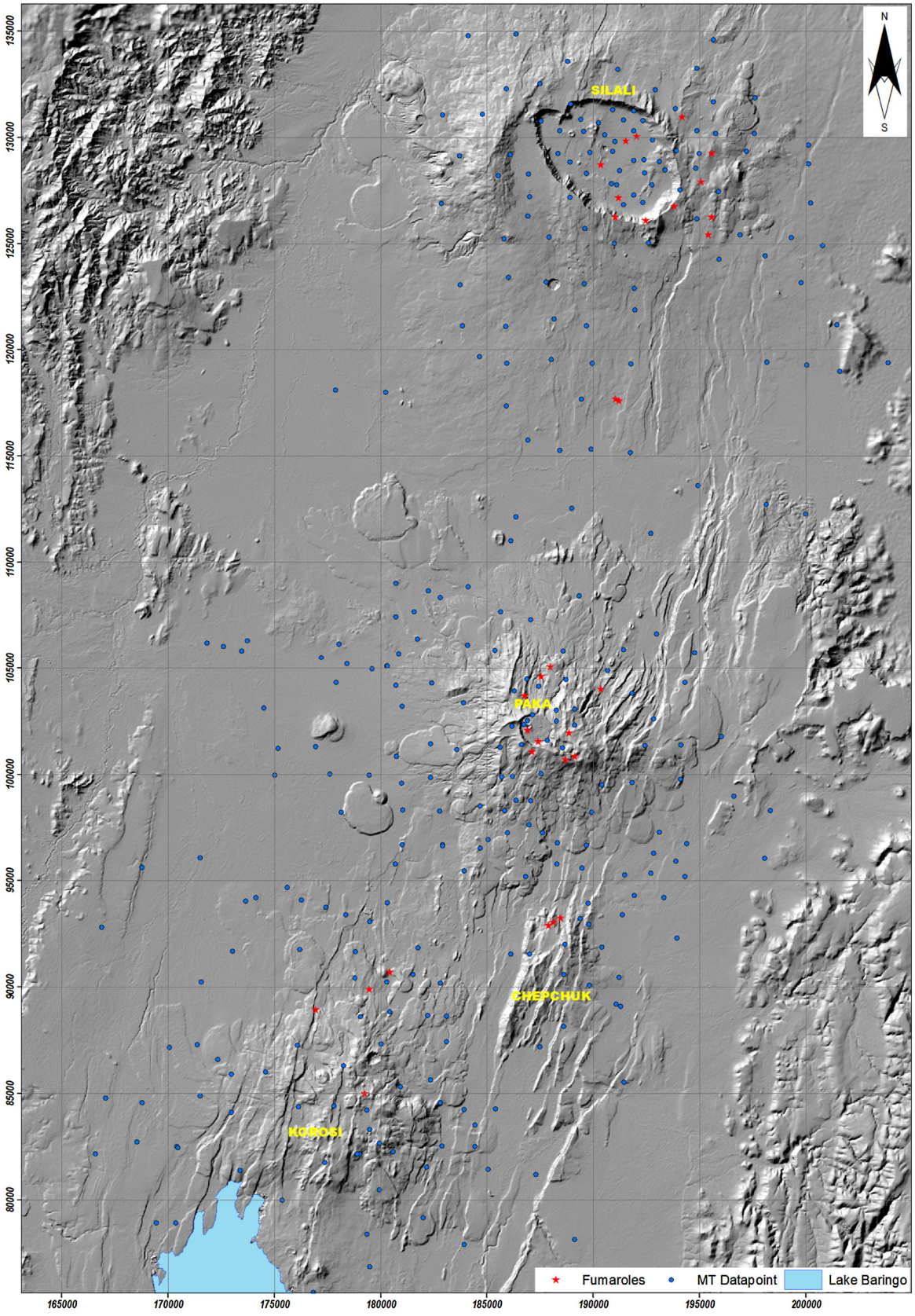

Fig. 2. Location of MT stations (blue dots) across the three main volcanic centres, Korosi, Paka and Silali. Red stars correspond to fumarole locations. Coordinates are UTM, zone 37, Arc 1960 datum. (For interpretation of the references to colour in this figure legend, the reader is referred to the web version of this article.)

about 10 ka which led to formation of the caldera at the summit (Dunkley et al., 1993). Post caldera eruptions produced trachyte and mugearite lava (oligoclase-bearing basalt) in the caldera floor. Structurally Paka is dominated by a NNE-zone of normal faulting (about 10 km wide) which cuts across the volcano and extends both northwards and southwards to Silali and Korosi respectively. Synthetic Aperture Radar Interferograms (InSAR) show that Paka volcano was active in the period 2006 and 2007 with an uplift of 21 cm centered at the Paka caldera (Briggs et al., 2009). The uplift has been attributed to an intrusion of magma into the uppermost crust, which Briggs et al. (2009) suggest is due to a magma body centered at a depth of 2.8 km with a lateral conduit that channels magma aside during deflation episodes.

Geothermal manifestations are extensive at Paka comprising fumaroles and areas of altered and steaming ground at up to 97 °C, mainly at the Paka summit craters and on the northern flank (Fig. 2). The manifestations are spread over a broad NNE – structural trending zone covering an area of about 32 km^2 (Dunkley et al., 1993; KenGen, 2007). These surface expressions occur on scoria and pumice cones aligned along the NNE-trending faults.

2.3. Geology and structure of Silali

Silali shield construction began at about 460 ka and continued until 225 ka (Dunkley et al., 1993). Ongoing eruptions culminating in a withdrawal of magma led to caldera collapse at between 64 ± 2 ka and 7 ± 3 ka based on the radiometric age of the lavas on the caldera wall (Dunkley et al., 1993). The youngest dated trachyte lavas are dated at 4 ± 2 ka and occur to the east of the caldera and basaltic lavas erupted on the northern flank and northeast of the volcano a few hundred years ago. Silali hosts a caldera at the summit measuring 7.5 km by 5 km with major axis in the NNW-ESE direction and is suggested to have initiated when the stress field around the volcano was in that orientation (Bosworth et al., 2003). The occurrence of the younger NE-SW alignment of volcanic cones to the east of the caldera suggest that a new stress field is evident within the rift valley axis whose minimum horizontal stress direction (SHmin) is sub-parallel to the long axes of the Silali caldera (Bosworth et al., 2000). Satellite radar interferometry observations in 2007–2008 (Briggs et al., 2009) has shown that the summit area at Silali has recently been undergoing active subsidence. Due to absence of a substantial amount of pyroclastic deposits younger than the lavas Dunkley et al. (1993) suggests that caldera collapse could have been triggered by magma withdrawal which drained laterally beneath the volcano. A north to north-northeast trending volcanic rift zone, 10 km wide and 30 km long which is characterized by an area of intense faulting, fracturing and minor grabens and shows horizontal tensile openings and aligned volcanic vents bisects the Silali shield.

The main geothermal manifestations around Silali caldera consist of areas of surface alteration and steaming ground, hot springs, and fumaroles (Fig. 2). The hottest and most extensive manifestations occur in the eastern half of the caldera floor where areas of surface alteration and fumaroles are aligned to the NNE fissure zone with recorded temperature up to 96.8 °C. Both CO_2 and radon concentrations are elevated in the areas of high temperature, suggesting deep controlling fractures from where the fumarolic fluids flow sub-vertically from deep aquifers towards the surface (Marini, 2014). Hot springs are found to the immediate west (Kapedo) and north-west (Lorusio) of Silali with measured temperatures of 55 °C and 82 °C respectively. These hot springs discharge water from a deep geothermal aquifer below the caldera mixed with shallow ground water.

3. Previous geophysical exploration

Geothermal exploration in the Kenyan northern Rift area began in the 1970s with gravity and geochemistry (Searle, 1970; Lippard and Truckle, 1978). The first significant advances occurred during the 1980s and 1990s with several deep crustal and upper mantle studies using refraction seismic and gravity data (Keller et al., 1994a, 1997, 1994b; Maguire et al., 1994; Mechie et al., 1997; Prodehl et al., 1997). The first MT and TEM surveys in the study area were completed in 2005 by the Kenya Electricity Generating Company (KenGen, 2007) and GDC followed up with extensive MT and TEM surveys from 2011 to 2014 (GDC, 2011). The data from these surveys are the basis of the resistivity imaging in this study.

The refraction seismic and gravity studies revealed high velocity and high density material within the rift zone attributed to upper crustal dikes, thought to connect to the volcanic centers (Ebinger, 2005; Swain, 1992). Mechie et al. (1997) suggest that the lower crust reflectors are due to solidified magmatic bodies at the crust-mantle boundary. Crustal thinning in the northern part of the Kenya rift (Mariita and Keller, 2007; Simiyu and Keller, 1997) has been attributed to crustal extension, probably due to plume activity beneath the rift segment. A positive gravity anomaly within the rift graben has been postulated to reflect dyke injection, related to magma reservoirs in the crust (Keller et al., 1994b; Mariita and Keller, 2007; Simiyu and Keller, 2001). Chorowicz, (2005), has suggested that sediments and volcanic layers in the graben are 3 km thick.

In 2010, a new geothermal exploration phase was initiated (GDC, 2011) as part of an initiative to explore for geothermal resources within the Kenyan Rift. Extensive MT and TEM surveys were carried out on all the three volcanoes considered here to be prospective areas for drilling (Lichoro, 2013; Cumming, 2014; Wamalwa and Serpa, 2013). The surveys revealed a detailed image of the resistivity pattern in the uppermost 2 km in Silali area, which is in agreement with the typical resistivity pattern expected for trachyte-hosted geothermal reservoirs. From 2010 to date over 400 soundings have been carried out in this region (Fig. 2). Some of the stations were excluded from the present study because of poor data quality or because the MT was missing TEM data to provide a static correction (Sternberg et al., 1988). Recently a microearthquake network has been installed on Korosi, Paka and Silali, to monitor local seismicity and a gravity survey is being been carried out in the area, both of which will be used in subsequent research and publications on this area.

4. MT and TEM data acquisition and processing

The MT and TEM surveys carried out in the Korosi-Paka-Silali area were designed to image resistivity from the near-surface to several kilometers depth in order to detect the characteristic resistivity patterns associated with occurrence of geothermal resources in the context of the geophysics of the major volcanic centers of the north Kenyan EARS. A total of over 400 MT and TEM soundings have been acquired in field campaigns between 2005 and 2014 in the entire study area (see Fig. 2). For most but not all survey sites, both MT and TEM were acquired.

The MT data were acquired with Phoenix MTU-5A 24-bit recording systems using porous pot electrodes and three induction coils providing a frequency range of 0.001–320 Hz. Telluric dipole lengths of either 70 or 100 m were used depending on terrain limitations. Although only a small proportion of the MT data were processed using a remote reference, electrical noise is very low at most MT sites in the study area and quality assurance procedures indicated that estimation bias due to the use of self-referenced processing (Chave and Jones, 2012) was seldom significant at fre-

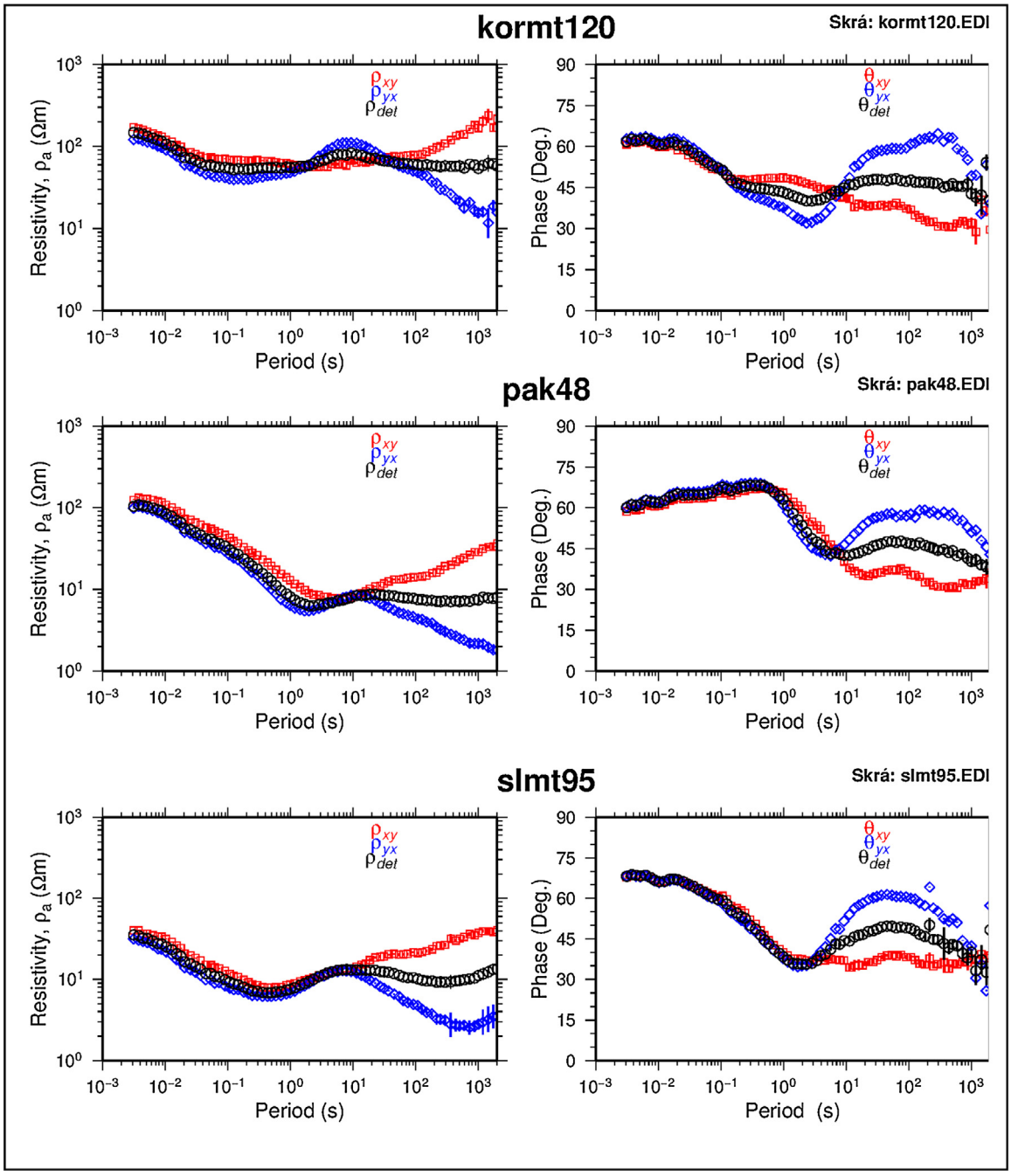

Fig. 3. Typical examples of apparent resistivity and phase curves of MT soundings (red and blue are xy and yx respectively) and determinant apparent resistivity in black symbols for Korosi, Paka and Silali respectively. A non-1D resistivity pattern is indicated by divergence of the red and blue apparent resistivity curves for periods longer than 1 s. (For interpretation of the references to colour in this figure legend, the reader is referred to the web version of this article.)

quencies higher than 0.1 Hz. However, this limited the reliable depth of investigation of the MT to about 2 or 3 km in much of the study area. The MT time series were processed using the programs SSMT2000 and MTeditor (Phoenix Geophysics, 2005), based on the robust approach described by Egbert and Booker (1986), to produce cross-power estimates and generate EDI files (Wight, 1991). Graphical displays of standard MT and TEM indicators of noise, static distortion, and dimensional distortion were used to produce a quality assurance table proposed by Cumming (2014) to assess the range of frequencies of each MT station that were suitable for 1D and 3D inversion. A sample of the MT apparent resistivity and phase curves from Korosi, Paka and Silali are shown (Fig. 3). The red and blue curves are apparent resistivity for the two polarizations with the black response showing the calculated invariant (determinant) apparent resistivity from which the 1D inversion was computed.

TEM data were collected using a Zonge GDP-32 data logger and a transmitter with current loop sizes ranging between 100×100 and 300×300 m square. A receiver coil with an effective area of 10,000 m^2 was placed in the centre of the transmission loop to measure the decay of the secondary magnetic field. For this survey, the transmitter square wave current ranged from 9 to 20 A at repetition frequencies of 16, 8 and 4 Hz. The measured TEM data was processed using the TemxZ program (Arnason, 2006) which provided editing, selection, averaging and error estimation tools to calculate late time apparent resistivity as a function of time. Since

the shield volcanoes in the study area have subdued topographic relief, TEM distortion due to topography is expected to be minimal.

4.1. 1D joint inversion of MT and TEM soundings

The program TEMTD (Arnason, 2006) was used to compute joint MT-TEM 1D Occam inversions of the TEM simultaneously with the MT determinant resistivity and phase. These joint 1D Occam inversions were interpolated to generate the resistivity maps and cross-sections in this study. In addition to adjusting the model parameters, TEMTD adjusts a shift multiplier for the MT apparent resistivity so that both the MT and TEM apparent resistivity can be fit by the same model. The Occam 1D inversion (Constable et al., 1987) used fixed exponentially increasing layer thicknesses and smoothly varying resistivities (Fig. 4). The MT apparent resistivity shown in Fig. 4 in blue was multiplied by 0.402 to fit the pseudo-MT curve generated from TEM sounding, shown in red (Sternberg et al., 1988), providing a consistency check of the two datasets. Noisy data points were masked to ensure smoothness in the Occam inversion and, for most of the stations, there was relatively good fit between the MT and TEM responses. In some cases where the fit was poor due to noisy data or non-one dimensional structures, the data was not considered in this study. MT data were also excluded at periods that were expected to introduce artifacts or seemed inconsistent with 1D inversion.

5. Joint 1D inversion results

5.1. Iso-resistivity maps

The results for the 1D Occam inversions of the MT invariant apparent resistivity and phase mode (Arnason, 2006) are presented as iso-resistivity contour maps and cross-sections across the area of study. 1D resistivity inversion maps and cross-sections from many geothermal fields have reliably imaged the resistivity pattern of geothermal systems to the base of the clay cap, above the reservoir (Cumming and Mackie, 2010; Ussher et al., 2000; Volpi et al., 2003; Árnason et al., 2010).

In the Korosi-Paka sector, the resistivity map at 800 m a.s.l (about 400 m depth) in Fig. 5a shows a conductive zone (<10 Ω m) on the western flank of Korosi volcano striking in a SW-NE direction (Fig. 5a) extending to west of Paka with a branch towards Chepchuk volcano. Elsewhere to the east moderately higher (10–100 Ω m) resistivities dominate. The section between Paka and Silali volcanoes is predominantly high resistivity (>100 Ω -m), inferred to be associated with the lava pile from the Katemening eruption (Dunkley et al., 1993). The flanks of Silali volcano are moderate in resistivity (10–100 Ω m) with a more conductive zone (<10 Ω m) within the caldera and extending to the east and southeast. The conductive zone within the caldera is interpreted to be due to hydrothermal clay alteration at this depth, which is in agreement with the surface manifestations.

In Fig. 5b, the resistivity pattern at 600 m a.s.l (about 600 m depth), is similar to the pattern at 800 ma.s.l but low resistivity (<10 Ω m) is more prominent on both east and west flanks of Korosi and Paka volcanoes and at the Silali caldera, although low resistivity is more extensive to the east and southeast of the caldera, tentatively interpreted as hydrothermally altered sediments. Elsewhere intermediate resistivity (10–100 Ω m) appears to align with the inner trough of the rift where numerous fractures and faults are mapped between the Korosi and Silali volcanoes. This zone is bounded by very conductive segments on both sides.

Resistivity pattern at sea level (Fig. 5c) shows continuation of low resistivity (<10 Ω m) as seen in the shallower levels above. These conductive segments seem to be more widespread bounding a resistive zone between Korosi and Paka volcano aligned to inner SW-NE striking rift boundaries. To the north of Paka volcano, the low resistivity connects to the inferred altered sediments to the southwest and east of Silali caldera. Moderate higher resistivity dominates the Silali caldera increasing further to the south where high resistivity (<100 Ω m) has been inferred to be associated with buried lava pile (Dunkley et al., 1993).

Iso-resistivity maps are shown (Fig. 5d–f) 400 m b.s.l, 1000 m b.s.l and 2000 m b.s.l. respectively. The lower resistivity seen in the shallower levels above seems to diminish in areal extent going deeper from 400 m b.s.l to 2000 m b.s.l as the moderately higher resistivity (10 Ω m to 100 Ω m) becomes more dominant in the inner trough of the rift and beneath the volcanoes. At 1000 m b.s.l the moderate high resistivity zone seems to extend beyond the inner trough with pockets of (>100 Ω m) resistivity appearing at northeast of Korosi volcano, south and northeast flank of Paka volcano.

At 2000 m b.s.l higher resistivity (>100 Ω m) dominates in the northeast of Korosi volcano, south and north of Paka volcano and to the southwest of Silali volcano. At Silali, deep low resistivity appears to the east of the caldera and to the southeast flank. These are areas of massive surface manifestations and where the most recent eruption took place.

5.2. Cross-sections

Previous results have demonstrated that cross-sections stitched from a profile of MT stations using Occam 1D resistivity inversions of the invariant mode can provide a realistic and robust display of resistivity structure of a geothermal system and has been widely used to build geothermal resource conceptual models for well siting and resource assessment (Anderson et al., 2000; Cumming and Mackie, 2010). Studies from several geothermal fields in Iceland (Árnason et al., 2010) have indicated that smooth,

minimum structure 1D inversion of the rotationally invariant MT determinant data can reproduce complex 3D resistivity structures fairly well. However in presence of dimensional distortion 1D inversion might exaggerate and offset resistivity boundary (Dyaksa et al., 2016). We drew resistivity cross-sections in WNW-ESE direction to show resistivity variations between the summit area and the flanks of the volcanoes (Fig. 6). All the profiles map very prominent thick conductors on either side of the volcanoes which has been interpreted as altered sediments and/or volcanoclastics deposited in the rift during past eruptions (Cumming, 2014; Lichoro, 2013). However, beneath the inferred volcanoclastics there appear vertically oriented resistivity contours below 1500 mbsl (Fig. 6) which we think could be caused by MT distortion due to lateral boundaries that are closer in distance than the depth of the feature. This distortion might limit model resolution at the base of the inferred volcanoclastics.

In the summit areas the resistivity pattern is characterized by a thin resistive (>60 Ω m) surficial layer underlain by a more conductive layer that is about 10 Ω m at the Silali and Paka volcanoes and about 30 Ω m at the Korosi volcano. The conductive layer is generally thinner in the summit areas where it is likely to correspond to low temperature hydrothermal smectite clay alteration and thicker adjacent to the volcanoes where it is interpreted as volcanic sediments and weathered ash with high smectite clay content. A higher resistivity zone is detected below the conductive clay layer on all of the MT profiles. The value of the higher resistivity below the conductor is more ambiguous, both because of inherent limitations to MT (Chave and Jones, 2012) and local data quality issues (Cumming, 2014). However, the elevation of the transition from lower to higher resistivity at the base of the conductor is typically reliably resolved using 1D inversions of the MT invariant or TE-mode in geothermal settings, except near lateral discontinuities in

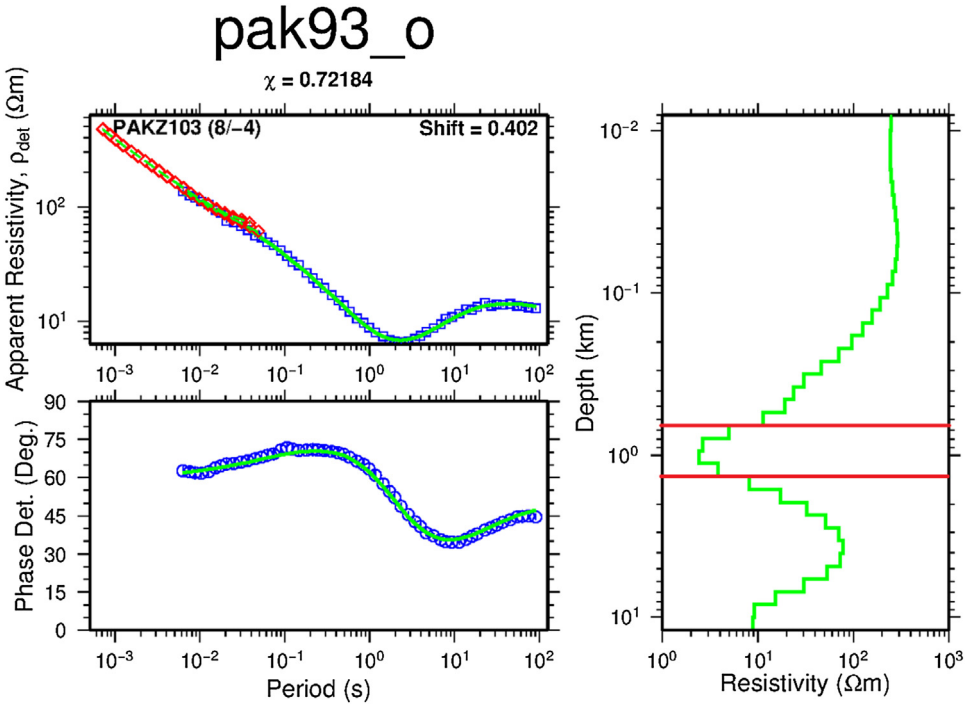

Fig. 4. Result of a joint 1D inversion of MT and TEM sounding. Red diamonds: TEM apparent resistivities transformed to a synthetic MT curve (Sternberg et al., 1988); blue squares: measured MT apparent resistivities; blue circles: apparent phase derived from the determinant of MT impedance tensor; green lines; synthetic MT and TEM responses calculated from the 1D resistivity model are shown in green in the right panel. Red lines show probable clay cap geometry. (For interpretation of the references to colour in this figure legend, the reader is referred to the web version of this article.)

the conductor (Dipippo, 2016) and this has been an important diagnostic in geothermal exploration. A local apex in this transition is sometimes correlated with the top of a high temperature geothermal reservoir (Anderson et al., 2000), although such features are ambiguous since they can also be correlated with warm bouyant outflows from a geothermal reservoir, shallow smectite clay overlying the resistive illite clay (phyllic) cap of a deeper geothermal reservoir, or relict alteration over an old reservoir that has cooled (Cumming, 2016). The base of the conductive zone (the top of the resistive zone) is more elevated below the eastern half of the Silali volcano, below the Paka summit area and to the SE of Korosi volcano, possibly corresponding to the apex of a high temperature geothermal reservoir. The ambiguity in the interpretation of the elevated base of the conductor and of the lateral transition from the hydrothermal clay cap over a potential geothermal reservoir to the adjacent clay-bearing sediments is addressed by interpreting the MT resistivity in the context of an integrated conceptual model that is consistent with all available geoscience data and thermodynamic constraints.

In order to characterize resistivity along the rift we constructed a cross-section cutting through all the volcanoes in the north-south direction and aligning with the orientation of the rift (Fig. 7). The profile shows a succession of resistive-conductive-resistive layers commonly associated with high temperature geothermal systems hosted in volcanic systems (Árnason et al., 2000, 2010). It shows a thin top resistive layer continuous along the entire section interpreted as volcanic piles in the shallow sub-surface. They overlie a conductive layer (~14 Ω m) with variable thickness and depths along the profile with a break in the region between Paka and Silali volcanoes where an inferred thick lava pile from the Katemening eruption (Dunkley et al., 1993) has been proposed. In both sectors, the conductive layer domes beneath Korosi-Paka area and beneath the eastern part of the Silali caldera before deepening significantly to the NE of Silali caldera where volcanoclastic deposition has been suggested. The doming of the conductive layer in the area between Korosi and Paka and in eastern half of Silali caldera could be related with up-flow zones below these areas. This is validated by high hydrogen concentrations measured in the discharged steam from the fumaroles at the summit areas at Silali, Paka and at the Korosi crater which might indicate proximity to a high temperature resource (Kipng'ok, 2011; GDC, 2011). Outside the summit areas lack geothermal surface expressions probably due to thick pyroclastic cover as seen in the Olkaria-Domes area in the southern rift where geothermal reservoirs have been discovered (Onacha, 2006).

6. Geothermal properties of the Korosi-Paka-Silali Block

Young calderas and volcanic edifices with surface manifestations of geothermal activity are indicators of potential geothermal resources. Using MT, we further identify and characterize areas of promising geothermal potential within different sectors of the study area. It should be noted that lack of any conductor would imply high risk of encountering an underlying commercial geothermal system. On the other hand, the presence of a conductor over a resistor is ambiguous because, although this pattern is typical of almost all geothermal reservoirs, it is also commonly observed in non-prospective areas. For example, it is typical of clay-rich sediments overlying older volcanics or metamorphic basement in rift basins. However, the presence of a conductor overlying a resistor with the base of the conductor rising towards thermal manifestations with high temperature geothermometry is a more reliable indication of a geothermal reservoir and, in such cases, the resistivity pattern is the principal constraint on resource size.

A volcano-hosted geothermal system within the Silali caldera and extending east and southeast of the caldera (Fig. 6a) is characterized by low resistivity at shallow depths that may be due to higher smectite clay content. Beneath the smectite cap east of caldera, an extensive higher resistivity zone, interpreted in part as hosting a geothermal reservoir, is apparent if we are to consider

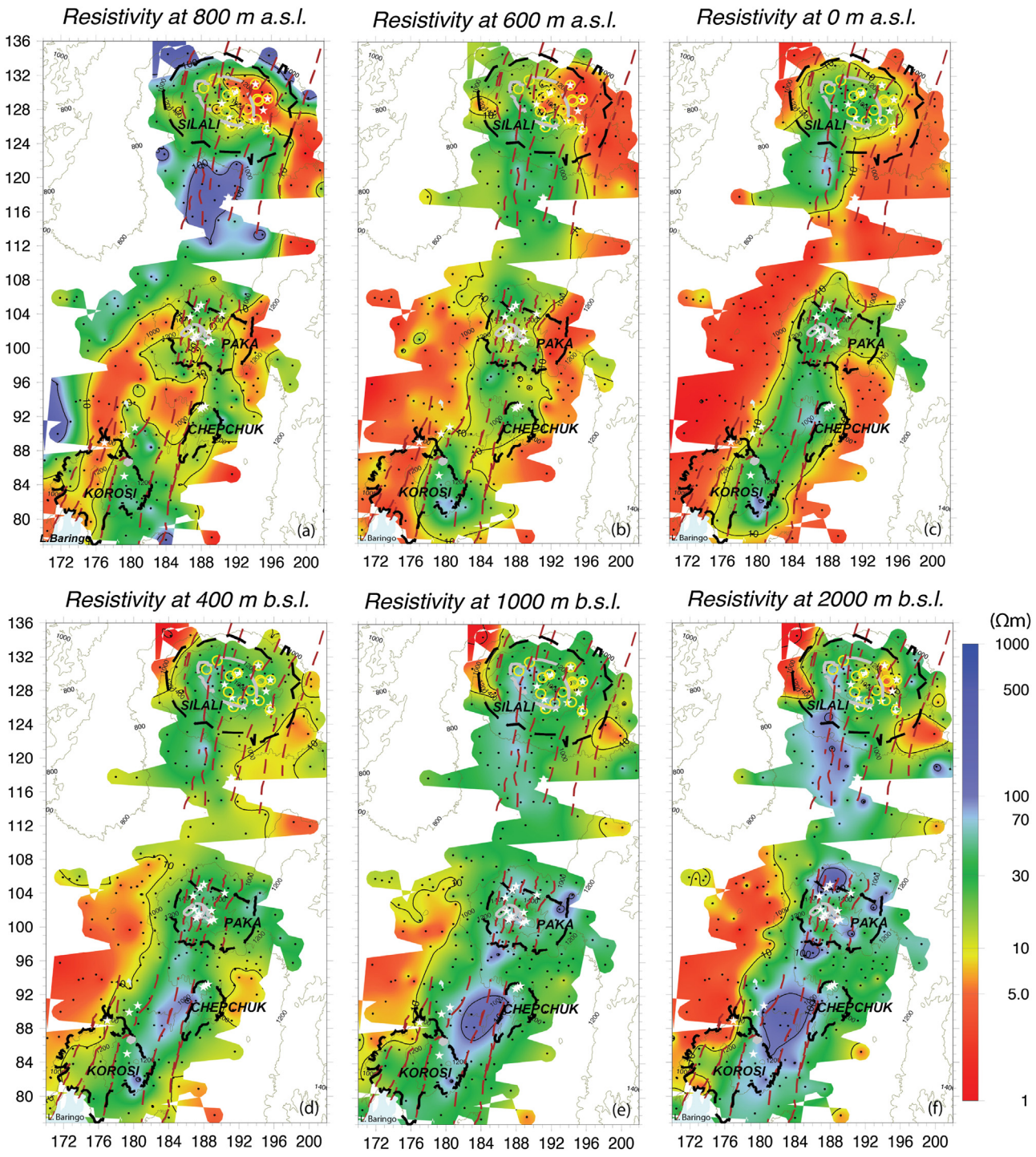

Fig. 5. Resistivity at (a) 800 m a.s.l; (b) 600 m a.s.l; (c) sea level; (d) 400 m b.s.l; (e) 1000 m b.s.l and (f) 2000 m b.s.l in the Korosi – Paka – Silali area based on 1D joint inversion of MT and TEM data: Main surface faults and fissures are shown in brown, broken black lines delineate the outline of individual volcanoes and craters/calderas are shown in grey. White stars and yellow rings: geothermal surface manifestations; black dots: MT/TEM stations; thin green lines: topographic contour lines in m a.s.l. Coordinates are UTM in km, zone 37, Arc 1960 datum. (For interpretation of the references to colour in this figure legend, the reader is referred to the web version of this article.)

the most optimistic (P10) model (Cumming, 2016) but the south-east area is more like a P90 model based on the thickening and deepening of the conductor.

In the Paka volcanic zone (Fig. 6c), a low resistivity cap (<14 Ω m) overlays a resistive zone up doming at the summit caldera and deepening on either side of the volcano. Paka is an area of enhanced permeability as evidenced by massive fumaroles particularly within the summit area (Fig. 6c). The massive occurrence of fumaroles along faults suggests leakage of steam where the cap is cut by the faults. The presence of shallow low resistivity at the location of these fumaroles suggests that they are a surface expression of a major up-flow zone of the deeper heat sources.

In contrast, the Korosi area (Fig. 6e) shows resistivity structure with medium resistivity (about 30 Ω m) at the summit area which departs from the low resistivity cap. This could be due to the dominance of trachytic rocks in the volcano and hence lack of the smectite alteration as discussed previously, resulting in a moderate resistivity (>30 Ω m). This is caused by lack of magne-

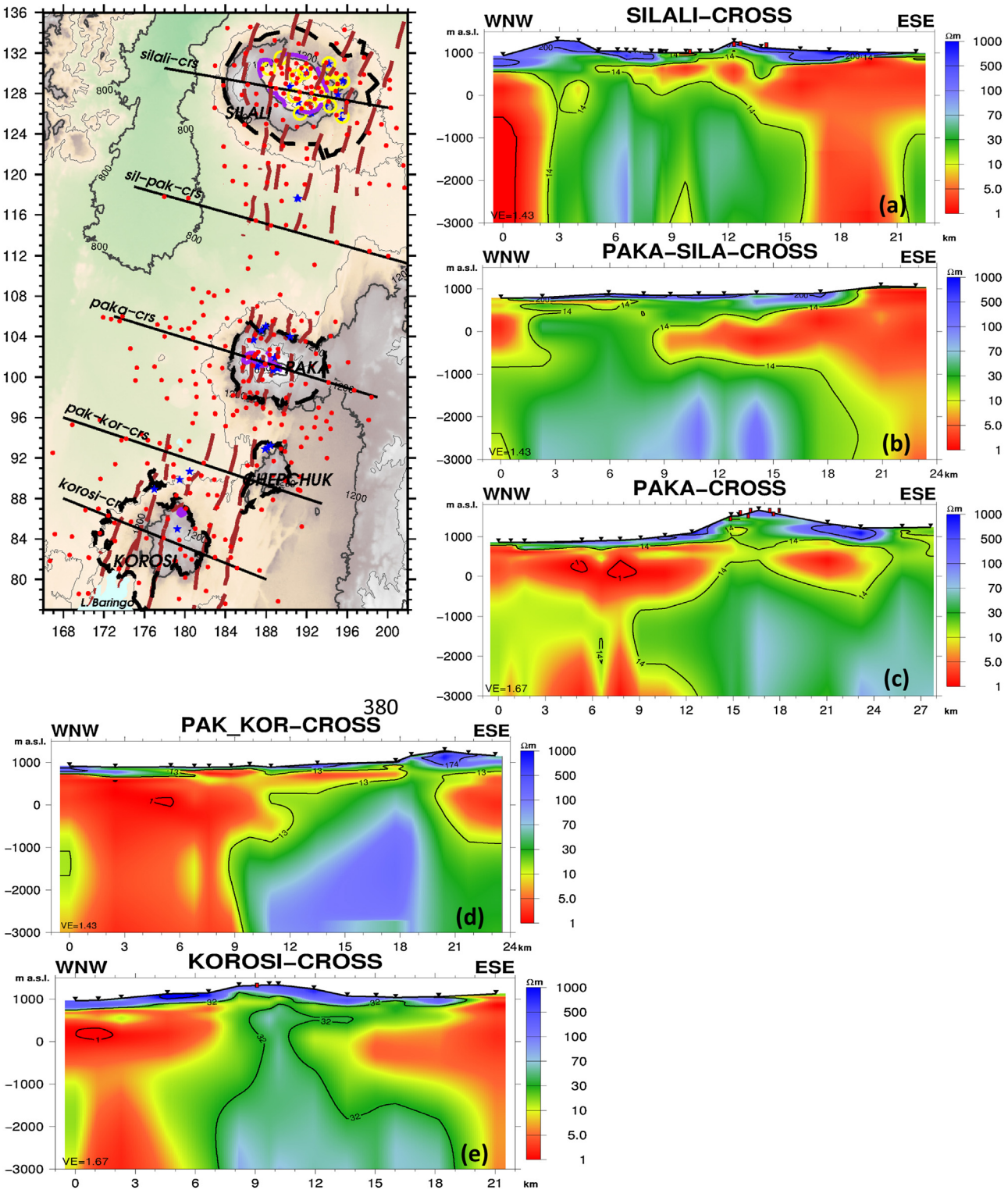

Fig. 6. Resistivity cross-sections across Korosi, Paka and Silali based on 1D joint inversion of MT and TEM data: From top; (a) across Silali; (c) between Paka and Silali; (c) Paka; (d) Chepchuk and (e) Korosi volcanoes as shown on the location map to the left. Inverted triangles are MT stations and Red symbols on cross-sections are fumaroles. Volcanoes are shown in broken black lines and craters in purple. Blue stars and yellow rings: geothermal surface manifestations. Vertical contours are caused by distortions due to lateral boundaries that are closer in distance than the depth of the feature. (For interpretation of the references to colour in this figure legend, the reader is referred to the web version of this article.)

sium in trachyte lava that inhibits smectite alteration (Cumming, 2016). Trachyte ash and breccia exposed to meteoric water can alter to smectite because an external source of Mg is available. Beneath the inferred 'trachyte cap' higher resistivity dominates with deeper and thicker low resistivity on both sides. For cross-sections plotted on the flanks of the volcanoes (Fig. 6b and c) the same resistivity sequence prevails but the low resistivity zones are more uniform in thickness in the middle portion which corresponds to the margins of the inner rift. All the cross-sections are characterized by thicker and deep low resistivities on both the northwest and south-

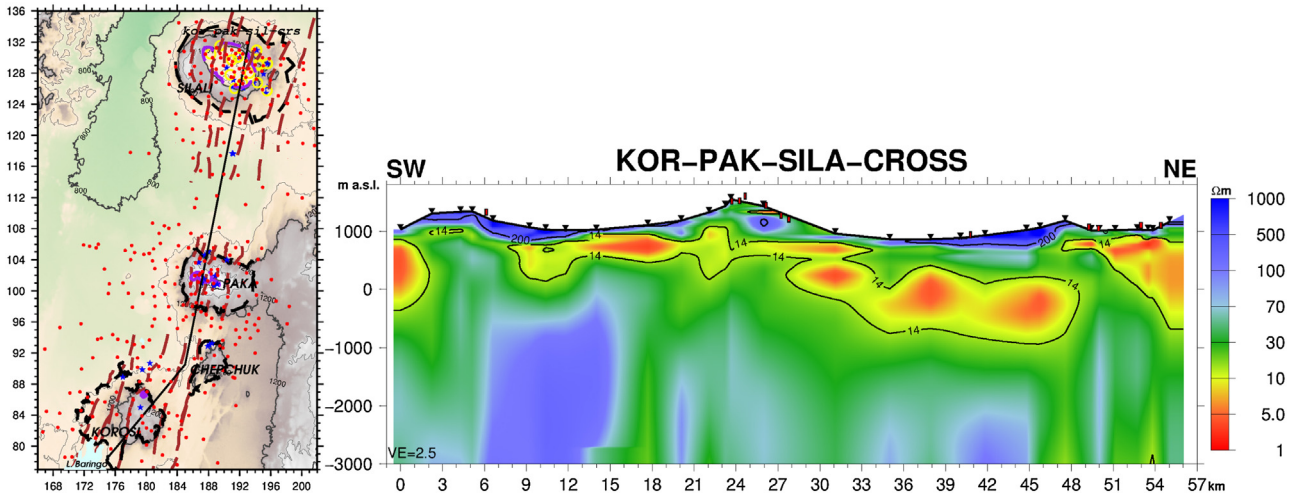

Fig. 7. Resistivity cross-section cutting through Korosi-Paka-Silali area based on 1D joint inversion of MT and TEM data as shown on the location map to the left. Inverted triangles are MT stations Red symbols on cross-sections are fumaroles. Volcanoes are shown in broken black lines and craters in purple. Blue stars and yellow rings: geothermal surface manifestations. Vertical contours are caused by distortions due to lateral boundaries that are closer in distance than the depth of the feature. (For interpretation of the references to colour in this figure legend, the reader is referred to the web version of this article.)

east flanks. These low resistivities could be related to conductive sedimentary units/volcanoclastics deposited during past volcanic eruptions.

The area of study has undergone extensional tectonics as evidenced by numerous fractures and faults. In the sector between Korosi and Paka volcanoes the rift trends in the SW-NE direction and from Paka volcano northwards it changes trend to north-south (Fig. 2). Similarly the moderate high resistivity at sea level (Fig. 5c) mimics the same trend with a break in between Paka and Silali volcanoes where the resistivity trend is offset to the west. This break and the accompanying offset maps a possible buried structural shift in the rift alignment between Paka and Silali volcanoes. This implies that the rift axis at Silali volcano has recently moved to align with the Paka volcanic axis, as evidenced by the inactive alteration in the west of the caldera with more recent hydrothermal activity occurring in the eastern sector.

7. Discussion and conclusions

One-dimensional inversion of MT data indicates the geometry of geothermal systems associated with the Korosi, Paka and Silali volcanoes which are characterized by similar resistivity structure. A resistive top layer between 200 m to 500 m along the rift overlies a very conductive layer (~10 Ω m) in the Paka-Silali segment and a moderate resistivity layer (about 30 Ω m) beneath Korosi. Both are underlain by a higher resistivity core (~60 Ω m) which domes beneath the volcanoes. The resistive surface layer is associated with recent, well-drained tuffs and lavas. The second layer is low resistivity, reflecting hydrothermal alteration with conductivities dictated by the amount of smectite in the layer. The third layer is higher resistivity, potentially corresponding to a geothermal reservoir with upwelling zones represented by the higher resistivity doming beneath a low resistivity cap associated with thermal manifestations on individual volcanoes. Flanking the volcanoes are very thick and deep conductors, which have been interpreted as volcanoclastic sediments. It should, however, be noted that as MT high frequencies are attenuated at shallow depth, the resolution of 1D inversion deteriorates below the base of the low-resistivity layer representing the hydrothermal alteration zone. However, when carefully integrated with geological and surface manifestations the geometry of the hydrothermal alteration zone as mapped by 1D inversion can give very clear indication of location of geothermal reservoirs and upwelling zones. These upwelling zones are manifested by elevation of the base of clay cap (BOC) driven by the buoyancy of geothermal fluids that may suggest higher temperatures and hence geothermal system in that region. This can also be used to interpret the likely outflow direction from a geothermal upflow. The most elevated point of the BOC acts as a safe bet during well targeting. The trend of the resistivity at sea level (Fig. 5c) is aligned with the strike of the exposed faults, indicating that the rift controls volcanism and hence the resistivity trend could be related to the lithologic units.

The resistivity pattern is consistent with many geothermal systems around the world, where a low permeability, low resistivity clay cap overlays a more resistive high permeability reservoir. However, the low resistivity alteration layer is not well developed in some sectors due to lower production of smectite which is consistent with trachyte. This is because trachyte is lower in magnesium than basalt therefore magnesium must be added to trachyte or phonolite by groundwater to form smectite (Cumming, 2016). Reduced intensity of alteration might also be due to lower permeability in trachyte as compared to basalt. According to (Hjalti Franzson, personal communication, November 2016) trachyte reacts slowly to alteration, which might explain why trachyte rocks are more resistive against alteration compared to basalt. The lack of clay cap may occur in some high temperature volcanic-associated geothermal systems (Muñoz, 2014).

The resistivity structure in this study can be interpreted in terms of alteration mineralogy where the low resistivity cap can be associated with the smectite which transition to illite/chlorite in the high resistivity core (Árnason et al., 2000; Gunderson et al., 2000; Ussher et al., 2000). These clay transitions are controlled by both temperature and kinetics (Essene and Peacor, 1995) in a rock matrix where smectite is roughly proportional to its water content. According to Gunderson et al. (2000), as smectite-bearing rocks are compacted and indurated, smectite becomes more dehydrated as it transitions to mixed layer smectite-chlorite/illite, and also gradually increases in resistivity. As a result, temperature at the base of a low to moderate resistivity smectite and mixed layer clay cap can vary widely. Alteration of precursor minerals to smectite can begin at 60 or 70 °C and the transition from the smectite to chlorite and illite takes place over a wide range of temperature up to 240 °C (Ussher et al., 2000), making the transition from low to high resistivity a poor predictor of specific temperature.

Although temperature is the most important factor in clay transitions, there are many other controls on the transition from low resistivity smectite to more resistive clays, and so these transitions occur through a wide range of temperature. Therefore, it is seldom possible to reliably assign a temperature to a specific resistivity in rocks that include a significant quantity of hydrated smectite clay. However, based on interpretations of the water table, geochemistry and resistivity pattern, a pattern of isotherms can be constrained in order to produce the resource conceptual model needed to guide geothermal well targeting (Cumming, 2016). The clay transitions considered include; 1) alteration of precursor minerals to low resistivity smectite, and 2) alteration of smectite to moderate resistivity mixed layer clays, and 3) alteration to high resistivity chlorite (basalt) and illite (andesite etc). The factors that control the clay transitions include; 1) temperature, 2) pore water saturation, 3) pore water and gas chemistry, 4) the evolution of permeability/porosity, 5) mineral chemistry, 6) burial/compaction history), 7) fluid pressure (albeit mostly through its effect on phase and gas dynamics in shallow epithermal cases), 8) the thermodynamics of clay alteration, etc. Essene and Peacor (1995) focus on a thermodynamic model to explain why clay geothermometry is unreliable but also review the literature relevant to the processes that affect the clay transitions.

With respect to resistivity interpretation in the EARS, one basic point is that low resistivity shallower than 2 km is very likely to correspond to low permeability smectite clay. Its relationship to thermal manifestations can indicate its likelihood of acting as a cap over a high temperature geothermal reservoir. Although the transition from low to high resistivity over a high temperature geothermal reservoir is sometimes correlated with a specific temperature range, this depends on its context within the overall conceptual model. Outflows of hot water from a geothermal reservoir at temperatures below 200 °C also create a low resistivity smectite cap. Unless the outflow has cooled from a period when the geothermal reservoir was at higher temperature, the chlorite and illite content of the permeable rocks associated with the outflow may be relatively low, although alteration is often intense, dominated by other resistive alteration minerals like silica that deposits as water cools below 180 °C. A low resistivity smectite zone has been interpreted as capping an outflow that extends west of Silali caldera, for example (Melosh et al., 2014).

In addition, sometimes more resistive types of clay can form a cap that supplements a smectite cap (Melosh et al., 2010). For example, based on hydrology, thermodynamics, geological analogs and MT resistivity, Cumming (2014) and Melosh et al. (2014) suggested that Silali was likely to have something like a phyllic cap below its smectite cap in some area, which in many developed geothermal systems, corresponds to reservoir but might also signify older hydrothermal system and a deeper resource.

7.1. Gas and water geochemistry

The geochemistry of the fumaroles, hot springs, cold springs and soil gas indicate that one or more geothermal reservoirs suitable for power production are very likely to occur within the Silali-Paka-Korosi volcanic segment. As is typical of geothermal exploration, the location and chemistry of fumaroles and hot springs interpreted in the context of the resistivity pattern and geology provide the most reliable constraints on the general properties of a resource conceptual model, including its permeability geometry, chemistry, pressure and temperature (Dipippo, 2016). Because this study is directed at assessing the occurence of the geothermal systems with respect to major volcanic centers, fissure eruption zones and other geophysically prominent features of the north Kenyan segment of the EARS, the geochemistry is reviewed to establish confidence in the existence of a geothermal system, not to build the detailed range of geothermal conceptual models used in risk assessments of drilling targets and resource capacity.

Because Silali geochemistry (Marini, 2014) has been integrated with other geoscience data in a range of resource conceptual models to support a well targeting and resource capacity assessment at Silali (Melosh et al., 2014), the high likelihood for the existence of a geothermal resource at Silali is well established. A recently active magmatic heat source is suggested by anomalous $^{3}He/^{4}He$ isotope ratios as high as 8 from several fumaroles. Gas geothermometry of 310–350 °C indicates a likely liquid reservoir below the fumaroles on the southeast rim of the caldera, implying a relative deep resource of at least 1.3 km, up to 2.3 km. Fumaroles outside the caldera show evidence of boiling and atmospheric interaction that makes geothermometry unreliable. The geometry of the base of the MT low resistivity zone is consistent with an interpretation of these fumaroles as a boiling outflow. The bicarbonate-chloride Kapedo and Lorusio hot springs, located at the base of the west and northwest flank of Silali, establish a water table and their cation and silica geothermometry of about 120–125 °C is consistent with gradual cooling in a > 10 km outflow from a 310–350 °C resource. The distribution of anomalous CO_2 content in soil is generally consistent with, but likely to be more reliable than, the ^{222}Rn activity in soil, implying that an area of over 25 km^2 has been affected by high temperature upflow and lower temperature outflow at Silali (Marini, 2014).

Because the geochemistry for the Paka and Korosi volcanoes has not been integrated with the geophysics and geology data sets and tested for consistency in geothermal resource conceptual models with the same detail that has been applied at Silali, the geochemistry results are more ambiguous, particularly with respect to the reliability of the geothermometry. The large number and extent of fumaroles at Paka, the gas geothermometry up to 300 °C and the $^{3}He/^{4}He$ isotope ratios as high as 8 (Dunkley et al., 1993; Kipng'ok and Nyamongo, 2013) provides reliable evidence for the existence of a high temperature system. The gas geothermometry of Korosi fumaroles is reported as 240 °C with an ambiguous hint of temperature over 350 °C. CO2 and H2S Gas geothermometry at Korosi indicate temperatures of 357 and 267 °C respectively (Kipng'ok, 2011; Ofwona et al., 2006). The areas of anomalous CO_2 content in soil of 33 km^2 at Paka and 16 km^2 at Korosi (GDC, 2011) likely reflect both upflow and outflow zones. The smaller area for Korosi may be due to the limited extent of the survey in the likely direction of outflow to the northeast. The fumaroles with the high geothermometry are located in areas where the base of the MT low resistivity clay cap is at a local high in elevation.

References

Árnason, K., Karlsdottir, R., Eysteinsson, H., Flóvenz Ó, G., Thor, S., 2000. The resistivity structure of high-temperature geothermal systems in Iceland. Proc. World Geotherm. Congr., 923–928.

Árnason, K., Eysteinsson, H., Hersir, G.P., 2010. Joint 1D inversion of TEM and MT data and 3D inversion of MT data in the Hengill area, SW Iceland. Geothermics 39, 13–34, http://dx.doi.org/10.1016/j.geothermics.2010.01.002.

Achauer, U., 1992. A study of the Kenya rift using delaytime tomography analysis and gravity modelling. Tectonophysics 209, 197–207.

Anderson, E., Crosby, D., Ussher, G., Zealand, N., 2000. Bulls-Eye! – simple resistivity imaging to reliably locate the geothermal reservoir. World Geotherm. Congr., 909–914.

Arnason, K., 2006. TEMTD. A program for 1D inversion of central-loop TEM and MT data. In: A Short ManualR, Reykjavík. ISOR, Iceland Geosurvey, Reykjavik (16 pp.).

Bosworth, W., Burke, K., Strecker, M., 2000. Magma chamber elongation as an indicator of intraplate stress field orientation: borehole break-out mechanism and examples from the Late Pleistocene to Recent Kenya Rift Valley. A volume in honour of W D. Means. Eds: M.W. Jessell and J.L.Urai. volume 2.

Bosworth, W., Burke, K., Strecker, M., 2003. Effect of stress fields on magma chamber stability and the formation of collapse calderas. Tectonics 22, 1–21, http://dx.doi.org/10.1029/2002TC001369.

Briggs, J., Anthony, E.Y., Ebinger, C., 2009. Multiple inflation and deflation events at Kenyan volcanoes, East African Rift. Geol. Soc. Am. 37, 979–982, http://dx.doi.org/10.1130/G30133A.1.
Chave, Jones (Eds.), 2012. The Magnetotelluric Method: Theory and Practice. Cambridge University Press (552 pp.).
Chorowicz, J., 2005. The East African rift system. J. Afr. Earth Sci. 43, 379–410, http://dx.doi.org/10.1016/j.jafrearsci.2005.07.019.
Constable, S.C., Parker, R.L., Constable, C.G., 1987. Occam's inversion: a practical algorithm for generating smooth models from electromagnetic sounding data. Geophysics 52, 289, http://dx.doi.org/10.1190/1.1442303.
Corti, G., 2009. Continental rift evolution From rift initiation to incipient break-up in the Main Ethiopian Rift, East Africa. Earth-Sci. Rev. 96, 1–53.
Cumming, W., Mackie, R., 2010. Resistivity imaging of geothermal resources using 1D, 2D and 3D MT inversion and TDEM static shift correction illustrated by a glass mountain case history. Proc. World Geotherm. Congr. 2010, 1–10.
Cumming, W., 2014. UNEP Silali Resource Review –Geophysics; report to the United Nations Environmental Program, 71 pp.
Cumming, W., 2016. Resource conceptual models of volcano-Hosted geothermal reservoirs for exploration well targeting and resource capacity assessment: construction, pitfalls and challenges. Geotherm. Resour. Council Trans. 40, 623–638.
Darling, W.G., 1998. Hydrothermal hydrocarbon gases: 2, application in the east African rift system. Appl. Geochem. 13, 825–840.
Dipippo, R., 2016. In: Dipippo, Ron (Ed.), Geothermal Power Generation. Elsevier (654 p.).
Dunkley, P.N., Smith, M., Allen, D.J., Darling, W.G., 1993. The geothermal activity and geology of the northern sector of the Kenya Rift Valley, British Geological Survey Research Report.
Dyaksa, D.A., Ramadhan, I., Ganefianto, N., 2016. Magnetotelluric Reliability for Exploration Drilling Stage: Study Cases in Muara Laboh and Rantau Dedap Geothermal Project, Sumatera, Indonesia 1–5.
Ebinger, C.J., Bechtel, T.D., Forsyth, D.W., Bowin, C.O., 1989. Effective elastic plate thickness beneath the East African and Afar plateaus and dynamic compensation of the uplifts. J. Geophys. Res. 94, 2883–2901.
Ebinger, C., 2005. Continental break-up: the east african perspective. Astron. Geophys. 46 (2. 16-2.21).
Egbert, G.D., Booker, J.R., 1986. Robust estimation of geomagnetic transfer functions. Geophys. J. R. astr. Soc. 87, p173–p194.
Essene, E., Peacor, D., 1995. Clay mineral thermometry: a critical perspective. Clays Clay Miner. 43, 540–553.
GDC, 2011. Geothermal inverstigation of Korosi, Paka and Silali geothermal prospects, Unpublished report.
Gunderson, R., Cumming, W., Astra, D., Harvey, C., Ussher, G., Harvey, C., Johnstone, R., Anderson, E., Zealand, N., 2000. Analysis of smectite clays in geothermal drill cuttings by the methylene blue method: for well site geothermometry and resistivity sounding correlation. Proc. World Geotherm. Congr., 1175–1181.
Keller, G.R., Khan, A.M., Morganc, P., Wendlandt, R., Baldridge, S.W., Olsen, K.H., Prodehl, C.L.B., 1991. A comparative study of the Rio Grande and Kenya rifts. Tectonophysics 197, 355–371.
Keller, G.R., Mechie, J., Braile, L.W., Mooney, W.D., Pradehl, C., 1994a. Seismics tructure of the uppermost mantle beneath the Kenya rift. Tectonophysics 236, 201–216.
Keller, G.R., Prodeh, C., Mechie, J., Fuchs, K., Khan, A.M., Maquire, P.K., Mooney, W.D., Achauer, U., Davis, P.M., Meyer, R.P., Braile, L.W., Nyambok, I.O., Thompson, G.A., 1994b. The East African rift system in the light of KRISP 90. Tectonophysics 236, 465–483.
Keller, G.R., Simiyu, S.M., Keller, G.R., Corti, G., Masotti, R., Maguire, P.K.H., Mechie, J., 1997. Further remarks on the interpretation of the KRISP 90 cross-rift line. Tectonophysics 278, 291–313, http://dx.doi.org/10.1016/S0040-1951(97)00108-X.
KenGen, 2007. Geothermal feasilibilty report for Paka geothermal prospect, Unpublished report.
Kipng'ok, J., 2011. Geochemical assessment of Korosi-Chepchuk geothermal prospect, Kenya rift valley. Geotherm. Resour. Counc. Trans. 36.
Kipng'ok, J., Nyamongo, J., 2013. Fumarole gas geochemistry of Paka geothermal prospect, North Rift , Kenya. Geotherm. Resour. Counc Trans. 37, 411–416.
Lichoro, C.M., 2013. Multi-dimensional Interpretation of Electromagnetic Data from Silali Geothermal Field in Kenya: Comparison of 1-D, 2-D and 3-D Mt Inversion Msc Thesis. Univ. Icel, 185pp.
Lippard, S.J., Truckle, P.H., 1978. Spatial and temporal variations in basalt geochemistry in the northern Kenya rift. In: Neumann, R., Ramberg, I.B. (Eds.), Petrology and Geochemistry of Continental Rifts. Reidel, Dordrecht, pp. 123–132.
MacDonald, R., 2003. Magmatism of the Kenya rift valley: a review. Earth Sci. 93, 239–253.
Macdonald, R., Davies, G.R., Upton, B.G.J., Dunkley, P.N., Smith, M., Leat, P.T., 1995. Petrogenesis of Silali volcano Gregory rift, Kenya. J. Geol. Soc. Lond. 152, 703–720.
Maguire, P.K.H., Swain, C.J., Masotti, R., Khan, M.A., 1994. A crustal and uppermost mantle cross-sectional model of the Kenya Rift derived from seismic and gravity data. Tectonophysics 236, 217–249, http://dx.doi.org/10.1016/0040-1951(94)90178-3.
Manzella, A., Volpi, G., Zaja, A., Meju, M., 2004. Combined TEM-MT investigation of shallow-depth resistivity structure of Mt. Somma-Vesuvius. J. Volcanol. Geotherm. Res. 131, http://dx.doi.org/10.1016/S0377-0273(03)00313-5.
Mariita, N.O., Keller, G.R., 2007. An integrated geophysical study of the northern Kenya rift. J. Afr. Earth Sci. 48, 80–94, http://dx.doi.org/10.1016/j.jafrearsci.2006.05.008.
Marini, L., 2014. UNEP Silali Resource Review – Geochemistry; report to the United Nations Environmental Program, 71 pp.
Mechie, J., Keller, G.R., Prodehl, C., Khan, M.A., Gachiri, S.J., 1997. A model for the structure, composition and evolution of the Kenya rift. Tectonophysics 278, 95–119.
Melosh, G., Cumming, W., Benoit, D., Wilmarth, M., Colvin, A., Winick, J., Soto-, E., Sussman, D., Urzúa-monsalve, L., Powell, T., Peretz, A., 2010. Exploration results and resource conceptual model of the Tolhuaca Gethermal Field, Chile. In: Proc World Geotherm. Congr., Bali, Indonesia, 25–29 April, p. 2010.
Melosh, G., Cumming, W., Marini, L., 2014. Conceptual model of the Silali Prospect – Technical review; Rreport to the United Nations Environmental Program, 47 pp.
Muñoz, G., 2014. Exploring for geothermal resources with electromagnetic methods. Surv. Geophys. 35, 101–122, http://dx.doi.org/10.1007/s10712-013-9236-0.
Nyblade, A.A., Pollack, H.N., Jones, D.L., Podmore, F., Mushayandebvu, M., 1990. Terrestrial heat flow in east and southern Africa. J. Geophys. Res. 95, http://dx.doi.org/10.1029/JB095iB11p17371.
Ofwona, C., Wambugu, J.M., Omenda, P., Mariita, N., Mwawongo, G., Kubo, B., 2006. Surface Geothermal Exploration Of Korosi And Chepchuk Prospects. In: Ofwona, C. (Ed.). Internal report, 2006, Unpublished, 45–62.
Onacha, S.A., 2006. Hydrothermal Fault Zone Mapping Using Seismic and Electrical Measurements. Duke Univ.225–$9, Ph.D Thesis.
Pellerin, L., 1990. Transient electromagnetic inversion: a remedy for magnetotelluric static shifts. Geophysics 55, 1242.
Phoenix Geophysics, 2005. Data Processing User Guide. Phoenix Geophysics Ltd, ON, Canada.
Prodehl, C., Ritter, J.R.R., Keller, G.R., Khan, M.A., Jacob, B., Fuchs, K., Nyambok, I.O., Obel, J.D., Riaroh, D., 1997. The KRISP 94 lithospheric investigation of southern Kenya experiments and their main results the 278, 121–147.
Ring, U., Livingstone, D., Stanley, H.M., Fischer, G., 2014. The east African rift system. Aust. J. Earthsci. 107/1, 132–146.
Rosenkjaer, G.K., Gasperikova, E., Newman, G.A., Arnason, K., Lindsey, N.J., 2015. Comparison of 3D MT inversions for geothermal exploration: case studies for Krafla and Hengill geothermal systems in Iceland. Geothermics 57, 258–274, http://dx.doi.org/10.1016/j.geothermics.2015.06.001.
Sceal, J.S.C., 1974. The Geology of Paka Volcano and the Country to the East, Baringo District, Kenya. University of London, Unpublished PhD thesis.
Searle, R.C., 1970. Evidence from gravity anomalies for thinning of the lithosphere beneath the rift valley in Kenya. Geophys. J. R. Astron. Soc. 21, 13–31.
Simiyu, S.M., Keller, G.R., 1997. An integrated analysis of lithospheric structure across the East African plateau based on gravity anomalies and recent seismic studies. Tectonophysics 278, 291–313, http://dx.doi.org/10.1016/S0040-1951(97)00109-1.
Simiyu, S., Keller, G.R., 2001. An integrated geophysical analysis of the upper crust of the southern Kenya rift. Geophys. J. Int. 147, 543–561, http://dx.doi.org/10.1046/j.0956-540x.2001.01542.x.
Smith, M., Dunklley, P.N., Denio, A., Williams, L.A.J., McCall, G.J.H., 1995. Geochronology, stratigraphy and structural evolution of Silali volcano, Gregory Rift Kenya. J. Geol. Soc. 152, 297–310.
Sternberg, B.K., Washburne, J.C., Pellerin, L., 1988. Correction for the static shift in magnetotellurics using transient electromagnetic soundings. Geophysics 53, 1459–1468, http://dx.doi.org/10.1190/1.1442426.
Swain, C.J., 1992. The Kenya rift axial gravity high: a re-interpretation. Tectonophysics 204, 59–70.
Ussher, G., Harvey, C., Johnstone, R., Anderson, E., Zealand, N., 2000. Understanding the resistivities observed in geothermal systems. Proc. World Geotherm. Congr., 1915–1920.
Volpi, G., Manzella, A., Fiordelisi, A., 2003. Investigation of geothermal structures by magnetotellurics (MT): an example from the Mt. Amiata area, Italy. Geothermics 32, 131–145.
Wamalwa, A.M., Serpa, L.F., 2013. The investigation of the geothermal potential at the Silali volcano, Northern Kenya Rift, using electromagnetic data. Geothermics 47, 89–96, http://dx.doi.org/10.1016/j.geothermics.2013.02.001.
Wight, D., 1991. MT/EMAP data interchange standard: Tulsa, Oklahoma. Soc. Explor. Geophys. 2, 108.
Williams, L.A.J., Macdonald, R., Chapman, G.R., 1984. Late quatenary caldera volcanoes of the Kenya rift valley. J. Geophys. Res. 89, 8553–8570, http://dx.doi.org/10.1017/CBO9781107415324.004</DOI.

Paper II

Joint interpretation of gravity and resistivity data from the Northern Kenya volcanic rift zone: Structural and Geothermal significance

Charles Muturia Lichoro, Knútur Árnason, William Cumming
Journal of Geothermics, 77 (2019) 139–150

Geothermics 77 (2019) 139–150

Contents lists available at ScienceDirect

Geothermics

journal homepage: www.elsevier.com/locate/geothermics

Joint interpretation of gravity and resistivity data from the Northern Kenya volcanic rift zone: Structural and geothermal significance

Charles Muturia Lichoro[a,d,e,*], Knútur Árnason[b], William Cumming[c]

[a] Geothermal Development Company Ltd, P.O. Box: 17700-20100, Polo House, Nakuru, Kenya
[b] ISOR Iceland GeoSurvey, Grensasvegur 9, 108 Reykjavik, Iceland
[c] Cumming Geoscience, 4728 Shade Tree Lane, Santa Rosa, CA, 95405, USA
[d] Department of Earth Sciences, University of Iceland, Askja, Sturlugata 7, 101, Reykjavík, Iceland
[e] UNU-GTP, Orkustofnun, Grensásvegi 9, IS-108 Reykjavík, Iceland

ARTICLE INFO

Keywords:
Bouguer anomaly
Residual anomaly
Density contrasts
Resistivity
Intrusions
Kenyan rift

ABSTRACT

The Northern Kenya Rift has been the least studied sector of the Kenyan part of the East African Rift due to its remote location. Geothermal exploration conducted in the last ten years has greatly improved the geophysical constraints on the geology of this area. Recently, about 515 gravity stations have been surveyed around the Korosi, Paka and Silali volcanoes and analysed in conjuction with resistivity data from over 300 MT stations in order to jointly interpret the density and resistivity distribution of the Northern Kenya rift. Our models of the gravity data are in good agreement with previous MT and TEM resistivity studies of the individual volcanoes. The new Bouguer gravity map is characterized by a 10 to 15 km wide gravity high of 8 mGal amplitude striking NNE along the inner rift corresponding to resistivity > 50 Ωm below 2 km depth. Gravity lows due to structures shallower than 2 km depth at the Paka and Korosi volcanoes have been interpreted as low density bodies within their edifices, likely to consist of either unaltered near-surface pyroclastics or deeper tuffs altered at 60 to 180°C to hydrothermal smectite clay. Magnetotelluric (MT) resistivity models were used to further constrain the 2D gravity models. The high resistivity, low density near-surface rocks on the flanks of the volcanoes are interpreted to represent unaltered pyroclastics above the water table, whereas low resistivity, low density bodies underneath the Paka and Korosi volcanoes indicate low density tuffs, hydrothermally altered to hydrated smectite clay. Below 2 km depth the deeper high density zone beneath the volcanic inner rift is likely to be a combination of higher temperature, low porosity alteration associated with geothermal reservoirs and/or denser rocks related to intrusions. As expected, the greater proportion of dense lavas associated with fissure swarms mapped at the surface coincide with both relatively high gravity and MT resistivity south of Paka volcano. However, farther north between Paka and Silali volcanoes, the trends in higher gravity and resistivity lie west of the currently active fissure zone. This apparently inconsistent trend in the gravity and resistivity has been interpreted as lavas buried below recent tuffs and clastics associated with a former alignment of fissure eruptions in the rift about 7 km to the west of the current axis of eruption between Paka and Silali.

1. Introduction

1.1. Rift tectonics and overview of the Kenya Rift

The Kenya Rift is part of the East African Rift (EAR) system that runs from the Gulf of Aden in the north to Mozambique in the south and acts as a boundary between the Nubian and the Somalian plates. The Kenya Rift stretches from Lake Turkana in the north to northern Tanzania in the south and is centred on the Kenya domal uplift (Fig. 1a). The dome has been attributed to the presence of an underlying mantle plume (Ebinger and Sleep, 1998; Nyblade, 2011) that is the source of the volcanic rocks that have been erupted across the plateau over the last approximately 30 Ma. This is consistent with geophysical data suggesting that the rift formed above a mantle plume (Nyblade et al., 1990; Ebinger et al., 1989; Green et al., 1991; Achauer, 1992). The upwelling of the mantle plume has caused extensional strains and fracturing of the brittle crust into a series of normal faults giving the classic horst and graben structure of present rift valleys. A combination of crustal extension and plume-related thermal erosion at the base of the crust (Corti, 2009; Ring et al., 2014) has been postulated to be the cause of

* Corresponding author at: Department of Earth Sciences, University of Iceland, Askja, Sturlugata 7, 101, Reykjavík, Iceland.
E-mail address: cmuturia@gmail.com (C.M. Lichoro).

https://doi.org/10.1016/j.geothermics.2018.09.006
Received 3 August 2018; Received in revised form 14 September 2018; Accepted 16 September 2018
Available online 28 September 2018
0375-6505/

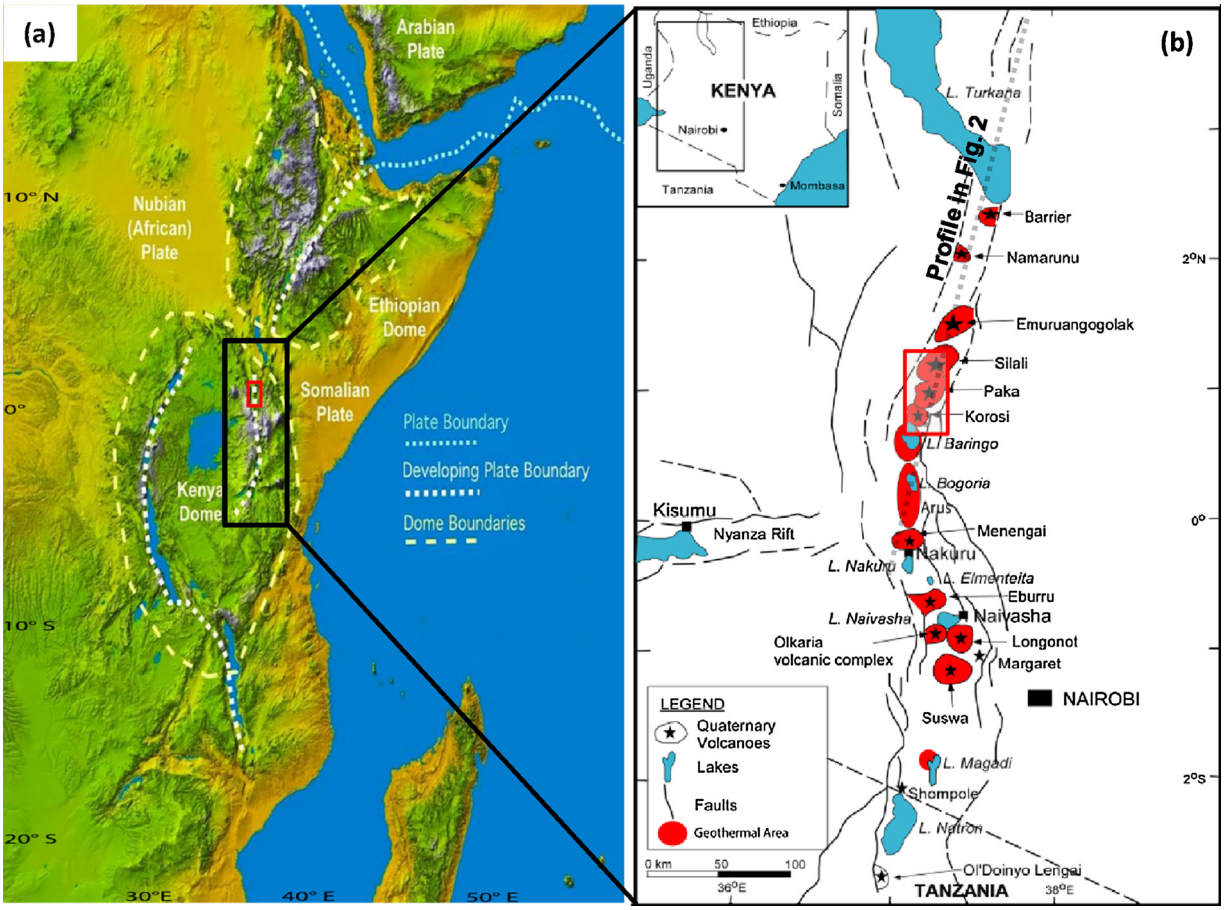

Fig. 1. (a) Map of the East African Rift System showing the Kenyan and Ethiopian domes that overlay the rift and the associated plate boundaries (EARS; from SRTM; Wood and Guth, 2015). The black rectangle shows the Kenya rift segment, the red box shows the area of study. (b) Map of the Kenya Rift showing geothermal prospects in Kenya (modified from Clarke et al., 1990). The rectangular red box outlines the volcanoes considered in this study and the area shown in subsequent maps in Figs. 3, 6 and 7. The gray-dotted line indicates the location of profile in Fig. 2. (For interpretation of the references to color in this figure legend, the reader is referred to the web version of this article).

crustal thinning beneath the Kenyan rift (Ebinger, 2005).

The EAR is reported to be opening at a rate of 3–5 mm/yr (Stamps et al., 2008; Calais et al., 2006); If the African plate is also drifting northwards as reported by George et al., (1998), it complicates extensional motion of the rift such that the rate of rift opening in the east-west direction is counteracted by the northwards plate drift due to impact with Arabian plate, thereby reducing the effective rift extension. Rift extension has been reported to be greater in Afar 1200 km northeast of the Northern Kenyan Rift (Schilling et al., 1992; Keller et al., 1994b; Ebinger et al., 1989).

Crustal thickness varies in the Kenyan Rift from 35 km at the apex of the Kenyan dome around Lake Naivasha, 200 km south of the study area, to 20 km in the thinned section at Lake Turkana, 150 km north of the study area (Ebinger et al., 1989; Maguire et al., 1994; Mechie et al., 1997; Keller et al., 1994b;). Beneath the thinned rift section, lies a low P-wave velocity mantle of 7.5 km/s implying magma residence in the upper mantle (Achauer, 1992; Mechie et al., 1994). The extensional strains that caused crustal thinning (Mechie et al., 1997; Maguire et al., 1994) could have been accompanied by partial melt leading to dike injection and volcanism. Additionally, upper crustal studies suggest that large amounts of mantle derived intrusions all along the rift axis penetrated to depths of 3–6 km in the shallow sub-surface (Baker and Wohlenberg, 1971; Mohr, 1987; Swain, 1992). Williams (1972) has estimated that about 144,000 km^3 of volcanics have erupted all along the present Kenya rift since early Miocene. However, this volume alone is not sufficient to account for the greater than 30 km of crustal extension suggested by regional gravity (Prodehl et al., 1997; Morley, 1994) which means that part of the extension has been accomodated by emplacement of intrusions in the subsurface. The Kenya rift is still active as evidenced by recent observations, ranging from high rate of seismicity, evidence of high surface heat flow, recent volcanism and more recent inflation events at some of the volcanoes (Biggs et al., 2016, 2009).

Within the rifts, as reported both in Iceland (Bjornsson et al., 1977; Sigmundsson, 2006) and Afar triangle in the Ethiopian rift, (Wright et al., 2006; Grandin et al., 2009; Rowland et al., 2007) rift opening is commonly characterized by surface faulting and widening, followed by dike injections from the volcanic centres. In some instances such dike intrusions have apparently propagated laterally from the base of the volcanoes in the northern Kenya rift and sometimes resulted in fissure eruptions (Dunkley et al., 1993). This is supported by the low volumes of erupted lava at the volcanoes. An example is the Silali volcano, which was subject to withdrawal of large volumes of magma beneath the volcano and subsequent caldera formation (Dunkley et al., 1993). Subsidence of 2 cm/yr occurred at Silali volcano in the period 2006–2010 (Biggs et al., 2016) pointing to on-going extensional tectonic forces generating space in the crust to allow magma drainage from a shallow magma chamber.

Volcanic development in the Northern Kenya Rift initiated with the formation of Quaternary volcanoes less than 1 Ma ago. Korosi, Paka and Silali volcanoes are located in the inner trough of the rift where they form low-angle shield volcanoes composed predominantly of trachytic and basaltic lavas and pyroclastic deposits (MacDonald, 2003; Dunkley et al., 1993; Williams et al., 1984). The volcanoes at Korosi, Silali and

Paka formed about 500 ka, 460 ka and 390 ka respectively with caldera collapse at Silali and Paka occurring at about 64 ka and 10 ka, respectively (Dunkley et al., 1993). Subsequently, volcanic domes formed at all three volcanoes. All of these volcanoes are intersected by the 10 km axial rift wide fault zone that strikes in a NNE-SSW direction.

Geothermal development in the East Africa region has been ongoing for about 40 years which has led to substantial geothermal power production (~600 MWe) in Olkaria and drilling is ongoing and power plant construction under way in the Menengai geothermal field in the central Kenya Rift (Fig. 1b). Some power production is also at Aluto Langano in the Ethiopian part of the EAR. Exploration for geothermal energy in the northern Kenya rift began in the 1990s but was intensified in 2010 after the formation of the Geothermal Development Company (GDC). This was motivated by earlier results that hinted at potential geothermal resources. Numerous hot springs, altered ground and fumaroles within the study area have created interest for geothermal exploration.

The area under study here includes three major volcanoes namely Korosi, Paka and Silali (KPS) that lie within the Northern Kenya rift segment. The KPS sector was chosen for this study since it is the next frontier for geothermal exploration in Kenya after earlier studies had indicated possible geothermal potential. Preliminary studies (Cumming, 2014; Ofwona et al., 2006; Lichoro, 2013) along the rift had detected thick zones of low resistivity on the flanks of the volcanoes that were interpreted as infilling by clastics of the rift adjacent to the fissure and volcanic eruption zones, a conclusion that could be verified using gravity data. In a previous study (Lichoro et al., 2017), we discussed the resistivity structure of the KPS segment inferred from an extensive magnetotelluric (MT) and transient electromagnetic (TEM) resistivity survey.

In the current study, we present a gravity survey meant to complement earlier resistivity studies in order to further constrain the geologic setting of the potential geothermal resources. Over several field campaigns between 2014 and 2017, a total of 515 gravity stations were occupied. The analysis of the gravity data in this study includes assessing density within the elevation range of the gravity stations to compute Bouguer gravity, estimating regional and residual gravity, reviewing of gravity maps with respect to geology and producing models of subsurface density variation that are consistent with the resistivity structure revealed by the MT/TEM survey (Lichoro et al., 2017). We expect the locally close spacing of the gravity stations to reduce ambiguity in the shallow and deep parts of the gravity models and reveal sub-surface structures that are otherwise unidentified by surface geological mapping.

Since interpretation/modelling of gravity data is ambiguous (many models can explain the gravity data), the density models derived in this study have been constrained by jointly interpreting the gravity with the MT resistivity and geology. For example, on the volcanoes, a resistive zone near the surface above the water table will likely correspond to unaltered volcanics, which could be either lavas or pyroclastics. However, if correlated with relatively high gravity, then the resistive zone is more likely to be dense lava. On the other hand, a low resistivity zone above the water table on a volcano that is correlated with a local gravity low is likely to be associated with pyroclastics altered to low temperature clays in the vicinity of a boiling geothermal field or an active volcano. In contrast, a thick low resistivity below the water table that correlates with low gravity in the flat areas between the volcanoes is likely to correspond to clay-rich volcanoclastics. The low gravity in this case is due to the low density of the relatively high porosity sediment and volcanic ash, whereas the low resistivity is due to the high clay content from weathering. Low density pyroclastics below the water table or above a boiling zone will typically alter to low density smectite clay at roughly 70 to 150 °C near a geothermal system (Ussher et al., 2000). At higher temperature within a geothermal system, the clay loses water as the smectite further alters to chlorite-illite, and the rock becomes significantly denser. Rocks found in the study area range from basalt and trachyte with typical density of 2.55 g/cm^3 to pyroclastics with density ranges from 1.2 to 2.5 g/cm^3 (Cantini et al., 1990).

We review previous geophysical surveys before presenting the details of the more recent gravity survey and its interpretation. 2D gravity models along MT resistivity profiles helped constrain the geometry of the density model while considering the geology, subsurface densities.

2. Previous geophysical studies

Most of the published geophysical studies in the Kenyan rift have been regional in scope both areally and with depth extending into the mantle. Broadly, gravity anomalies within the Kenya rift have been characterized by a long-wavelength minimum due to mantle structure and shorter-wavelength anomalies due to crustal structure (Swain et al., 1994). The large scale gravity low aligned with the rift, with wavelength generally over 250 km perpendicular to the rift strike, has been attributed to shallowing of the lithosphere-aesthenosphere interface (Ebinger et al., 1989). Simiyu and Keller (1997) have modelled gravity of the entire East Africa plateau showing distinct gravity low associated with the Kenya dome suggesting a deep anomalously low mantle density beneath (lithosphere-aesthenosphere interface). In the northern Kenya rift, Mariita and Keller (2007) have modelled variations in crustal thickness and upper mantle structure which supports earlier studies (Mechie et al., 1994) that indicated crustal thinning from 35 km near Menengai in the south to 20 km at L. Turkana in the north (Fig. 2). This is indicative of the Moho topography which has a characteristic low gravity over high gravity.

Beneath the rift where the asthenosphere comes to the base of the crust, the regional gravity low would be expected to be a minimum; however, a narrower gravity high is aligned within the overall low due to magmatic modification of the upper crust (Swain, 1992). This magmatic modification of the upper crust is more prominent below the major Quaternary volcanic centers that produce a series of isolated axial gravity highs (Simiyu and Keller, 2001). Mariita and Keller (2007) have modelled a Bouguer gravity profile across the Barrier complex in the North rift, indicating a broad high gravity anomaly consistent with a mafic body in the upper crust. Similarly, the axial gravity profile from Lake Turkana in the north to Menengai volcano in the south show a

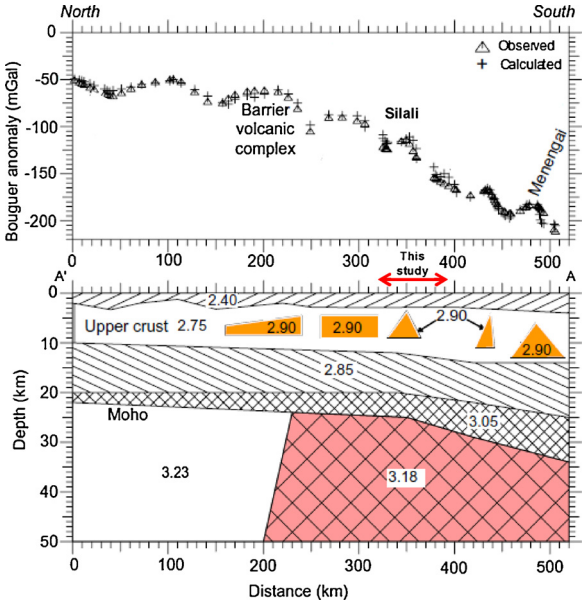

Fig. 2. North-South gravity model along the axis of the rift shown in Fig. 2b (modified from Mariita and Keller, 2007). It illustrates the thinned crust in the northern Kenya rift.The red arrow shows approximate area of study. (For interpretation of the references to color in this figure legend, the reader is referred to the web version of this article).

series of gravity highs corresponding to major volcanic centres (Fig. 2). Simiyu and Keller, (2001) reported similar correspondence between gravity highs and Menengai, Eburru, Olkaria and Suswa volcanic centers in the southern Kenya rift (see locations on Fig. 1b). Mariita and Keller (2007) attributed the axial gravity high associated with the main volcanic centers to mafic bodies and the less prominent adjacent highs and to densification of the upper crust due to diking and Precambrian basement horst blocks. Elsewhere within the rift, south of Suswa volcano, there is no indication of a broad gravity high or crustal thinning as seen in the north which is consistent with the lack of mafic intrusions, increased low-density volcanic deposits and reduced crustal extension southwards (Baker and Wohlenberg, 1971).

The high gravity along the inner axis of the rift (Fig. 1b) corresponds to high seismic velocity (6.0–6.1 km/s) implying presence of denser rocks at 3–6 km depth (Swain, 1992; KRISP, 1987). In the part of the rift considered in this study, the positive anomalies also generally coincide with intense faulting and fissuring at the surface. Refraction seismic and gravity studies have revealed high velocity and high density material within the rift zone attributed to upper crustal dikes that connect to the volcanic centers in the rift floor (Ebinger, 2005; Swain, 1992). Additional evidence of axial high density and high velocity along the rift (Swain, 1992) is corroborated by the high P-wave velocity zones that Keller et al. (1994a) attributed to mafic intrusives and crustal thinning.

Direct density measurements of rock samples from deep geothermal wells in Olkaria (Simiyu and Keller, 2001) show density variation from 2.4 g/cm^3 in the shallow part of the wells to 2.7 g/cm^3 at 3000 m depth which is representative of upper crustal density. Elsewhere rock samples from Suswa volcano (Cantini et al., 1990) show that a wide range of densities would likely occur in the study area. For example trachyte and basalt lavas with typical density of 2.55 g/cm^3 were identified at most depths and alteration states, while pyroclastics on the other hand have densities in the range of 1.2–2.5 g/cm^3, depending on their saturation state and alteration rank.

Recent MT resistivity studies in the area between L. Baringo and Silali volcano (Lichoro et al., 2017) have mapped 2–3 km thick low resistivity structures on both the northwest and southeast flanks of the rift and an axial high resistivity along the inner rift (Fig. 6d). The low resistivity is related to conductive sedimentary units/volcanoclastics deposited during past volcanic eruptions wheareas the high resistivity reflects buried intrusions beneath the fractured rift segment. In the sector between Korosi and Paka volcanoes (Lichoro et al., 2017), the high resistivity at sea level and mapped fissure swarm trends in the NNE direction. However, from Paka volcano northwards the high resistivity is offset westwards as the fissure swarm continues straight NE of Silali caldera. This break and the accompanying offset maps a possible buried structural shift in the rift alignment between Paka and Silali volcanoes (Fig. 6d). This implies that the rift axis at Silali volcano has recently moved to align with the Paka volcanic axis, as evidenced by the inactive alteration in the west of the Silali caldera with more recent hydrothermal activity occurring in the eastern sector (Lichoro et al., 2017; Dunkley et al., 1993).

3. The gravity survey

The gravity survey discussed here covers the area between Lake Baringo in the south to Silali volcano in the north (Fig. 3). The coverage was focused mostly on the Korosi, Paka and Silali volcanoes in order to better constrain conceptual models being developed for geothermal resources that have been associated with these volcanoes based on a wide variety of geoscience data (Melosh et al., 2014). A total of 515 gravity stations were measured by Geothermal Development Company (GDC) between 2014 and 2017. The gravity station spacing ranges from 200 to 500 m along traverses spaced from 2 to 10 km apart (Fig. 3). The survey coverage was limited by the slower progress of off-road surveys along more regional traverses and by topographical access limitations in the volcanic areas of greatest interest.

Field measurements were made using a Scintrex CG-5 gravimeter (0.001 mGal resolution) with between 3–5 readings taken at every station. A gravity base station (Lat: 0.602038, Lon: 36.003956, Elev.: 1036.7 m, g: 977,668.989 mGal) was established by GDC at the junction of the Kampi Samaki and the Marigat-Loruk roads (Fig. 3). Readings were tied to this base station with reoccupation at the start of each loop in the morning and again about 8 to 12 h later after the day's readings. The standard deviation of the differences in daily readings at the reoccupations of the base station was 0.013 mGal for the entire survey period. Elevation and location measurements were achieved through post-processing of data collected by Trimble GeoXT DGPS instrumentation with nominal precision of less than 0.05 m in x, y and less than 0.10 m for z, implying a gravity uncertainty related to elevation of less than 0.03 mGal.

4. Gravity data processing

In the data processing, gravity corrections were performed to prepare the standard Total Bouguer gravity data set used to prepare maps where relatively high or low gravity values will be correlated with relatively high or low density in the subsurface. Standard gravity reduction procedures were followed (Telford et al., 1990).

Both the Bouguer and Terrain corrections are geological in nature as they depend on density of rocks within the range of elevation of the survey area. The Bouguer gravity reduction formula is given by:-

$$\Delta g = G_{obs} - G_n + 0.3086\,h - 0.04191\rho h + Tc. \quad (1)$$

Where Δg is the Bouguer anomaly, G_{obs} is observed gravity value at a station after drift and tide corrections, while G_n is the gravity value that would be observed if the earth was a perfect rotating ellipsoid, ρ is the density of the horizontal slab in g/cm^3, h is the height of the station in meters relative to sea level and Tc is the terrain correction.

The processing was completed using the “Gravos” gravity reduction program developed at Iceland GeoSurvey (ISOR), which converts initial station readings into absolute gravity values (G_{obs}). Input parameters to “Gravos” include observed gravity readings at each station of each survey loop, the instrument calibration table, known absolute gravity value at the base station and the gravity station coordinates.

4.1. Elevation corrections

The output from Gravos program is further processed by the “Terra” program developed at ISOR that calculates terrain corrections. This program is developed on the principle of the Hammer chart method (Hammer, 1939) which divides the area into several zones and skips the first two zones near the observation station which are assumed to be relatively flat within 20 m radius. Terrain correction was done with a digital elevation model drawn from the ASTER DEM with cell size of 30.8 m and extending for 50 km region beyond the survey area.

Due to limited accuracy of the DEM, we evaluated the differences between DGPS measured heights and corresponding DEM heights at every gravity station. This difference varied between 0 m to about 50 m (see example for the Paka area in Fig. 4). We therefore eliminated all gravity data points that had elevation difference greater than 15 m before plotting the Bouguer maps. This difference in elevation is likely brought about by the inaccuracy of the ASTER terrain model since there are no ground control points in this area and also the elevation consistency of the ASTER DEM has not been fully reviewed globally. Because the mean difference indicates that the ASTER DEM has a datum shift of about 5 m relative to the geodetic datum used for the gravity station DGPS survey, terrain corrections are computed relative to the elevation of the ASTER DEM at the gravity station.

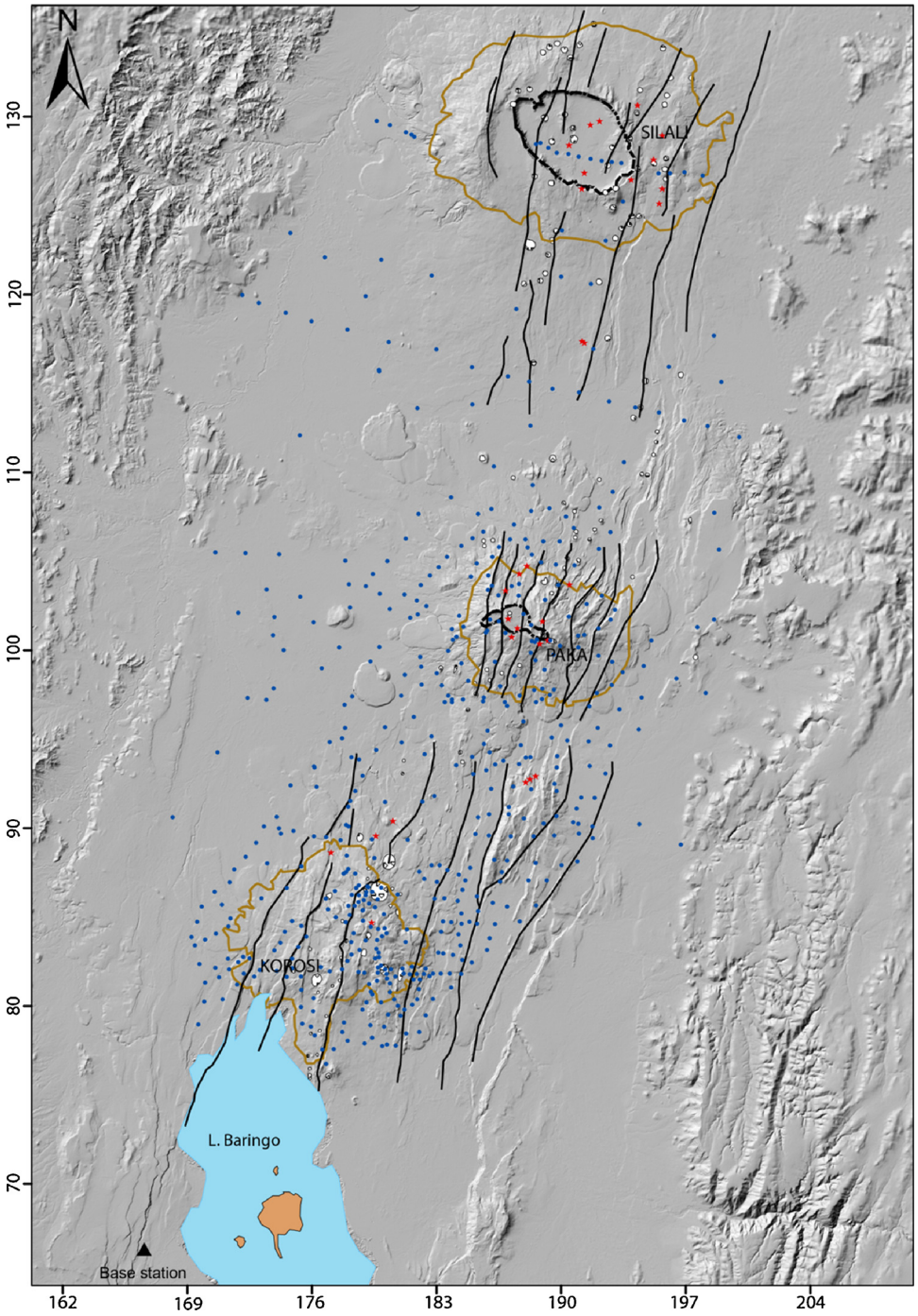

Fig. 3. Location of gravity stations (blue dots), the black triangle marks the base station. Black lines show the mapped fissure swarms; brown lines outline the three main volcanic centres: Korosi, Paka and Silali. Black dotted lines represent calderas, white circular features craters and red stars fumaroles. Coordinates are in UTM-km zone 37 (WGS84). For the location of this area refer to Fig. 1. (For interpretation of the references to color in this figure legend, the reader is referred to the web version of this article).

4.2. Near-surface density determination

In order to produce maps where high and low gravity do not simply mimic topography but indicate areas with relatively high and low density in the subsurface, a density that is representative of the average rock density within the topographic relief of the survey area must be estimated to compute Bouguer and Terrain corrections. In the area of study, there exist no core samples since drilling has not been done yet; however, surface samples have been taken at a geologically comparable area at Suswa volcano and provide reasonable constraints on likely density variation (Cantini et al., 1990).

We estimated near-surface density by applying both Nettleton and Parasnis techniques and by comparing maps computed with different densities. For Nettleton we plotted Bouguer gravity values against elevation for selected densities along profiles crossing the three volcanoes. The density that gave the least correlation between topography and the gravity pattern within the range of elevation of the gravity stations was adopted as an estimate of average bulk density of the rocks in the subsurface through the elevation range of the stations. The values varied from 2.55 g/cm^3, 2.2 g/cm^3 and 2.1 g/cm^3 for profiles across

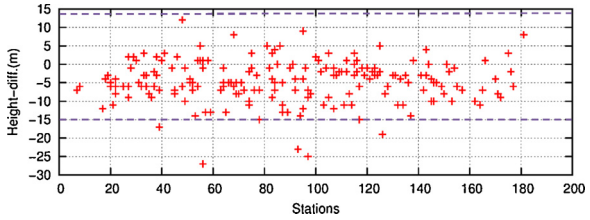

Fig. 4. Plot of elevation difference between DGPS measured heights and corresponding ASTER DEM heights for stations at Paka volcano. The crosses are gravity stations. Purple dotted lines show the data bounds of terrain elevation considered for Bouguer gravity analysis. (For interpretation of the references to color in this figure legend, the reader is referred to the web version of this article).

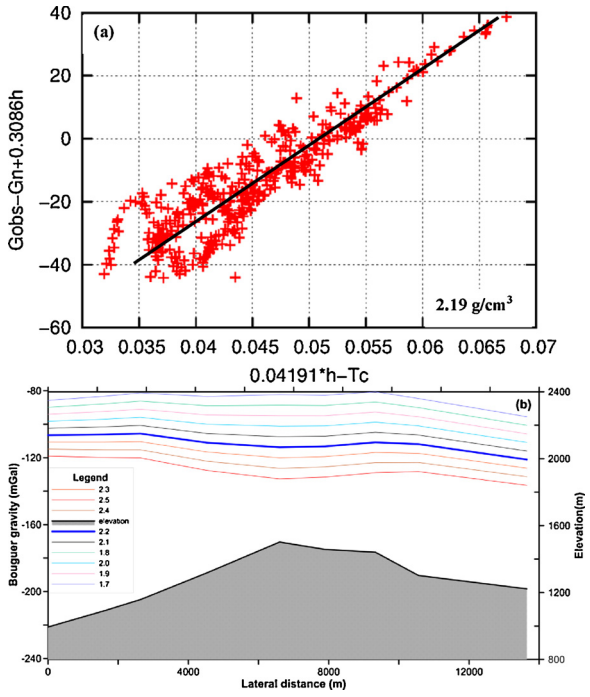

Fig. 5. Bouguer density estimation using (a) Parasnis method. Crosses are gravity readings, (b) Nettleton method; thick blue line (density 2.2 g/cm^3) shows the best estimate. Shaded area represents topography at Paka volcano. (For interpretation of the references to color in this figure legend, the reader is referred to the web version of this article).

Korosi, Paka and Silali volcanoes, respectively (see sample in Fig. 5b). This is consistent with the surface geology where there are mostly dense lavas at Korosi and more pyroclastic cover at both Paka and Silali volcanoes (Dunkley et al., 1993). This indicates the variability in the density of shallow formations in the study area.

To provide an explicit estimate of a near-surface density that would be reasonably representative of the entire study area, we used the Parasnis approach. The Parasnis technique assumes that subsurface density variations will not be correlated with topography, so that plotting terms in the Bouguer reduction formula independent of density (G_{obs}–G_n + 0.3086 h) as a function (of the negative) of the terms multiplying density (0.04191*h-Tc) will give a straight line with a slope equal to the density (assuming that the lateral variation of density within the survey area is not correlated with topography and that the local topographic variation is not correlated with a regional gradient in gravity caused by a large-scale density contrast outside the survey area).

Granted these assumptions are valid, the variation of gravity due to lateral variation in rock density inside the survey area will be manifested as offsets from the straight line with a slope representative of the average rock density within the elevation range of the survey stations. Fig. 5a shows such a plot for the gravity data from this study with a best fit line for the entire data set corresponding to a density of 2.19 g/cm^3. This average density is consistent with the volcanic clastic and ash formations found in surface exposures over most of the survey area. Fig. 5b shows, however, that a part of the data set deviates considerably from the best fit line, as would be expected from the Nettleton analyses.

5. Bouguer gravity map

After applying the described gravity data reductions using the Bouguer density of 2.19 g/cm^3, we gridded the Bouguer anomaly map in Fig. 6(a) using a spherical-splines-in-tension algorithm (Wessel et al., 2013) as implemented in Generic Mapping Tools software. The Bouguer anomaly map reveals a spatial pattern with gravity varying from -95 to -130 mGal, with relatively low values shaded red in the Fig. 6(a) to the western, southern and eastern parts of the study area with a narrower relatively higher gravity trend in the centre. This is in accord with the earlier results that showed a relative high gravity along the axis of the rift (Searle, 1970 McCall, 1967; Swain, 1992). The overall pattern is consistent with generally higher density rocks near the rift axis and at the volcanoes and lower density rocks on the flanks (Swain, 1992). The survey is not wide enough to resolve the larger scale (250 km wide) gravity low interpreted as lower density material at the base of the lithosphere under the East African plateau (Simiyu and Keller, 1997; Swain et al., 1994) that probabaly becomes shallower beneath the rift segment due to mantle upwelling.

5.1. Regional and residual gravity fields

Because of the < 30 km east-west extent of the gravity survey considered in this study, it cannot reliably constrain the gravity features with a scale of 40 km to > 250 km in the regional surveys interpreted by Simiyu and Keller (2001); Mariita and Keller (2007) and Sippel et al. (2017) as caused by density variations in the lithosphere from 20 to 70 km depth. Because the planned depth of investigation for this more local gravity study was much shallower and because the regional data sets were not available for this study, a second order polynomial surface was fit to the gravity data to remove an assumed estimated regional field (Fig. 6b) that was subtracted from the Bouguer gravity (Fig. 6a) to produce a residual gravity map (Fig. 6c).

The residual anomaly map (Fig. 6c) shows an elongated north-south gravity “high”, with amplitude of about > 4 mgal, and “low” gravity values outside the active fissure swarm. The northern trend of gravity high is consistent with the shallowing of Moho northwards in the narrow zone of considerable dike intrusions and east-west variation related to Moho topography on either side of the inner rift zone. An important feature of the residual anomaly map that emerges from this work is the alignment of the high gravity anomaly with the inner rift fissure trend (Fig. 6c). The mapped fissure swarm (Fig. 3) agrees with a gravity high south of Paka volcano but northwards between Paka and Silali volcanoes there is inconsistency where the recent fissure swarm trends NE but the gravity and MT resistivity high (Fig. 6d) trend west of the currently active fissure zone.

6. Gravity models

We have drawn some representative gravity profiles across the study area as shown in Fig. 7 in order to further study the structural features. A location map is inset showing the position of the profiles from north to south. These profiles are drawn in NW-SE directions across the volcanoes to detect density variations within the volcanoes and their flanks. The figure shows residual gravity profiles (Fig. 6c) and the regional anomalies (Fig. 6b) superimposed with the left axis representing the residual anomalies and right axis representing the regional trend. The regional anomalies vary smoothly along the profiles,

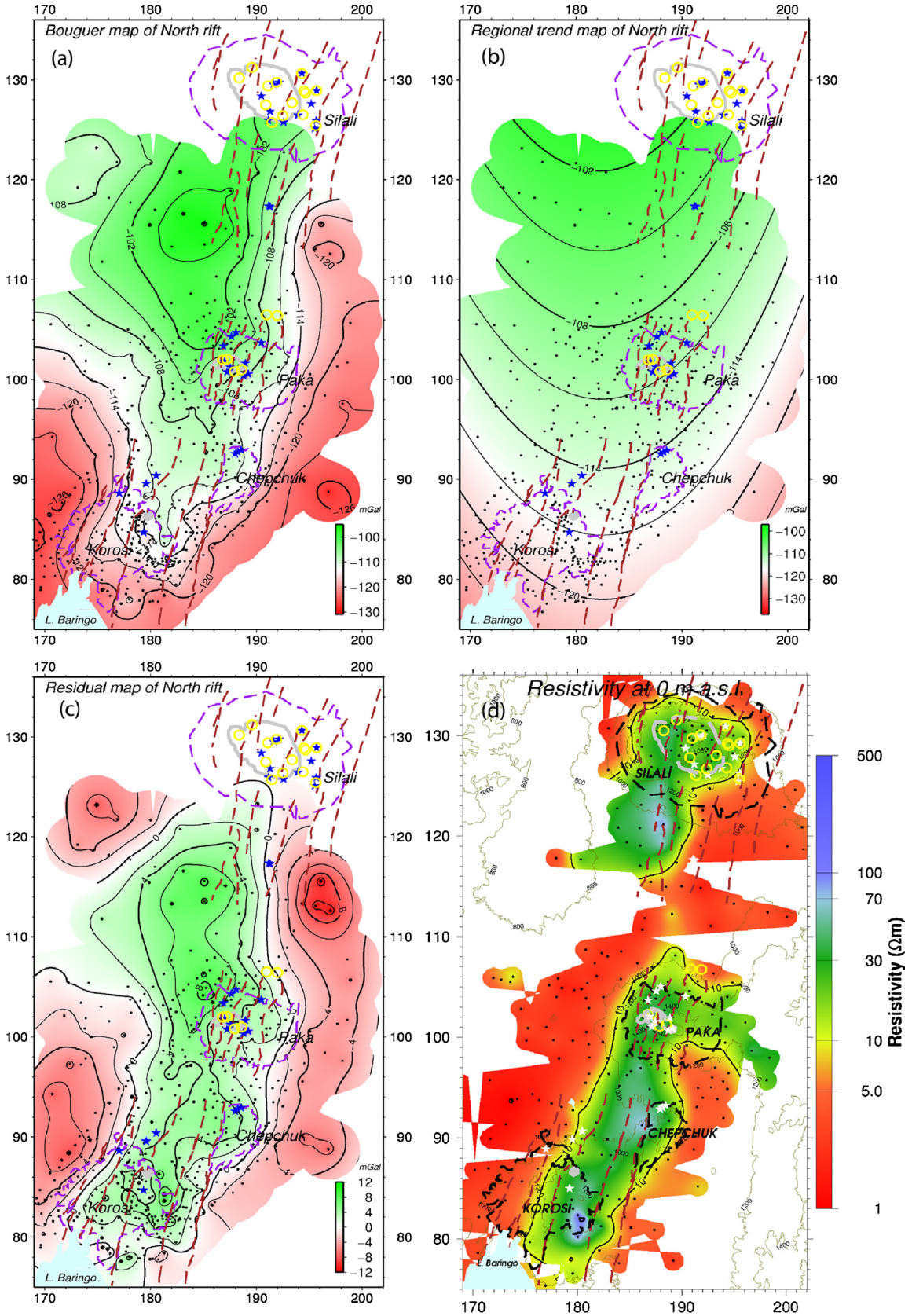

Fig. 6. Gravity and resistivity maps for study area, showing (a) Bouguer gravity (b) Regional gravity (c) Residual gravity and (d) Resistivity at sea level. Stars and yellow rings are geothermal surface manifestations, purple and black dashed line outline the boundaries of the volcanoes, and brown dashed lines show fissure swarm. Coordinates are in UTM in km zone 37 (WGS84). For the location of this area refer to Fig. 1. (For interpretation of the references to color in this figure legend, the reader is referred to the web version of this article).

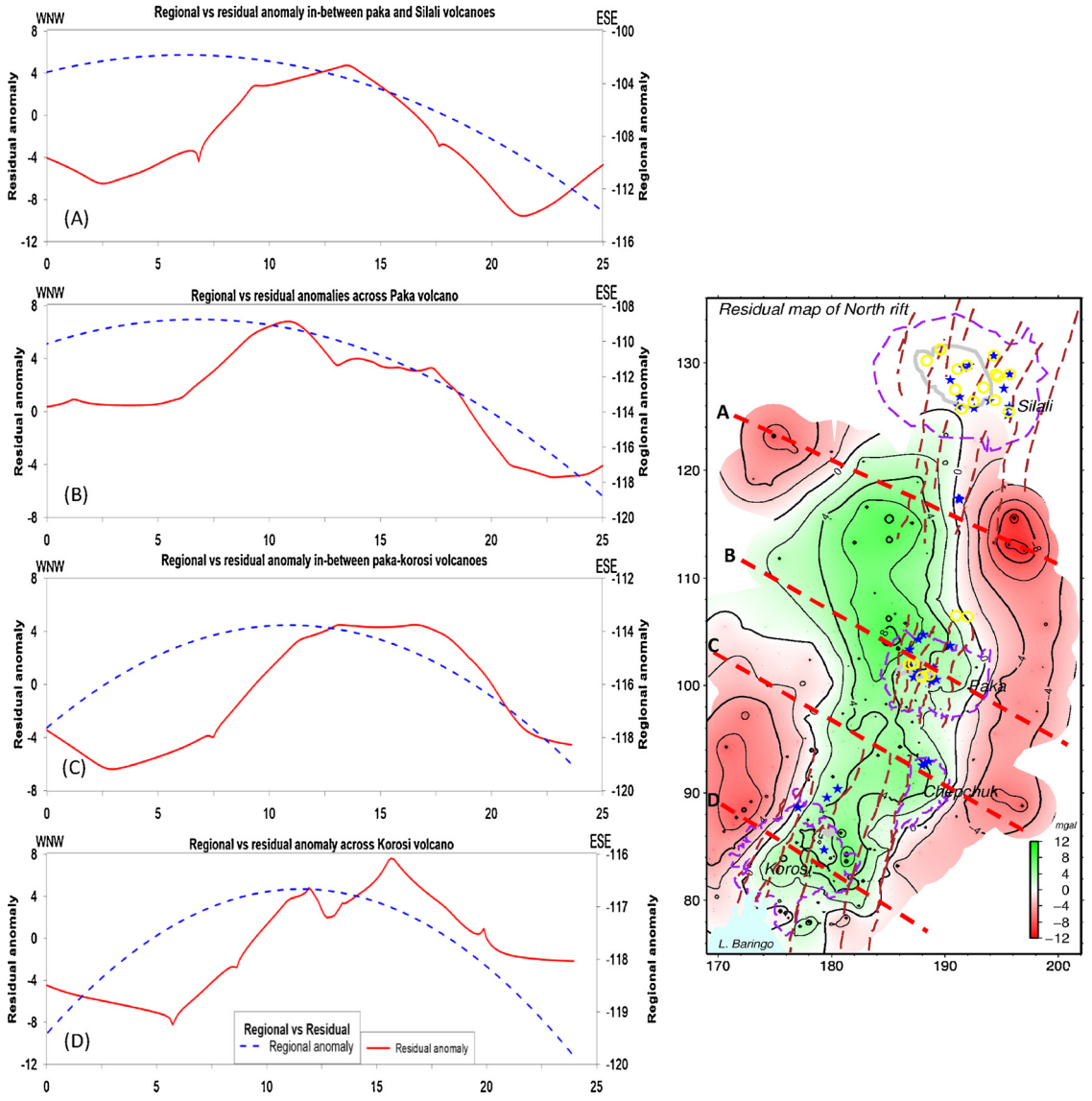

Fig. 7. Residual gravity anomalies (red) and regional field (blue). Profile locations are shown as dashed lines on the inset map; y-axis is in mGal and x-axis is distance in km. (For interpretation of the references to color in this figure legend, the reader is referred to the web version of this article).

reflecting deeper density variations.

7. 2D Gravity modelling constrained by resistivity

Prior to gravity modelling, MT resistivity profiles were prepared along the gravity profiles of interest in order to provide independent constraints on the ambiguous interpretations of the gravity. Because of the size of the area, the inhomogeneous MT station distribution and the large number and variable quality of MT stations, completing a 3D MT inversion was beyond the scope of the project. Because the 2D strike is not consistent across the volcanoes, 1D inversions of the MT TE-mode (polarizations along the rift) were stitched into profiles oriented to fit the gravity profiles. To avoid distortion at depths where the 1D MT inversions would not be expected to be valid, the 1D models were truncated at the skin depth corresponding to the lowest reliable frequency of noisy stations or at the skin depth where indications of 3D distortion such as large on-diagonal impedance elements (large Z_{xx} & Z_{yy} amplitudes) became prominent. The MT cross-sections generated (Figs. 8, 9 & 10) generally show a resistivity structure with a thin resistive (> 60 Ωm) surficial layer underlain by a lower resistivity layer of about 7–30 Ωm flanked by even much lower resistivity (< 7 Ωm) on

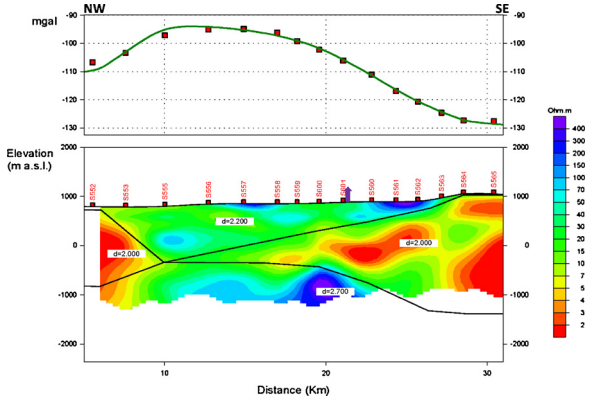

Fig. 8. 2D density model for profile A (Fig.7) passing in between Paka and Silali volcanoes overlaid on MT resistivity to match gravity profile. Red squares are measured gravity points, green curve is the modelled gravity and the purple arrows are fumaroles. Black lines on MT cross-section mark boundaries of density bodies. Numbers give densities in g/cm^3. Vertical exaggeration 3.0. (For interpretation of the references to color in this figure legend, the reader is referred to the web version of this article).

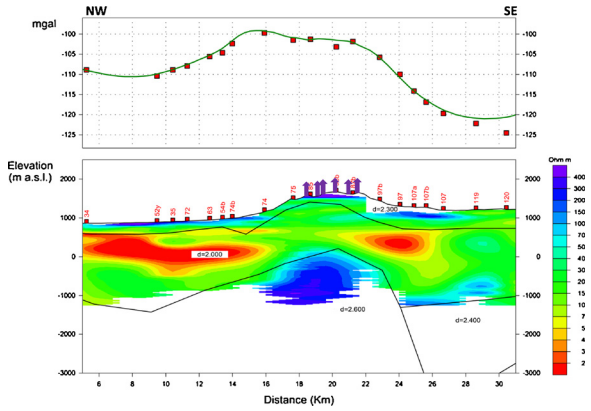

Fig. 9. 2D density model for profile B (Fig.7) across Paka volcano overlaid on MT resistivity to match gravity profile. Red squares are measured gravity points, green curve is the modelled gravity and the purple arrows are fumaroles. Black lines on MT cross-section mark boundaries of density bodies. Numbers give densities in g/cm^3. Vertical exaggeration 2.33. (For interpretation of the references to color in this figure legend, the reader is referred to the web version of this article).

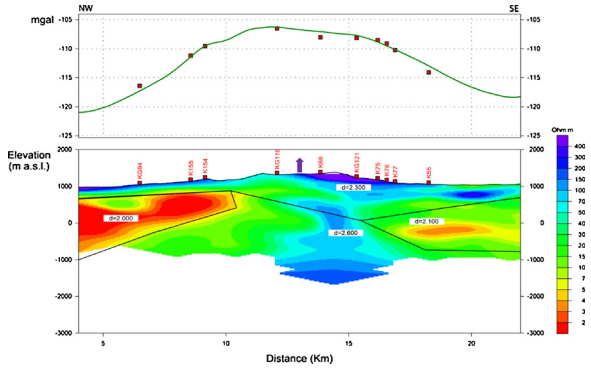

Fig. 10. 2D density model for profile D (Fig.7) across Korosi volcano overlaid on MT resistivity to match gravity profile. Red squares are measured gravity points, green curve is the modelled gravity and the purple arrows are fumaroles. Black lines on MT cross-section mark boundaries of density bodies. Numbers give densities in g/cm^3. Vertical exaggeration 2.0. (For interpretation of the references to color in this figure legend, the reader is referred to the web version of this article).

both the NW and SE ends of the profiles. A higher resistivity zone (> 60 Ωm) is detected at the base of the profile on all the MT profiles and domes up beneath the volcanoes. The value of the higher resistivity below the conductive zone is more ambiguous, both because of inherent limitations to MT (Chave and Jones, 2012) and local data quality issues (Cumming, 2014). However, the doming up of the transition from lower to higher resistivity at the base of the conductor is typically reliably resolved using 1D inversions of the MT TE-mode.

In order to estimate the depth, density and geometry of subsurface bodies, we used Winglink (®Schlumberger) 2D gravity modelling tools to compute gravity along cross-sections perpendicular to the strike of the overall gravity trend. The MT resistivity cross-sections (Figs. 8, 9 & 10) were used as a background constraint during the modelling of the gravity profiles. In this modelling, the Bouguer density was set to 2.2 g/cm^3 (rounded off from reduction density of 2.19 g/cm^3), which is the background density for all undefined parts of the model. The variations in Bouguer gravity were fit to the MT resistivity models placed in the background with shorter wavelength features corresponding to shallower bodies.

We iteratively fit the 2D density model to the Bouguer gravity through forward modelling of bodies with geometry and density contrasts guided by surface geology and the background electrical resistivity. The calculated gravity response was compared with the observed gravity anomaly and the model geometry and densities were adjusted by trial and error until a satisfactory fit between the observed and calculated anomaly was obtained.

The current models are different from earlier ones (Mariita and Keller, 2007), mainly because we are able to map shallow densities related to the volcanoes due to the closer spacing of the survey stations and use of independent constraints on gravity models to 3000 m depth provided by MT resistivity. Earlier models (e.g. Mariita and Keller, 2007) were based on regional surveys and focused on resolving deeper density structure to the base of the lithosphere. In this study residual gravity was computed so as to resolve shallow features that underlie the inner-rift segment (see Fig. 6c). In the models (Figs. 8, 9 & 10), there is likely to be a density gradient due to lava (higher density) being more prevalent at the volcanoes and close to axial fissure eruptions along the rift axis, whereas pyroclastics and volcanoclastics (lower density) are likely to be more prevalent in the moat between the rift axis and the rift bounding faults. Since these models are shallow and gradual they can fit both short and long wavelength gravity variations. The low MT resistivity zones (red) likely correlate with hydrated smectite clay that are low density in the gravity model. The intermediate resistivities (green) are ambiguous but, in this context they are likely to correspond to volcanic rocks with clays that have mostly altered from smectite to higher resistivity and density illite at over 200 °C or to rocks like lavas that had low initial porosity and, therefore, higher resistivity and density. The higher resistivity and density at the base of the profile models are consistent with a shallower transition to high temperature and related chlorite-illite alteration along the axis of eruption (e.g Fig. 9) across the volcanoes but not between the volcanoes. Cumming (2014) hypothesized that the transition to Precambrian crystalline rocks might be relatively flat across much of the Silali area, i.e. at about -1000 masl. This study however suggests that the elevation of the transition to Precambrian crystalline rocks dips away from the volcanoes towards the gravity lows on the outer margin of the high gravity zone. The shallowing of the high density at the base of the models could also be due to emplacement of numerous axial dikes or a massive intrusion into lower density volcanic rocks.

In the models (Figs. 8, 9 & 10), the upper panels show the fit of the observed Bouguer gravity to the gravity computed from the density models. Red squares are the observed data, the calculated gravity anomaly curve is shown in green and the purple arrows are fumaroles. Fig. 8 shows gravity model south of Silali volcano in a NW-SE direction. The calculated response of the model shows a fairly good fit to the observed data and the modelled bodies agree quite well with the resistivity structure displayed in the background. The low density (2.0 g/cm^3) in the NW agrees with the area mapped with thick low resistivity. This is bordered to the SE (right) by a denser (2.2 g/cm^3) formation that thins eastwards, likely to be a combination of intercollated pyroclastics and lava. The high density and high resistivity feature appearing between stations S555 and S556 with its base at 1 km depth seems to be the southern extent of the hypothesized buried lava (Cumming, 2014) SW of Silali volcano. To the SE another low density, low resistivity body with a thickness of about 2 km narrows towards the NW. The deepest body in the model, is a higher density zone (2.7 g/cm^3) that is consistent with high resistivity and domes up along the profile.

The density structure modelled in the profile across Paka volcano (Fig. 9) shows a sequence from the surface of medium, low and high density. The modelled density bodies fit the data and are consistent with the background resistivity profile. The shallowest layer to 300 m depth is modelled as an average of 2.3 g/cm^3, an average of pyroclastics and lavas (Cantini et al., 1990). A prominent low density, low resistivity zone is present from about 300 to 1700 m depth and thickens on both NW and SE ends of the profile. At greater depth, higher density and resistivity is probably associated with intrusions, higher temperature alteration and, on the flanks, the transition to Precambrian crystalline rocks. Both the deeper high density structure and the overlying less

dense zone seem to dome up below the Paka volcano in the zone dominated by fumarolic activity (see Fig. 3). This occurrence is consistent with the up doming of high resistivity at the base of the moderate clay cap (green in Fig. 9) reported beneath the volcano (Lichoro et al., 2017).

The density profile across Korosi volcano (Fig. 10) samples topographic variations from the lowlands in NW through the volcanic highland to the lowlands in the SE, along which surface rocks vary widely (Dunkley et al., 1993). The top intermediate density layer (2.3 g/cm^3) similarly thickens beneath the volcano while thinning on both NW and SE along the profile. On both sides of the profile a low density zone (~ 2.0 g/cm^3) flanks the higher density volcanic core (2.6 g/cm^3).

For all the density zones resistivity seem to be an effective constraint to gravity modelling as demonstrated by both the low resistivity on the flanks of the volcano and the "horst-like" high density structure beneath the Korosi volcano.

8. Correlation of gravity anomalies and resistivity structure

The overall results shown in our gravity residual map (Fig. 6c) agree fairly well with earlier observations from resistivity study (Fig. 6d) reported by Lichoro et al., (2017). Specifically the high resistivity in the rift axis correlates with the high gravity in the same area. However, in the area between Paka and Silali volcanoes the (green) high resistivity trend is interrupted by a (red) conductor but the green gravity high is continuous, albeit with a shift to the west of the axis of the gravity low. This inconsistency could be due to thick, compacted high temperature-altered low porosity tuffs with high density but low resistivity. On the flanks of the volcanoes, where low resistivity was imaged, low gravity reveals low densities, which have been interpreted as volcanoclastics/buried pyroclastic units. Surface geothermal manifestations like fumaroles are mainly located at the margin of the high gravity, potentially controlled by faults and those occurring at the summit of Paka caldera are within a more local zone of relatively low gravity.

Similarly, the gravity results (Fig. 6c) are in fair agreement with the westward offset in high gravity in the Silali sector north of Paka volcano seen in the resistivity (Fig. 6d) which has been interpreted as a possible buried structural step-over in the rift alignment between Paka and Silali volcanoes. Both studies suggest that Silali volcano lies west of the currently active rift zone, which has gradually moved eastwards (based on younger eruption centers) to align with the Paka volcanic axis (Lichoro et al., 2017). This is also consistent with the lack of geothermal activity on the western caldera sector in Silali. Further studies are necessary to establish whether this offset could be related to presence of a transform.

Within the inner rift volcanic zone where surface thermal manifestations are found, the combined 2D resistivity and gravity models include three density categories, from shallowest to deepest: 1) a high resistivity surface layer modelled as intermediate density and consisting of low density tuffs and high density lavas; 2) a low resistivity smectite clay cap modelled as low density altered tuffs; and 3) a resistive layer modelled as high density volcanic, intrusive and Precambrian metamorphic rocks. The combined effect of these layers on all of the profiles is a gravity high related to the third layer, except for lower amplitude local gravity lows at the summits of the Paka and Korosi volcanoes related to very low density tuffs at the surface. The higher density of the third higher resistivity layer has an ambiguous correlation with geology since it is likely to be correlated with a shallower transition from smectite to illite/chlorite alteration below the volcanic centers, dike intrusions denser than the volcanic and Precambrian rocks, and/or uplift in the Precambrian crystalline rocks along the rift axis. A domed pattern of high resistivity beneath a low resistivity clay cap associated with fumaroles on a volcano is diagnostic of either a geothermal reservoir or the acid/vapor-core of an active volcano (Ussher et al., 2000; Árnason et al., 2010; Cumming, 2016).

9. Discussion

The residual gravity anomaly map of the Korosi-Paka-Silali region reveals a coherent pattern with gravity varying over a range of about 20 mGal (Fig. 6c). It delineates a clear NNE-SSW positive gravity anomaly extending through the inner rift segments. The gravity processing and modelling illustrate how the overall gravity trend correlates with the mapped fissures of the axis of the rift. The 2D models discussed above show that the MT resistivity models can constrain modelled density bodies that match the observed gravity. The MT resolves the top of the low resistivity clay alteration zone better than its base overlying the top of the deep resistive high temperature alteration, intrusions and Precambrian basement. This is illustrated (Chave and Jones, 2012) by the modelled high density at the base of the profile in the high resistivity zone as shown in Figs. 8 & 9 . The results suggest that a ~2.7 g/m^3 high density, high resistivity zone becomes shallower at the volcanic centers and northwards along the axis of the rift, whereas ~2.0 g/cm^3 lower density, low resistivity clay-rich volcanoclastics fill the zone between the rift axis and the rift margin.

The mapped rock units in the area are mainly made of trachyte lava with a likely density of 2.55 g/cm^3 (Dunkley et al., 1993; Swain et al., 1981), but the volcanoclastic deposition in the rift would imply a lower overall density. The models demand higher densities of ~2.7 g/cm^3 at depth, which suggests the presence of > 250 °C hydrothermal alteration and/or dense dikes and intrusions below the volcanoes and along the rift axis (see Figs. 8, 9 & 10).

Comparison with a previous MT resistivity study (Lichoro et al., 2017), shows a strong correspondence between the gravity high along the rift axis and a eastwards shallowing of high resistivity from depths of about 2 km to 1 km, correlated with the volcanic centers and the zone of intense faulting and fracturing within the inner rift. Correlation between MT resistivity and gravity show a good match between low resistivity and low gravity, especially on the flanks of the volcanoes, attributed to greater thicknesses of low density, high clay pyroclastics and sediments. Also, a shallow layer below the Paka caldera follows the same pattern, where the conductive clay layer corresponds to a density of 2.2 g/cm^3. Elsewhere surficial fracture zones within the rift are characterized by higher resistivity lavas and probably propylitic alteration (Frolova et al., 2010) at depth of about 2 km corresponding to > 2.6 g/cm^3 density. These have significant implications for the geothermal potential within this part of the volcanic rift zone.

This study is consistent with earlier gravity surveys (e.g. Mariita and Keller, 2007) in that it resolved a positive gravity anomaly along the rift axis in the northern Kenya rift with flanking gravity lows. The high gravity corresponds to the zone of recent faulting, fissure eruptions, and the centers of geothermal activity at large volcanoes within the rift. We have attributed the gravity high to intrusion of dense material and to high temperature alteration (Frolova et al., 2010) in the shallow crust which is consistent with earlier interpretations by (Searle, 1970; Swain, 1992; McCall, 1967). It is now more likely that the positive gravity anomaly within the rift graben is caused by both dense lava at shallow depths and combination of high temperature alteration at 1–3 km depth and dyke injection at depths greater than 2 km. For example, the high-density anomalies (~2.7 g/cm^3) in the shallow subsurface within the rift segment correlate with the surface volcanics or inferred upper crustal dikes (Ebinger, 2005; Swain, 1992) whereas the low gravity anomalies (~2.0 g/cm^3) on the summit of the volcanoes correspond to volcanoclastic/sedimentary deposits.

Previous studies (Simiyu and Keller, 2001; Mariita and Keller, 2007) have been more regional and have lacked support from MT resistivity data and therefore have not focused on modelling local gravity variations associated with density variations shallower than 2 km. Low residual Bouguer gravity on the flanks of the volcanoes coincide with low-lying areas stretching from the flanks of the volcanoes to the outer rift fault scarps east and west of the rift segment and represent the low-density sediments infill of the valleys. Another point of departure with

several of the earlier studies is the inferred offset towards the west of the trend in the gravity high between Paka and Silali, interpreted as a buried former axis of fissure eruptions that has more recently shifted east to match the surface fissure trend in the inner rift south of Silali volcano.

Since the areal extent of the current survey is small, the larger regional feature (with half-width of about 70 km) was removed in the regional-residual separation inorder to allow modelling of smaller residual features. Therefore the current data set is adequate to model the details of the central gravity high and the immediate gravity low flanking inner rift axis but not the outer edge of the rift. The residual gravity anomaly profiles (Fig. 7) show that change in slope in the low gravity at the inner rift boundary is likely due to the volcanoclastics filling the rift.

Rock samples from a geologically comparable area at Suswa volcano (Cantini et al., 1990) showed that a wide range of densities are expected in the study area. Trachyte and basalt lavas have a typical density of 2.55 g/cm^3 at most depths and alteration states. In contrast, trachytic pyroclastics have a density ranging from 1.2 to 2.5 g/cm^3, depending on whether they are dry or wet, altered to smectite clay and still hydrated and low density, altered at higher temperature to more crystalline chlorite-illite clay has much higher density; or if buried to greater depth and so more compacted to higher density. Volcanoclastic sediments have a similar density range of 1.8 to 2.5 g/cm^3, with similar sources of the variation. The metamorphic rocks that outcrop adjacent to the rift and are expected to floor the rift are likely to have a density of about 2.8 g/cm^3.

The non-uniqueness of the gravity modelling was addressed by intergrating the MT resistivity, the surface geology and measured densities for EAR rocks derived from Cantini et al. (1990). Unfortunately there is no drill-hole information in the area to constrain depth of the different density units. In volcanic areas hosting geothermal systems like the study area, compaction and alteration tend to make both density and resistivity more uniform at greater depth and, in this case, the Precambrian metamorphic rocks that floor the volcanics are expected to be uniformly high density and resistivity.

Gravity has been modelled along profiles perpendicular to the strike of the rift similar to those used in earlier resistivity interpretations (Lichoro et al., 2017) to derive a structural model consistent with the MT resistivity cross-sections and gravity constraints on density. The purpose of this comparison is to further constrain the published resistivity structure of the area, particularly with respect the variations detected in the alignment of the rift axis. Although the interpretation of gravity data alone is relatively ambiguous, 2D density models that are constrained by MT resistivity cross-sections, geological mapping and measured densities of rocks from other volcanoes in the rift have reduced the model ambiguity and have provided an improved understanding of this rift segment and its sub-surface structures.

10. Conclusion

We have investigated the shallow structure of the northern Kenya volcanic rift zone using residual gravity models. Profiles have been constructed across the study area showing density variation across the inner volcanic rift zone. The residual gravity map reveals an axial gravity high corresponding to the currently active fissure zone boundaries and flanking gravity lows. The low gravity zones flanking the high have been interpreted as thick zones of sedimentary infill and pyroclastics on the flanks of the volcanoes and the rift fissure eruptions aligned with the rift axis. The relatively high gravity trend aligned with the rift axis has been attributed to a shallowing of dike intrusions and/or a shallower transition to high rank alteration below the volcanic centers and may also be due to a greater proportion of trachyte, basalt and rhyolite lavas along fissure eruption zones.

This study focused on models that matched gravity variation within the rift using density variations shallower than 3 km instead of focusing on the deeper density variations used in earlier large scale regional studies. In this study, models deeper than (~5 km) could not be supported by the more limited gravity data distribution (20 to 30 km wide). This disadvantage was offset by reducing the model ambiguity in several ways, including jointly interpreting the gravity model with MT resistivity imaging, by correlating the gravity with local geology (Dunkley et al., 1993), by using measured densities (Cantini et al., 1990) from other EAR volcanoes, and by considering the petrophysical properties from boreholes in roughly analogous areas. Based on these considerations, the pattern of the gravity could be fit using models to a depth of only 3 km. Formations like the low density pyroclastic and volcanoclastic rocks on the flanks of the rift axis have a density of 1.6 to 2.2 g/cm^3, which strongly contrasts with respect to the much higher density lavas, intrusions and high temperature alteration found along the rift axis above 3 km depth, typically with densities of 2.5 to 2.7 g/cm^3. Depending on thickness and depth of burial of the clays, when subjected to high temperature fluids, they get consolidated, hardened and decreases in both porosity and permeability hence high density. On the other hand, density contrasts are expected to be much smaller between rocks found below 3 km depth such as dike intrusions, high temperature alteration in trachyte, and the Precambrian crystalline rock. Moreover, the dikes and intrusive rocks interpreted along the axis are likely to be slightly less dense than the Precambrian crystalline rock, which would produce a gravity variation inconsistent with the observed gravity. In any case, the axial gravity high along the rift is consistent with the earlier interpretation of magmatic intrusion aligning with the rift trend.

The joint gravity and MT resistivity interpretations along cross-sections show that a high resistivity and high density zone becomes shallower from east and west along the eruption axis of the rift and at the volcanoes. We interprete this as lava, dike intrusives and higher temperature alteration, possibly associated with a geothermal reservoir. The zone of low resistivity and low gravity on the flanks of the volcanoes and fissure eruption zones supports the conclusion that a thick zone of volcanclastics flanks these zones. The surface manifestations are mainly located at the margin of the high gravity, perhaps controlled by faults and those occurring at the summit of Paka caldera are within a more local zone of relatively low gravity (interpreted as tuff), implying potentially fractured shallow geothermal system.

This study shows that if resistivity and gravity are interpreted together, the independent constraints provided by resistivity pattern can improve confidence in the gravity models, particularly where they are supported by geology and petrophysical data. Results are in accord with more regional study where the gravity high correlates with diking/fissure eruption flanked by sediments/pyroclastics. The mapped fissure swarm agrees with both gravity and resistivity south of Paka volcano but northwards between Paka and Silali volcanoes there is inconsistency where fissure swarm trends NE but both gravity and resistivity maps trend west of the currently active fissure zone. The more westerly trend is not discernible from surface geological mapping and has been interpreted as a buried fissure eruption west of the current fissure trend. Further gravity data acquisition north of Paka volcano would better constrain the evolution of the segmentation in this part of the rift and the apparent rift offset that may have existed in the past between Paka and Silali volcanoes.

Acknowledgements

The authors would like to thank the Geothermal Development Company Ltd (GDC) for allowing use of the data, and the geophysics staff of GDC for assistance in data collection over several field campaigns. We are indebted to Ingvar Þór Magnússon for availing his programs to process gravity data. Bryndís Brandsdóttir is also thanked for proof reading the manuscript and assisting in formating of maps. The project was funded by the Geothermal Development Company Limited of Kenya and the United Nations University – Geothermal

Training Programme of Iceland.

References

Achauer, U., 1992. A study of the Kenya rift using delaytime tomography analysis and gravity modelling. Tectonophysics 209, 197–207.

Árnason, K., Eysteinsson, H., Hersir, G.P., 2010. Joint 1D inversion of TEM and MT data and 3D inversion of MT data in the Hengill area, SW Iceland. Geothermics 39, 13–34. https://doi.org/10.1016/j.geothermics.2010.01.002.

Baker, B.H., Wohlenberg, J., 1971. Structure and evolution of the Kenya Rift Valley. Nature 229, 538–541.

Biggs, J., Anthony, E.Y., Ebinger, C.J., 2009. Multiple inflation and deflation events at Kenyan volcanoes, East African Rift. Geology 37, p979–982 10.1130G30133A.1:2.

Biggs, J., Robertson, E., Cashman, K.V., 2016. The lateral extent of volcanic interactions during unrest and eruption. Nat. Geosci. 9, 308–311. https://doi.org/10.1038/ngeo2658.

Bjornsson, A., Saemundsson, K., Einarsson, P., Tryggvason, E., Gronvold, K., 1977. Current rifting episode in north Iceland. Nature 318–323.

Calais, E., Ebinger, C., Hartnady, C., Nocquet, J.M., 2006. Kinematics of the East African Rift from GPS and earthquake slip vector data. Geol. Soc. London Spec. Publ. 259, 9–22. https://doi.org/10.1144/GSL.SP.2006.259.01.03.

Cantini, P., Cataldi, A., Pinna, E., 1990. Gravity study of the structure of Suswa volcano and basement in the Kenya Rift. Geothermics 19, 367–384. https://doi.org/10.1016/0375-6505(90)90039-E.

Chave, Jones (Eds.), 2012. The Magnetotelluric Method: Theory and Practice. Cambridge University Press, pp. 552.

Clarke, M.C.G., Woodhall, D.G., Allen, D., Darling, G., 1990. Geological, Volcanological and Hydrogeological Controls of the Occurrence of Geothermal Activity in the Area Surrounding Lake Naivasha, Kenya. Ministry of Energy report, Kenya.

Corti, G., 2009. Continental rift evolution: from rift initiation to incipient break-up in the Main Ethiopian Rift, East Africa. Earth Sci. Rev. 96, 1–53.

Cumming, W., 2014. UNEP Silali Resource Review – Geophysics; Report to the United Nations Environmental Program. pp. 71.

Cumming, W., 2016. Resource conceptual models of volcano-hosted geothermal reservoirs for exploration well targeting and resource capacity assessment: construction, pitfalls and challenges. Geotherm. Resour. Counc. Trans. 40, 623–638.

Dunkley, P.N., Smith, M., Allen, D.J., Darling, W.G., 1993. The geothermal activity and geology of the northern sector of the Kenya Rift Valley. British Geological Survey Research Report.

Ebinger, C., 2005. Continental break-up: the East African perspective. Astron. Geophys. 46 (2) 16–2.21.

Ebinger, C.J., Sleep, N.H., 1998. Cenozoic magmatism throughout east Africa resulting from impact of a single plume. Nature 395, 788–791. https://doi.org/10.1038/27417.

Ebinger, C.J., Bechtel, T.D., Forsyth, D.W., Bowin, C.O., 1989. Effective elastic plate thickness beneath the East African and Afar plateaus and dynamic compensation of the uplifts. J. Geophys. Res. 94, 2883–2901.

Frolova, J.V., Ladygin, V.M., Rychagov, S.N., 2010. Petrophysical alteration of volcanic rocks in hydrothermal systems of the Kuril- Kamchatka Island Arc. World Geotherm. Congr. pp. 25–29.

George, R.M.M., Rogers, N.W., Kelley, S., 1998. Earliest magmatism in Ethiopia: evidence for two mantle plumes in one flood basalt province. Geology 923–926.

Grandin, R., Socquet, A., Binet, R., Klinger, Y., Jacques, E., De Chabalier, J.B., King, G.C.P., Lasserre, C., Tait, S., Tapponnier, P., Delorme, A., Pinzuti, P., 2009. September 2005 Manda hararo-dabbahu rifting event, Afar (Ethiopia): constraints provided by geodetic data. J. Geophys. Res. Solid Earth 114. https://doi.org/10.1029/2008JB005843.

Green, W.V., Achauer, U., Meyer, R.P., 1991. A three-dimensional seismic image of the crust and upper mantle beneath the Kenya rift. Nature 354, 199–203. https://doi.org/10.1038/354199a0.

Hammer, S., 1939. Terrain corrections for gravimeter stations. Geophysics 4, 184–194.

Keller, G.R., Mechie, J., Braile, L.W., Mooney, W.D., Pradehl, C., 1994a. Seismics tructure of the uppermost mantle beneath the Kenya rift. Tectonophysics 236, 201–216.

Keller, G.R., Prodeh, C., Mechie, J., Fuchs, K., Khan, A.M., Maquire, P.K., Mooney, W.D., Achauer, U., Davis, P.M., Meyer, R.P., Braile, L.W., Nyambok, I.O., Thompson, G.A., 1994b. The East African rift system in the light of KRISP 90. Tectonophysics 236, 465–483.

KRISP, 1987. Structure of the Kenya rift from seismic refraction. Nature 325, 239–242.

Lichoro, C.M., 2013. Multi-dimensional Interpretation of Electromagnetic Data From Silali Geothermal Field in Kenya: Comparison of 1-D, 2-D and 3-D MT Inversion. MSc Thesis. Univ. Icel 185pp.

Lichoro, C.M., Árnason, K., Cumming, W., 2017. Resistivity imaging of geothermal resources in northern Kenya rift by joint 1D inversion of MT and TEM data. Geothermics 68, 20–32. https://doi.org/10.1016/j.geothermics.2017.02.006.

MacDonald, R., 2003. Magmatism of the Kenya Rift Valley: a review. Earth. Rev. 93, 239–253.

Maguire, P.K.H., Swain, C.J., Masotti, R., Khan, M.A., 1994. A crustal and uppermost mantle cross-sectional model of the Kenya Rift derived from seismic and gravity data. Tectonophysics 236, 217–249. https://doi.org/10.1016/0040-1951(94)90178-3.

Mariita, N.O., Keller, G.R., 2007. An integrated geophysical study of the northern Kenya rift. J. Afr. Earth Sci. 48, 80–94. https://doi.org/10.1016/j.jafrearsci.2006.05.008.

McCall, G.J.H., 1967. Geol. Surv. Kenya Rep. pp. 78.

Mechie, J., Keller, G.R., Prodehl, C., Gaciri, S., Braile, L.W., Mooney, W.D., Gajewski, D., Sandmeier, K., 1994. Crustal Structure Beneath the Kenya Rift From Axial Profile Data 236. pp. 179–200.

Mechie, J., Keller, G.R., Prodehl, C., Khan, M.A., Gachiri, S.J., 1997. A model for the structure, composition and evolution of the Kenya rift. Tectonophysics 278, 95–119.

Melosh, G., Cumming, W., Marini, L., 2014. Conceptual Model of the Silali Prospect - Technical Review; Rreport to the United Nations Environmental Program. 47 pp. .

Mohr, P., 1987. Structural style of continental rifting in Ethiopia: reverse decollements. Eos, Trans. Am. Geophys. Union 68, 721–730. https://doi.org/10.1029/EO068i035p00721.

Morley, C.K., 1994. Interaction of deep and shallow processes in the evolution of the Kenya rift. In: Prodehl, C., Keller, G.R., Khan, M.A. (Eds.), Crustal and Upper Mantle Structure of the Kenya Rift, pp. 81–91 Tectonophysics.

Nyblade, A.A., 2011. The Upper-mantle Low-velocity Anomaly Beneath Ethiopia, Kenya, and Tanzania: constraints on the Origin of the African Superswell in Eastern Africa and Plate Versus Plume Models of Mantle Dynamics. 2478. pp. 37–50. https://doi.org/10.1130/2011.2478(03).

Nyblade, A.A., Pollack, H.N., Jones, D.L., Podmore, F., Mushayandebvu, M., 1990. Terrestrial heat flow in east and southern Africa. J. Geophys. Res. 95. https://doi.org/10.1029/90JB01347.

Ofwona, C., Wambugu, J.M., Omenda, P., Mariita, N., Mwawongo, G., Kubo, B., 2006. Surface geothermal exploration of Korosi and Chepchuk prospects. In: Ofwona, C. (Ed.), Internal Report, pp. 45–62 Unpublished.

Prodehl, C., Ritter, J.R.R., Keller, G.R., Khan, M.A., Jacob, B., Fuchs, K., Nyambok, I.O., Obel, J.D., Riaroh, D., 1997. The KRISP 94 Lithospheric Investigation of Southern Kenya Experiments and Their Main Results the 278. pp. 121–147.

Ring, U., Livingstone, D., Stanley, H.M., Fischer, G., 2014. The East African Rift system. Aust. J. Earth Sci. 107 (1), 132–146.

Rowland, J.V., Baker, E., Ebinger, C.J., Keir, D., Kidane, T., Biggs, J., Hayward, N., Wright, T.J., 2007. Fault growth at a nascent slow-spreading ridge: 2005 Dabbahu rifting episode. Afar. Geophys. J. Int. 171, 1226–1246. https://doi.org/10.1111/j.1365-246X.2007.03584.x.

Schilling, J., Kingsley, R.H., Hanan, B.B., McCully, B.L., 1992. Nd-Sr-Pb isotopic variation along the Gulf of Aden: evidence for Afar mantle plume-continental lithosphere interaction. J. Geophys. Res. 97, 10927–10966. https://doi.org/10.1029/92jb00415.

Searle, R.C., 1970. Evidence from gravity anomalies for thinning of the lithosphere beneath the Rift Valley in Kenya. Geophys. J. R. Astron. Soc. 21, 13–31. https://doi.org/10.1111/j.1365-246X.1970.tb01764.x.

Sigmundsson, F., 2006. Iceland Geodynamics: Crustal Deformation and Divergent Plate Tectonics. Springer.

Simiyu, S.M., Keller, G.R., 1997. An integrated analysis of lithospheric structure across the East African plateau based on gravity anomalies and recent seismic studies. Tectonophysics 278, 291–313. https://doi.org/10.1016/S0040-1951(97)00109-1.

Simiyu, S., Keller, G.R., 2001. An integrated geophysical analysis of the upper crust of the southern Kenya rift. Geophys. J. Int. 147, 543–561. https://doi.org/10.1046/j.0956-540x.2001.01542.x.

Sippel, J., Meeßen, C., Cacace, M., Mechie, J., Fishwick, S., Heine, C., Scheck-Wenderoth, M., Strecker, M.R., 2017. The Kenya rift revisited: insights into lithospheric strength through data-driven 3-D gravity and thermal modelling. Solid Earth 8, 45–81. https://doi.org/10.5194/se-8-45-2017.

Stamps, D.S., Calais, E., Saria, E., Hartnady, C., Nocquet, J.M., Ebinger, C.J., Fernandes, R.M., 2008. A kinematic model for the East African Rift. Geophys. Res. Lett. 35, 1–6. https://doi.org/10.1029/2007GL032781.

Swain, C.J., 1992. The Kenya rift axial gravity high: a re-interpretation. Tectonophysics 204, 59–70.

Swain, C.J., Khan, M.A., Wilton, T.J., Maguire, P.K.H., Griffttths, D.H., 1981. Seismic and gravity surveys in the Lake Baringo-Tugen Hills area, Kenya rift valley. J. Geol. Soc. 93–102.

Swain, C.J., Maguire, M.A., Khan, P.K.H., 1994. Geophysical experiments and models 01 the Kenya Rift before 1989. In: Prodehl, C., Keller, G.R., Khan, M.A. (Eds.), Crustal and Upper Mantle Structure of the Kenya Rift, pp. 23–32 Tectonophysics, 236.

Telford, W.M., Geldart, L.P., Sherif, R.E., 1990. Applied Geophysics. Cambridge University Press.

Ussher, G., Harvey, C., Johnstone, R., Anderson, E., Zealand, N., 2000. Understanding the resistivities observed in geothermal systems. Proc. World Geotherm. Congr. pp. 1915–1920.

Wessel, P., Smith, W.H.F., Scharroo, R., Luis, J.F., Wobbe, F., 2013. Generic mapping tools: improved version released. EOS Trans. AGU 94, 409–410.

Williams, L.A.J., 1972. The Kenya Rift volcanics: a note on volumes and chemical composition. Tectonophysics 15, 83–96. https://doi.org/10.1016/0040-1951(72)90054-6.

Williams, L.A.J., Macdonald, R., Chapman, G.R., 1984. Late quatenary caldera volcanoes of the Kenya rift valley. J. Geophys. Res. 89, 8553–8570. https://doi.org/10.1017/CBO9781107415324.004.

Wood, J., Guth, A., 2015. East Africa's Great Rift Valley: A Complex Rift System. Michigan Technological University Accessed on 1st January, 2018. http://geology.com/articles/east-africarift.shtml.

Wright, T.J., Ebinger, C., Biggs, J., Ayele, A., Yirgu, G., Keir, D., Stork, A., 2006. Magma-maintained rift segmentation at continental rupture in the 2005 Afar dyking episode. Nature 442, 291–294. https://doi.org/10.1038/nature04978.

Paper III

A review and comparison of developed and undeveloped geothermal systems in the Kenya Rift based on resistivity, gravity studies and geological structure.

Charles Muturia Lichoro, William Cumming, Knútur Árnason

Submitted to Journal of Volcanology and Geothermal Research

A review and comparison of developed and undeveloped geothermal systems in the Kenya Rift based on resistivity, gravity studies and geological structure.

Charles Muturia **Lichoro**[a,d,e], William Cumming[b], Knútur Árnason[c],

[a] *Geothermal Development Company Ltd, P.O. Box: 17700-20100, Polo House, Nakuru, Kenya*
[b] *Cumming Geoscience, 4728 Shade Tree Lane, Santa Rosa CA 95405, USA*
[c] *ISOR Iceland GeoSurvey, Grensasvegur 9, 108 Reykjavik, Iceland*
[d] *Department of Earth Sciences, University of Iceland, Askja, Sturlugata 7, 101 Reykjavík, Iceland*
[e] *UNU-GTP, Orkustofnun, Grensásvegi 9, IS-108 Reykjavík, Iceland*

Keywords: Kenya Rift, geothermal systems, comparison, resistivity, gravity, magmatic heat sources.

Abstract

A comparison is made of surface geology, resistivity and density structure of seven volcanic centres distributed along a 300 km segment of the Kenya Rift, including two very different developed geothermal fields and five undrilled geothermal systems/prospects. We are looking for similarities and differences in order to infer likely geothermal characteristics of the undeveloped prospects in the northern Kenya Rift. A comparison of MT and TEM images of resistivity with subsurface resource properties of the Olkaria geothermal field helps to validate and assess the uncertainty of interpretations of similar MT and TEM data combined with gravity survey constraints on density at three prospects in the northern Kenya Rift for which exploration drilling is being planned. For example, data from Olkaria illustrate both how mapping of the low resistivity, temperature-sensitive smectite clay cap constrains the top and margins of the reservoir but is limited by ambiguity related to relict alteration. To provide a consistent comparison among the areas, the MT resistivity images were computed using joint 1D inversions of the MT invariant mode and co-located TEM. To test how this might limit the detection of deeper features, the 1D MT imaging is compared to a 3D MT inversion at the Paka prospect and the resolution of the 1D inversions is tested on synthetic MT data computed for magma bodies of differing dimensions. Wells at Menengai have encountered magma as shallow as 2000 m depth, limiting the producible reservoir volume whereas numerous wells to over 3000 m depth throughout Olkaria have encountered widespread temperature over 250°C but not magma, contributing to its larger capacity. Although detecting shallow magma is important to geothermal resource assessment in the Kenya Rift, it cannot be reliably done using the available MT data due to noise that limits the reliability of 3D inversion and inherent limitations of 1D inversion, as demonstrated by a 2D model sensitivity study. Therefore, for those prospects of the Kenya Rift where magma might be expected at depths shallower than 3 km depth, more focused microearthquake monitoring and InSAR monitoring of deformation are likely to improve assessments of resource capacity. Comparisons of developed geothermal fields to undrilled prospects has confirmed that, although the patterns of MT resistivity imaging supported by gravity constraints on density do correlate with geothermal reservoirs in systematic ways, assessments of well targets and resource capacity will more reliably be determined by integrating MT, gravity and geology interpretations with geochemistry and thermodynamic constraints into more comprehensive geothermal resource conceptual models.

1. Introduction

The Kenyan rift has been extensively studied both for understanding of rift structures and for geothermal exploration. About 14 high temperature geothermal prospects have been identified along the Kenyan rift valley, of which 3 are being developed while the rest are at different exploration stages. Presently, about 700 MW_e of electricity generation have been developed at the Olkaria (Axelsson et al., 2017; Rop et al., 2018) and Eburru geothermal fields in the south of the Kenya rift (Mwarania, 2014) and the first 35 MW_e power plant of a planned 105 MW_e development is under construction at Menengai in the Central Kenyan Rift. Seven volcanoes (Fig. 1) undergoing active geothermal development or ongoing exploration are considered here, three of them in the southern Kenya Rift (Suswa, Longonot and Olkaria), three in the northern Kenya Rift (Korosi, Paka and Silali) and one in the central Kenya Rift (Menengai). The MT, TEM, supporting surface exploration information and drilling results from the Olkaria geothermal field are used in this study to compare to undeveloped geothermal prospects within the Kenya Rift and look for similarities and differences in order to improve resource identification, capacity assessment and well targeting.

Geothermal exploration has been focused on the volcanoes more than on the fissure eruption vents on the rift floor or the lake-filled calderas because most thermal manifestations are located on the volcanoes. The volcanoes host more repetitive magmatic activity likely to heat a large volume of water to over 230°C in fractured permeable volcanic rocks with rapid heat loss due to boiling or chilling due to cold water influx limited by an overlying cap of impermeable clay alteration. Most of the volcanoes are aligned with the central axis of the rift, although variations in the elongation strike of the calderas and the offset of volcanoes from the axis of the rift are attributed to the influence of the Precambrian structures (Robertson et al., 2015). For example, the Olkaria and Longonot volcanic centres have the most prominent offset from the axis of the rift and are aligned with each other almost perpendicular to the rift axis (Fig. 1). The volcanoes are built on varying thicknesses of volcanic ash and sediments accumulated between the volcanic eruption centers and the rift margins. The morphology of the volcanoes varies depending on the predominant rock type and volatile content of the source magma. Most of the volcanoes in the Kenyan Rift are dominantly trachyte shield volcanoes with large calderas formed by magma withdrawal related to lower flank eruptions. Longonot is a small trachyte stratocone with a significant ash content. Uniquely in the Kenyan Rift, Olkaria is dominated by a very large rhyolite dome complex, possibly related to it also hosting the largest discovered geothermal field in the Kenyan Rift.

The geophysical methods that have been used at regional and continental scales to understand the Kenyan Rift as part of the East African Rift System include regional earthquake monitoring, regional refraction seismic analyses, gravity surveys, InSAR monitoring of vertical deformation and DGPS monitoring of lateral deformation. These surveys cover areas extending over 100s to 1000s of km and are directed at resolving geological features to 100s of km depth, whereas geothermal exploration surveys usually cover areas extending over a few 10s of km to resolve geological features shallower than 10 km depth, often shallower than a few km.

The most commonly used geophysical methods in geothermal exploration are electromagnetic methods used to image the subsurface resistivity structure, including magnetotelluric (MT) and transient electromagnetic (TEM) surveys. These are complementary methods, with MT capable of imaging resistivity to many 1000s of m depth while, in this context, TEM compensates for the static distortion that sometimes increases the ambiguity of MT. Resistivity is sensitive to many rock properties including water saturation, cation exchange capacity (surface conduction in clays), porosity, pore connectivity, temperature, salinity and presence of magma. In a geothermal context, the very low resistivity of the temperature sensitive smectite clay alteration that caps almost all geothermal reservoirs is the most important factor used to constrain geothermal resource

conceptual models. A total of 700 MT stations covering 7 volcanoes in the Kenya rift are reviewed in order to construct 1D resistivity inversion models correlated with mapped geological structures in the vicinity of the volcanoes and with previous gravity studies. The resistivity pattern imaged by EM methods conducted over a geothermal reservoir from the surface down typically includes near-surface unaltered rocks (>100 Ωm) underlain by low resistivity smectite-zeolite alteration (<10 Ωm in andesite, rhyolite, basalt and sedimentary rocks and <20 Ωm in trachyte and phonolite rocks), that are, in turn, underlain by a more resistive zone (>10 Ωm) that is ambiguous but may correspond to the high-temperature chlorite/illite-epidote alteration associated with a productive geothermal reservoir, and possibly further underlain by deeper low resistivity associated with partial melt (Árnason et al., 2010; Gasperikova et al., 2015; Manthilake et al., 2016).

The current study aims at reviewing geothermal systems/prospects within three rift segments by comparing geoscientific results of developed geothermal fields to those of undeveloped fields. With this analysis we hope to: (a) illustrate the role played by the rift in the occurrence of geothermal resources; (b) give an overview of similarities and differences between the volcano-hosted geothermal reservoirs and prospects in the Kenyan rift; (c) illustrate how the pattern of the base of the low resistivity smectite clay can constrain the minimum geothermal reservoir depth and maximum reservoir bounds and highlight ambiguities in the use of this transition in the Kenyan Rift; (d) use 2D modelling to evaluate the detectability of magmatic heat sources of different size and depth given the limitations of available MT data; and (e) based on evidence from developed fields, discuss implications of depth to the magma for undeveloped geothermal systems. Eburru geothermal field to the north of Olkaria has been drilled and a 2.5 MWe capacity power plant installed, however, this field lack sufficient geophysics data especially MT to warrant consideration in this study.

2. Rift volcanic setting and selected previous geophysical studies

The Kenya rift is the classic example of an active continental rift. It forms part of the eastern branch of the East African Rift System (EARS) which is characterised by extensive volcanism associated with high rates of magma production. This is evidenced by numerous volcanoes and fissure eruptions and associated geothermal surface manifestations. The Kenya Rift has been subdivided into three zones namely, the Southern Kenya Rift (SKR), the Central Kenya Rift (CKR) and the Northern Kenya Rift (NKR) based on structural architecture (Chorowicz, 2005). The rift strike direction changes from NNW in the SKR to N-S in CKR and then trends NNE in the NKR (Fig. 1), corresponding to respective orthogonal extension of the individual sectors and rotation of rift axis (Strecker et al., 1990; Bosworth et al., 1992).

Magmatic activity initiated about 30 Ma in the NKR and progressed southward reaching tip-end of the SKR about 7 Ma (MacDonald, 2003). Volcanic activity continued into the Quaternary resulting in build-up of several volcanoes on the inner rift floor. Rift propagation progressed further southwards, reaching the Northern Tanzania where it splayed due to the interaction with the Tanzania craton. Rift propagation in the Kenya Rift was accompanied by normal faulting and crustal extension which is estimated at 35 km in the NKR (Mechie et al., 1997) reducing to 5-10 km in the SKR. Crustal thinning and increased extension northwards is reflected by the Bouguer gravity increase from -250 mGal in the south to -50 mGal in the north (Mechie et al., 1994).

Regional refraction seismic studies like the Kenya Rift International Seismic Project (KRISP) (Henry et al., 1990; KRISP Working Group, 1991; Mechie et al., 1997, 1994) constrained the velocity structure of the crust and upper mantle beneath the Kenyan Rift and with refined

resolution at several of the central volcanoes. Seismic refraction and wide-angle reflection profiles along and across the rift revealed the existence of a high P-wave velocity region (Vp 6.8 km/s) at the base of the crust corresponding to crustal thinning from 35 km in the SKR to 20 km in NKR, which Mechie et al. (1994) and Keller et al. (1994) have attributed to magmatic intrusions. The KRISP program run in phases between 1985 and 1994 and mapped relatively high velocity in the volcanics corresponding to Quaternary volcanic centres at Menengai, Olkaria and Suswa. The KRISP 85 refraction survey produced a P-wave model with three layers comprised of rift volcanics and sediments with a velocity range of 2.8 - 5.6 km/s above the Precambrian basement from Lake Baringo in the NKR to south of Suswa in the SKR (Simiyu and Keller, 2001).

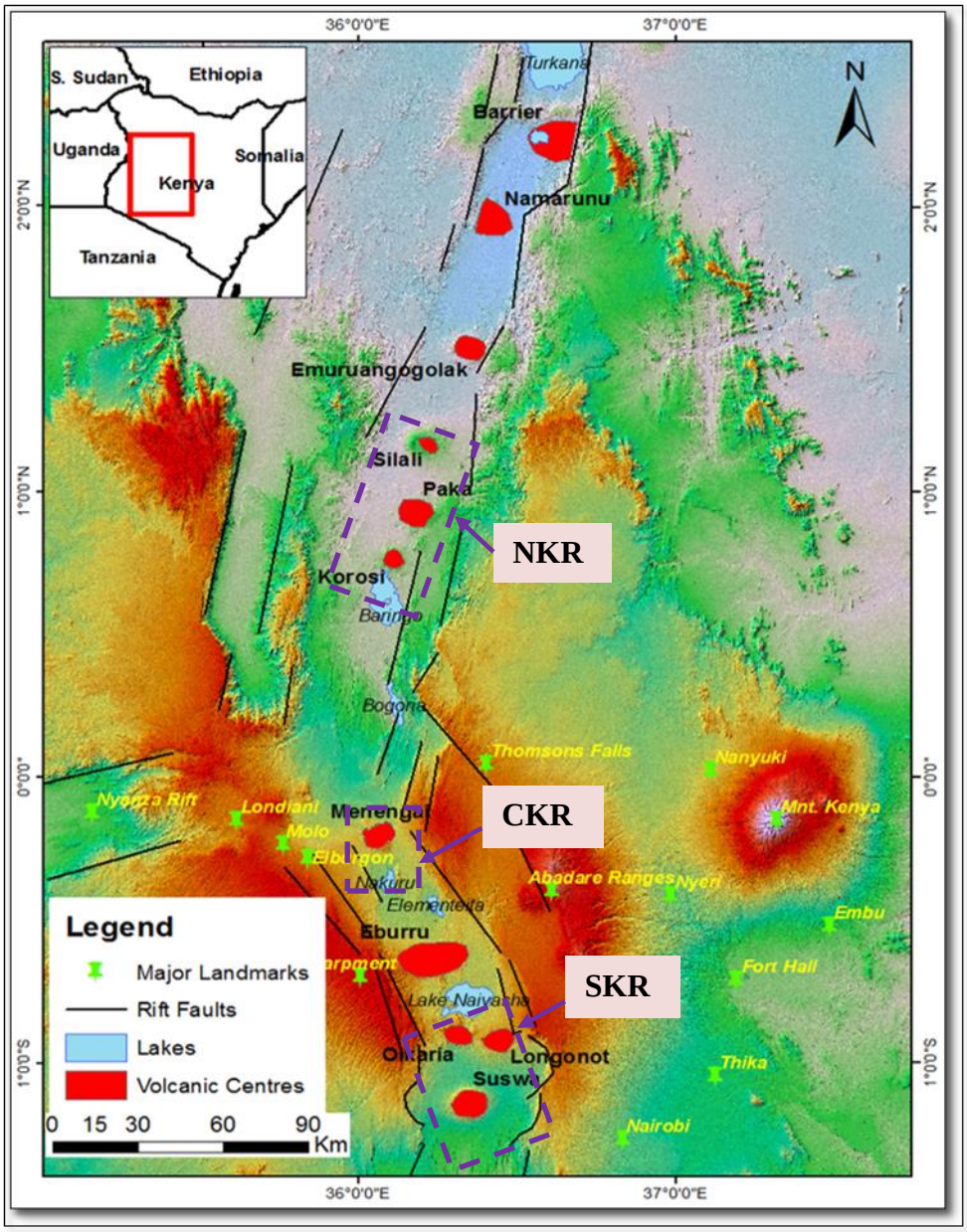

Figure 1: Map showing volcanic areas in the Kenya rift. The dashed-purple rectangles represent the areas of study. Coordinates are WGS84.

The KRISP 94 profile across the Kenya rift about 60 km south of Suswa shows a 4 to 5.5 km thick layer of 5.6 km/s material above a 6.0 km/s basement (Simiyu and Keller, 1997). The lower velocity rift fill and the thickening of crust from north to south are consistent with a greater proportion of tuff and sediments to the south where the crust is thicker and more intrusions and lava to the north.

Using travel times from local earthquakes recorded at Olkaria geothermal field, Simiyu (2000), constructed models of Vp/Vs and Poisson's ratio beneath the geothermal field in the upper 6 km of the crust. Results show that Vp/Vs ratios vary from 1.58 in the East production field to 1.82 in the Olkaria central field and Poisson's ratio of 0.15 to 0.30 respectively suggestive of higher temperature and steam saturation in the East production field. This study also imaged shallow S-wave attenuating bodies beneath the Olkaria volcanic complex interpreted as zones of recent magma emplacement. The maximum hypocentre depth for the earthquakes of 4 to 5 km was interpreted as the brittle-ductile transition near 450°C, consistent with the 350°C temperature measured in wells at 3000 m depth.

Recent seismicity recorded by a temporary local network at volcanoes in Menengai, Korosi, Paka and Silali (Patlan et al., 2017), identified two seismic swarms at Paka and Menengai volcanoes occurring vertically in pipe-like shape between 3 to 6 km depth with estimated b-value of 0.83 and 1.24 respectively. Although these shallow clusters of seismicity were consistent with failure due to tectonic stress, they may have been triggered by deep magma movement associated with the active volcano.

InSAR monitoring of volcanoes has commonly detected rapid variations in uplift and subsidence that, in the context of the Kenya Rift, are likely to be related to the interaction of tectonic deformation with the movement of magma in the upper few km of crust. When integrated with a conventional conceptual model of a volcano-hosted geothermal reservoir and combined with microearthquake monitoring, InSAR probably provides the most reliable constraint on the likely depth and location of magma movement. Although detection of shallow magma movement increases the likelihood of a geothermal exploration well encountering high temperature, it also implies a higher risk of eruption and a higher risk of a shallow reservoir base that would limit conventional capacity. InSAR studies have reported uplift at Paka, uplift and subsidence at Longonot, and subsidence at Suswa, Menengai and Silali (Biggs et al., 2013, 2009). At Menengai, Suswa and Silali, recent subsidence was coincident with the calderas and may be due to magma withdrawal. Although the subsidence at Menengai is symmetrically located with respect to the magma detected by wells at 2 km depth, it may reflect magma movement at a different depth. At both Paka and Longonot, uplift was offset from their calderas. The case of Longonot illustrates the complexity of InSAR data interpretation. The most recent Longonot eruptions are on the NNW flank at <1000 years and on the SSE flank at <200 years. The InSAR from 2004-2006 detected a 9 cm elliptical uplift modelled as a crack or dike intruding below the west flank at 3 to 4 km depth whereas from 2006 to 2010 detected 1 cm of subsidence SE of the crater, modelled as a collapsing point source at 3 to 4 km depth. Alexander and Ussher (2011) interpreted MT as detecting magma at 2 or 3 km depth just south of the crater. Without microearthquake monitoring data to confirm seismogenic magma movement, the InSAR at Longonot might be taken as an indication that magma might exist shallower than 3 km generally near the Longonot crater.

Gravity studies have shown that the inner trough of the Kenya Rift between L. Baringo and Suswa volcano is underlain by relatively dense material (Swain, 1992). At lateral scales of 5 to 20 km and depths under 4 km, Cantini et al. (1990) suggested that the gravity variation could be accounted for by the higher proportion of lavas relative to pyroclastics closer to the volcanic centre and/or by

dense intrusions into the base of the volcanics. An axial gravity profile from Lake Turkana in the north to Menengai volcano in the south show a series of gravity highs corresponding to major volcanic centres (Mariita and Keller, 2007). Simiyu and Keller, (2001) reported similar correspondence between gravity highs and Menengai, Eburru, Olkaria and Suswa volcanic centres in the southern Kenya rift. By considering the gravity together with MT resistivity, (Cumming, 2017, 2014) attributes gravity highs at the Silali and Suswa volcanoes to a greater proportion of lava relative to tuff near eruption centres, a shallower transition to higher density >200°C alteration and intrusive rocks penetrating the volcanics below the volcanoes.

Detailed magnetotelluric (MT) and transient electromagnetic (TEM) studies have been carried out at most of the volcanoes in the Kenyan Rift for geothermal exploration and have reliably resolved resistivity patterns to about 3 km depth that are consistent with the existence of geothermal reservoirs below parts of the surveyed volcanoes (Wamalwa and Serpa, 2013; Lichoro, 2013; Cumming, 2014, 2017; Lichoro et al., 2017). Because of their more direct relevance to the geothermal assessments, the MT resistivity patterns for most of the volcanoes reviewed in this study have been directly compared.

3. Geologic setting of geothermal systems in the SKR and CKR

The part of the SKR segment of the Kenya Rift valley considered here hosts three volcanic centres namely, Suswa, Longonot and Olkaria. The rift valley here is a 50 - 60 km wide and about 150 km long, north-south trending depression bounded by major normal faults and prominent fault escarpments up to 2 km high (Fig. 1) (Baker and Wohlenberg, 1971). The rift floor is marked by a system of fissure swarms within an overall horst and graben structure (Baker et al., 1972). The southern rift volcanoes form a NNW volcanic-tectonic alignment from Suswa volcano in the south to Eburru volcano in the northern part of the SKR.

Quaternary volcanism in the SKR has led to development of a system of caldera volcanoes and craters spread along the rift axis. Caldera formation at both Suswa and Longonot were synchronous highlighting the role played by regional tectonism between the two volcanoes (Scott and Skilling, 1999; Skilling, 1993). Structurally, the fissures, volcanic vents and collapse craters in the SKR are aligned parallel to the major rift faults which can be traced from south of Suswa volcano to the Olkaria geothermal complex (Fig. 1). Olkaria and Longonot are aligned perpendicular to the rift axis, reflecting Precambrian structure. Despite their close proximity, the Suswa, Longonot and Olkaria volcanoes have different rock compositions (Scott, 1980), with Olkaria dominated by rhyolites, Suswa by trachyte and phonolite and Longonot by peralkaline trachyte. The distribution of the geothermal resources in these fields is interpreted to be associated with the rift floor faults and the ring structures that act as both zones of permeability and as bounding structures. Geothermal resources have been developed so far in the Olkaria and Eburru fields in the SKR, and at the Menengai field in the CKR.

Suswa volcano

Suswa is the southern-most Quaternary volcano found in the Kenya Rift valley located about 45 km west of Nairobi and 30 km south of Olkaria geothermal field (Fig. 1). It is a trachyte-phonolite shield volcano formed less than 400 ka ago and continued erupting into the late Pleistocene leading to formation of an outer caldera (12 km in diameter) between 200-100 ka and a later inner caldera (about 5 km in diameter) with a central uplifted “island” block. The caldera collapses have been attributed to magma drainage at depth, as no syn-caldera deposits have been identified (Skilling, 1993), whereas flank eruptions are extensive. Later eruptions produced lavas which partly filled the

caldera, and later built the highest elevation Ol Doinyo Nyukie volcano on the southwest caldera rim. The most recent volcanic activity at Suswa volcano was marked by eruption of porphyritic lavas at the summit of Ol Doinyo Nyukie on the south-western part of the caldera forming a 460 m deep pit crater and depositing lavas on the moat. The freshness of the lavas suggest that these flows are probably about 100 to 200 years old (Johnson, 1969). Recent subsidence of about 2-5 cm has been reported at the centre of Suswa caldera in the period 1997 to 2000 (Biggs et al., 2009), possibly pointing to the location of a recent movement of magma in the volcano plumbing system.
Suswa has numerous volcanic fissure vents aligned with the NNW-trending volcano-tectonic axis on the western part of the caldera, also aligned with fault trends linking Suswa to the south end of Olkaria. This orientation is expected to have exerted control on the siting, drainage and recharge of magma chambers (Skilling, 1993). However, Suswa volcano as a whole is more symmetrically circular than the other volcanoes in the Kenyan Rift. The south of the Suswa volcano is cut by numerous faults which are concealed northwards as they enter the Suswa edifice. The geothermal manifestations include fumaroles and surface alteration associated with both structures and shallow unconsolidated tuffs. Active fumaroles occur mainly on the rims of the outer and inner calderas, the northern portion of the outer caldera floor and the southern flank with more clustering along the Suswa tectono-volcanic axis. The most intense alteration occurs within the inner caldera where sulphur deposits and gas from associated fumaroles suggest the existence of a 250 to 300°C hydrothermal resource (ICEIDA, 2016).

Longonot volcano

Longonot volcano is located southeast of Lake Naivasha and east of the Olkaria volcanic complex, offset to the east of the SKR axis and, therefore, potentially overlying more sediments than volcanoes located closer to the rift axis. It is a stratovolcano built of peralkaline trachyte lavas and pyroclastics, with small volumes of mixed hawaiite-peralkaline trachyte lavas. Syn- and post-caldera pyroclastic eruptions partly infilled the caldera depression and mantled the caldera wall. Ash from Longonot eruptions can be traced westwards covering Olkaria geothermal complex to the western flank of the rift. Volcanic development initiated about 400 ka with major explosive eruptions occurring over period from 21 – 6 ka resulting in caldera collapse (Scott and Skilling, 1999). Later eruption of pyroclastics at 3.5 ka formed the present summit crater with the most recent flank eruption of trachyte about 150 years ago. The main structural feature is the NNW-SSE alignment of 14 eruptive centres which cuts through the summit crater, and includes the source region of the younger lava flows (Scott, 1980). This structural alignment is parallel to the general trend of the SKR rift wall faults (Fig. 1) and marks a possible sub-surface magma channel (Clarke et al., 1990). There are no visible surface tectonic structures at Longonot due to thick pyroclastic cover, which have probably altered into thick clay-zeolite cap. The only thermal manifestations are weak fumaroles within the summit crater, along the volcanic alignment to the SSE and along the southern caldera rim.

Olkaria volcanic complex

Olkaria geothermal field is located between Lake Naivasha and Suswa but it is aligned perpendicular to the rift axis with respect to Mt. Longonot immediately to the east. As the first geothermal field to be developed on large scale in Africa, Olkaria has an installed electrical generation capacity of about 700 MWe. The exposed geologic units (Fig. 9) at Olkaria are mainly the result of Pleistocene-Holocene magmatism consisting of comenditic rhyolite, pumice and trachyte (Omenda, 1998). The youngest eruption is the Ololbutot rhyolite flow dated at about 180+/-50 yr BP (Clarke et al., 1990). Numerous rhyolitic domes are scattered across the Olkaria

volcanic complex and many are aligned along structures like the Ololbutot Fault and the southern ring structure that may be associated with the rim of a buried volcanic caldera (Clarke et al., 1990). The most prominent structures at Olkaria are the ESE Olkaria Fault Zone, N-S faults like the Olkaria Hills and Ololbutot faults, NW-SE faults aligned with the SKR including the Suswa and Gorge Farm Faults, and faults associated with the southern ring structure (Omenda, 1998). Other authors have also reported NE, NNW and ENE trends. Ogoso-Odongo (1986) have interpreted the Ol'Njorowa gorge as a structural zone where rock weakened by fracturing and alteration and had been subsequently eroded by an outwash from Lake Naivasha during a period of relatively higher lake level. Fracture permeability of the Olkaria geothermal reservoir has been interpreted as being predominantly controlled by the NW-SE and NE-SW trending faults as well as by the proposed ring structure and intersections of such structures (Mwania, 2015). Some structures aligned with numerous rhyolite domes are associated with leakage of cold water to several km depth, for example along the northern NS segment of the Olobutot Fault and along the southern ring structure and Gorge Farm Fault. The Ololbutot Fault has also been interpreted as a barrier, hydrologically dividing the reservoir into the Olkaria northeast field producing mainly from trachytes and the Olkaria west field producing mainly from the Mau Tuff units (Owens et al., 2015). The general permeability patterns inferred from the fault interpretation are consistent with well interference tests and tracer return patterns.

Thermal manifestations occur in form of fumaroles, hot altered ground, and sulphur deposits that are mainly located to the west of the Ol'Njorowa gorge. To the east of the gorge in the Olkaria-Domes area, there are no surface manifestations, probably due to the thick clay cap over this highly productive sector.

Menengai volcano

Menengai is a Quaternary shield volcano built on the floor of the CKR less than 10 km north of Nakuru town. Volcanic development initiated about 180 ka (Leat et al., 1984), with the growth of a trachyte lava shield. Later remarkable eruptions include two ash-flow tuffs that resulted in the formation of a 12 x 8 km caldera with almost vertical walls up to 300 m high. The dated tephra has placed the probable age of caldera formation at about 29 to 12.8 ka (Leat, 1984). Post caldera eruptions produced mainly trachyte, phonolite and basalt lavas, sheet-forming air-fall pumice deposits and Strombolian cinder cones most of which were deposited on the floor of the caldera. The most recent eruptions of lava may be few hundred years old. The prominent structural patterns at Menengai include the caldera ring fracture fault system and the younger NNE-SSW normal fault defining one side of the Solai half graben that cuts through the caldera rim in the northeast (Mibei et al., 2016). The N-S faults are older, as are the NNW-SSE faults that are aligned with the tectono-volcanic axis and mark the Molo graben that hosts sulphur-depositing fumaroles to the north of the caldera. Very young NNE-SSW structures are associated with a trend of young eruption vents across the southern caldera. Active sulphur-depositing fumaroles within the Menengai caldera are associated with structures crossing the central dome area. Most wells drilled at this summit area encountered magma at depth of about 2000 m (Mibei et al., 2016). The geothermal development is underway at Menengai caldera with planned installation of a 105 MWe power plant by the year 2020. Because the magma as shallow as 2000 m depth limits the conventional geothermal resource capacity at Menengai and because the confirmation of magma by drilling provides an important constraint on the reliability with which MT, gravity, InSAR and microearthquake data sets are likely to detect magma in the Kenyan rift.

4. Geologic setting of geothermal systems in the NKR

This study focuses on three volcanoes in the NKR, namely, Korosi, Paka and Silali. Here the inner rift is a narrow zone (about 10 km wide) of intense faulting and fracturing where recent volcanism has taken place (Dunkley et al., 1993). Similar to the other rift segments, Quaternary volcanism in this region has led to development of a system of caldera volcanoes and craters spread along the rift axis. Geothermal systems are manifested by surface expressions found on the Quaternary volcanic centres which include hot, hydrothermally altered ground and fumaroles above the water table and hot springs at lower elevation where liquid thermal outflows meet the water table. The most vigorous areas of fumarolic activity are associated with hot, hydrothermally altered ground on the upper flanks, summit craters and caldera areas of the volcanic centres close to NNE-trending faults and/or caldera structures. Intense fracturing in the inner rift likely forms a zone of high permeability that will promote buoyant up-flow or outflow of hydrothermal fluids or, in areas not capped by clay, down flow of cold water.

Korosi volcano

Korosi is a trachytic shield volcano located in the axial graben just north of Lake Baringo and adjacent to Paka volcano. The shield build-up started about 0.5 Ma with alternating sequences of trachyte and basalt eruptions (Dunkley et al., 1993). The volcano is bisected by a fracture zone of NNE-trending faults which step progressively eastwards across the volcanic complex between the two major bounding faults. Other structural features include summit collapse craters, mostly less than a km in diameter, which are thought to be associated with lateral drainage of magma. Most of the surface thermal manifestations occur between the two major structural systems, the Nakaporon fault to the west and Nagoreti fault to the east. Thermal manifestations occur in form of hot ground, steaming ground and fumaroles where temperatures above 95°C have been measured (Ofwona et al., 2006). Sinter indicates locations of fossil hot springs consistent with the elevated local water table about 11.8 to 12.7 ka (Dunkley et al., 1993).

Paka volcano

Activity at Paka volcano initiated about 582-390 ka with the build-up of the shield from effusive flank eruptions of mugearite and trachyte on the western margins of the volcano (Dunkley et al., 1993; Friese, 2015). The eruptions migrated progressively to the eastern side with sustained eruption of trachyte. The final eruptions were concentrated in the summit caldera and along fissures to the NNE aligned with axis of the rift, consisting of trachyte, basalts and pyroclastics between 35-10 ka (Dunkley et al., 1993; Friese, 2015). Post-caldera magmatic activity is dated at around 8 ka. InSAR has detected recurring episodes of inflation of up to 21 cm at Paka between 2007 and 2010 (Biggs et al., 2009; 2013), suggesting active injection of magma.

Tectonic activity is characterised by regional faulting events mainly towards rift margins with later faulting concentrated toward axis of volcanoes in the region perhaps driven by magma activity below. The final phase of mapped faulting involved rejuvenation and reactivation of older faults at 35 ka accompanied by further geothermal activity as seen in mineral veining in syn-caldera rocks (Geoffrey Mibei, pers. comm. November, 2018). A 10 km wide zone of N-S and NNE – striking normal faulting and fracturing cuts across the Paka volcano and most of the fumaroles occur on this zone, implying that these mapped faults provide permeable pathways for steam and gas to reach the surface. Silica sinters at Paka indicate 180°C water near the surface but, given its date of about 64 ka (Dunkley et al., 1993), it is too old to be relevant to any current geothermal system.

Silali volcano

The oldest exposed volcanic products at Silali date between 460 - 225 ka when shield construction began on the 50 km wide former rift, with voluminous basalt and trachyte flows overlying Tertiary tuff and sediments (Dunkley et al., 1993). These continued eruptions led to build-up of a 700 m thick, 27x33 km shield volcano above the rift floor and the subsequent collapse of its 7.5 x 5 km caldera at 64 ka, due to withdrawal of magma below the summit and lateral injection into dikes and flank eruptions (Dunkley et al., 1993). The youngest volcanism at Silali includes the 4±2 ka Black Hills trachyte on the northeast flank of the caldera and the later basaltic eruption on the N and NE flank, probably as recently as a few hundred years ago. Older fissures, faults and volcanic cones are aligned NS to N10E, parallel to the rift margins while the younger volcanic cones and vents are aligned NE-SW, consistent with the general trend of eastwards migration of recent magmatism.

Hydrothermal activity is widespread at Silali with boiling point fumaroles and extinct hot spring mineralization below the SE rim of the caldera, cooler, wispy fumaroles on the east flank of the shield, 50°C to 80°C hot springs at Kapedo and Lorusio on the western margin of the volcanic shield, and warm springs and steam vents at Kalnangi on the northern flank of Silali volcano. These surface expressions are indicative of a potential 250 to 300°C hydrothermal system. Recent satellite radar interferometry observations (Biggs et al., 2009, 2013) show that the summit area at Silali volcano underwent subsidence, up to 4 cm between 2007-2010.

5. Geological comparison between volcanoes in SKR, NKR and CKR

The Kenya rift initiation started in the north and progressed southwards with time which is consistent with the increased extension and thinning of the crust northwards from 35 km in the south to about 20 km thick in the north (Maguire et al., 1994; Keller et al., 1994a; Mechie et al., 1997). Alignment of volcanic features, including calderas, fissure eruptions, domes and pyroclastic cones indicate the orientation of shallow crustal stresses in the Kenyan Rift (Biggs at al., 2016). The thickening crust southwards is consistent with a larger magma body producing differentiated magma, accounting for the Olkaria rhyolites and consistent with the large Olkaria geothermal reservoir.

In terms of caldera morphology, the NKR calderas long axes orient parallel to NW–SE-trending Proterozoic faults whereas, in the SKR segment, the calderas long axes are oriented in a NE-SW direction, parallel with the Precambrian (about 500 ma) fault orientation. At Olkaria, the proposed caldera ring structure marked by rhyolite domes and pyroclastic cones is aligned with Longonot to the east, almost perpendicular to the rift axis, also likely related to older structure. Therefore, although alignments in the NKR and SKR are controlled by the rift opening axis and the main volcanic edifices are controlled by cross-cutting Proterozoic structure but, important with differing strike in each case.

Calculated magma volume erupted from some calderas is much less than the volume of caldera collapse signifying lateral magma injection into the crust from draining shallow magma chambers. At Suswa erupted magma volume account for 5.2 km^3 of the 22 km^3 caldera volume (Skilling, 1993) while at Longonot magma volume of 11.25 km^3 out of 26.5 km^3 caldera volume has been calculated (Scott, 1980). A more extreme example has been reported at Silali volcano in the NKR with a huge caldera structure and very little erupted mass (Dunkley et al., 1993). At Menengai in the CKR, a total collapse volume of 50 km^3 is indicated but only 22.5 km^3 of erupted magma is accounted by the lava on the surface (Leat et al., 1984). Among the implications of these observations is that magma movement and storage in the crust is not necessarily directly related to

eruption risk, the processes involved are more complex than can be inferred only from uplift and subsidence alone, and applications to resource assessment are ambiguous.

6. Magnetotelluric (MT) data acquisition and processing

MT is a passive electromagnetic method in which the natural electric (E) and magnetic field (H) are recorded at the ground surface and used to compute an impedance tensor (Z) (Cagniard, 1953; Vozoff, 1972), to derive information on the resistivity structure of the subsurface (Vozoff, 1991).

From 2004 to 2017 about 700 MT soundings have been acquired in many field campaigns for geothermal exploration in the study areas of the Kenya rift, covering Suswa, Longonot and Olkaria in the SKR and Korosi, Paka and Silali in the NKR (Fig. 2). A further 200 MT stations have also been acquired at Menengai volcano in the CKR, part of which have been used for the comparison to the undeveloped geothermal fields. All stations were occupied with Phoenix Geophysics 5-channel MTU-5A time series data acquisition systems with magnetic induction coils, telluric dipoles, GPS time synchronization. For each sounding, the horizontal electric and magnetic fields were recorded continuously for a period of about 15 to 21 hours with grounded dipoles and induction coils oriented in magnetic north (x) and east (y) directions. These time-series data were all processed using a single site robust processing. To correct MT static shift distortion, transient electromagnetic (TEM) data has been acquired close to a majority of the MT stations. For those MT stations that were not occupied with TEM soundings, alternative static shift correction methods were attempted, for example, by shifting according to the topographic models of Jiracek (1990) where polarization at 100 Hz was consistent with topography. While parts of this dataset have been previously published (e.g. Lichoro et al., 2017), we have included an additional ~350 new soundings from the southern Kenya rift volcanic segment.

7. Data analysis and inversion

The SSMT2000 MT time series processing suite (Phoenix Geophysics, 2005) was used for Fourier transformation of time series into the frequency domain, computation of a suite of cross-powers at each frequency, and robust estimation of the impedance tensor (Egbert and Booker, 1986). The cross powers and impedances were converted to the standard Electronic Data Interchange (EDI) format and input into TEMTD software (Árnason, 2006) for further analysis and interpretation. TEMTD program is based on the one dimensional (1D) Occam inversion (minimum structure) algorithm of Constable et al., (1987). The program does joint inversion of MT and TEM, adjusting shift multiplier for MT apparent resistivity so that both the MT and TEM apparent resistivity can fit the same model.

The data considered here typically have good quality for periods from 0.01 to 3 s, allowing almost all of the MT data to support a 1D inversion that will resolve the geometry of the clay cap. However, less than 50% of sites have reliable data from 0.01 to 100 s and so will be less effective in resolving deeper features. Editing prior to inversion included omitting data at periods affected by severe noise and omitting MT data at longer periods affected by 3D structure as indicated by parameters like high on-diagonal impedance magnitude or high dimensional parameters like ellipticity. The 1D resistivity versus depth results computed for each station have been interpolated to contour resistivity maps and cross-sections for comparison between the study areas.

Figure 3 shows a representative MT sounding done at Paka volcano in the northern Kenya rift. At period below 10 seconds, the resistivity exhibits a 1D character, where the off-diagonal components, Zxy and Zyx are parallel and equal in amplitude. The diagonal elements Zxx and Zyy (shown in faint colours in Fig. 3 lower panel) are significantly lower in amplitude (at least an order

of magnitude) than the off-diagonal elements for most frequencies. Above 10 seconds the two impedances diverge signifying higher dimensionality. The curve with black symbols represents the determinant impedance, the rotationally invariant response that is used in the joint 1D inversion. Given the limitations of the MT data and the likely resistivity pattern of the Kenyan rift volcanoes, 1D Occam resistivity inversions computed from the MT determinant mode were chosen for comparing the resistivity pattern among prospects because they were likely to produce consistent results to the base of the low resistivity smectite clay cap, with some caution needed where the cap is particularly thick or low in resistivity, potentially inducing dimensional distortion that would exaggerate the depth to the base of the cap.

The value of the resistivity in the higher resistivity below the conductor is more ambiguous, both because of inherent limitations to MT (Chave and Jones, 2012), local data quality issues at many Kenyan Rift volcanoes and the limitations of 1D inversions (Cumming, 2014). However, the elevation of the transition from lower to higher resistivity at the base of the conductor is typically reliably resolved in geothermal settings using 1D inversions of the MT invariant mode in more resistive terrain outside and near the edges of a clay cap and or TE-mode over the clay cap, except near lateral discontinuities in the cap (Dipippo, 2016). Cross-sections constructed by stitching together such 1D inversions have been an important diagnostic in geothermal exploration, with a particular focus on the geometry of the base of the shallow smectite clay cap that caps geothermal upflow and steers the buoyant outflow in an updip direction.

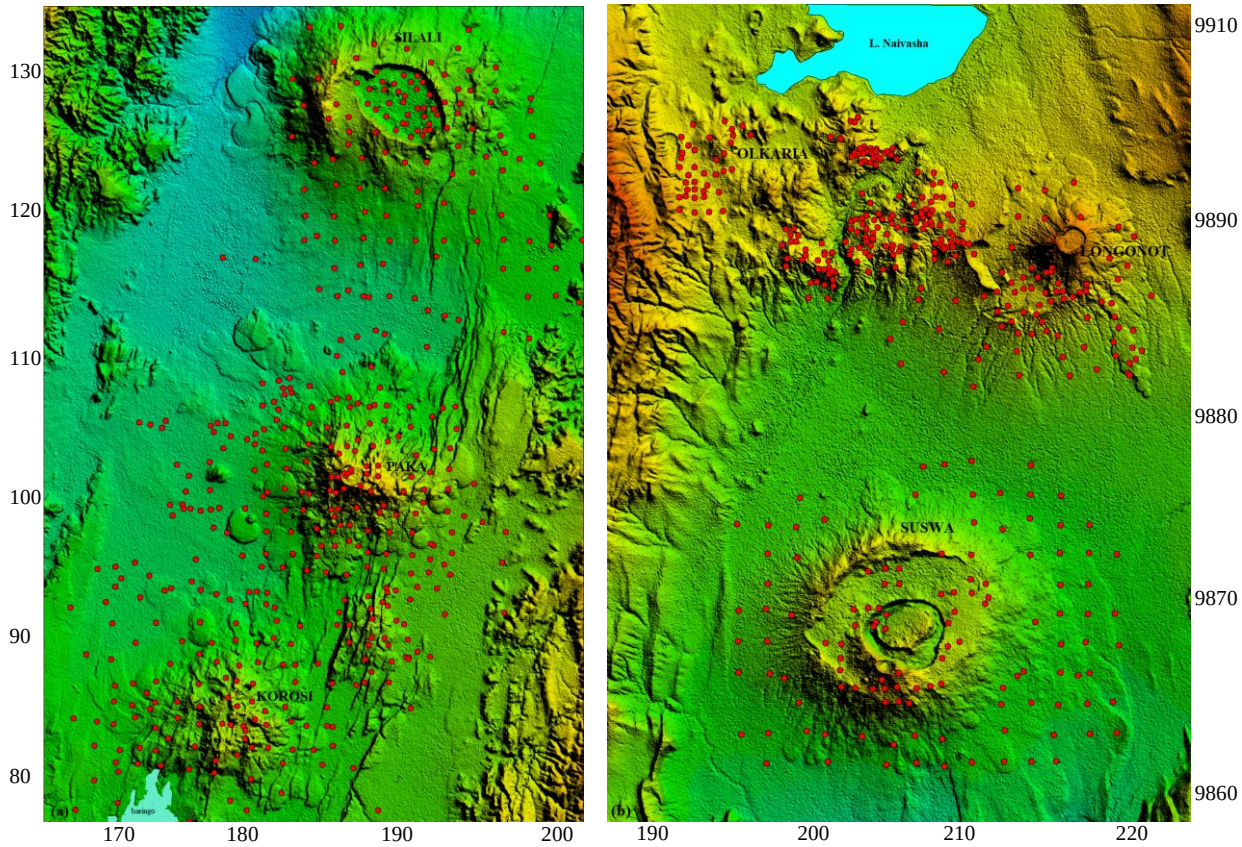

Figure 2: Digital elevation maps showing MT station locations at (a) Korosi, Paka & Silali in north rift and (b) Suswa Longonot & Olkaria in south rift.Coordinates are WGS84-UTM in km.

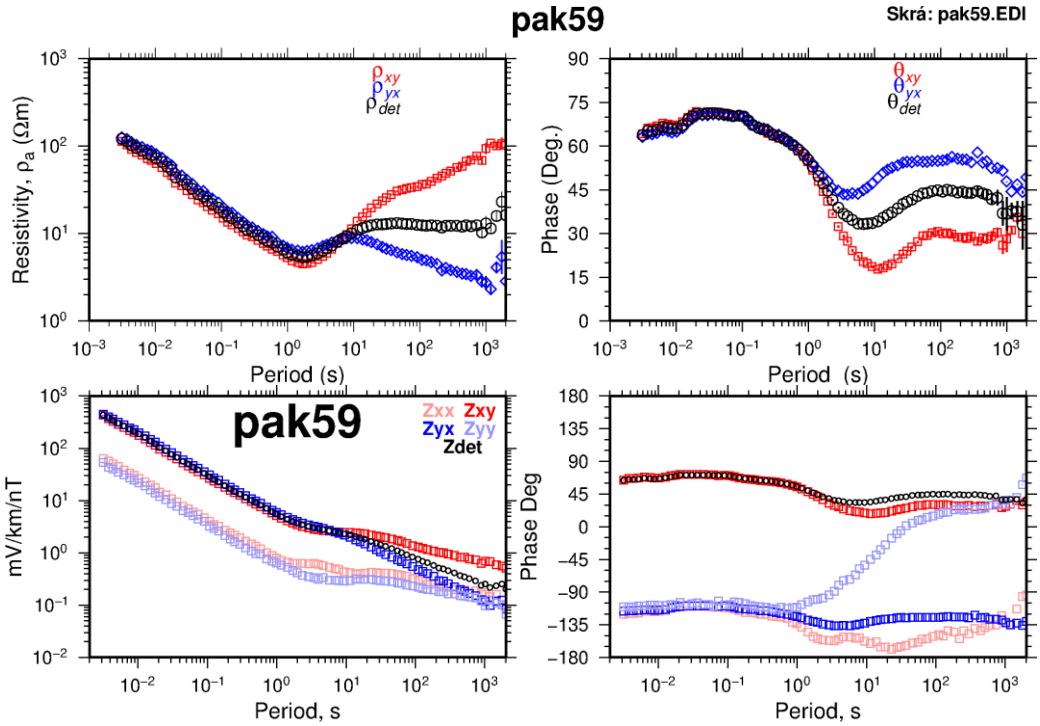

Figure 3: An example of MT data from Paka volcano showing MT impedance; At period below 10 sec., parallel apparent resistivity and phase curves of Zxy and Zyx components indicate that the earth resistivity is one dimensional at periods less than about 5s, corresponding to shallow depths. The black symbols represent the determinant impedance.

8. 1D inversion versus 3D inversion

To illustrate the utility and limitations of the 1D inversions of the MT invariant mode used to produce the comparative resistivity cross-sections in Fig. 6, the resistivity cross-section across the Paka volcano generated using 1D inversions of the MT invariant mode (Fig. 4a) is compared to a cross-section generated from a 3D MT inversion (Fig. 4b). The 3D inversion had been computed by CGG using the Mackie conjugate-gradient approach (Soyer et al., 2017). The inversions produce similar models shallower than 1000 m, with a thin high resistivity surface layer overlying a low resistivity (<10 Ωm) smectite-zeolite alteration zone, which is underlain by a much higher resistivity rocks. In both inversion, the conductive layer is thinner below the summit area and thicker on the east and west flanks. However, below the west flank of Paka volcano, the 1D inversion shows a conductive zone that extends to the base of the profile (Fig 4a) while the 3D inversion indicates that the base of the clay alteration is at a depth of about 2000 m. bsl (Fig. 4b). This is a limitation of 1D invariant mode which extends the depth of base of the clay cap and exaggerates the depth of the conductors on the flanks. At depth of about 4000 m. bsl, 1D inversion displays reducing resistivity in the eastern part of the mapped area where the 3D inversion shows a consistently higher resistivity. This suggests that the 1D resolution of the base of the clay is fairly reliable below the peak but the TE-mode will be more reliable over thick conductors on the flank. Overall, both inversions resolve features consistent with the shallow resistivity structure of high temperature geothermal systems i.e. a conductive clay cap with temperature (<220°C) overlying resistive higher temperature (>240°C) reservoir. It is notable that deeper conductor is not resolvable in 3D inversion suggesting that the magma body at Paka volcano is too small.

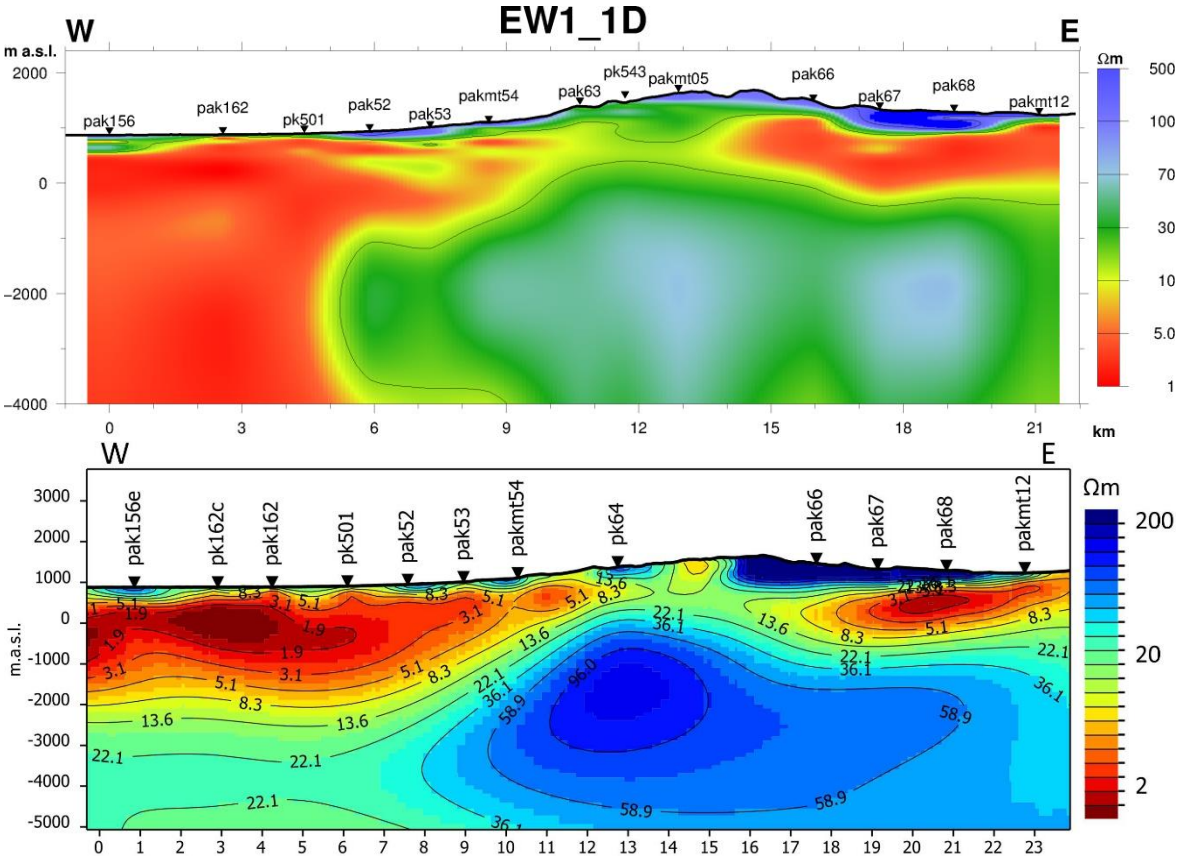

Figure 4: West-east resistivity sections across the Paka volcano; (a) obtained from stitched joint 1D inversions of TEM and determinant MT data, (b) from 3D inversion of MT data. Inverted triangles: MT stations.

9. Testing magma detection by 1D MT inversions using 2D MT modelling

In the volcanic systems of the EARS, calderas are assumed to indicate the geometry of past magma reservoirs. This, however, does not provide the depth or current state. Geophysical observations including InSAR, microearthquake locations, Vp and Vs seismic tomography, teleseismic S-wave shadows, MT and gravity data sets have been used to detect and characterize liquid and near-liquid magma. Where most MT stations over and immediately adjacent to a suspected magma body have high quality from 0.01 to 100 Hz, a 3D MT inversion could probably detect magma bodies that are about as wide as their depth of burial to 7 km depth. To be reliably resolved by 1D MT, a magma body would have to be much wider than its depth of burial. As a result, in the EARS, MT surveys have ambiguously appeared to detect magma at relatively shallow depths beneath Menengai and Longonot volcanoes and have been more speculatively interpreted at others.

The 3D resistivity inversion reported by Mibei et al. (2016) at Menengai produced a conductor at about the 2 km depth corresponding to the magma that was intercepted in wells but the sensitivity of this feature has not been tested. That is, it may indicate that the MT are consistent with the magma rather than indicate reliable independent resolution of it. However, the 1D MT inversions do not reliably resolve the magma body, suggesting that the dimensions of the magma body are too small to be resolved by 1D inversion in this context. This is similar to the case that Gasperikova et al. (2015) demonstrated at Krafla in Iceland where silicic intrusions have been intercepted in form of isolated pockets not detectable by MT.

To test in what conditions a 1D inversion of the invariant MT mode used in this analysis would be expected to detect a magma body in noise free conditions, synthetic data has been computed for a 2D model with magma bodies of various sizes and inverted using the 1D invariant to test whether a plausible magma body could be resolved in the cross-section plots presented in this study. This is achieved by use of the 2D forward modelling and inversion software included in the WinGlink software (WinGLink, 2005; Rodi and Mackie, 2001). A 2-D resistivity mesh was designed incorporating topography and a model for a geothermal system from the surface to the base of the clay cap was built using the stitched 1D models. Below the base of the cap, resistivity is set to a 50 Ωm half space in which a "magma body" consisting of blocks of various dimensions that are being tested for resolution. Synthetic data for stations spaced 200 m apart are computed from the 2D forward model algorithm for periods from 0.01 to 1000 Hz with 5 frequencies per decade. To test noise cases, a very low level of 5% random noise was added. Representative synthetic examples were prepared for all the volcanic areas considered in Fig. 6. However, only the case for Paka volcano is shown in Fig. 5 to illustrate the limitations of 1D inversion and test the size of magma that can be detected. This is aimed at illustrating typical resolution of 1D smooth inversions of the MT invariant mode below the base of the clay cap (see Fig. 5b).

Fig. 5c shows one example of an initial model (forward model) for a magma body 4 km wide, 0.7 km thick, with a top at 4 km depth, that was used to generate the data used in the 1D inversions shown in Fig. 5a for the TE-mode (electric field along strike) and Fig. 5b for the invariant mode. Although the TE-mode arguably performed better than the invariant mode, as is commonly observed over a prominent conductor (Cumming and Mackie, 2010), neither 1D invariant nor TE-mode consistently resolved models for the magma body that were narrower than the depth of burial. The TE-mode detects magma with dimensions greater than 4 km across while invariant detect magma size larger than 7 km across, consistent with only the largest magma bodies expected at 3 km depth. On the other hand, 1D invariant mode resolves the resistive features adjacent to the conductive clay cap in a more realistic manner. For dimensions of magma 7 km by 1.2km or 10 km by 2 km, both are detected by the inversions of the TE- and invariant modes; that is, as might be

expected, 1D inversion works for those models where the lateral extent of conductors is large enough that the MT looks 1D.

For cases where the near-surface clay layer is very low resistivity and thick (that is, high conductance) then resolution of a deeper conductor is likely to be very limited in 1D unless the deeper conductor is particularly low in resistivity, laterally extensive, with a thickness that is a significant fraction of its depth of burial (that is, its conductance should be comparable to the clay cap conductance). But, when the conductance of the near surface is moderate, chances of resolving a deeper conductor improves. An overall rule-of-thumb is that magma can only be resolved below the clay cap if its resistivity is low and lateral dimensions are larger than their depth. However, if MT data quality is good enough 3D inversion might resolve deep low resistivity better.

Within the >200 km wide overall gravity low associated with the roots of the Kenyan Rift at 50 to 70 km depth, the details of the <20 km wide gravity high that extends along the centre of NKR can be effectively modelled using density variations to a depth of 2500 m with boundaries between bodies of differing density constrained by the MT resistivity boundaries and the densities themselves constrained by measurements of rocks at the surface and in boreholes. Although this depth range includes the magma at Menengai, the ambiguity in the gravity model precludes directly constraining the depth to magma in a meaningful way.

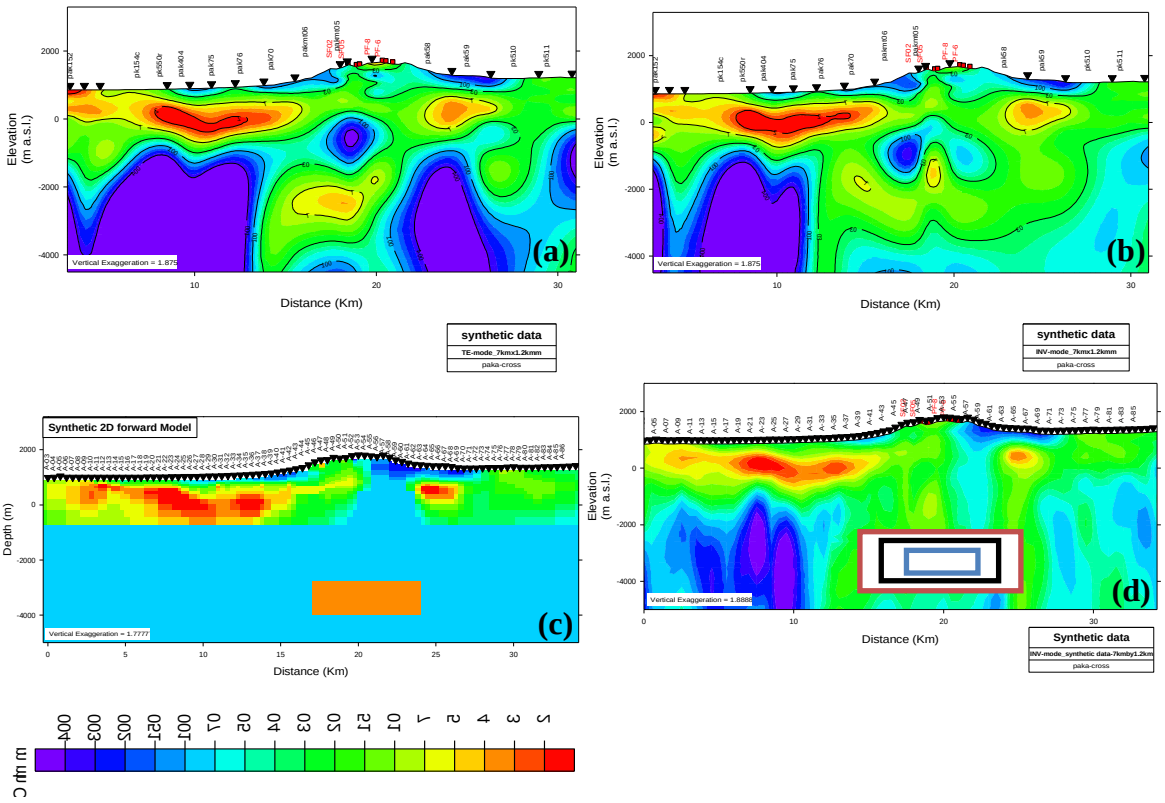

Figure 5: A representative Magma detectability test using synthetic modelling of MT data at Paka volcano for magma size 7 km across and 1.2 km thick centred at 3.5 km. b.sl (a) 1D TE-mode (b) 1D Invariant mode (c) initial model (d) 1D invariant mode showing sizes of magma tested; blue: 4 km by 700m; black: 7 km by 1.2 km and red: 10 km by 2 km.

S-wave shadows have been observed beneath some volcanoes and, at least at Olkaria, where there appears to be a correlation between these zones and the high temperature upflows (Simiyu, 2000). Given the low frequency of the S-waves and the low resolution inherent to S-wave shadows,

extended volumes of magma must be present in the crust, which would likely be observed by MT as low resistivity. Therefore, the lack of detection of such features by the MT is unlikely to be due a small size but it might be attributed to a higher than expected resistivity (i.e. lower conductance) of the magma relative to the conductance of the overlying clay cap. As part of an integrated magma detection study including teleseismic monitoring, local microearthquake monitoring and InSAR, a 3D MT magma detection study based on the available MT data quality could address both the reliability of different approaches to imaging magma beneath geothermal prospects in the Kenya Rift and assess the potential value of investing in higher quality MT acquisition.

10. Resistivity results

Many geothermal fields have been explored using 1D inversions of MT data that usually provided adequate characterization of the geometry of the conductive clay cap overlying the high temperature reservoir, although it was not expected to reliably resolve variations in resistivity below the cap (Cumming and Mackie, 2010). In this study, either smooth joint inversion of invariant MT and TEM or 1D inversion of invariant MT without TEM data was done for all 700 soundings. The resulting 1D models of individual soundings are stitched to form 2D cross-sections. Using this approach, the resolution deteriorates beneath the clay cap making details of resistivity structure at reservoir depths uncertain. However, to illustrate the overall pattern of resistivity depicted by the 1D inversions, the resistivity cross-sections in Figure 6 are plotted to the full depth of the section, unlike the plots shown in Lichoro et al. (2017) where similar plots were truncated at the depth that dimensional analyses suggested that the 1D inversion was less reliable. Figure 6 includes cross-sections through the volcanic centres discussed here i.e. Silali, Paka, Korosi, Olkaria, Longonot and Suswa. Figure 7 shows a cross-section through Menengai and Figure 4 compares 1D and 3D inversions at Paka to indicate what part of the 1D inversions are more likely to be reliable.

To avoid large data gaps related to access limitations and noise from power plants at Olkaria, the MT cross-section used for Olkaria shown in Fig. 6e does not follow the published cross-sections shown in Fig. 9 and 10. At Olkaria the resistivity pattern is consistent with the smectite-zeolite zone, resulting in doming up of the base of the low resistivity (<10 Ωm) zone over the entire reservoir. Where temperature exceeds 200°C at shallower depth and temperature-sensitive smectite-zeolite alteration is also found at shallower depth. Ongoing work will clarify the overall pattern found in the base of the low resistivity zone at most of the volcanoes (Fig. 11b). This area at the western end of the profile is close to the western margin of the rift and is underlain by the thick Pliocene Mau Tuff (Omenda, 1998) and, because of the easily altered thick section of tuff at the margin of the field, the base of the low resistivity is very deep. The resistivity structure in the Olkaria east field and Domes is consistent with the high temperature resource (Fig. 6e). Where the Olkaria cross-section (Fig. 6e) crosses the gorge and to the east, the Domes ring structure (9 km along the profile), low resistivity features appear to dome from below 3000 m depth. The vertical contours are likely to be artifacts caused by extending 1D MT inversion to depths distorted by the effect of lateral boundaries. Drilling at Olkaria has shown that it is consistently capped by zone of argillic alteration dominated by smectite with associated zeolite, amorphous silica and calcite, typically associated with formation temperatures less than 180°C but, at Olkaria, the range of temperature is locally lower in areas of relict alteration (Mwania, 2015). The resistivity corresponding to this alteration zone is below 10 Ωm (Fig.6e) and temperature < 200°C in some areas and <80°C in others (Fig. 10). The resistivity profile shows a transition to propylitic reservoir with resistivity above 14 to 20 Ωm consistent with depths where smectite-zeolite transitions to chlorite-illite. At depths between 1000-3000 m below surface and resistivity between 30-100 Ωm,

high temperature propylitic alteration zone is associated with epidote, chlorite, albite, illite, prehnite, actinolite and wollastonite (Mwania, 2015) corresponding to reservoir temperatures over 250°C to as high as 340°C (Axelsson et al., 2017).

A resistivity cross-section through the Menengai caldera is shown in Figure 7 with wells projected onto it. The shallow high resistivity overlies a zone of lower resistivity of <20 Ωm about 1 km thick where low resistivity, low temperature clays dominate before transitioning to moderate resistivity of >32 Ωm, usually shallower than 1600 m depth. The resistivity pattern at Menengai shares some of the complications in interpretation encountered at Olkaria, such as low resistivity smectite capping outflows over a temperature reversal (Mibei et al., 2016; Mbia et al., 2015) and a resistive quartz-illite cap below the zeolite zone that locally results in a reservoir much deeper than the base of the zeolite zone.

Several drilled wells at the summit area have encountered magma (GDC, 2017) at about 2.1 km depth (shown in red in fig. 7) while syenitic intrusions dominate in wells to the west. Based on the wells that encountered magma, we can speculate on the geometry of the magma to be about 1.2 km wide, although it might be more extensive deeper than the wells. Although the invariant 1D inversion does not detect the magma, this would be expected given its lateral dimension is half of the depth below a clay cap conductor, although a 3D inversion was reported to have resolved the magma, which is possible given high quality data. Two wells drilled in the Krafla geothermal field, NE Iceland, have encountered silicic magma at depth of about 2.1 km, similar to the depth of magma in Menengai (Friðleifsson et al., 2010) and (Elders et al., 2011). This magma was not reliably resolved by MT 1D inversions or by several elaborate 3D MT inversions, probably due to the noise in the MT data that limited the reliability of the inversions below the cap (Gaspericova et al., 2015). Moreover, the magma encountered in Krafla wells was a re-melt of altered basalt and so is probably in disconnected pockets below the plausible resolution of MT. The MT at Menengai shares the limitations of the MT elsewhere in Kenya complicated by high contact resistance on extensive lava flows over the reservoir and high cultural noise related to drilling activity, so MT data quality below 1 Hz is more problematic at Menengai than at most geothermal prospects in Kenya, making magma detection using MT especially challenging at Menengai. A recommendation based on this study is that a revised 3D MT inversion at Menengai should be conducted along with 3D model sensitivity tests with and without the magma constraints from the wells in order to assess how reliably a 3D inversion of the available MT could be expected to resolve the magma at Menengai and other prospects.

The Suswa cross-section in Fig. 6 stands out as having the most ambiguous evidence for the existence of a conventional smectite clay cap, with a moderate resistivity zone of 20 to 50 Ωm in the upper 1500 m of the volcanic edifice. (Fig. 6g), and with minor lower resistivity zones appearing on both east and west edges of the profile on the outer flank of the volcano. This resistivity pattern is consistent with the phonolite and trachyte rocks at Suswa, which are less likely to alter to smectite. The geochemistry of the fumaroles in the outer caldera suggest that they are associated with boiling at <140°C, possibly associated with outflow or with boiling near the water table above low permeability conductively heated rocks. By analogy to Olkaria and Menengai, it is possible that the moderate resistivity is due to higher temperature illite-chlorite alteration that is now relict, due to cooling, in which case any permeable high temperature reservoir below the northern outer caldera would have to be deep. Unfortunately, access limitations did not permit acquisition of MT near the fumarole with >250°C geothermometry within the inner caldera but, again by analogy to Menengai, the recent eruption vents may provide an entry of cold water below a moderate resistivity cap. Moreover, evidence of very recent eruptions favours an interpretation of

shallow magma at Suswa, making concerns of a relatively thin reservoir analogous to Menengai plausible at Suswa (ICEIDA, 2016).

The resistivity cross-section across Mt. Longonot shown in Fig. 6f also differs from the other Kenyan Rift examples in that it has an almost flat <10 Ωm low resistivity layer about 500 m thick extending across the lower southern flank of the volcano. This profile did not go through the summit caldera because of limited availability of MT stations. However, the base of the conductor is shallower southeast of Longonot crater. Alexander and Ussher (2011) summarized results of a 3D MT inversion that appeared to resolve a <10 Ωm conductor 2000 m below the south rim of crater that was interpreted as a magma chamber, with some ambiguity related to the lack of MT coverage within the summit crater. Seismic tomographic studies through Longonot have identified low P-wave velocities in the crust that are interpreted as zones of partial melt, albeit with low resolution (Karson and Curtis, 1989). The elevation changes detected by InSAR are near but not coincident with the feature detected by MT, perhaps because the InSAR is responding to shorter term, smaller volume magma movement. By analogy to Menengai, a Longonot reservoir near a magma body at 2000 m depth is likely to be boiling point, consistent with the elevated base of the clay cap shown to the south of the interpreted magma in Alexander and Ussher (2011).

The resistivity structure across the Korosi, Paka and Silali volcanoes (Fig. 6a, b & c) shows a relatively thin low resistivity cap over an elevated high resistivity zone bordered by thicker low resistivity to northwest and southeast between the lower flanks of the volcanoes and the edge of the rift. In the summit areas, the resistivity pattern is characterized by a thin resistive (>60 Ωm) surficial layer underlain by a more conductive layer of about 10 Ωm at the Silali and Paka volcanoes and about 30 Ωm at the Korosi volcano. The conductive layer is generally thinner in the summit areas where it is likely to correspond to low temperature hydrothermal smectite-zeolite alteration and thicker to the sides of the volcanoes where it is interpreted as volcanic sediments and weathered ash with high smectite clay content. A higher resistivity zone is detected below the conductive clay layer on all of the MT profiles. The base of the conductive zone (the top of the resistive zone) is more elevated below the eastern half of the Silali volcano, below the Paka summit area and to the SE of Korosi volcano, possibly corresponding to the apex of a high temperature geothermal reservoir or the path of updip outflow. The thickening of the low resistivity zone on the margins of these profiles, especially on the northwest side, probably reflects more volcaniclastic deposition towards the west margin of the rift. The thickening and deepening of these conductors might mark reservoir boundaries, as does the thickening of the conductor on the margin of Olkaria (Kandie et al., 2016) and Menengai (Mibei et al., 2016).

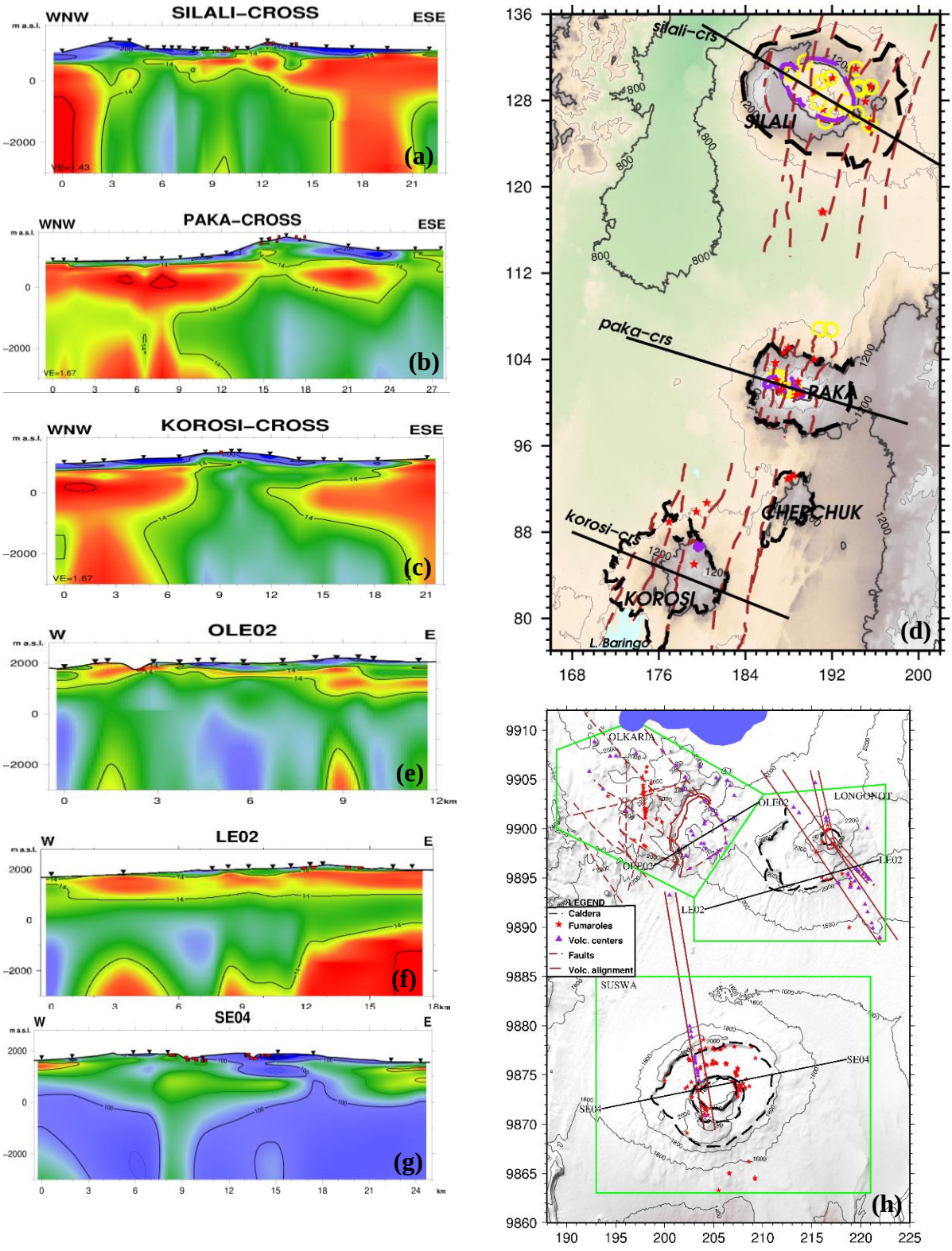

Figure 6: Resistivity cross-sections through the volcanoes in the north and south rift segments (a) Silali (b) Paka (c) Korosi (d) N. rift location map (e) Olkaria (f) Longonot (g) Suswa and (h) S. rift location map. Inverted triangles are MT stations, red rectangles are fumaroles on-profile. On the location maps volcanoes/calderas are marked by broken-black lines, broken-brown lines are faults and fissures, stars are fumaroles, yellow rings are altered surfaces, purple triangles are volcanic centres, brown lines mark volcanic alignments and green boxes show geothermal prospect boundaries in south rift.

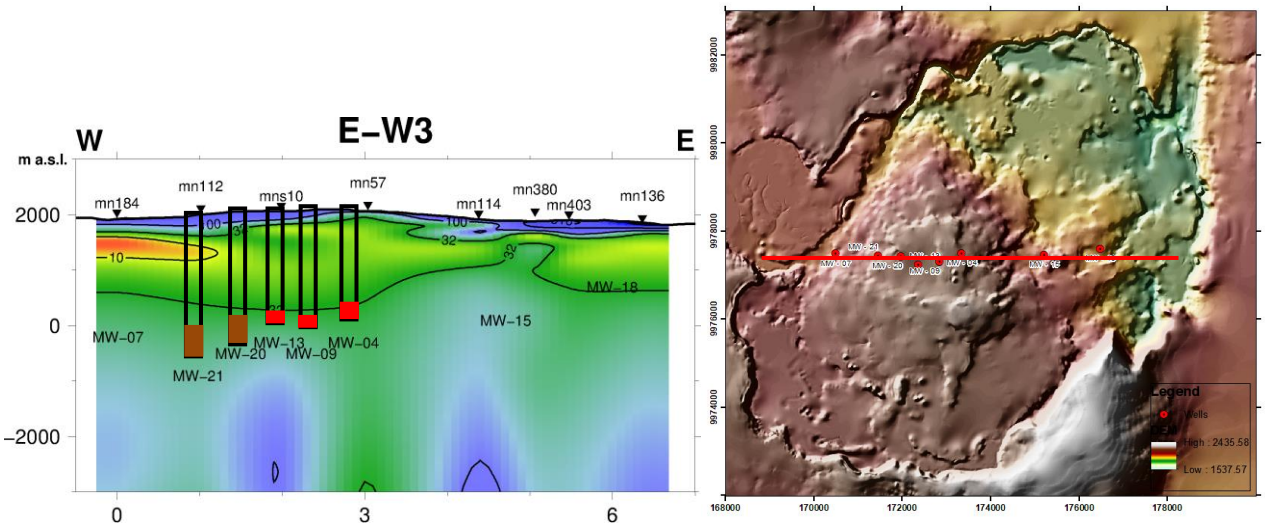

Figure 7: (a) *Resistivity cross-sections through the Menengai caldera in the central rift segments showing the wells projected on the profile. The red colour shows magma intercepted and the brown colour indicates syenitic intrusions. (b) Location map showing profile in red.*

11. Gravity surveys

Most of the gravity surveys in the Kenyan rift have been carried out to understand the overall rift structure or of a particular volcano but no comparative assessment of individual volcanoes has been conducted. Most surveys at volcanoes have detected isolated gravity highs aligned with the volcano and overall rift axis (e.g. Simiyu and Keller,2001; Mariita and Keller, 2007). The east African plateau is characterized by a negative Bouguer anomaly of an amplitude of up to 150 mGal over 1000 km W-E distance (Sowerbutts, 1969; Searle, 1970; Fairhead, 1976; Mariita and Keller, 2007). This anomaly has been attributed to a body of low-density material at the base of the lithosphere which becomes shallower (about 50 to 70 km) beneath the rift valley.

Gravity surveys within the Kenyan rift agree that a gravity high is nested within the much larger scale and larger amplitude regional gravity low, implying that a relatively dense body is aligned with the rift axis (Swain, 1992; Simiyu and Keller, 1997; Mariita and Keller, 2007; Lichoro et al., 2019). Lichoro et al. (2019) indicate that the axial gravity high in the NKR has a positive amplitude of about 12 mGal and 15 km wide.

Earlier gravity surveys at Suswa, Longonot and Olkaria by Geotermica Italiana (1989), identified localised positive anomalies which they attributed to shallow buried dense lava flows and large scale negative anomalies related to deeper sources. They claimed that Mt. Longonot crater collapse area has a gravity low probably associated with a greater pyroclastic cover at the volcano and possibly a low density trachytic magma chamber beneath the caldera. Recent studies by Alexander and Ussher (2011) confirmed that the gravity low extended beyond the boundaries of the mapped Longonot caldera, suggesting that the pyroclastics and perhaps a buried caldera extended outside the mapped caldera. A Bouguer gravity map from gravity survey covering Suswa, Longonot and Olkaria (KenGen, internal report) is shown in Fig. 8a. The map shows a gravity low at Longonot caldera and reveals a gravity high at both the Suswa and Olkaria complex.

A gravity profile across Olkaria complex shows a trend of decreasing gravity towards the margins of the rift valley at the western escarpment (Ndombi, 1981). A series of N-S aligned high gravity are superimposed on the gravity low corresponding to major structural features, i.e. Olkaria and

Ololbutot fault zones and Ol'Njorowa gorge and a broad positive gravity residual anomaly in the central part of Olkaria (Simiyu and Keller, 2001). The gravity low to the west of Olkaria fault zone is a consequence of thick low density volcanic sequences in that zone. A detailed residual gravity map at Suswa shows a N-NE trending positive anomaly which Cantini et al. (1990), attribute to cooling dense magma body intruded into the basement to within 3 km depth. Cumming (2017) modelled a combined MT and gravity profile across the Suswa caldera that showed that the gravity high was consistent with a dense lava flow and a shallower transition to denser, high temperature alteration.

In the northern rift segment, an extensive gravity survey was carried out from 2014 to 2017, covering the Korosi, Paka and Silali volcanic zone (Lichoro et al., 2019). Figure 8b shows a residual Bouguer gravity map based on these data. The map shows a consistent gravity high aligning with the NNE-trend of the fissure swarm in the inner rift axis and through the volcanoes. A gravity low has been mapped between the axial gravity high and the rift margins and likely extends east and west of the survey area as part of the large scale gravity low related to density contrasts deeper than can be resolved by this survey. The transition from gravity high to gravity low is marked by a steep gradient on either side implying a relatively shallow source. Based on correlations with MT resistivity, Lichoro et al. (2019) attributed the axial high to a higher proportion of high density lavas closer to the eruptive centres and more tuffs and sediments on the flanks, shallower transition to denser high temperature alteration beneath the volcanic centres and dense intrusions intruding the volcanic rocks below the volcano. Even steeper gradients related to local gravity lows were associated with thin tuffs at the summit areas. All thermal manifestations occur either within the gravity high or at the boundary with the gravity low. Lichoro et al. (2019) interpret a change in the axial gravity alignment north of Paka volcano as a move of the active rift fissure eruptions from an older more central axis to the currently active rift to the east of Silali volcano.

The gravity highs associated with the volcanoes at Suswa and Silali are consistent with the relatively shallow transitions from smectite to chlorite/illite alteration and the associated loss of porosity at Olkaria and Menengai and the generally higher density near eruption centres due to the greater proportion of lavas and intrusions in contrast with the tuffs and sediments farther from the volcanoes. However, the major fault and contrast between west and east Olkaria, more pyroclastics to the west and more lavas and intrusions to the east, implies that local geology will likely be important to local gravity patterns throughout the rift.

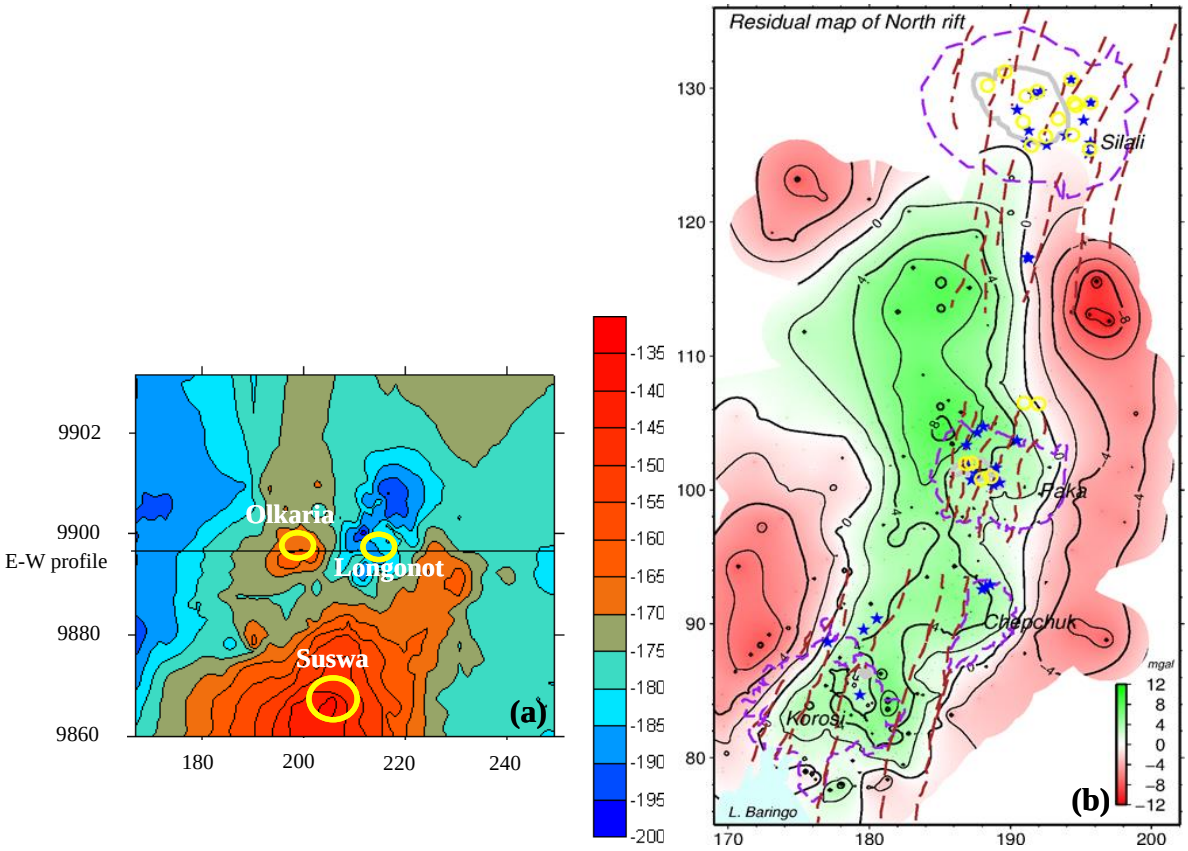

Figure 8: (a) Bouguer gravity (in mGal) map covering the south rift segment, the yellow rings show approximate locations of Olkaria, Longonot and Suswa respectively. (b) Residual Bouguer gravity map of the northern Kenya rift covering Korosi, Paka and Silali volcanoes (Lichoro et al., 2019). Blue stars are surface manifestations, purple dashed line outline the boundaries of the volcanoes, and brown dashed lines show the faults. Coordinates are in UTM, WGS84, zone 37 in km.

12. Stratigraphy and Alteration

A generalized stratigraphy for the Quaternary shield volcanoes in the rift is characterized by an upper 1 km of bimodal basalt and trachyte interlayered with tuffs. A second zone of tertiary formations comprising of Pliocene pyroclastics and lavas overlaying Miocene basalt and volcaniclastics which have been intruded by dikes and sills in places. The rift is floored at about 3 km depth by Precambrian metamorphic rocks intruded by dike complexes that are mostly aligned with the rift (Dunkley et al., 1993; Skilling 1993).

The lithology variations in Olkaria that, in part, affect the gravity pattern are illustrated by the east-west profile shown in Fig. 9 from Olkaria-west field to Olkaria northeast. To the west, volcanics and tuffs such as the Mau tuff are intercalated with trachyte and rhyolite lavas in the uppermost 2 km, whereas to the north east, the shallow stratigraphy is dominated by layers of rhyolite and Olkaria basalt overlying a thick segment of plateau trachyte (Omenda, 1998). This lithology variation is consistent with the lower gravity at Olkaria-west and higher gravity at Olkaria northeast (Ndombi, 1981). The lithology of Olkaria-Domes differs from Olkaria northeast and west, with shallow pyroclastics overlying rhyolites intercalated with basalt and trachyte lavas and sills. Based on the lithology of the wells, the shallow subsurface (to ~ 3000 m depth) at Olkaria is dominated

by series of dikes and sills laterally contrasted with tuffs and erupted lava breccias with sufficient density contrasts to accommodate the local gravity pattern (Ndombi, 1981).

The hydrothermal alteration pattern in the Olkaria field generally fits the pattern expected for volcano-hosted geothermal reservoirs but also features many of the complications in this pattern found at other fields related to lithology, permeability, temperature and reservoir evolution. For example, magma chemistry in the Kenyan Rift favours the eruption of trachyte and phonolite rocks that have a mineral composition unfavourable to smectite clay alteration, resulting in low temperature alteration with a relatively large proportion of zeolite rather than the more typical geothermal cap dominated by smectite. Because the near surface rocks at Olkaria are mainly rhyolite, low temperature alteration is mixed smectite-zeolite with a moderately low resistivity of about 5 to 10 Ωm. Another alteration complication at Olkaria is that, although the relatively low resistivity smectite-zeolite zone is generally conformal to the top of the permeable reservoir in most of the field area, the smectite-zeolite alteration overlies a chlorite-illite alteration zone that acts as a deeper low permeability, high resistivity cap, as is commonly found in many reservoirs. A dynamic complication is that, in the Domes area, the base of smectite-zeolite corresponds to temperature below 100°C instead of the usual 180°C and epidote is found at 150°C instead of the usual 240°C, consistent with the relict alteration of a cooled reservoir. Where recent rhyolite dome eruptions pierce the clay cap and provide a conduit for cold water into the reservoir, the smectite-smectite zone locally caps <240°C outflows at about 900 m depth overlying a temperature reversal to under 180°C, with reservoir at temperature at >300°C deeper than 3000 m in some cases or absent in others. The effect of all of these complications is that, although the low resistivity zone associated with smectite-zeolite alteration locally caps the geothermal reservoir (Lichoro, 2010), the top of the Olkaria permeable reservoir is generally significantly deeper than the base of low resistivity zeolite-smectite cap (Ronoh, 2015). These alteration patterns at Olkaria should be considered in the interpretation of MT surveys at other geothermal prospects in the Kenyan Rift.

The relatively shallow transition from the low density smectite-zeolite alteration to higher density chlorite-illite alteration at about 600 m depth and the high density actinolite-epidote-chlorite-illite zone below 3000 m depth at temperature over 320°C at Olkaria are likely to contribute to the overall gravity high mostly associated with the greater proportion of higher density lavas and intrusions at the volcanoes, in comparison to ash and sediments adjacent to the volcanoes.

The Menengai stratigraphy is dominated by trachyte lava interlayered with tuff in several sequences which in turn overlie Pleistocene trachyte and basalt lavas. In several wells in the centre of the caldera, trachyte lavas and intrusions overlie syenitic intrusions that immediately overlie magma at about 2 km depth (Mbia et al., 2015). Because of the predominantly trachyte composition of the rocks, low resistivity zeolites (Reynolds and Williford, 1991) are reported to be more dominant than smectite in the low temperature alteration to about 600 m depth over the centre of the field. In the central reservoir zone at Menengai, the base of the zeolite-smectite zone and transition to an illite-quartz zone corresponds to >240°C but it may correspond to <100°C where cold water is leaking down through structures that penetrate the cap below recent eruption vents. The base of the zeolite-smectite zone locally also overlies >200°C outflows that overlie temperature reversals (Mibei at al., 2016). Although these features are analogous to Olkaria, the cold leakage at Menengai has been more challenging because the high temperature reservoir is much smaller than the Olkaria reservoir and magma is shallower, issues that may apply to other prospects in the Kenya Rift. The Menengai wells confirm that the gravity high is associated with both a greater proportion of lavas and intrusive rocks near eruption centres and the shallower alteration transition from zeolite to illite with much lower porosity. The Olkaria geothermal field

has been more thoroughly studied during its longer history of development and so provides important conceptual support, the trachyte-dominated geology of Menengai is more closely analogous to the typical volcano in the Kenya Rift than the rhyolite-dominated geology of Olkaria.

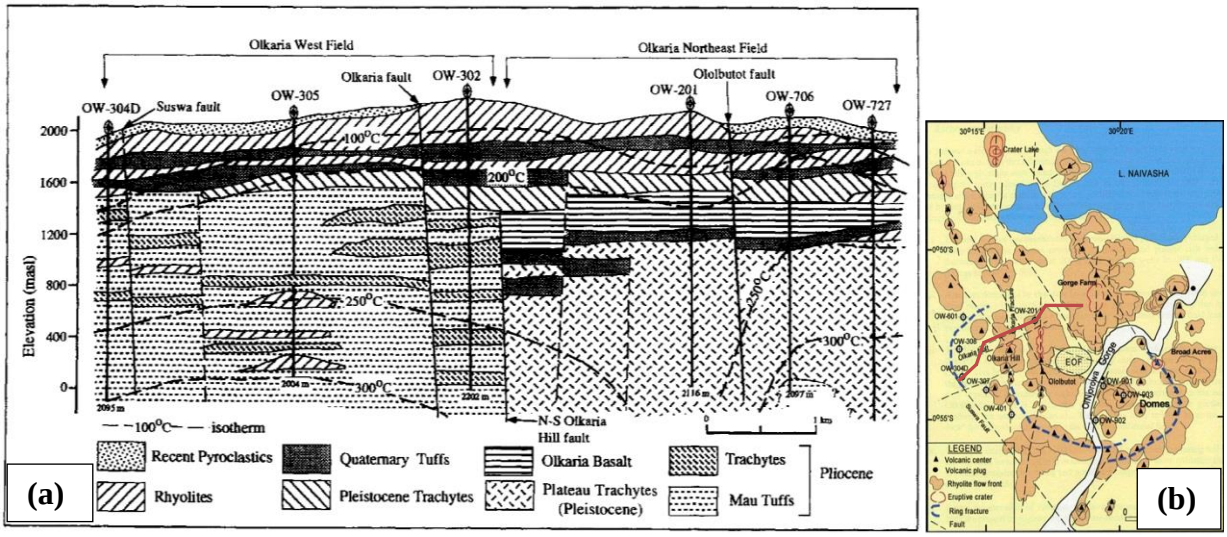

Figure 9: (a) Lithological cross-section of subsurface geology of wells on a SW-NE profile between Olkaria-west and Olkaria northeast geothermal fields (Adapted from Omenda, 1998). (b) Location map showing the profile in red. The white strip is the Ol'Njorowa gorge.

13. Permeability

In volcanic geothermal systems like those found in the Kenyan Rift, deep reservoir permeability is controlled mainly by fracturing of formations with stress state and rock properties favourable to forming open space. At the surface, fumaroles and alteration associated with faults and fracture segments are indicators of permeable connections through the cap to underlying fractured rocks at the boiling point. If geothermometry of fumarole gases indicates a likely origin over 240°C, the fault is more likely to be correlated with fracture permeability in a reservoir. At depths shallower than 1500 m and temperature lower that 300°C, lava breccias and flow contacts form laterally distributed permeable zones that, for example, might host a >240°C outflow (Mibei et al., 2016). Fracturing and recent eruption vents that penetrate the clay cap may also provide a conduit for meteoric water entry into the geothermal reservoir, locally reducing its temperature. Detailed surface mapping of fault geometry and motion and the interpretation of where these faults create volumes of highly stressed rock that will favour open fractures in the context of the local lithology has been a successful approach to predicting permeability (Hinz, 2018). Where structures are largely concealed by recent tuffs and a thick cap and a deep water table prevents buoyant flow of steam, gas or water to the surface, a >230°C reservoir may exist with no faults or fumaroles detected at the surface. For example, despite the limited surface manifestations and lack of exposed faults in the Olkaria-Domes sector of the Olkaria geothermal field, recent deep drilling has discovered an extensive geothermal reservoir with permeable fractures supporting a model of sub-surface structural patterns that are consistent with adjacent structural patterns at Olkaria central and Olkaria-west. The fissure swarms aligned with the rift axis are likely to have permeability higher along the fissures and generally lower across the fissures, except where they intersect a main cross-cutting structure.

At Suswa, permeable reservoir zones over 280°C have been predicted where inner caldera faults intersect rift-aligned faults near fumaroles with high gas geothermometry (ICEIDA, 2016). Surface mapping shows that faults aligned with the rift axis terminate south of Suswa and re-appear north of the volcano, implying that they may be concealed below the volcanic massif. Numerous fumaroles associated with unconsolidated tuffs exposed on the wall of the inner caldera, along WE faults on the floor of the northern outer caldera, and along the northern rim of the outer caldera have gas geochemistry that suggests that they are not connected to a high temperature reservoir but more likely tap a boiling zone near the water table. However, the gas geochemistry of fumaroles near the N and NE end of the central island-block and in the SW moat are more likely to be connected to an underlying zone over 280°C. The permeability is likely to be associated with the intersection of the NNW striking fractures and the inner caldera ring faults. Given the recent volcanic cover, as in the case of Olkaria-Domes, faults might be buried at the Suswa volcano, in which case drilling might reveal more widespread permeability. Like at Menengai, the relatively unaltered eruption centres may host downflows into chilled aquifers over the reservoir and recent eruptions and InSAR indications of magma movement suggest that shallow magma may be encountered. Therefore, the resource capacity assessment and well targeting plan is based on conceptual models with a wide range of reservoir area and thickness.

Because of the extensive recent pyroclastic cover, Longonot volcano has relatively limited fault exposures and thermal manifestations. The manifestations consist of weak fumaroles and hot ground within the summit crater and a fumarole along the fault and eruption alignment to the SSE of the crater. The intersections of this SSE striking volcanic fracture zone and both the outer caldera ring fault and the summit crater have been proposed as potential targets for a permeable underlying reservoir (Clarke et al., 1990; Alexander and Ussher, 2011).

In the NKR, at the Paka and Silali volcanoes, a greater probability of encountering permeability has been interpreted from correlation with fumaroles with intersections of NNE-trending normal faults with caldera ring faults. At the Korosi volcano, permeability is expected to be correlated with the Nakaporon and Nagoreti faults located on the west and east flanks of the volcano respectively, where major fumarolic activity occurs. At Silali, the gas in the fumaroles is interpreted to have originated at a depth of ~2.3 km based on geothermometry (Marini, 2014), which might imply that the smectite cap overlies a thick resistive chlorite-illite cap, like at part of the Olkaria Domes. Overall, the widespread network of faults and fractures and the corresponding occurrence of fumaroles with gas geothermometry indicating high temperature, as well as less indicative surface alteration and steam vents, supports an expectation for encountering sufficient fracture permeability within a high temperature geothermal reservoir in these areas. An assessment of whether the thick conductors on the flanks of the volcanoes might conceal additional permeability at high temperature would depend on the development of integrated conceptual models and comparisons to the case histories at Olkaria (e.g. Kandie et al., 2016) and Menengai (e.g. Mibei et al., 2016), where similar features mark a transmission from the geothermal system to cooler temperatures associated with the rift margins.

Although permeability in geothermal fields declines with depth as vertical stress increases and closes fractures with shallow dip, wells that encounter sparse near-vertical open fractures with moderate permeability can be very productive if higher temperatures are found at greater depth, as is characteristic of up-flow zones. However, at temperatures over 350°C, silica scaling commonly limits production and fractures tend to close by ductile creep as temperature approaches 400°C near magma which places an absolute limit on the base of a conventional geothermal reservoir. Although several wells have exceeded 340°C at Olkaria, the base of the permeable reservoir has not

yet been delineated since major feed zones and circulation losses have been encountered by wells deeper than 3000 m (Axelsson et al., 2017).

14. The geothermal system at Olkaria

The first well discovered a geothermal system at Olkaria in 1973 after many years of exploration (Svanbjornsson et al., 1983). Earlier exploration methods included geological mapping, DC resistivity methods and gravity. Exploration by geological mapping at Olkaria-Domes was challenging due to thick ash cover and lack of thermal manifestations. The geothermal system there was outlined using the DC resistivity measurements. Since then over 240 wells have been drilled and have constrained the properties of the reservoir (Axelsson et al., 2017; Owens et al., 2015). The natural state reservoir at Olkaria had been liquid dominated with a local steam cap. Temperatures in excess of 340°C have been recorded in several sectors of the field. The correlation of temperature with exploration geophysics in the context of Olkaria is primarily related to hydrothermal alteration. Although low permeability, low resistivity smectite-zeolite alteration does cap part of the >240°C high resistivity Olkaria reservoir (Lichoro, 2010), the relationship between resistivity and temperature exhibits several variations on this pattern at Olkaria that complicate the interpretation, such as where cold water down-flow has chilled the reservoir so that the low resistivity smectite-zeolite alteration overlies high resistivity <100°C relict alteration.

A temperature profile across Olkaria field from Olkaria-west to the Domes area (Fig. 10) shows reservoir up-flows from below -1000 masl at Olkaria 1 and at the Domes area and a smaller up-flow in the Olkaria-west field (Fig. 10). Ascending fluids are confined by a cap consisting of a low permeability and low resistivity smectite-zeolite layer extending to about 500 m depth that, in most parts of the Domes area, overlies a deeper high resistivity chlorite-illite cap. The chlorite-illite zone caps the top of the >240°C permeable reservoir characterized by epidote-chlorite-illite alteration, except in areas where cold water leakage has cooled the reservoir and the chlorite-epidote alteration is relict, reflecting an earlier high temperature reservoir (Lagat et al., 2005; Ronoh, 2015). The high temperature reservoir is hosted in the deeper part of the high resistivity zone which extends to the base of the profile in Fig. 6e, where granite intrusions have been intercepted by some drill holes. Such intrusives may contribute to the large scale observed gravity high associated with the field, although most rock types in the actinolite-garnet-epidote-illite alteration zone at >320°C in the reservoir would be expected to be relatively dense. The on-going wireline density logging being done by KenGen will reduce the ambiguity in the density model used to match the observed gravity.

Where the smectite-zeolite cap is locally breached by structures near a boiling zone in the upper reservoir, steam and gas leak to the surface as fumaroles. Zones of ascending hot water in Fig. 6e are separated by cold down-flows near wells 903 and 204, associated with structures that likely host intrusive necks that penetrate the clay cap below recent dome eruption centres, allowing cold surface aquifers to overcome the reservoir pressure gradient associated with buoyant hot up-flow. The resulting cold water down-flow into the reservoir occurs along the Ololbutot Fault within the field and along structures at the edges of the field including the Gorge Farm Fault to the NE, the Suswa Fault to the west and the ring structures to the south.

The heat source of the Olkaria geothermal system is assumed to be a complex of magma chambers at 6 to 8 km depth determined from S-wave attenuation inversion (Simiyu, 2000). These magma bodies and associated hydrothermal upflow zones are proposed to lie beneath Olkaria Hill (Olkaria-west), in the Olkaria-northeast beneath the Gorge farm volcanic centre (Fig. 9b), and in the Domes

area, roughly corresponding to the geothermal up-flows (Axelsson et al., 2017) identified in the cross-section (Fig. 10).

In the current conceptual model for Olkaria (Axelsson et al., 2017; Rop et al., 2018), permeability is associated with NW-SE trending faults aligned with the rift axis, NE-SW trending faults, the caldera ring structure and intersections between these structures. At relatively shallow depths, <1500 m, some very permeable zones are associated with rhyolite breccias and formation contacts (Ronoh, 2015). Some faults appear to be permeable in their plane but barriers across their plane, particularly on the margins of the resource. Structures aligned with recent rhyolite domes produce cold zones that penetrate deep into the reservoir, for example along the N-S segment of the Ololbutot Fault (Lagat et al., 2005) and along the rim faults to the south. Therefore, recharge to the geothermal model consists of several high temperature upflows, the deep regional hydrology of the rift valley and shallow cold influx zones.

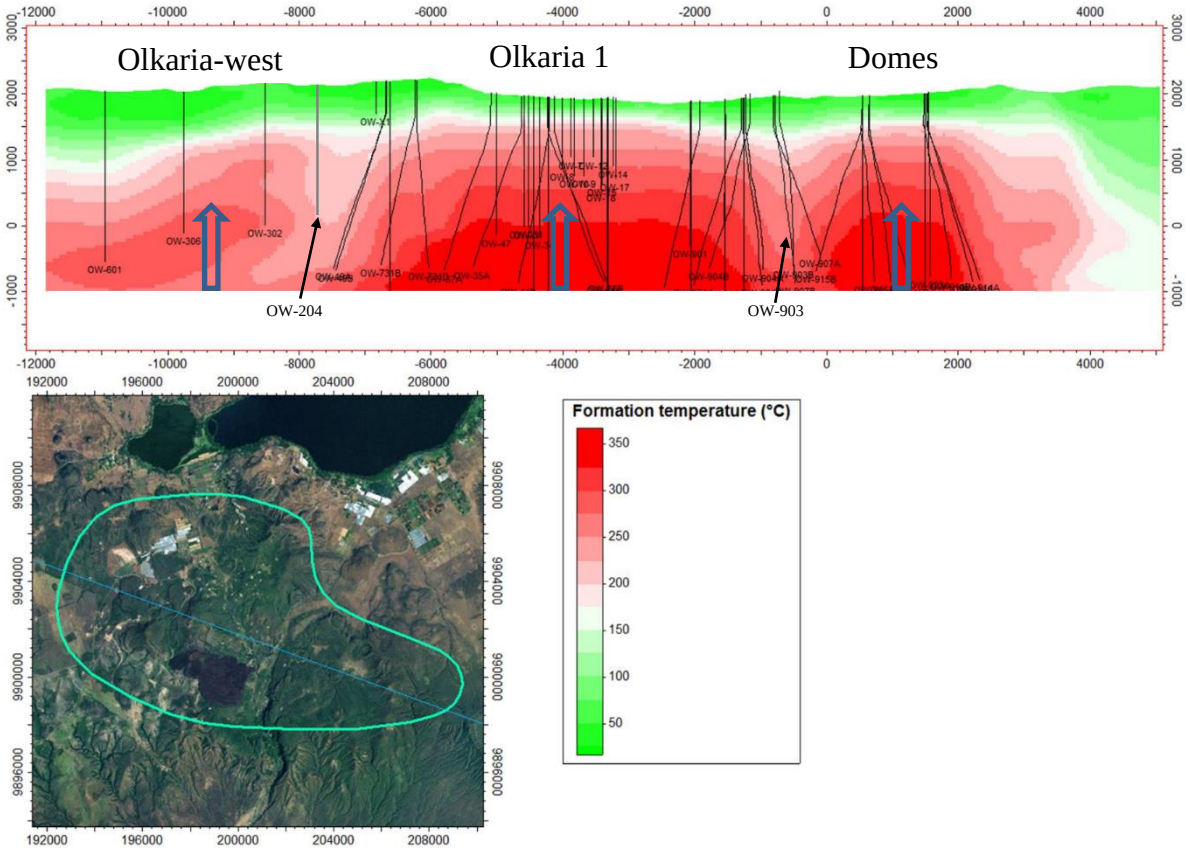

Figure 10: A view of the temperature distribution through Olkaria geothermal field in a NW-SE cross section through the Olkaria-west, Olkaria 1 (central) and Domes fields. Upflows are shown by arrows. (Modified from Axelsson et al., 2017).

15. Mapping of base of clay cap

Mapping the elevation of the base of the low resistivity smectite clay that caps an underlying geothermal reservoir is an important interpretation tool because it can help illustrate the location of the apex of the geothermal upflow, the path of the thermally buoyant flow updip against the base of the geothermal reservoir cap, and likely overall limits to the geothermal system at lateral boundaries like deep shale basins or major fault discontinuities. In the usual case for volcano-

hosted reservoirs, low resistivity smectite clays form at temperatures from about 50 to 90°C and are gradually converted to chlorite and/or illite as temperatures increase (Árnason et al., 2000) until hydrated smectite has entirely disappeared by about 220°C. In the most typical geothermal cases, a map of the base of the clay cap (BOC) marks the transition from low temperature cap to high temperature reservoir if the transition takes place over a geothermal reservoir and if the alteration mineralogy reflects current temperature.

The complexity of the interpretation of the base of the conductive clay cap in the Kenyan Rift is illustrated by the case histories at Olkaria and Menengai (Kandie et al., 2016; Ronoh, 2015; Mibei et al., 2016) that include at least six conceptual variations. 1) The base of smectite clay closely corresponds to the top of reservoir, the default assumption in geothermal exploration. 2) The base of smectite-zeolite cap is much shallower than the top of the reservoir due to an underlying impermeable chlorite-illite cap that is resistive, a common variation in geothermal case histories. 3) The base of smectite-zeolite zone is much shallower than the top of the reservoir or does not overly a reservoir because underlying chlorite-epidote alteration is relict and current formation temperature is much cooler than would be expected for such alteration minerals. 4) The base of smectite caps an outflow over a temperature reversal, which commonly occurs in fields where domes and lavas erupting along faults disrupt the clay cap and provide a path for cold water to penetrate to greater depth. 5) The base of the smectite clay is particularly deep and does not cap a geothermal reservoir where thick zones of smectite weathering and alteration form in the volcanic sediments adjacent to a volcano, often with the top of the low resistivity zone flat, corresponding to the water table. 6) The resistivity associated with the low temperature cap is not as low as usual (5 to 20 Ωm in trachyte instead of 2 to 10 Ωm in basalt) because trachyte and phonolite have a mineral composition unfavourable to the formation of smectite and so the low temperature alteration is predominantly zeolite rather than smectite. Provided that interpretation and related uncertainty are adjusted to allow for the complications observed at developed fields in the Kenyan Rift, the resistivity cross-sections in Figures 6 to 7 and the maps of the elevation of the base of conductor in Figure 11 confirm that a conventional geothermal interpretation of the base of the smectite-zeolite alteration zone can constrain resource conceptual models in conjunction with other geoscience data, in particular constraining buoyant thermal upflow and outflow and identifying resource boundaries.

The maps in Fig. 11 show the elevation of the base of the shallow low resistivity zone, typically less than 10 Ωm, from the 1D model for each MT station (Cumming, 2016). The maps for each of the of BOC for the southern rift shows that the transition occurs at elevation of above 1000 m. asl in the areas around Longonot, Olkaria-domes, Olkaria NE field and south of Suswa outer caldera (Fig. 11b) but appear to be deeper at the Suswa inner caldera where there is limited MT coverage and Olkaria-west field. In general, areas of shallow BOC correspond to locations where surface thermal manifestations like alteration and fumaroles are prevalent, consistent with a resistivity interpretation of a low resistivity cap doming up above geothermal upflow and outflow.

The map of the BOC at Menengai caldera show two distinct segments (Fig. 11c), a shallow BOC in the middle of the caldera (at elevation of ~1200 m. asl), and deeper BOC on both west and east of the caldera at elevation of <1000 m. asl. In the undrilled cases, the probability of encountering temperatures >200°C is higher below relatively shallow BOC than in other locations within the prospect area, particularly if the shallow BOC coincides with fumaroles with gas geochemistry consistent with an underlying high temperature reservoir. An area particularly worth highlighting is south of the Longonot volcano crater which has a thinned clay cap overlaying a thin resistive zone which is further underlain by a third zone of very low resistivity (< 10 Ωm) below 4 km depth

(Alexander and Ussher, 2011). This deeper conductor has been attributed to a magma chamber under Longonot rising to shallow depth south of the crater (and possibly also below the crater where there is no MT coverage). The up-doming of the BOC under the southern flanks of Longonot volcano is consistent with a geothermal system over and adjacent to a shallow magma body.

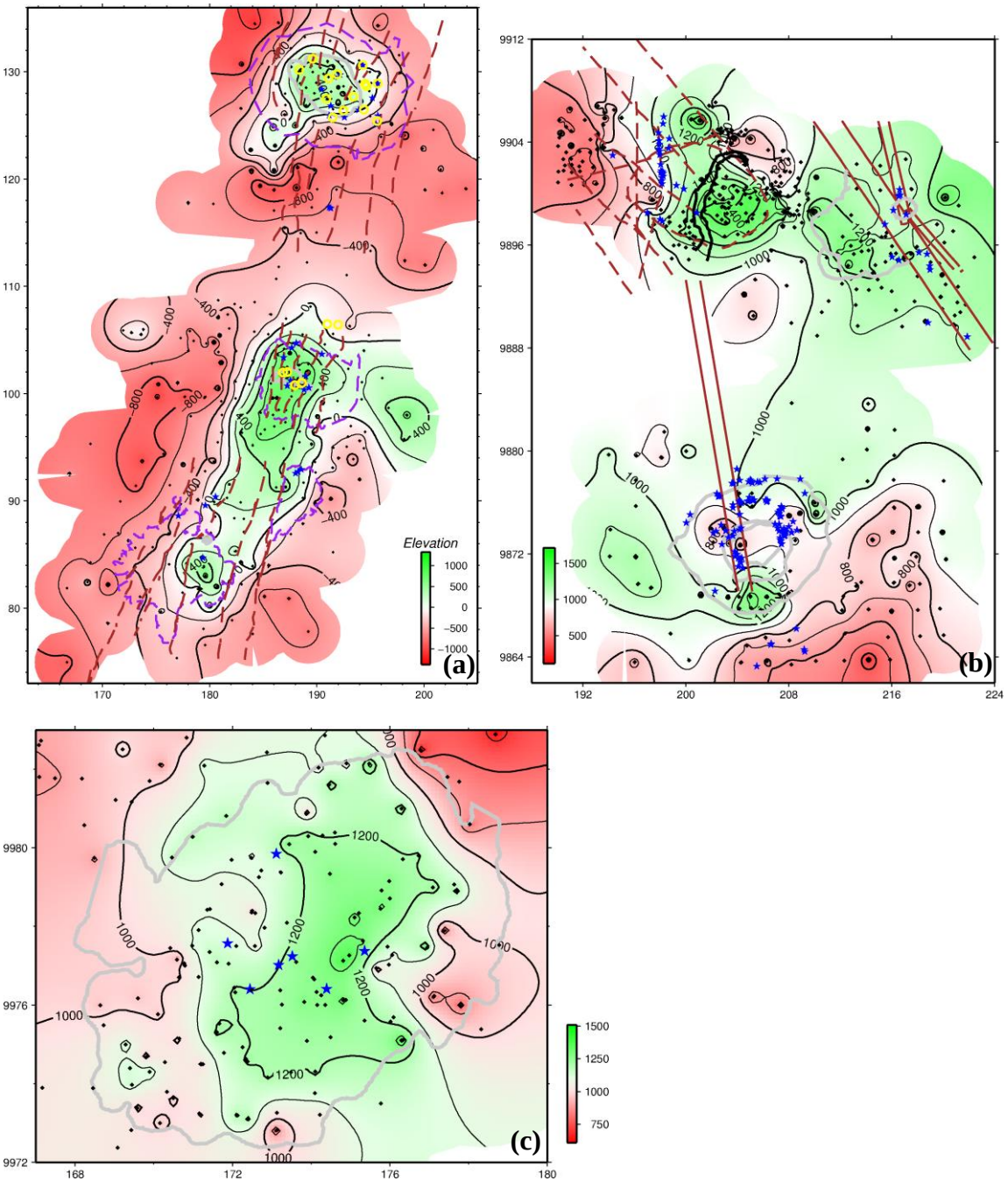

Figure 11: Elevation of the base of the clay cap (BOC), shown in meters above sea level (Elevation) for the three segments (note the different scales). (b) South rift (Suswa, Longonot & Olkaria (a) North rift (Korosi, Paka & Silali (c) Menengai caldera. Volcanoes are broken- purple lines, Grey lines are calderas, broken-brown lines are faults and fissures, blue stars are fumaroles, yellow rings are altered surfaces and brown lines mark volcanic alignments. Coordinates are UTM, WGS84, zone 37 in km.

Resistivity at Suswa caldera does not show clear extensive low resistivity geothermal cap rock like seen in other geothermal fields. The thick 7 to 50 ohm-m altered volcanic pile at Suswa, is interpreted to border a potential reservoir associated with the inner caldera, where the lack of MT coverage makes further resistivity interpretation speculative. This suggests that mapping of BOC is not effective at Suswa. Although the MT has failed to clearly resolve a clay cap at Suswa, the resistivity data is permissive of a resource underlying the fumaroles with high temperature geothermometry on the rim of the central island where a cap might be breached by permeable structures.

Depth to the base of clay cap in the northern rift segment (Fig. 11a) shows uniform elevation of about sea level along the central rift across Korosi, Paka and Silali volcanoes and aligning with the rift strike. This alignment coincides with high resistivity at sea level previously interpreted (Lichoro et al., 2017) to underlie that zone. Elsewhere within the rift but outside the volcanic axis, the BOC deepens, supporting the interpretations of thick volcaniclastics on the flanks of the axial rift.

16. Comparison of developed and undeveloped geothermal fields in the Kenya rift

An important validation step in geothermal resource assessment is the comparison of surface data from undrilled geothermal prospects to similar data from potentially analogous developed geothermal systems and the correlation of the surface data with subsurface properties encountered by drilling. Both Olkaria and Menengai and the other volcanoes in the Kenyan Rift share a common overall resistivity pattern, with a relatively thin, low resistivity smectite-zeolite cap domed up below the water table beneath a significant part of the volcano, with thicker low resistivity smectite-rich clastics and sediments on its flanks and extending to the margins of the rift. The low resistivity zones on the margins typically have a top near the water table. Importantly, at both Olkaria and Menengai, the reservoir is entirely within the area of elevated base of cap. However, because the zone where the base is elevated includes outflows, cold downflows, deeper reservoir tops below a non-smectite cap and similar complications, the part of the clay cap that is domed up is likely to be a much bigger area than the commercial reservoir. To address the resulting ambiguity, the MT imaging should be integrated with the geology, fumarole gas and spring water geochemistry and thermodynamic constraints in a range of conceptual models illustrative of the uncertainty to support an exploration risk assessment.

Although the Olkaria surface geology is dominated by rhyolite domes, uniquely in the Kenyan Rift, it shares the overall pattern of thinner low resistivity over the reservoir than on the margins of the field. However, based on drilling results, the reservoir at Olkaria is much deeper and thicker than at Menengai. The deeper reservoir top at Olkaria is apparent in the resistivity pattern. The base of clay cap beneath the Domes area and the Olkaria-northeast field seems shallower than in the Olkaria-west field, which is consistent with different lithologies (see Fig. 9), deeper reservoir and diverse temperature regimes in the west field (Omenda, 1998; Axelsson et al., 2017). However, the low resistivity cap in the west field is well formed but thicker than other areas at Olkaria.

At Menengai, the shallow low resistivity is correlated with a 600 m thick low intensity zeolite-smectite cap, especially at the centre of the caldera where majority of productive wells have been drilled (see Fig. 7a). Away from the central summit area, thicker moderate resistivity dominates and the wells drilled there have been less productive.

Most of the geothermal fields and prospects have a network of fissure swarms and faults that intersect caldera structures, except Longonot which has fewer exposed structures, in which case these intersections are interpreted to focus permeability.

Although the Longonot volcanic system is only about 10 km east of the Olkaria-Domes geothermal field, it has marked geological differences as well as differences in resistivity structure (Fig. 6). The reservoir below the clay cap is apparently thinner at Longonot compared to the deep reservoir drilled at Olkaria due to the inferred magma at shallow depth at Longonot, as indicated by deep low resistivity on the southern flank of the volcano. Based on this potential magma body at shallow depth, Menengai is the closest analog in the central Kenya rift.

Suswa lacks the typical shallow low resistivity cap, possibly because no MT was acquired within the inner caldera. It is possible that Suswa might not have a well-developed smectite-zeolite cap above the reservoir, perhaps due to the recent phonolytic rocks, resulting in the widespread fumarolic activity.

From the analysis, both Suswa and Silali volcanoes have deeper BOC (>1000 m). On the other hand, BOC at Longonot and Paka appear shallower. Korosi appears not to have a clay cap beneath the summit volcano but thick conductive volcaniclastics overly the flanks. However, BOC elevation at Korosi is fairly shallow (about sea level), especially on the eastern-half of the volcano pointing at a possible shallow reservoir in that zone.

Parts of Olkaria host a shallow-cooler reservoir on top of a deeper and thicker hot reservoir which can easily be cased off, while at Menengai cooler reservoirs are deeper but offset from the hot central dome area. This deduction is supported by the cooler intrusion below the production casing in some wells at Menengai outside the dome area and temperature inversion in the top section of some Olkaria wells.

17. Detection of magma

Magma has been intercepted by wells in only three geothermal fields and it has been encountered at depths shallower than 2.1 km only at Menengai in Kenya and at Krafla in Iceland. Therefore, Menengai and Krafla are viewed as analogues for characterizing the effect of shallow magma on geothermal resource potential and for reliably predicting the presence of magma bodies at depths shallow enough to significantly impact resource capacity. Although research in Iceland is being directed at the development of super-critical fluids associated with magma bodies (Friðleifsson, et al., 2014), using current technology, such fluids cannot be utilized to produce commercially viable geothermal energy. Moreover, rock at temperature over about 350°C is much less likely to host commercially viable permeability because of the tendency for permeable fractures to close near the brittle-ductile transition temperature and for fluids at such temperatures to deposit silica. Therefore, although shallow magma does indicate adequate heat to support a geothermal reservoir, magma that is shallower than a few km will tend to limit the potential volume available for a geothermal development and, as a result, will tend to limit the potential generation capacity of the reservoir.

A magma body was not specifically predicted at either Krafla or Menengai, although the possibility was acknowledged given the very young lavas in both areas and the historic eruption at Krafla. Subsequent to the discovery of the magma, a 3D inversion of the MT at Menengai had indicated that the MT data seemed to be at least compatible with the existence of the shallow magma (Mibei et al., 2016). However, it was not clear what level of confidence could have been given to such a prediction of magma based on MT resistivity imaging prior to drilling. Although similar claims had been made for the resolution of magma at Krafla using 3D MT inversion, an elaborate investigation

of the reliability of the 3D MT imaging suggested that the noise level of the MT data at Krafla was too high to support the reliable resolution of specific magma zones (Gasperikova et al., 2015).
Microseismic monitoring surveys are arguably a best practice for developed geothermal fields where produced water will be injected into rocks below 1 km depth that are >50°C hotter than the injection fluid or for undeveloped geothermal prospects where shallow magma may be present. After a limited initial survey has established that sufficient seismicity exists to warrant a larger scale survey, we recommend that seismic arrays be installed with capabilities suitable for magma detection at all seismically active prospects. For example, on-going microearthquake monitoring in the NKR volcanic zone has detected shallow seismicity at Paka volcano but not at Silali volcano, justifying a more detailed seismic monitoring survey at Paka. Detecting seismic swarms and events associated with magma emplacement is the highest priority. However, based on experience at Olkaria (Simiyu, 1999), detailed tomographic imaging of S-wave shadows that may indicate magma should also be investigated, although the long wavelength of teleseismic S-waves may limit resolution. Because hypocentre depths are important to the interpretation and are influenced by shallow seismic velocities that are not well resolved by conventional tomography, the seismic array design should support shorter term ambient noise tomography (ANT). This would aid in imaging of shallow magma in the upper most 5 km without the need to carry out expensive shear wave tomography.

18. Conclusions.

The development of new geothermal systems in Kenya will hinge on ability to apply experience gained from the already developed geothermal fields in the south Kenya Rift. This will involve evaluation of geoscientific information with regards to well productivity and applying it to similar undeveloped fields. At both Olkaria, Menengai and Eburru, reservoir and lithological studies suggest that permeability is potentially controlled by faults and other tectonic structures, particularly at the intersections of such structures. All volcanoes studied here are bound by the rift structures that are likely to influence the regional hydrogeology. Some faults might act both as barriers and channels of fluid flow as in the case of Olkaria. Locally, the patterns of faults will significantly determine the overall productivity of the geothermal wells.

The overview of analogy of the geothermal systems identifies the following aspects for the undeveloped geothermal systems:
i) The evaluation of geothermal prospects, especially the undeveloped fields, based on base of the clay cap is an essential approach in well targeting.
ii) Most of the structural and thermal features are consistent with geophysical data both for the developed and the undeveloped geothermal fields.
iii) 2D resistivity model studies of MT have shown that 1D MT inversions at volcanoes that hint at possible conductors deeper than the base of the clay cap are unreliable. Therefore, this study could not resolve such features. Although a 3D MT inversion of high quality MT data might resolve a magma body, most MT data are too noisy to reliably support such an inversion.
iv) Geophysics can effectively reveal sub-surface geothermal properties even in areas lacking thermal and structural features on surface but must be evaluated in the context of a conceptual model.

A full 3D inversion of the MT tensor gives results comparable at < 2km depth to the 1D joint inversion of MT and TEM data across the summit area of Paka volcano. The resolution of the

resistivity structure to the base of the clay cap is fairly consistent between the two models which gives us confidence to interpret the 1D inversion to the base of the clay cap.

Occurrence of shallow seismicity beneath volcanoes in the rift might be related to shallow magma likely to limit the potential volume of the geothermal reservoir. In this case the cut-of depth of seismicity marks the brittle-ductile transition which occurs at temperature range 370–400°C (Fournier, 1999). The occurrence of seismicity in the upper crust is an indication that temperatures are below the brittle/ductile transition. On the other hand, lack of seismicity as in the case of Silali might point at the uniform stress state of the crust with respect to the deeper magma chamber. Based on drilling into magma in Menengai, there is probability of encountering magma in other undeveloped volcanic systems in the Kenya Rift e.g. Longonot and Paka and potentially at some other major volcanoes in the EAR.

Resistivity, gravity and geology studies are not very conclusive on presence of magma, its locations and depth so any inferences from these data are very speculative. However, both tectonics, resistivity and gravity results are consistent with the setting of the rift, e.g. the area south of Paka volcano the resistivity and gravity pattern correspond to mapped fissure-eruptions but the trend of resistivity and gravity is offset westwards between Paka and Silali. This offset indicates a possible recent eastwards shift of the axis of the rifting alignment which is not discernible from surface geological mapping. There is no evidence of similar shift in either the south or central rift segments of the studied areas.

This is the first attempt to compare and look for similarities and differences of the geothermal fields in the Kenya Rift, while acknowledging the limitations of the data and the study. Once new data are available, e.g. from further exploration (especially geochemistry) and/or drilling, this comparison should be reviewed and updated to support the development of resource conceptual models for the respective geothermal systems.

This study shows that the data considered here, i.e. geology, resistivity and gravity, are capable of identifying potential geothermal resources, but they are not able to give reliable information on their inner structure and present characteristics. Passive seismic monitoring at both developed and prospective geothermal fields should be used. A dense seismic networks should be installed for monitoring seismicity and eventual ambient noise analysis to determine shallow velocity variation and constrain depth of earthquakes. Shallow seismicity could be a consequence of cooling in the shallow reservoir where cold-water flow interacts with hot rocks, presenting a risk to geothermal development due to the risk of encountering temperature inversion in the wells. Knowing this beforehand can aid in accurate well targeting and prediction of the resource capacity. Ground deformation monitoring by InSAR should also be regularly used to monitor temporal changes which can give important information on subsurface changes and magma movements. There is little doubt that subsurface resistivity is among the most diagnostic parameters in geothermal exploration. This study is based on joint 1D inversion of MT and TEM data. This gives approximate picture of the resistivity structure but the data contain more information. It is thus important to do a detailed 3D inversion of MT in all the areas once enough coverage of quality data is available. Overall this effort to get a wider picture of the geothermal systems variability along the Kenyan rift should be attempted in other sectors of the EARS.

- **References**

Alexander, K., Ussher, G., 2011. Geothermal Resource Assessment for Mt. Longonot, Central Rift Valley, Kenya. Geotherm. Resour. Counc. … 35, 1147–1154.

Árnason, K., 2006. TEMTD. A program for 1D inversion of central-loop TEM and MT data. A short ManualR, Reykjavík, 16 pp. Reykjavik: ISOR, Iceland Geosurvey.

Árnason, K., Eysteinsson, H., Hersir, G.P., 2010. Joint 1D inversion of TEM and MT data and 3D inversion of MT data in the Hengill area, SW Iceland. Geothermics 39, 13–34. https://doi.org/10.1016/j.geothermics.2010.01.002

Árnason, K., Karlsdottir, R., Eysteinsson, H., Flóvenz, Ó.G., Thor, S., 2000. The Resistivity Structure of High-Temperature Geothermal Systems in Iceland. Proc. World Geotherm. Congr. 2000 923–928.

Axelsson, G., Gudmundsdóttir, V., Arnaldsson, A., Ármannsson, H., Árnason, K., Einarsson, G., Franzson, H., Halldórsdóttir, S., Hersir, G., Kamunya, K., Níelsson, S., Okoo, J., Omiti, A., Ouma, P., 2017. Revision of the Conceptual Model for the Olkaria Geothermal System , Kenya. Proc. Stanford Geotherm. Work. 1–9.

Baker, B.H., Mohr, P.A., Williams, L.A., 1972. Geology of the Eastern rift system. Geol. Soc. Am. Spec. Pap. 136, 67.

Baker, B.H., Wohlenberg, J., 1971. Structure and evolution of the Kenya Rift Valley. Nature 229, 538–541.

Biggs, J.., Robertson, E.., Cashman, K.. V.., 2016. The lateral extent of volcanic interactions during unrest and eruption. . Nat. Geosci. , 9 , 308- 308–311. https://doi.org/10.1038/ngeo2658

Biggs, J., Anthony, E.Y., Ebinger, C.J., 2009. Multiple inflation and deflation events at Kenyan volcanoes, East African Rift. Geology v.37, p979-982. https://doi.org/10.1130G30133A.1:2

Biggs, J., Robertson, E., Mace, M., 2013. ISMER – Active Magmatic Processes in the East African Rift: A Satellite Radar Perspective. Earth Syst. Sci. 81–91.

Bosworth, W., Strecker, M.R., Blisniuk, P.M., 1992. Integration of East African Paleostress and Present-Day Stress Data - Implications for Continental Stress Field Dynamics. J. Geophys. Res. 97, 11851–11865. https://doi.org/10.1029/90JB02568

Briggs, J., Anthony, E.Y., Ebinger, C.J., 2009. Multiple inflation and deflation events at Kenyan volcanoes, East African Rift. Geol. Soc. Am. 37, 979–982. https://doi.org/10.1130/G30133A.1

Cagniard, L., 1953. The basic theory of magneto-telluric method of geophysical prospecting.

Cantini, P., Cataldi, A., Pinna, E., 1990. Gravity study of the structure of Suswa volcano and basement in the Kenya Rift. Geothermics 19, 367–384. https://doi.org/10.1016/0375-6505(90)90039-E

Chave and Jones, 2012. (eds), The Magnetotelluric Method: Theory and Practice , Cambridge University Press, 552 pp,.

Chorowicz, J., 2005. The East African rift system. J. African Earth Sci. 43, 379–410. https://doi.org/10.1016/j.jafrearsci.2005.07.019

Clarke, M.C.G., Woodhall, D.G., Allen, D., Darling, G., 1990. Geological, volcanological and hydrogeological controls on the occurrence of geothermal activity in the area surrounding Lake Naivasha Keuya. British Geological Survey report to the Ministry of energy, Kenya. 138 pp.

Constable, S.C., Parker, R.L., Constable, C.G., 1987. Occam's inversion: A practical algorithm for

generating smooth models from electromagnetic sounding data. Geophysics 52, 289. https://doi.org/10.1190/1.1442303

Cumming, W., 2017. Geophysical Section. In: Review of the Conceptual Model of Suswa Geothermal Prospect, Kenya. EFLA Final Report for ICEIDA Project ICE23066-1301NDF Kenya/1.

Cumming, W., 2014. UNEP Silali Resource Review – Geophysics; report to the United Nations Environmental Program, 71 pp.

Cumming, W., Mackie, R., 2010. Resistivity Imaging of Geothermal Resources Using 1D , 2D and 3D MT Inversion and TDEM Static Shift Correction Illustrated by a Glass Mountain Case History. Proc. World Geotherm. Congr. 2010 1–10.

Cumming, W.B., Nordquist, G.A., Astra, D., 2000. Geophysical Exploration for Geothermal Resources – An Application of Combined MT-TDEM, vol.19. Society of Exploration Geophysics, pp. 1071 – 1074 (extended abstracts).

Dipippo, R., 2016. "Geothermal Power Generation." Ron Dipippo (ed.). Elsevier, 2016, 654 p.

Dunkley, P.N., Smith, M., Allen, D.J., Darling, W.G., 1993. The geothermal activity and geology of the northern sector of the Kenya Rift Valley, British Geological Survey Research Report.

Egbert, G.D., Booker, J.R., 1986. Robust estimation of geomagnetic transfer functions. Geophys. J. R. Astron. Soc. 87, 173–194. https://doi.org/10.1111/j.1365-246X.1986.tb04552.x

Elders, W.A., Friðleifsson, G.Ó., Albertsson, A., Sigurdsson, Ó., Karlsdóttir, R., Pálsson, B., 2011. The Iceland Deep Drilling Project (IDDP): Planning for the Second Deep Well at Reykjanes, in: GRC Transactions, Vol. 35.

Fairhead, J.D., 1976. The structure of the lithosphere beneath the eastern rift, east africa, deduced from gravity studies.

Fournier, R.O., 1999. Hydrothermal processes related to movement of fl uid from plastic into brittle rock in the magmatic – epithermal environment. Bull. Soc. Econ. Geol. 94, 1193.1211.

Friðleifsson, G.O., Ármannsson, H., Guðmundsson, Á., Árnason, K., Mortensen, A.K., Pálsson, B., Einarsson, G.M., 2014. Site selection for the well IDDP-1 at Krafla. Geothermics 49, 9–15. https://doi.org/10.1016/j.geothermics.2013.06.001

Friðleifsson, G.Ó., Pálsson, B., Stefánsson, B., Albertsson, A., Gunnlaugsson, E., 2010. Iceland Deep Drilling Project . The first IDDP Drill Hole Drilled and Completed in 2009, in: Proceedings World Geothermal Congress 2010 Bali, Indonesia. pp. 4–7.

Friese, A., 2015. InSAR, structural analyses and dating of Paka volcanic products, Northern Kenya Rift.

Gasperikova, E., Rosenkjaer, G.K., Arnason, K., Newman, G.A., Lindsey, N.J., 2015. Resistivity characterization of the Krafla and Hengill geothermal fields through 3D MT inverse modeling. Geothermics 57, 246–257. https://doi.org/10.1016/j.geothermics.2015.06.015

GDC, 2017. Preliminary report on Menengai intrusives.

Geotermica Italiana, 1989. Supplement of surface investigations within the calderas of Longonot and Suswa Volcanoes. Unpublished Report to the UNDP. Vol. 1.

Henry, W.J., Mechie, J., Maguire, P.K.H., Khan, M.A., Prodehl, C., Keller, G.R., Patel, J., 1990. A seismic investigation of the Kenya rift valley. Geophys. J. Int., 100: 107-130.

Hinz, N., 2018. Suswa – Geology investigation.

ICEIDA, 2017. Review of the Conceptual Model of Suswa Geothermal Prospect, Kenya, ICE23066-1301NDF Kenya/1 NDF: C48.

Jiracek, G., 1990. Near-surface and topographic distortions in electromagnetic induction. Surv. Geophys., 11,163-203.

Johnson, W.R., 1969. Volcanic geology of Mount Suswa, Kenya. Philos. Trans. R. Soc. London 265, 383–412.

Kandie, R., Mbuthia, P., Stimac, J., 2016. Use of leapfrog geothermal software in data integration and 3D visualization case study of Olkaria, in: Proceedings, 6th African Rift Geothermal Conference Addis Ababa, Ethiopia.

Karson, J., Curtis, P., 1989. Tectonic and magmatic processes in the Eastern Branch of the East Africa Rift and implications for magmatically active continental rifts. Journal of African Earth Sciences, 8(2/3/4), 434-453.

Keller, G.R., Prodeh, C., Mechie, J., Fuchs, K., Khan, A.M., Maquire, P.K.., Mooney, W.D., Achauer, U., Davis, P.M., Meyer, R.P., Braile, L.W., Nyambok, I.O., Thompson, G.A., 1994. The East African rift system in the light of KRISP 90. Tectonophysics 236, 465–483.

KRISP Working Group, 1991. A compilation of data from the 1990 Kenya Rift International Seismic Project KRISP 90 seismic refraction-wide angle reflection experiment. Open-File Report 91-1, Univ. Karlsruhe, 80 pp.

Lagat, J., Arnorsson, S., Franzson, H., 2005. Geology , Hydrothermal Alteration and Fluid Inclusion Studies of Olkaria Domes Geothermal Field , Kenya. Proc. World Geotherm. Congr. 24–29.

Leat, P.T., 1984. Geological evolution of the trachytic caldera volcano Menengai, Kenya Rift Valley. J. Geol. Soc. London. 141, 1057–1069. https://doi.org/10.1144/gsjgs.141.6.1057

Lichoro, C.M., 2013. Multi-dimensional interpretation of electromagnetic data from Silali geothermal field in Kenya: Comparison of 1-D, 2-D and 3-D MT inversion. MSc thesis, Univ. Icel. 185pp.

Lichoro, C.M., 2010. Joint 1-D Inversion of TEM and MT Data from Olkaria Domes Geothermal Area, Kenya. Geotherm. Resour. Counc. Trans. 34, 873–880. https://doi.org/ISSN: 0193-5933; ISBN: 0-934412-95-2

Lichoro, C.M., Árnason, K., Cumming, W., 2019. Joint interpretation of gravity and resistivity data from the Northern Kenya volcanic rift zone: Structural and geothermal significance. Geothermics 77, 139–150. https://doi.org/10.1016/j.geothermics.2018.09.006

Lichoro, C.M., Árnason, K., Cumming, W., 2017. Resistivity imaging of geothermal resources in northern Kenya rift by joint 1D inversion of MT and TEM data. Geothermics 68, 20–32. https://doi.org/10.1016/j.geothermics.2017.02.006

MacDonald, R., 2003. Magmatism of the Kenya Rift Valley: A review. Earth Sci. 93, 239–253.

Maguire, P.K.H., Swain, C.J., Masotti, R., Khan, M.A., 1994. A crustal and uppermost mantle cross-sectional model of the Kenya Rift derived from seismic and gravity data. Tectonophysics 236, 217–249. https://doi.org/doi:10.1016/0040-1951(94)90178-3

Manthilake, G., Bolfan-Casanova, N., Novella, D., Mookherjee, M., Andrault, D., 2016. Dehydration of chlorite explains anomalously high electrical conductivity in the mantle wedges. Sci. Adv. 2. https://doi.org/10.1126/sciadv.1501631

Mariita, N.O., Keller, G.R., 2007. An integrated geophysical study of the northern Kenya rift. J. African Earth Sci. 48, 80–94. https://doi.org/10.1016/j.jafrearsci.2006.05.008

Marini, L., 2014. UNEP Silali Resource Review – Geochemistry; report to the United Nations Environmental Program, 71 pp.

Mbia, P.K., K., M.A., C., O.N., B.S., H., 2015. Sub-Surface Geology, Petrology and Hydrothermal

Alteration of the Menengai Geothermal Field, Kenya: Case Study of Wells MW-02, MW-04, MW-06 and MW-07. Proc. World Geotherm. Congr. 2015.

Mechie, J., Keller, G.R., Prodehl, C., Gaciri, S., Braile, L.W., Mooney, W.D., Gajewski, D., Sandmeier, K., 1994. Crustal structure beneath the Kenya Rift from axial profile data 236, 179–200.

Mechie, J., Keller, G.R., Prodehl, C., Khan, M.A., Gachiri, S.J., 1997. A model for the structure , composition and evolution of the Kenya rift. Tectonophysics 278, 95–119.

Mibei, G., Mutua, J., Njue, L., Ndongoli, C., 2016. Conceptual model of Menengai Geothermal field. Proc. ARGeo Conf.

Mwania, M.M., 2015. Evaluation of subsurface structures using hydrothermal alteration mineralogy- A case study of Olkaria South East field. GRC Trans. 39, 559–566.

Mwarania, F.M., 2014. Reservoir evaluation and modelling of the Eburru geothermal system, Kenya. Reykjavik.

Ofwona, C., Wambugu, J.M., Omenda, P., Mariita, N., Mwawongo, G., Kubo, B., 2006. Surface Geothermal Exploration Of Korosi And Chepchuk Prospects. Ofwona, C. (Editor). Internal report, 2006, Unpublished, 45-62.

Ogoso-Odongo, M.E., 1986. Geology of the Olkaria geothermal field. Geothermics 15, 741–748. https://doi.org/10.1016/0375-6505(86)90087-8

Omenda, P.A., 1998. The geology and structural controls of t h e olkaria g e o t h e r m a l system, kenya peter a. omenda* 27, 55–74.

Owens, L., Porras, E., Spielman, P., Walsh, P., 2015. Updated Geologic and Geochemical Assessment of the Olkaria III Field Following Recent Expansion to 110MW. Proc. World Geotherm. Congr. 2015.

Patlan, E., Velasco, A.A., Wamalwa, A., Kaip, G., Usgs, N., Ms, M.R., Park, M., 2017. Seismic Zone at East Africa Rift : Insights into the Geothermal Potential 1–15.

Phoenix Geophysics, 2005. Data processing user guide. Phoenix Geophysics Ltd, ON, Canada.

Reynolds, W., Williford, C., 1991. Zeolite and clay-mineral induced resistivity in simulated reservoir sand. J. Pet. Sci. Eng. 5–2, 163–172.

Robertson, E., Biggs, J., Cashman, K., Floyd, M.A., 2015. Influence of regional tectonics and pre-existing structures on the formation of elliptical calderas in the Kenyan Rift. Geol. Soc. Spec. Publ. 420, 43–67.

Rodi, W., Mackie, R.L., 2001. Nonlinear conjugate gradients algorithm for 2-D magnetotelluric inversion. Geophysics 66, 174–187. https://doi.org/10.1190/1.1444893

Ronoh, I., 2015. Appraising a Geothermal Field Using Hydrothermal Alteration Mineralogy; A Case Study of the East of Olkaria Domes Geothermal Field; Kenya. Proc. World Geotherm. Congr. 2015.

Rop, E., Fujii, H., Jalilinasrabady, S., 2018. An updated numerical model of the Greater Olkaria geothermal system, Kenya, in: PROCEEDINGS, 43rd Workshop on Geothermal Reservoir Engineering Stanford University, Stanford, California, February 12-14, 2018 SGP-TR-213. pp. 1–13.

Scott, S.C., 1980. The geology of Longonot volcano, central Kenya: a question of volumes. Philos. Trans. R. Soc. London, A 296, 437–465. https://doi.org/10.1098/rsta.1980.0188

Scott, S.C., Skilling, I.P., 1999. The role of tephrachronology in recognizing synchronous caldera-forming events at the Quaternary volcanoes Longonot and Suswa, south Kenya Rift. Volcanoes

Quat. 47–67. https://doi.org/10.1144/GSL.SP.1999.161.01.05

Searle, R.C., 1970. Evidence from gravity anomalies for thinning of the lithosphere beneath the rift valley in Kenya. Geophys. J. R. Astron. Soc. 13–31.

Simiyu, S.., Keller, G.R., 2001. An integrated geophysical analysis of the upper crust of the southern Kenya rift. Geophys. J. Int. 147, 543–561. https://doi.org/10.1046/j.0956-540x.2001.01542.x

Simiyu, S.M., 2000. Geothermal reservoir characterization: Application of microseismicity and seismic wave properties at Olkaria, Kenya rift. J. Geophys. Res. 105, 13,779-13,795,.

Simiyu, S.M., 1999. Seismic Velocity Analysis in the Olkaria Geothermal Field. Twenty Fourth Work. Geotherm. Reserv. Eng. Stanford Univ. California, January 25-27, 1999 SGP-TR-162.

Simiyu, S.M., Keller, G.R., 1997. An integrated analysis of lithospheric structure across the East African plateau based on gravity anomalies and recent seismic studies. Tectonophysics 278, 291–313. https://doi.org/10.1016/S0040-1951(97)00109-1

Skilling, I.P., 1993. Incremental caldera collapse of Suswa volcano, Gregory Rift Valley, Kenya. J. Geol. Soc. London. 150, 885–896. https://doi.org/10.1144/gsjgs.150.5.0885

Sowerbutts, W.T.C., 1969. Crustal Structure of the East African Plateau and Rift Valleys from Gravity Measurements. Nature 223, 143–146. https://doi.org/10.1038/223143a0

Soyer, W., Mackie, R., Hallinan, S., Pavesi, A., Multi-physics, C.G.G., Nordquist, G., Suminar, A., Intani, R., Nelson, C., 2017. Multi-Physics Imaging of the Darajat Field 41.

Strecker, M.R., Blisniuk, P.M., Eisbacher, G.H., 1990. Rotation of extension direction in the central Kenya Rift. Geology 18, 299–302. https://doi.org/https://doi.org/10.1130/0091-7613(1990)018<0299:ROEDIT>2.3.CO;2

Svanbjornsson, A., Matthiasson, J., Frimannsson, H., Arnosson, S., Bjornsson, S., Stefanson, V., Saemundsson, K., 1983. Overview of geothermal development at Olkaria in Kenya. Geotherm. Resour. Counc. Trans. 65–72.

Swain, C.J., 1992. The Kenya rift axial gravity high: a re-interpretation. Tectonophysics 204, 59–70.

Vozoff, K., 1991. The Magnetotelluric Method, in Electromagnetic method in applied geophysics, 2B, edited by M.N. Nabighian, soc Explor. Geophys, Tulsa Okla, 641-711.

Vozoff, K., 1972. The magnetotelluric method in the exploration of sedimentary basins. Geophysics 37, 98–141, 36.

Wamalwa, A.M., Serpa, L.F., 2013. The investigation of the geothermal potential at the Silali volcano, Northern Kenya Rift, using electromagnetic data. Geothermics 47, 89–96. https://doi.org/10.1016/j.geothermics.2013.02.001

WinGLink, 2005. WinGLink User’s Guide, 2nd edn, WesternGeco. [Formerly Geosystem Srl.].

Appendix A1: Magnetotelluric (MT) data

Table A: Magnetotelluric data

Station	Easting	Northing	Elevation		Station	Easting	Northing	Elevation
150p	171.916	105.891	863		pak55r	185.774	99.563	1300
korMT01	189.543	95.284	1115		pak562	195.003	113.289	901
kormt01r	189.832	93.632	1153		pak564	198.223	112.423	1068
korMT02	187.069	97.315	1182		pak565	200.073	111.96	1048
korMT03	189.882	92.64	1180		pak57	190.477	99.203	1327
korp	191.46	93.085	1163		pak58	191.91	99.312	1322
krmt203	177.498	93.448	898		pak59	194.178	99.455	1209
krmt204	179.568	92.77	892		pak61	182.421	101.124	1065
krmt208	187.083	91.256	1163		pak62	183.671	100.865	1160
krmt210	188.689	90.283	1277		pak63	185.689	100.955	1430
pak105b	182.897	108.037	886		pak67	192.515	101.039	1340
pak106r	184.194	108.528	892		pak68	194.211	101.059	1297
pak107	187.624	99.729	1460		pak70	183.986	103.041	1089
pak150	172.696	105.725	862		pak73	192.915	102.293	1310
pak152	173.55	105.515	858		pak75	180.808	103.867	937
pak153	173.819	105.988	862		pak76	182.482	103.974	1001
pak156	175.101	99.663	886		pak79r	186.942	104.17	1243
pak157b	175.248	100.896	880		pak80	188.786	104.153	1333
pak158	174.6	102.818	872		pak82	191.913	103.502	1217
pak159	177.995	104.002	899		pak84	194.38	104.016	1228
pak162	177.679	99.707	893		pak85	180.939	105.389	910
pak171	173.72	93.749	904		pak87	184.164	105.789	975
pak172	175.688	94.369	885		pak88	185.454	105.53	1090
pak180	186.453	111.834	847		pak92	191.494	105.562	1029
pak189	186.211	110.69	859		pak93	193.06	106.317	985
pak27	180.758	95.463	888		pak94r	194.848	105.442	1108
pak29	184.007	95.165	1029		pak95	180.805	10107.12	872
pak31	186.897	94.874	1104		pak98	185.728	107.365	964
pak32	188.358	95.463	1068		pak99	187.132	106.985	1023
pak33	191.545	94.972	1157		pakcrt01	186.816	102.041	1517
pak34	192.795	95.042	1166		pakcrt2r	186.976	102.229	1490
pak35	194.382	94.89	1184		pakcrt3	188.648	100.93	1560
pak36	181.087	96.382	923		pakmt00	191.156	88.903	1162
pak37	183.002	96.343	969		pakmt01	181.101	102.883	961
pak38	184.757	96.222	1098		pakmt03	187.132	98.452	1265
pak39	186.039	96.934	1154		pakmt05	187.908	101.279	1659
pak400	180.794	108.703	872		pakmt06	186.268	101.957	1518

Station	Easting	Northing	Elevation		Station	Easting	Northing	Elevation
pak404	179.685	104.664	907		pakmt07	186.362	103.617	1429
pak40	188.405	96.474	1090		pakmt08	187.228	102.479	1500
pak41	189.764	96.35	1139		pakmt09	188.342	102.693	1462
pak43a	181.122	98.023	928		pakmt12	196.107	101.457	1235
pak43	194.486	96.439	1186		pakmt14	182.861	97.963	984
pak43r	193.968	95.618	1179		pakmt15	181.662	107.371	891
pak45	184.746	98.205	1147		pakmt16	189.064	112.23	860
pak46	185.909	98.004	1208		pakmt17	192.776	111.059	882
pak48	189.994	97.924	1250		pakmt18	189.404	108.11	956
pak50rr	193.18	96.986	1189		pakmt20	180.364	104.798	906
pak52	181.067	99.277	949		pakmt21	180.83	100.529	947
pak53	182.42	99.547	998		pakmt23	185.14	96.635	1117
pakmt24	188.652	105.51	1092		slmt149	191.247	132.898	1148
pakmt25	190.744	104.583	1095		slmt153	194.944	132.931	1130
pk139	186.436	98.47	1273		slmt157	192.994	131.925	1160
pk154c	177.285	105.177	881		slmt164	193.949	131.039	1192
pk154	178.13	105.828	888		slmt166	195.731	131.36	1131
pk155	181.825	106.077	912		slmt167	197.678	131.548	1042
pk401	180.396	104.792	903		slmt169	194.947	129.993	1172
pk47a	187.708	96.956	1154		slmt16	192.838	127.462	1017
pk492	188.354	102.189	1528		slmt170	195.844	129.872	1161
pk493	189.189	102.001	1572		slmt171	197.654	129.873	1071
pk497	177.012	100.999	891		slmt172	193.993	129.062	1262
pk501	179.542	99.66	916		slmt173	195.052	128.938	1208
pk508r	178.229	97.899	890		slmt175	197.289	129.041	1080
pk510	196.706	98.666	1221		slmt177	194.893	128.238	1187
pk511	198.404	97.982	1231		slmt180	194.162	127.218	1265
pk512	186.27	99.599	1324		slmt182	195.963	127.139	1147
pk518	192.91	95.995	1171		slmt185	194.965	125.861	1127
pk520	198.133	95.754	1218		slmt188	196.991	125.097	1069
pk529	192.005	93.997	1163		slmt192	192.674	124.723	1154
pk533	194.006	91.992	1172		slmt194	191.072	124.703	1182
pk540	187.507	103.819	1301		slmt195	189.689	125.399	1254
pk541	189.193	102.757	1475		slmt197	188.009	125.004	1159
pk543	186.71	101.099	1545		slmt199	185.88	124.911	1081
pk550r	178.497	104.908	896		slmt19	189.757	127.997	1019
pk553	177.952	117.799	784		slmt219	184.203	134.464	933
pk555	180.322	117.68	797		slmt221	186.447	134.557	1022
pk558	187.007	115.433	850		slmt229	195.731	134.289	992
pk559	188.495	114.958	859		slmt239	185.993	117.051	860
pka5	182.31	108.351	873		slmt23	192.495	128.028	1016
slmt289	191.818	114.86	883		slmt241	189.527	117.361	882
slmt01	191.503	126.522	1013		slmt249	191.846	119.031	956
slmt03	192.407	126.632	1016		slmt250	190.024	119.048	928

Station	Easting	Northing	Elevation		Station	Easting	Northing	Elevation
slmt06	191.192	127.463	1001		slmt251	188.115	119.237	919
slmt07	191.99	126.983	1007		slmt252a	186.026	119.043	898
slmt100	187.004	125.974	1220		slmt253	184.739	119.37	891
slmt104	182.936	126.568	977		slmt254	183.921	120.815	878
slmt108	187.073	126.905	1274		slmt255	185.96	120.801	911
slmt110	188.991	126.86	1368		slmt256	188.231	121.146	982
slmt114a	185.605	127.872	1421		slmt257	189.753	120.816	980
slmt115	187.022	127.969	1300		slmt258	192.028	121.567	1020
slmt118	183.786	128.811	1114		slmt25	193.454	128.141	1022
slmt120	186.169	128.879	1319		slmt263	192.01	122.572	1060
slmt128	182.98	130.739	972		slmt264	189.662	122.811	1060
slmt12	190.941	127.501	1000		slmt265	187.858	122.871	1029
slmt130	184.865	130.771	1323		slmt266	186.104	123.1	1017
slmt136	185.983	131.966	1302		slmt267	183.817	122.746	904
slmt138	187.564	132.216	1270		slmt26	188.427	128.932	1036
slmt13	191.319	128.137	1002		slmt273	195.99	123.952	1075
slmt146	188.868	133.251	1214		slmt274	198.162	124.106	1048
slmt288	189.974	115.009	863		kor21	170.153	86.859	968
slmt321	200.87	124.593	970		kor22	171.459	86.987	971
slmt324	199.857	122.851	1021		kor24	178.857	90.127	1013
slmt328	201.55	120.876	1001		kor25	176.169	86.953	1127
slmt330	200.122	118.975	979		kor27	180.102	87.021	1211
slmt331	201.672	118.684	981		kor29	183.172	87.118	1062
slmt332	203.943	119.07	973		kor30a	184.524	82.195	1059
slmt34	191.991	128.594	1009		kor35	174.67	85.697	1125
slmt35	192.471	128.639	1025		kor40	182.438	85.338	1103
slmt37	193.189	128.565	1058		kor41	176.207	84.073	1148
slmt38	188.99	128.526	1026		kor44	171.596	84.574	1007
slmt42	189.928	128.98	1014		kor47	179.438	83.902	1336
slmt44	190.992	129.028	1001		kor49	182.876	84.271	1062
slmt54	190.616	129.822	1015		kor50	183.999	83.945	1037
slmt55	191.092	129.501	1000		kor51	185.478	83.965	1037
slmt59	192.874	129.567	1024		kor56	180.028	82.367	1308
slmt62	188.512	130.008	1043		kor57	182.968	82.215	1071
slmt65	189.616	129.973	1037		kor64	182.249	81.247	1067
slmt69	191.983	129.986	1008		kor78	176.281	91.454	972
slmt71	187.612	130.455	1045		kor80	178.886	91.348	972
slmt75	189.496	130.545	1039		kor82	181.835	91.542	962
slmt76	190.313	130.378	1034		korc	189.47	92.902	1190
slmt79	191.501	130.497	1007		kord	188.758	91.706	1324
slmt81	192.401	130.487	1018		korg	189.895	89.775	1205
slmt88	191.004	130.989	1008		kormt09a	188.69	87.855	1156
slmt91	189.024	131.262	1051		kormt100	174.212	93.9	902
slmt95	191.99	130.948	1015		kormt101	176.344	93.778	893

Station	Easting	Northing	Elevation		Station	Easting	Northing	Elevation
bamt132	179.554	76.563	1011		kormt102	178.448	93.094	930
barmt03	170.487	82.198	1002		kormt104	171.598	95.759	889
bmt101	166.678	74.966	1029		kormt107	187.563	86.887	1060
bmt105	170.45	78.617	993		kormt108	167.158	84.488	997
bmt106a	-169.527	78.602	993		kormt116	178.325	85.99	1343
bmt113	166.671	81.85	999		kormt118	181.008	85.01	1181
bmt114	168.608	82.427	1003		kormt119	177.891	84.102	1311
bmt115	170.539	82.161	997		kormt120	179.555	82.992	1332
bmt119	179.078	81.842	1227		kormt121a	181.235	82.394	1241
bmt120	180.662	81.973	1225		kormt121	181.235	82.394	1241
bmt121	184.519	83.219	1036		kormt122	177.462	81.44	1304
bmt123	180.03	80.178	1183		kormt13a	168.872	95.303	916
bmt124	182.087	78.855	1074		kormt16	179.132	88.316	1192
bmt129r	183.998	77.594	1013		kormt19a	182.981	96.395	970
bmt130	176.916	75.345	998		kormt21a	166.947	92.516	962
bmt24	175.437	79.677	1027		kormt25b	186.195	91.259	1021
bmt7	179.425	78.082	1026		kormt28a	168.854	84.256	988
kor05	180.38	89.926	980		kormt28	173.072	83.804	1052
kor06	181.612	90.285	1000		kormt29a	180.389	93.652	904
kor07	182.889	89.872	1015		kormt31a	191.52	85.216	1132
kor11	171.653	89.948	921		kormt34	173.055	85.609	1054
kor17	180.509	88.54	1070		kormt35a	172.421	86.298	1020
kor18	182.306	88.366	1068		kormt41a	193.407	93.898	1179
kor19	183.185	88.323	1023		kormt42a	189.191	77.84	1125
kormt43a	187.377	80.884	1060		kormt76	173.111	91.392	912
kormt55	178.976	81.848	1231		kormtm	191.3	90.158	1168
kormt60	173.476	81.068	1011		koru	190.475	91.57	1166
kormt66	185.136	81.134	1037					

Appendix A2: TEM data

Table B: Transient electromagnetic data

Station	Easting	Northing	Elevation		Station	Easting	Northing	Elevation
sltemz01	191.693	126.338	950		sltemz22	191.635	127.691	1000
sltemz05	190.090	127.005	997		sltemz239	185.996	117.172	866
sltemz08	192.500	126.750	1023		sltemz23	192.351	127.888	1011
sltemz100	187.008	125.952	1180		sltemz240	187.984	116.981	878
sltemz104	182.940	126.957	1345		sltemz241	189.656	117.066	876
sltemz114	185.584	127.838	1408		sltemz246	198.248	119.112	986
sltemz118	183.720	128.745	1099		sltemz247	198.208	116.999	977
sltemz120	186.336	128.902	1307		sltemz249	191.820	119.063	947
sltemz128	182.924	130.741	970		sltemz250	190.028	119.048	932
sltemz12	191.024	127.551	1000		sltemz251	188.104	119.246	920
sltemz130	184.864	130.774	1276		sltemz252	186.056	119.039	898
sltemz132	184.968	130.430	1277		sltemz253	183.776	119.085	852
sltemz136	185.952	131.932	1120		sltemz254	184.032	120.904	874
sltemz138	187.668	131.916	1102		sltemz255	185.956	120.753	910
sltemz141	183.872	132.961	956		sltemz256	188.264	120.921	979
sltemz144	186.908	132.477	963		sltemz257	189.784	120.816	1044
sltemz146	188.960	132.945	1280		sltemz258	192.003	121.532	1020
sltemz149	191.280	132.804	1145		sltemz25	193.448	128.150	1023
sltemz14	192.020	127.019	1008		sltemz262	192.824	122.618	1072
sltemz152	132.940	194.067	1132		sltemz263	192.004	122.564	1055
sltemz153	195.048	133.037	1106		sltemz266	185.960	122.981	1007
sltemz157	193.004	132.010	1155		sltemz267	183.820	122.756	901
sltemz160	190.108	131.759	1176		sltemz26	188.428	128.932	1036
sltemz161	195.340	132.000	1112		sltemz273	195.984	123.958	1067
sltemz164	193.948	131.038	1192		sltemz274	198.320	124.108	1045
sltemz166	195.728	131.357	1133		sltemz287	185.928	114.832	849
sltemz167	197.676	131.549	1152		sltemz288	188.103	115.002	868
sltemz169	194.944	129.995	1154		sltemz289	190.022	115.005	874
sltemz16	192.896	127.528	1011		sltemz290	191.816	114.859	881
sltemz170	195.836	129.885	1154		sltemz291	195.332	115.335	917
sltemz171	197.656	129.870	1140		sltemz292X	193.686	115.189	897
sltemz172	194.084	128.981	1220		sltemz293	197.628	115.447	974
sltemz173	195.052	128.925	1215		sltemz294	179.648	116.905	796
sltemz175	197.044	129.036	1153		sltemz295	179.632	114.572	801
sltemz176	194.272	128.128	1221		sltemz297	179.824	119.040	794
sltemz177	194.984	127.990	1181		sltemz299	180.024	120.958	795
sltemz178	195.864	129.320	1179		sltemz300	179.828	122.953	815
sltemz179	198.012	126.605	1054		sltemz315E	200.236	128.276	1010
sltemz180	194.168	127.217	1259		sltemz318	200.302	126.543	995

Station	Easting	Northing	Elevation		Station	Easting	Northing	Elevation
sltemz182	195.928	126.975	1151		sltemz321	200.792	124.686	980
sltemz187	199.412	125.153	1018		sltemz324	200.048	122.929	1019
sltemz188	196.992	125.097	1000		sltemz328	201.268	120.958	999
sltemz190	194.872	125.950	1114		sltemz330	200.124	118.972	993
sltemz192	193.256	125.100	1154		sltemz331	201.680	118.684	986
sltemz195	189.692	125.465	1245		sltemz332	203.948	119.068	976
sltemz19	189.912	127.974	1043		sltemz333	199.924	117.011	980
sltemz219	184.492	134.278	918		sltemz334	202.028	117.066	985
sltemz221	186.564	134.332	1059		sltemz335	203.564	117.062	995
sltemz229	195.144	134.499	959		sltemz336	199.980	114.964	986
sltemz337	202.007	115.049	999		kort101	176.340	93.782	896
sltemz338	203.701	114.477	1019		kort102	178.412	93.038	929
sltemz34	191.782	128.554	1000		kort103	169.508	92.882	909
sltemz358	180.064	124.776	802		kort104	171.600	95.759	889
sltemz35	192.400	128.666	1000		kort105	185.880	83.882	1044
sltemz360	199.832	130.015	994		kort106	189.496	84.026	1121
sltemz361	199.744	131.504	988		kort107	187.560	86.890	1057
sltemz37	193.144	128.562	1057		kort108	167.160	84.492	983
sltemz38	189.044	128.532	1022		kort114	189.632	90.296	1237
sltemz42	190.048	129.131	1019		kort116	178.332	85.989	1345
sltemz44	190.992	129.028	1001		kort119	177.888	84.106	1308
sltemz49	189.056	129.450	1033		kort120	179.556	82.992	1330
sltemz55	191.084	129.337	1003		kort121	181.232	82.394	1239
sltemz56	191.465	129.670	999		kort122	177.448	81.457	1311
sltemz59	192.736	129.509	1017		kort15	173.996	87.113	1038
sltemz62	188.545	129.993	1039		kort16a	179.220	88.000	1194
sltemz65	189.620	130.019	1034		kort16	167.656	91.980	944
sltemz66	190.548	129.845	1018		kort19	187.240	88.524	1095
sltemz69	191.988	129.987	1011		kort22a	171.548	86.680	980
sltemz71	187.640	130.474	1013		kort23a	173.224	86.855	1061
sltemz75	189.496	130.578	1000		kort26	186.484	90.894	1024
sltemz77	190.320	130.715	1039		kort29	184.088	94.854	1028
sltemz79	191.508	130.503	1023		kort36a	176.132	84.384	1150
sltemz81	192.192	130.454	1012		kort47a	179.528	83.591	1339
sltemz88	191.004	130.993	1012		kort48a	181.161	83.727	1346
sltemz91	189.112	131.157	989		kort55a	179.064	81.543	1217
sltemz95	191.964	130.934	1016		kort56a	180.124	82.058	1270
bar03	170.480	82.264	1008		kort60a	173.476	80.913	992
bar28	184.436	83.011	1082		kort62a	176.856	79.732	1105
batem36	173.744	68.576	1072		kort76a	173.204	91.080	925
batemZ65	168.152	60.368	996		kort78a	176.368	91.146	998
kor04	177.132	89.939	1000		kort80a	178.956	91.049	991
kor05	180.172	90.122	974		kort82a	181.928	91.232	1001
kor06	181.368	89.997	1055		kortc	189.416	92.664	1169

Station	Easting	Northing	Elevation		Station	Easting	Northing	Elevation
kor07	182.804	89.793	1019		kortd	188.816	91.440	1316
kor115	174.156	88.440	974		kortf	188.572	89.504	1218
kor117	181.176	85.666	1136		kortg	190.012	89.541	1204
kor17	180.292	88.411	1095		kortm	194.472	94.582	1047
kor18	182.148	88.532	1062		kortp	191.520	92.764	1164
kor19	183.144	88.622	1039		korts	190.520	93.417	1187
kor27	180.100	86.944	1238		korzd	188.596	91.306	1324
kor29	183.012	86.886	1062		korzf	188.440	90.010	1254
kor40	182.444	85.563	1102		korzk	189.540	87.337	1125
kor49	182.708	84.113	1079		korzl	191.436	88.624	1131
kor50	183.944	83.967	1035		korzm	191.240	90.172	1168
kor57	183.000	82.141	1074		korzu	190.408	91.524	1165
kor64	182.056	80.834	1096		kro01	172.332	88.799	941
kor65	183.392	80.957	1054		kro02	184.352	86.110	1035
kort100	174.208	93.900	904		kro03	178.388	95.174	893
kro04	175.928	89.875	971		korzf	188.440	90.010	1254
kro05	171.624	92.595	903		pak01	190.076	92.518	1174
kro06	189.668	94.979	1120		pak07	189.724	93.948	1155
kro07	187.372	96.949	1185		pak08	191.064	89.205	1155
kro08	190.144	92.178	1188		pak09	189.554	87.866	1134
kro09	188.784	87.800	1157		pak10	181.956	108.703	1078
kro10	168.148	86.145	977		pak11	181.440	108.812	867
kro11	174.828	95.722	888		pak135	182.432	107.950	881
kro12	173.912	92.142	935		pak136	186.528	110.134	882
kro13	169.016	95.064	914		pak141	178.012	103.980	902
kro14	185.420	89.349	1030		pak148	181.844	106.067	915
kro15	186.364	92.221	1015		pakv70	183.932	103.151	1087
kro16	187.948	94.451	1070		pakv76	182.384	103.994	1019
kro17	187.494	85.060	1064		pakv77	184.152	104.262	1130
kro18	192.768	90.484	1181		pakz103	193.064	106.324	989
kro19	182.968	96.335	974		pakz121	190.076	92.518	1174
kro20	184.508	81.486	1061		pakz122	192.792	94.760	1164
kro21	166.940	92.542	970		pakz123	193.080	97.262	1183
kro22	181.048	87.727	1093		pakz124	192.784	96.657	1174
kro23	168.156	89.108	950		pakz125	192.164	95.627	1163
kro24	178.544	89.918	1011		pakz126	193.872	95.921	1181
kro25	176.240	87.829	1138		pakz127	189.724	93.948	1150
kro26	171.884	90.061	936		pakz154	177.284	105.176	881
kro27	171.347	84.848	1015		pakz33	191.324	94.935	1157
kro28	168.752	84.173	995		pakz34	192.848	95.020	1190
kro29	180.428	93.701	909		pakz35	194.488	94.885	1182
kro30	181.160	82.078	1230		pakz404	179.684	104.664	907
kro31	191.568	85.236	1135		pakz41a	189.784	95.879	1132
kro32	176.504	83.655	1145		pakz41	189.768	96.349	1137

Station	Easting	Northing	Elevation		Station	Easting	Northing	Elevation
kro33	176.908	81.939	1270		pakz43	194.580	96.136	1185
kro34	173.444	83.973	1080		pakz48	189.992	97.973	1249
kro35	172.428	86.200	1028		pakz497	177.016	100.999	890
kro36	176.788	86.894	1129		pakz49	191.612	97.000	1226
kro37	181.308	85.119	1145		pakz50	193.166	97.948	1192
kro38	166.556	81.514	1005		pakz510	196.500	98.500	1221
kro39	182.368	92.229	968		pakz511	198.500	98.000	1231
kro40	184.620	77.752	1016		pakz513	176.000	95.999	884
kro41	193.264	93.880	1178		pakz518	192.912	96.000	1171
kro42	189.188	77.837	1131		pakz520	198.080	95.754	1218
kro43	187.416	80.949	1063		pakz529	192.004	94.000	1161
kro44	164.992	87.911	1003		pakz533	194.000	92.000	1172
kor01	189.636	95.070	1111		pakz550	178.496	104.908	893
kor06	189.668	94.980	1055		pakz553	177.952	117.798	784
kor07	187.372	96.950	1185		pakz558	187.008	115.432	857
kor19	182.970	96.336	974		pakz559	188.492	114.953	859
kort29	184.088	94.854	1028		pakz562	195.008	113.289	906
korz203	177.500	93.400	898		pakz57	190.504	99.189	1321
korz204	179.800	92.800	892		pakz59	194.218	99.481	1207
korz208	187.084	91.255	1161		pakz67	192.552	100.980	1336
korz210	188.688	90.282	1272		pakz68	194.180	101.092	1295
pakz73	192.988	102.249	1303		pkz22	180.388	104.819	917
pakz74	194.320	102.504	1293		pkz232	181.048	99.269	949
pakz75	180.808	103.867	937		pkz236	185.704	100.953	1431
pakz80	188.492	104.091	1242		pkz23	188.648	105.518	1091
pakz82	191.556	104.191	1138		pkz242	180.800	103.868	930
pakz84	194.380	104.048	1226		pkz247	182.008	105.871	915
pakz90	188.508	105.571	1110		pkz24	190.744	104.585	1097
pakz92	191.504	105.544	1103		pkz250	180.792	107.110	879
pakz94	194.898	105.520	1094		pkz255	178.227	105.542	882
pkz01	180.176	100.514	930		pkz256	182.364	108.087	878
pkz02	181.648	107.400	894		pkz25	192.708	107.046	988
pkz03	185.436	110.260	876		pkz492	188.180	102.269	1545
pkz04	185.640	107.444	973		pkz493	189.184	102.002	1567
pkz05	181.168	102.604	964		pkz501	179.544	99.654	918
pkz06	179.912	102.057	940		pkz508	177.296	98.300	893
pkz07	187.316	98.238	1275		pkz509	186.140	98.016	1231
pkz08	187.760	99.771	1483		pkz512	186.296	99.690	1321
pkz09	188.020	100.931	1664		pkz514	177.940	96.049	893
pkz10	186.372	101.738	1522		pkz536	186.352	98.723	1273
pkz11	186.420	103.324	1445		pkz539	187.656	104.609	1189
pkz12	187.300	102.500	1505		pkz540	187.504	103.817	1305
pkz13	188.432	102.402	1476		pkz541	189.184	102.725	1476
pkz14	190.184	102.258	1419		pkz543	186.720	101.134	1546

Station	Easting	Northing	Elevation
pkz15	192.520	100.099	1290
pkz16	196.248	101.121	1237
pkz17	193.104	96.783	1191
pkz18	182.980	97.686	992
pkz19	189.104	112.210	869
pkz200	172.056	105.679	866
pkz206	184.196	108.571	894
pkz208	173.936	105.682	863
pkz209	175.200	99.360	886
pkz20	192.800	111.077	891
pkz210	175.332	100.593	884
pkz212	174.696	102.514	877
pkz213	178.064	103.689	895
pkz214	177.772	99.403	889
pkz215	173.884	93.407	905
pkz216	175.768	94.063	891
pkz217	186.536	111.514	853
pkz218	186.296	110.398	874
pkz219	180.464	96.534	913
pkz21	189.416	108.133	972
pkz220	180.664	95.490	904
pkz223	188.396	95.459	1065
pkz224	186.084	96.982	1155
pkz225	180.872	108.377	873
pkz226	188.384	96.445	1081
pkz228	181.120	98.023	1050
pkz564	198.228	112.421	1067
pkz565	200.072	111.960	1044

Appendix A3: MT-TEM Joint inversion

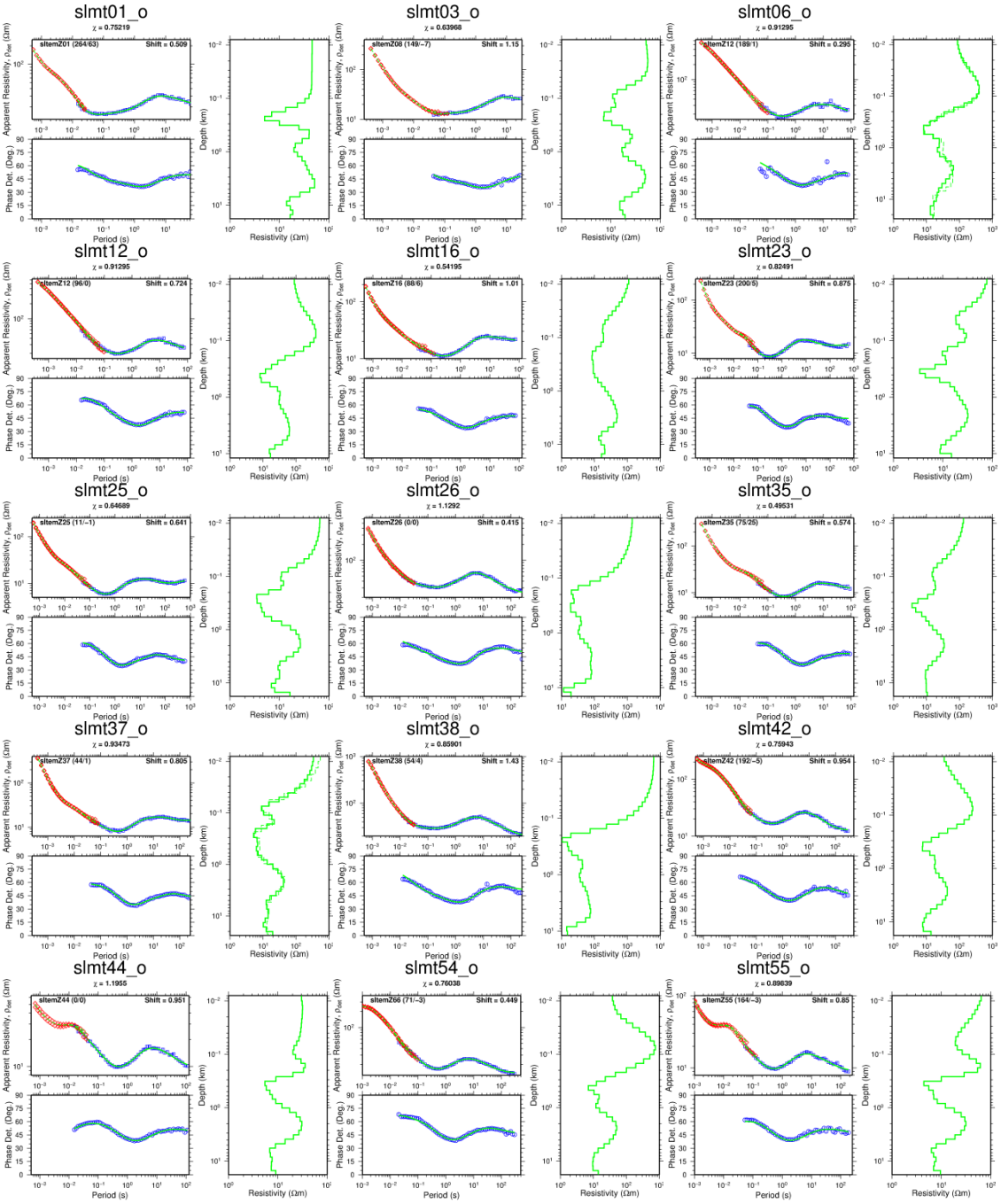

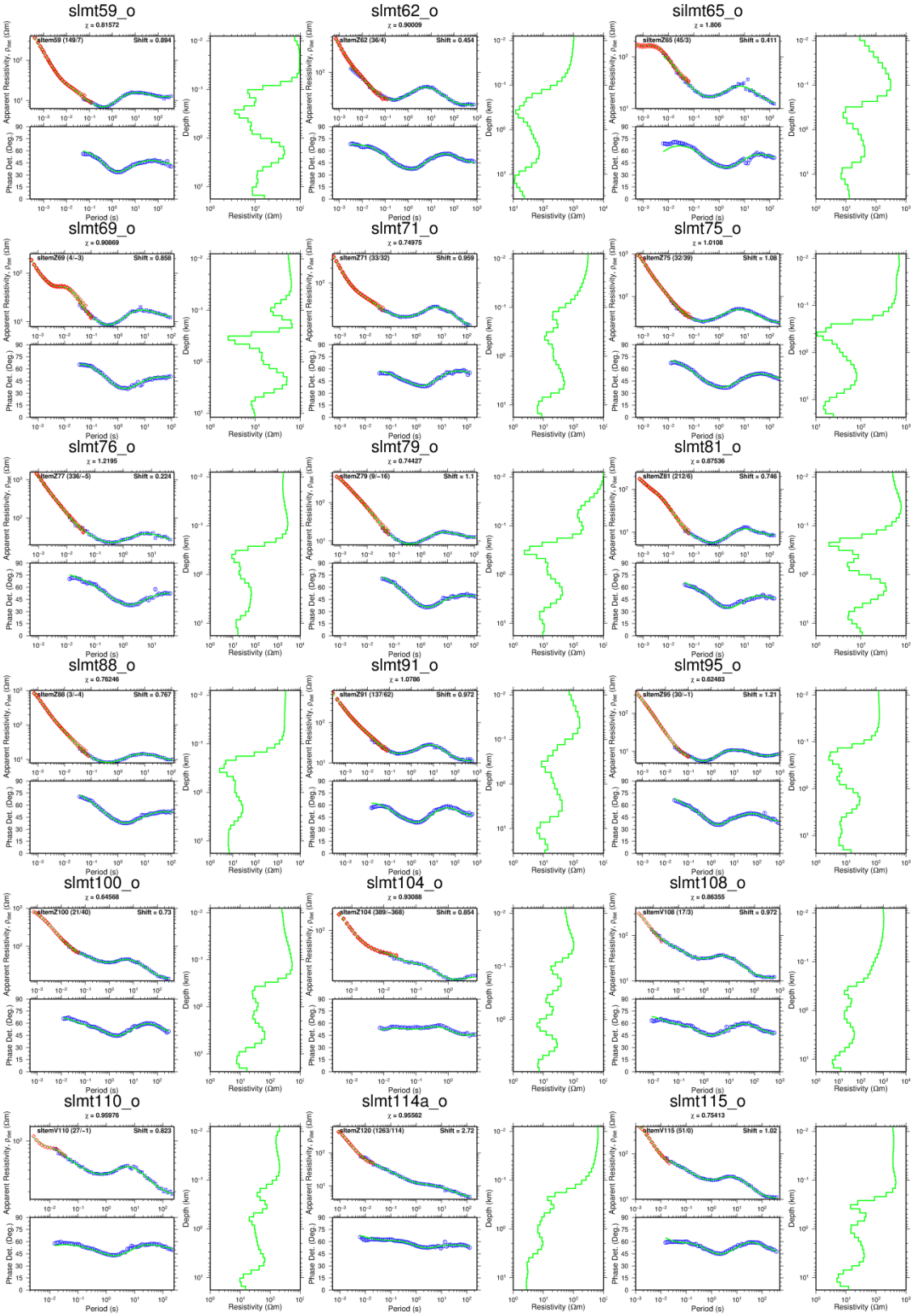
slmt59_o
χ = 0.81572
sItemZ59 (149/7)
Shift = 0.894
slmt62_o
χ = 0.90009
sItemZ62 (36/4)
Shift = 0.454
silmt65_o
χ = 1.806
sItemZ55 (45/3)
Shift = 0.411
slmt69_o
χ = 0.90869
sItemZ69 (4/−3)
Shift = 0.858
slmt71_o
χ = 0.74975
sItemZ71 (33/32)
Shift = 0.959
slmt75_o
χ = 1.0108
sItemZ75 (32/39)
Shift = 1.08
slmt76_o
χ = 1.2195
sItemZ77 (336/−5)
Shift = 0.224
slmt79_o
χ = 0.74427
sItemZ79 (9/−16)
Shift = 1.1
slmt81_o
χ = 0.87536
sItemZ81 (212/6)
Shift = 0.746
slmt88_o
χ = 0.76246
sItemZ88 (3/−4)
Shift = 0.767
slmt91_o
χ = 1.0786
sItemZ91 (137/62)
Shift = 0.972
slmt95_o
χ = 0.62483
sItemZ95 (30/−1)
Shift = 1.21
slmt100_o
χ = 0.64568
sItemZ100 (21/40)
Shift = 0.73
slmt104_o
χ = 0.93088
sItemZ104 (389/−368)
Shift = 0.854
slmt108_o
χ = 0.86355
sItemV108 (17/3)
Shift = 0.972
slmt110_o
χ = 0.95976
sItemV110 (27/−1)
Shift = 0.823
slmt114a_o
χ = 0.95562
sItemZ120 (1263/114)
Shift = 2.72
slmt115_o
χ = 0.75413
sItemV115 (51/0)
Shift = 1.02
Apparent Resistivity, ρapp (Ωm)
Phase Det. (Deg.)
Period (s)
Depth (km)
Resistivity (Ωm)

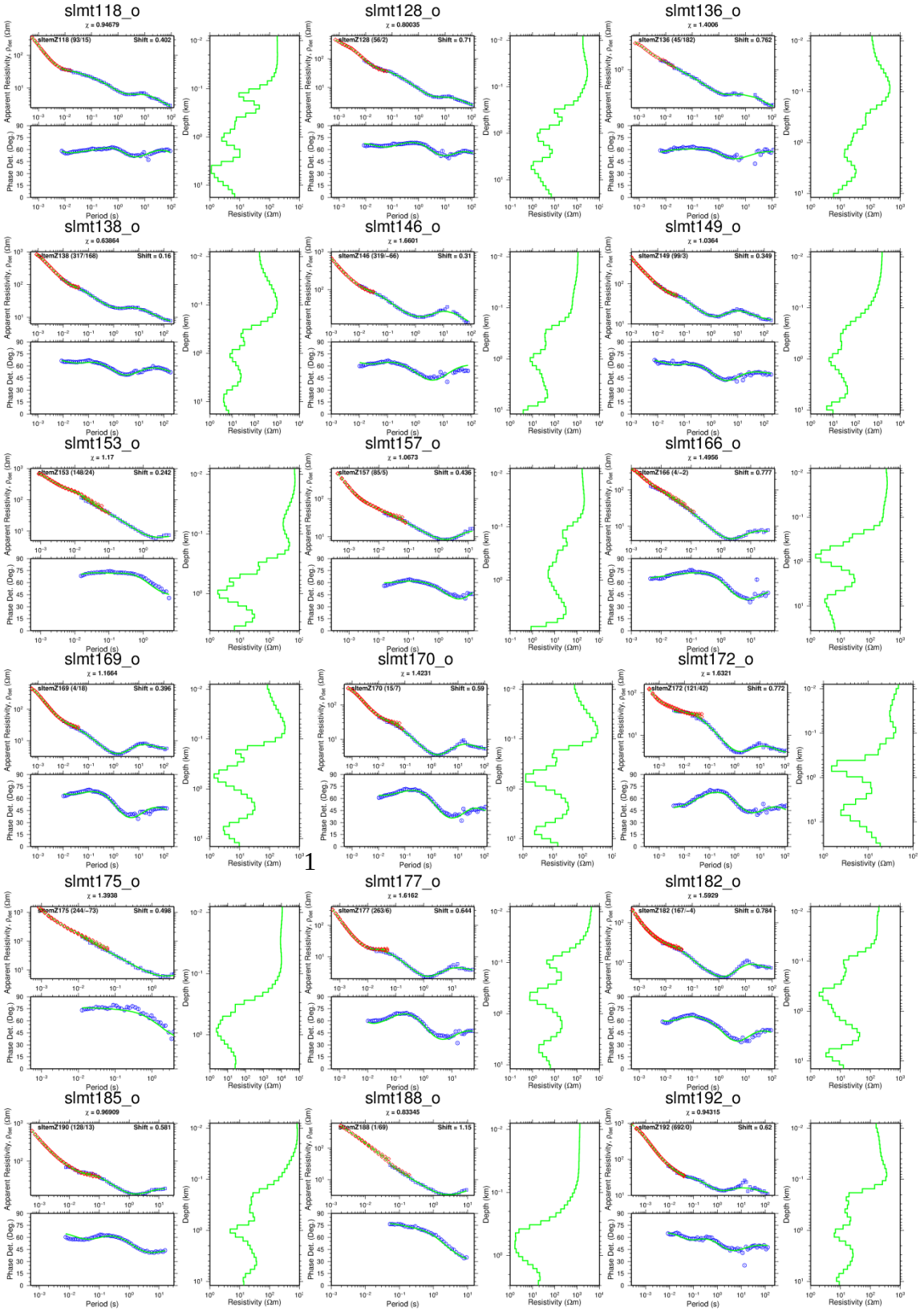
slmt118_o
χ = 0.94679
slmt128_o
χ = 0.80035
slmt136_o
χ = 1.4006
slmt138_o
χ = 0.63864
slmt146_o
χ = 1.6601
slmt149_o
χ = 1.0364
slmt153_o
χ = 1.17
slmt157_o
χ = 1.0673
slmt166_o
χ = 1.4956
slmt169_o
χ = 1.1664
slmt170_o
χ = 1.4231
slmt172_o
χ = 1.6321
slmt175_o
χ = 1.3938
slmt177_o
χ = 1.6162
slmt182_o
χ = 1.5929
slmt185_o
χ = 0.96909
slmt188_o
χ = 0.83345
slmt192_o
χ = 0.94315
Apparent Resistivity, ρapp (Ωm)
Phase Det. (Deg.)
Period (s)
Depth (km)
Resistivity (Ωm)

1

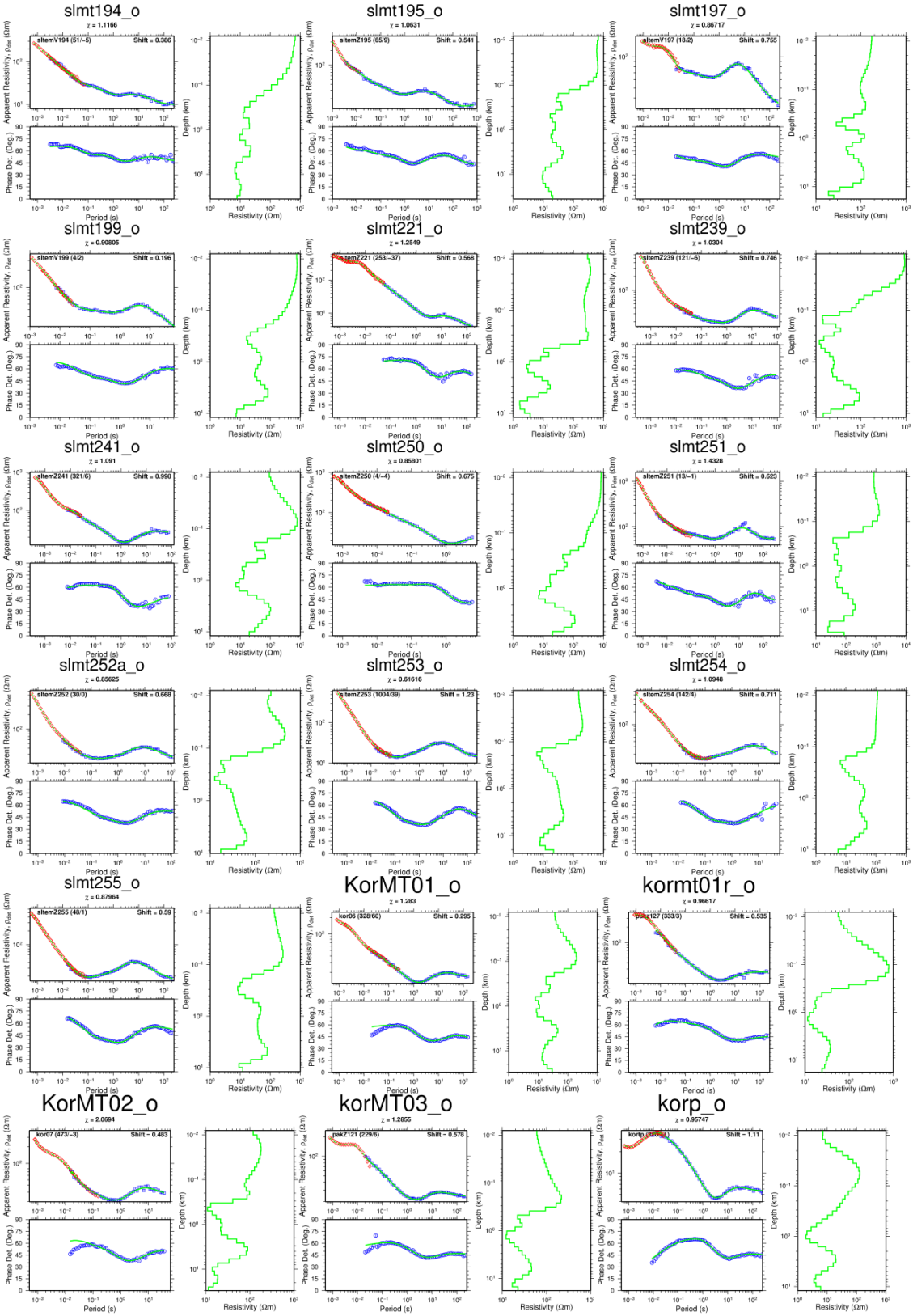
slmt194_o
slmt195_o
slmt197_o
slmt199_o
slmt221_o
slmt239_o
slmt241_o
slmt250_o
slmt251_o
slmt252a_o
slmt253_o
slmt254_o
slmt255_o
KorMT01_o
kormt01r_o
KorMT02_o
korMT03_o
korp_o
Apparent Resistivity, ρapp (Ωm)
Phase Det. (Deg.)
Period (s)
Depth (km)
Resistivity (Ωm)

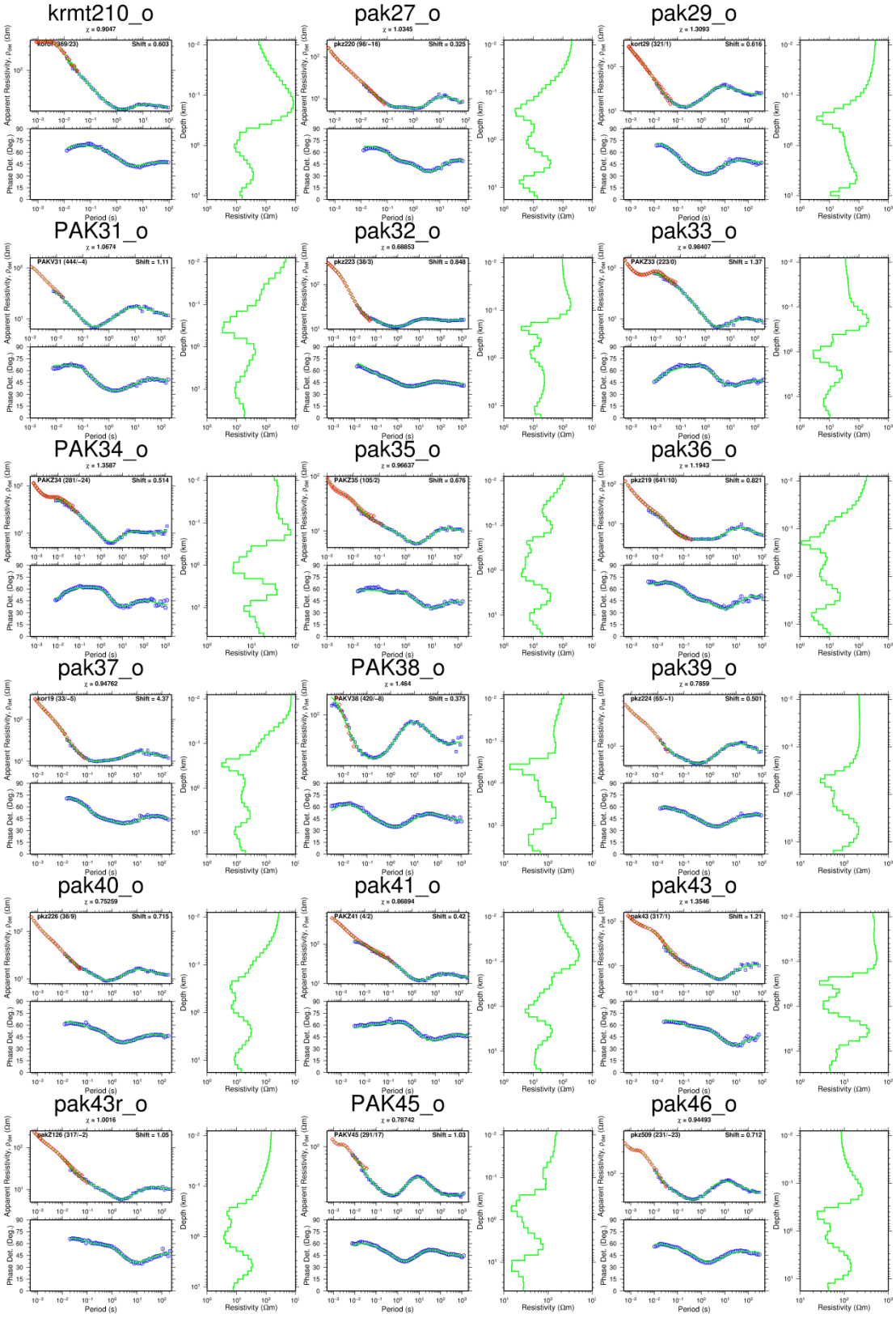
krmt210_o
χ = 0.9047
kor07 (369/23)
Shift = 0.603
pak27_o
χ = 1.0345
pk2220 (98/–16)
Shift = 0.325
pak29_o
χ = 1.3093
kor29 (321/1)
Shift = 0.616
PAK31_o
χ = 1.0674
PAKV31 (444/–4)
Shift = 1.11
pak32_o
χ = 0.68853
pk2223 (38/3)
Shift = 0.848
pak33_o
χ = 0.98407
PAKZ33 (223/0)
Shift = 1.37
PAK34_o
χ = 1.3587
PAKZ34 (281/–24)
Shift = 0.514
pak35_o
χ = 0.96637
PAKZ35 (105/2)
Shift = 0.676
pak36_o
χ = 1.1943
pk2219 (641/10)
Shift = 0.821
pak37_o
χ = 0.94762
kor19 (33/–5)
Shift = 4.37
PAK38_o
χ = 1.464
PAKV38 (420/–8)
Shift = 0.375
pak39_o
χ = 0.7859
pk2224 (65/–1)
Shift = 0.501
pak40_o
χ = 0.75259
pk2226 (36/9)
Shift = 0.715
pak41_o
χ = 0.86894
PAKZ41 (4/2)
Shift = 0.42
pak43_o
χ = 1.3546
pak43 (317/1)
Shift = 1.21
pak43r_o
χ = 1.0016
pakZ126 (317/–2)
Shift = 1.05
PAK45_o
χ = 0.78742
PAKV45 (291/17)
Shift = 1.03
pak46_o
χ = 0.94493
pkz509 (231/–23)
Shift = 0.712
Apparent Resistivity, ρapp (Ωm)
Phase Det. (Deg.)
Period (s)
Depth (km)
Resistivity (Ωm)

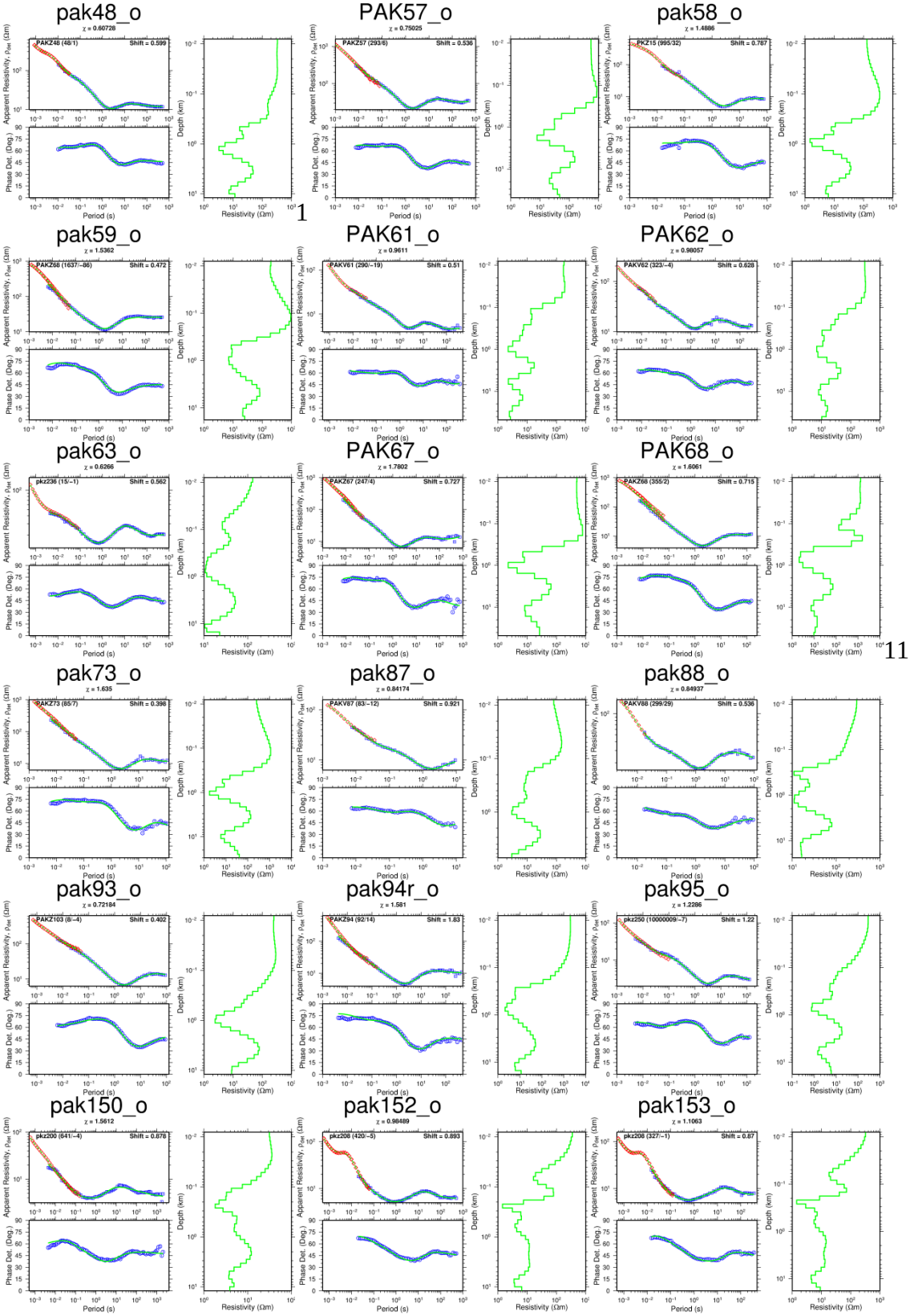
pak48_o
PAK57_o
pak58_o
pak59_o
PAK61_o
PAK62_o
pak63_o
PAK67_o
PAK68_o
pak73_o
pak87_o
pak88_o
pak93_o
pak94r_o
pak95_o
pak150_o
pak152_o
pak153_o
Apparent Resistivity, ρapp (Ωm)
Phase Det. (Deg.)
Period (s)
Depth (km)
Resistivity (Ωm)

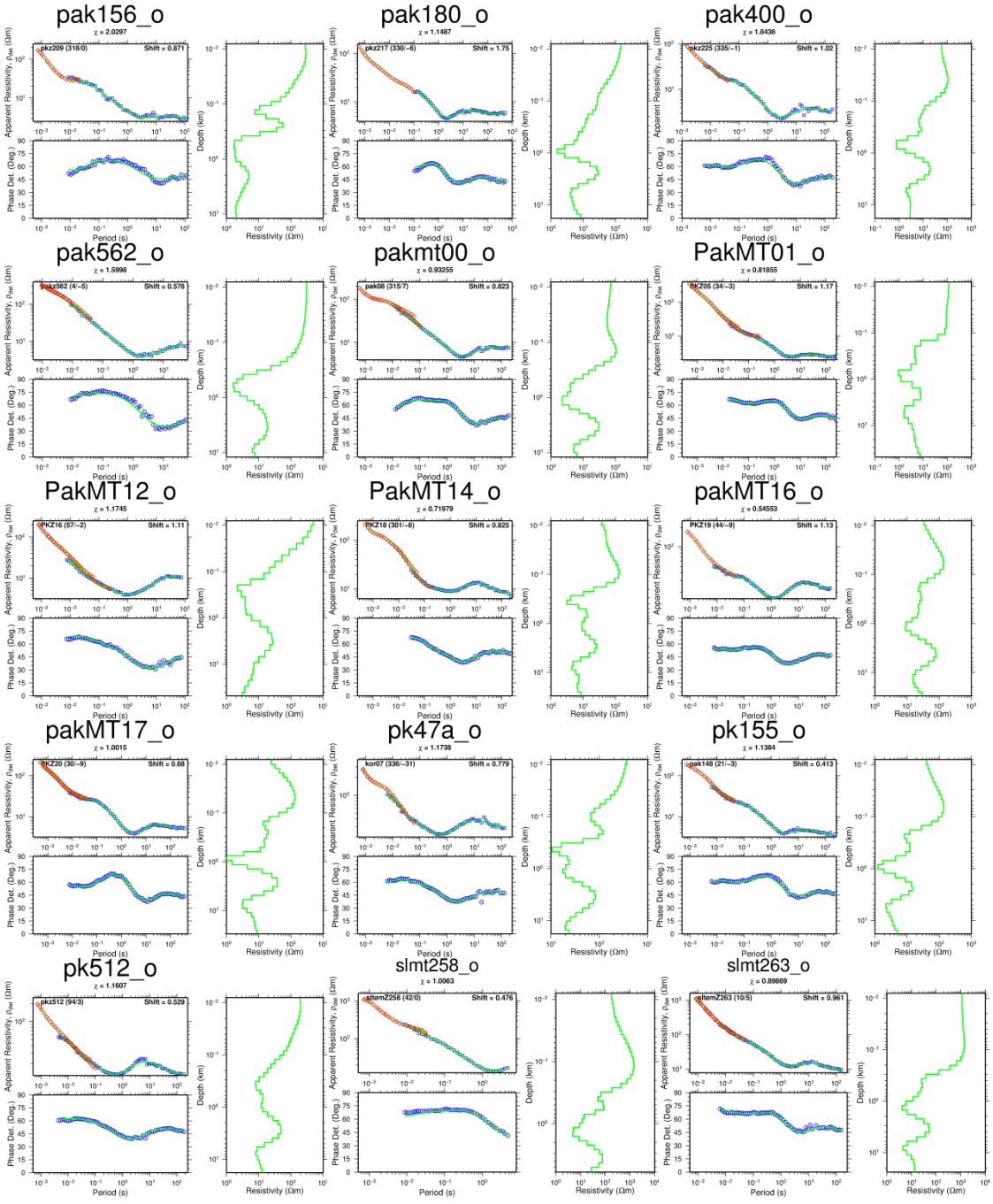
pak156_o
χ = 2.0297
pkz209 (318/0)
Shift = 0.871
pak180_o
χ = 1.1487
pkz217 (330/−6)
Shift = 1.75
pak400_o
χ = 1.8436
pkz225 (335/−1)
Shift = 1.02
pak562_o
χ = 1.5998
pkz562 (4/−5)
Shift = 0.576
pakmt00_o
χ = 0.93255
pak08 (315/7)
Shift = 0.823
PakMT01_o
χ = 0.81855
PKZ05 (34/−3)
Shift = 1.17
PakMT12_o
χ = 1.1745
PKZ16 (57/−2)
Shift = 1.11
PakMT14_o
χ = 0.71979
PKZ18 (301/−6)
Shift = 0.825
pakMT16_o
χ = 0.54553
PKZ19 (44/−9)
Shift = 1.13
pakMT17_o
χ = 1.0015
PKZ20 (30/−9)
Shift = 0.68
pk47a_o
χ = 1.1738
kor07 (336/−31)
Shift = 0.779
pk155_o
χ = 1.1384
pak148 (21/−3)
Shift = 0.413
pk512_o
χ = 1.1607
pkz512 (94/3)
Shift = 0.529
slmt258_o
χ = 1.0063
slitemZ258 (42/0)
Shift = 0.476
slmt263_o
χ = 0.89869
slitemZ263 (10/5)
Shift = 0.961
Apparent Resistivity, ρapp (Ωm)
Phase Det. (Deg.)
Period (s)
Depth (km)
Resistivity (Ωm)

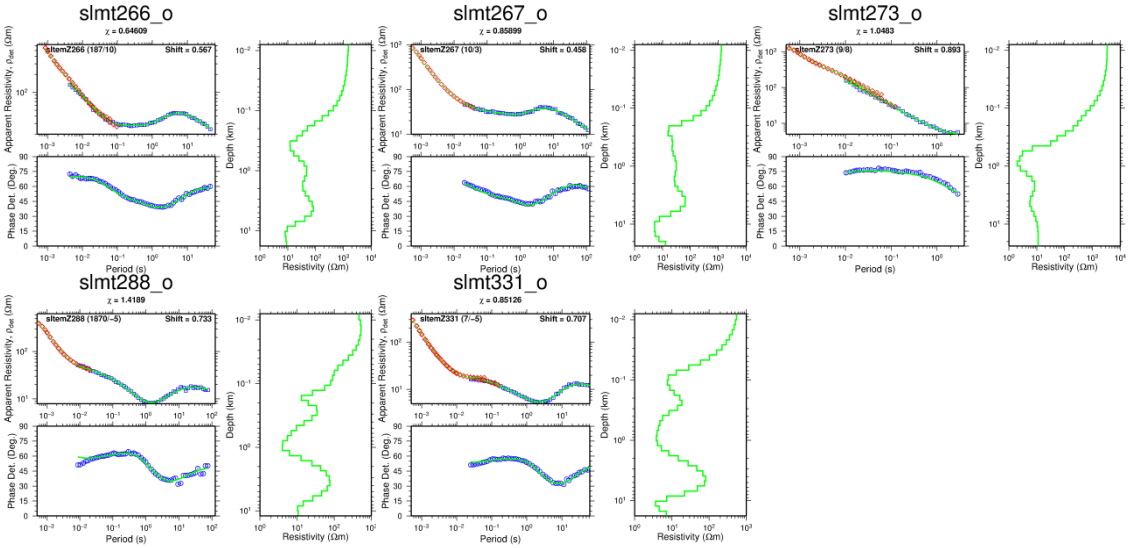
slmt266_o
χ = 0.64609
slmt267_o
χ = 0.85899
slmt273_o
χ = 1.0483
slmt288_o
χ = 1.4189
slmt331_o
χ = 0.85126
Apparent Resistivity, ρapp (Ωm)
Phase Det. (Deg.)
Period (s)
Depth (km)
Resistivity (Ωm)

Appendix B1: Gravity data

Table C: Reduced gravity data

Gravity station	Latitude	Longitude	Elevation	Gravity value	Terrain correction	FAA	Bouguer
K01	0.7157	36.0323	986.4	977693.23	0.36	-35.1	-125.28
K02	0.7251	36.0350	984.4	977693.10	0.37	-35.9	-125.86
K03	0.7348	36.0355	999.9	977690.57	0.37	-33.7	-125.04
K04	0.7441	36.0326	993.4	977691.16	0.33	-35.1	-125.93
K05	0.7536	36.0302	978.3	977693.40	0.35	-37.5	-126.97
K06	0.7579	36.0285	973.2	977694.24	0.35	-38.3	-127.24
K07	0.7656	36.0315	974.3	977694.33	0.33	-37.9	-126.94
K09	0.7809	36.0402	966.9	977696.48	0.37	-38.0	-126.39
K10	0.7857	36.0478	951.8	977699.19	0.44	-40.0	-126.90
K11	0.7923	36.0501	936.8	977701.88	0.49	-42.0	-127.42
K12	0.7986	36.0558	925.1	977704.48	0.50	-43.0	-127.37
K13	0.8057	36.0611	918.7	977707.33	0.48	-42.1	-125.94
K14	0.8141	36.0651	911.7	977711.17	0.45	-40.5	-123.66
K15	0.8189	36.0715	915.9	977712.80	0.44	-37.6	-121.15
K16	0.8350	36.0784	906.6	977715.61	0.40	-37.7	-120.44
K17	0.8440	36.0905	878.8	977723.29	0.49	-38.6	-118.72
K18	0.8569	36.0982	874.6	977725.83	0.47	-37.4	-117.14
K19	0.8589	36.1044	874.6	977728.00	0.47	-35.2	-114.97
K20	0.8482	36.1129	883.3	977727.04	0.53	-33.5	-113.97
K21	0.8397	36.1148	899.7	977724.53	0.55	-30.9	-112.88
K22	0.8321	36.1111	906.5	977722.76	0.60	-30.5	-113.10
K23	0.8241	36.1075	919.4	977718.08	0.73	-31.2	-114.84
K24	0.8150	36.1064	958	977711.05	0.65	-26.3	-113.56
K25	0.8072	36.1037	982.5	977704.29	0.75	-25.5	-114.89
K26	0.7992	36.1068	1060.6	977689.09	0.90	-16.6	-112.99
K27	0.7901	36.1111	1125.8	977675.03	1.12	-10.5	-112.68
K28	0.7829	36.1116	1221.8	977654.51	1.32	-1.4	-112.19
K29	0.7738	36.1108	1328.6	977630.95	1.72	8.0	-112.18
K30	0.7662	36.1150	1360.4	977620.93	1.81	7.8	-115.20
K31	0.7135	36.0320	983.8	977693.33	0.37	-35.8	-125.72
K32	0.7262	36.0442	998.5	977692.16	0.38	-32.5	-123.73
K33	0.7338	36.0516	1047.2	977683.10	0.60	-26.5	-122.03
K34	0.7394	36.0549	1076.9	977677.63	0.69	-22.9	-120.99
K35	0.7471	36.0578	1064.3	977679.72	1.02	-24.7	-121.32
K36	0.7411	36.0630	1055.7	977683.22	0.48	-23.8	-120.21
K37	0.7407	36.0715	1117.5	977671.89	0.71	-16.1	-117.91

Gravity station	Latitude	Longitude	Elevation	Gravity value	Terrain correction	FAA	Bouguer
K38	0.7376	36.0766	1127.9	977669.28	0.72	-15.5	-118.25
K39	0.7378	36.0838	1169.2	977661.50	0.96	-10.5	-116.84
K40	0.7311	36.0840	1111.3	977672.04	1.32	-17.8	-118.48
K41	0.7224	36.0838	1026.4	977692.48	0.68	-23.6	-117.06
K42	0.7138	36.0845	1014.7	977686.10	0.55	-33.5	-126.07
K43	0.7079	36.0907	1036.3	977683.53	0.49	-29.4	-124.01
K45	0.6935	36.0965	1094.7	977675.42	0.76	-19.5	-119.17
K46	0.7010	36.1003	1078.7	977682.73	0.47	-17.1	-115.63
K47	0.7051	36.1073	1064.1	977688.76	0.50	-15.6	-112.74
K48	0.7040	36.1159	1029.2	977691.04	0.49	-24.1	-118.04
K49	0.7026	36.1247	1017.7	977688.16	0.54	-30.5	-123.35
K50	0.7028	36.1316	1027.2	977686.33	0.60	-29.4	-123.07
K51	0.7089	36.1368	1042.6	977680.97	0.60	-30.0	-125.10
K53	0.7181	36.1467	1066.8	977686.34	0.58	-17.2	-114.52
K54	0.7264	36.1504	1056.2	977686.98	0.63	-19.9	-116.16
K55	0.7322	36.1595	1050.7	977685.92	0.57	-22.6	-118.48
K56	0.7392	36.1646	1054.3	977683.82	0.54	-23.6	-119.84
K57	0.7394	36.1587	1067.9	977684.38	0.56	-18.9	-116.32
K58	0.7395	36.1543	1069	977684.09	0.62	-18.8	-116.31
K59	0.7395	36.1504	1075.3	977685.81	0.77	-15.2	-113.08
K60	0.7515	36.1776	1039.9	977683.05	0.53	-28.9	-123.78
K64	0.7584	36.1246	1378.4	977615.25	2.12	7.7	-116.65
K65	0.7600	36.1269	1436	977601.73	3.86	12.0	-115.95
K67	0.7520	36.1218	1324.4	977630.02	1.15	5.8	-114.54
K68	0.7478	36.1231	1326.3	977629.80	1.30	6.2	-114.19
K69	0.7424	36.1226	1327.8	977629.28	1.65	6.2	-114.02
K70	0.7398	36.1225	1299.7	977634.58	1.38	2.8	-115.07
K71	0.7368	36.1271	1246.6	977647.32	1.14	-0.8	-114.07
K72	0.7379	36.1314	1215.9	977654.05	1.10	-3.6	-114.04
K73	0.7394	36.1355	1214.6	977654.79	0.97	-3.2	-113.71
K74	0.7390	36.1386	1197.6	977658.19	1.04	-5.1	-113.92
K75	0.7393	36.1422	1171.4	977664.01	1.06	-7.3	-113.76
K76	0.7392	36.1457	1112.6	977676.36	1.09	-13.1	-114.13
K77	0.7380	36.1486	1072	977684.53	0.93	-17.5	-114.90
K78	0.7364	36.1437	1135.5	977672.36	1.18	-10.1	-113.07
K79	0.7364	36.1404	1172.2	977665.20	1.08	-5.9	-112.36
K80	0.7393	36.1270	1273.3	977643.60	1.29	3.7	-111.86
K81	0.7415	36.1263	1300.6	977636.85	1.44	5.4	-112.55
K82	0.7435	36.1242	1354.7	977624.58	2.25	9.8	-112.29
K83	0.7472	36.1212	1320.5	977632.26	1.27	6.9	-113.01
K84	0.7450	36.1699	1069.1	977683.53	0.52	-19.4	-116.96
K87	0.7496	36.1555	1056.4	977688.84	0.75	-18.0	-114.19
K88	0.7501	36.1530	1059.4	977688.26	0.91	-17.7	-113.95

Gravity station	Latitude	Longitude	Elevation	Gravity value	Terrain correction	FAA	Bouguer
K90	0.7659	36.1554	1087.6	977683.79	0.60	-13.5	-112.66
K91	0.7655	36.1595	1078.1	977685.63	0.72	-14.6	-112.77
K92	0.7647	36.1647	1032.6	977694.49	0.65	-19.7	-113.83
K93	0.7656	36.1688	1031.1	977694.60	0.59	-20.1	-114.11
K95	0.7700	36.1646	1021.4	977694.80	0.62	-22.9	-115.99
K96	0.7710	36.1731	1017.6	977695.77	0.73	-23.1	-115.73
K97	0.7764	36.1628	1019.7	977695.46	0.68	-22.8	-115.65
K98	0.7777	36.1561	1058	977686.99	0.55	-19.4	-115.95
K100	0.7860	36.1523	1046.1	977692.76	0.55	-17.3	-112.78
K101	0.7876	36.1459	1037.3	977695.50	0.93	-17.3	-111.57
K102	0.7945	36.1495	1042.9	977694.30	0.51	-16.8	-112.00
K106	0.7930	36.1691	1017.3	977697.71	0.63	-21.3	-114.01
K107	0.7868	36.1666	1016.8	977696.34	0.58	-22.8	-115.52
K108	0.7819	36.1652	1019.1	977696.57	0.59	-21.9	-114.78
K109	0.7787	36.1724	1019	977696.54	0.60	-21.9	-114.81
K110	0.7594	36.1632	1026.8	977693.62	0.67	-22.4	-115.93
K111	0.7537	36.1641	1029.1	977692.43	0.66	-22.8	-116.61
K112	0.7415	36.0475	986.2	977695.36	0.70	-33.1	-122.91
K114	0.7479	36.0547	994.3	977694.64	0.82	-31.4	-121.77
K115	0.7469	36.0469	1000	977693.39	0.42	-30.8	-122.18
K116	0.7373	36.0424	997	977692.86	0.45	-32.3	-123.31
K117	0.7423	36.0406	990	977694.39	0.36	-32.9	-123.40
K119	0.8759	36.1056	887.3	977729.19	0.47	-30.1	-111.08
K120	0.8784	36.0662	878.8	977723.43	0.36	-38.5	-118.80
K121	0.8516	36.0416	889.5	977714.41	0.37	-44.2	-125.42
K122	0.8187	36.0189	927.2	977706.04	0.36	-40.8	-125.54
K124	0.7406	36.0983	1248	977642.78	1.66	-4.9	-117.81
K126	0.7401	36.1127	1363.2	977617.92	2.85	5.7	-116.50
K127	0.7397	36.1157	1309.6	977630.92	1.95	2.2	-116.02
K128	0.7302	36.1191	1190.8	977655.36	0.96	-10.0	-118.29
K129	0.7248	36.1241	1200	977654.74	1.06	-7.7	-116.80
K132	0.7033	36.1271	1007.7	977691.30	0.59	-30.5	-122.34
K133	0.7500	36.1229	1341.8	977630.10	1.38	11.3	-110.45
K134	0.7554	36.1365	1336	977633.93	1.94	13.3	-107.34
K135	0.7618	36.1372	1167	977670.45	2.99	-2.3	-106.40
K137	0.7796	36.1325	1164.2	977673.04	1.03	-0.6	-106.42
K141	0.7123	36.0888	1031.4	977688.89	0.53	-25.6	-119.69
K142	0.7421	36.0793	1170.5	977661.32	0.86	-10.3	-116.85
K143	0.7379	36.0601	1041.6	977686.59	0.52	-24.8	-119.85
K145	0.8087	36.0964	995.4	977700.14	0.63	-25.7	-116.37
K147	0.8118	36.0798	923.9	977711.98	0.55	-35.9	-120.11
K148	0.8132	36.0726	915.4	977712.46	0.50	-38.0	-121.52
KG97	0.7953	36.0667	955.9	977701.57	0.55	-36.4	-123.54

Gravity station	Latitude	Longitude	Elevation	Gravity value	Terrain correction	FAA	Bouguer
KG96	0.7939	36.0840	977.3	977699.96	1.17	-31.4	-119.89
KG95	0.7829	36.0765	1059.5	977684.01	0.73	-22.0	-118.44
KG94	0.7776	36.0638	1021	977689.18	0.53	-28.6	-121.80
KG101	0.7981	36.1207	1093	977685.56	0.95	-10.1	-109.45
KG102	0.7911	36.1435	1062.5	977692.03	0.65	-13.0	-109.87
KG100	0.8073	36.1375	1018.1	977701.43	0.58	-17.4	-110.20
KG99	0.8075	36.1195	1013.6	977700.83	0.80	-19.4	-111.56
KG111	0.7767	36.1154	1313.1	977631.34	1.62	3.6	-115.26
KG112	0.7749	36.1180	1301	977634.72	1.42	3.3	-114.70
KG6	0.7731	36.1211	1247	977647.85	1.40	-0.3	-113.28
KG113	0.7771	36.1224	1264.5	977643.71	1.35	1.0	-113.69
KG1	0.7830	36.1243	1280.6	977637.60	2.96	-0.2	-114.72
KG114	0.7809	36.1197	1307.4	977632.17	2.54	2.7	-114.76
KG115	0.7561	36.1164	1327.3	977629.24	1.16	5.9	-114.69
KG29	0.7598	36.1104	1292.2	977639.30	1.42	5.2	-111.98
KG116	0.7554	36.1090	1287.8	977640.20	1.15	4.7	-112.31
KG117	0.7491	36.1092	1348.4	977624.88	1.50	8.1	-114.12
KG118	0.7458	36.1071	1363	977621.48	1.82	9.2	-114.04
KG119	0.7514	36.1133	1328.5	977632.64	1.21	9.7	-110.96
KG120	0.7414	36.1291	1282.6	977639.75	1.53	2.7	-113.46
KG121	0.7419	36.1349	1214.8	977654.61	1.16	-3.4	-113.67
KG122	0.7429	36.1397	1138.8	977668.83	1.90	-12.6	-115.17
KG123	0.7419	36.1466	1091.1	977679.67	1.30	-16.5	-115.26
KG124	0.7792	36.1129	1284.1	977640.19	1.74	3.5	-112.57
KG125	0.7793	36.1094	1238.2	977651.69	1.43	0.9	-111.34
KG126	0.7737	36.1077	1336.2	977628.25	2.40	7.7	-112.55
KG127	0.7692	36.1083	1325.4	977631.37	1.49	7.5	-112.67
KG128	0.7655	36.1063	1311.5	977633.63	1.23	5.4	-113.67
KG129	0.7680	36.1013	1284.6	977639.54	1.35	3.1	-113.48
KG130	0.7721	36.0973	1213.1	977655.56	1.11	-3.0	-113.21
KG131	0.7775	36.0962	1122.2	977674.30	1.27	-12.3	-114.02
KG132	0.7813	36.1009	1152	977670.04	1.04	-7.4	-112.05
KG133	0.7344	36.1286	1232.8	977650.83	0.98	-1.6	-113.71
KG134	0.7300	36.1287	1217.8	977653.32	1.08	-3.7	-114.36
KG135	0.7262	36.1308	1187.7	977658.46	1.11	-7.8	-115.70
KG136	0.7231	36.1326	1159.8	977663.09	1.35	-11.8	-116.86
KG137	0.7180	36.1341	1074.3	977680.21	0.79	-21.0	-118.82
KG138	0.7211	36.1360	1082.1	977680.42	0.80	-18.4	-116.92
KG139	0.7236	36.1399	1067.1	977683.95	0.82	-19.5	-116.63
KG140	0.7263	36.1424	1067.7	977684.34	0.84	-19.0	-116.09
KG142	0.7357	36.1220	1286.3	977636.31	1.62	0.4	-115.99
KG143	0.7341	36.1181	1201.7	977654.77	1.17	-7.2	-116.32
KG144	0.7288	36.1197	1191.8	977657.35	0.92	-7.7	-116.11

Gravity station	Latitude	Longitude	Elevation	Gravity value	Terrain correction	FAA	Bouguer
KG145	0.7246	36.1168	1108.2	977672.73	1.19	-18.1	-118.57
KG146	0.7211	36.1148	1066.2	977680.62	1.04	-23.1	-119.93
KG147	0.7131	36.1188	1041.6	977686.37	0.63	-25.0	-119.91
KG148	0.7067	36.1197	1026.5	977689.63	0.52	-26.3	-120.01
K149	0.7097	36.1046	1074.3	977678.88	0.47	-22.4	-120.45
K150	0.7144	36.1055	1088	977677.12	0.57	-19.9	-119.16
K151	0.7469	36.0792	1169.7	977662.47	0.78	-9.4	-115.96
K152	0.7528	36.0824	1164.6	977664.40	0.72	-9.1	-115.21
K153	0.7581	36.0865	1142.3	977671.03	0.87	-9.3	-113.28
K154	0.7635	36.0839	1161.6	977665.87	0.78	-8.6	-114.36
K155	0.7660	36.0793	1124.5	977672.52	0.74	-13.4	-115.80
K156	0.7606	36.0756	1109.4	977675.76	0.58	-14.8	-115.97
K157	0.7549	36.0734	1090	977679.14	0.59	-17.4	-116.78
K158	0.7512	36.0703	1093.6	977678.62	0.61	-16.8	-116.49
K159	0.7445	36.0648	1071.3	977681.68	0.57	-20.6	-118.28
K160	0.7832	36.1177	1297	977635.03	1.91	2.3	-114.79
K161	0.7808	36.1167	1314.8	977630.60	1.99	3.4	-115.26
K162	0.7792	36.1163	1317.3	977630.66	1.96	4.2	-114.70
K163	0.7757	36.1127	1343.4	977625.16	2.11	6.8	-114.38
K164	0.7717	36.1150	1348.3	977622.61	1.85	5.8	-116.11
K165	0.7902	36.1052	1161.3	977667.41	0.97	-7.2	-112.76
K166	0.7909	36.1065	1146.5	977671.73	0.92	-7.4	-111.70
K167	0.7926	36.1076	1123.3	977675.73	0.89	-10.6	-112.76
K168	0.7566	36.0355	986.6	977692.26	0.35	-36.1	-126.30
K169	0.7596	36.0409	992.2	977692.66	0.35	-34.0	-124.71
K170	0.7634	36.0472	988.8	977694.03	0.41	-33.7	-124.02
K171	0.7674	36.0482	985.5	977694.36	0.40	-34.4	-124.42
K172	0.7743	36.0439	984.7	977694.55	0.35	-34.5	-124.47
K173	0.8104	36.0736	919.7	977709.56	0.52	-39.6	-123.47
K174	0.8342	36.0915	904.8	977718.55	0.56	-35.3	-117.73
69	0.9112	36.0695	890	977726.89	0.36	-31.7	-113.01
89	0.9037	36.0749	890	977726.29	0.39	-32.3	-113.56
109	0.8944	36.0941	882	977727.47	0.37	-33.5	-114.10
110	0.8802	36.1095	883	977729.48	0.55	-31.2	-111.65
130	0.8641	36.1060	883	977728.53	0.45	-32.1	-112.66
121	0.8805	36.1342	922	977725.40	0.64	-23.2	-107.19
112	0.8772	36.1562	973	977713.67	0.97	-19.2	-107.53
101	0.8912	36.1360	946	977718.82	0.63	-22.4	-108.61
111	0.8979	36.1187	908	977723.71	0.62	-29.3	-111.99
51	0.9206	36.0702	878	977729.92	0.30	-32.4	-112.66
70	0.9177	36.0900	882	977730.74	0.44	-30.3	-110.83
122	0.8786	36.1598	992	977708.91	1.24	-18.1	-107.91
133	0.8786	36.1655	1076	977691.40	0.98	-9.7	-107.48

Gravity station	Latitude	Longitude	Elevation	Gravity value	Terrain correction	FAA	Bouguer
123	0.8796	36.1758	1151	977675.39	0.85	-2.6	-107.36
124	0.8773	36.1865	1160	977671.48	0.73	-3.7	-109.44
114	0.8854	36.1841	1233	977657.24	1.22	4.5	-107.40
104	0.8979	36.1815	1318	977636.94	1.73	10.4	-108.80
94	0.9136	36.1776	1451	977607.14	3.93	21.6	-107.63
85	0.9124	36.1867	1563	977583.37	4.54	32.4	-106.51
76	0.9165	36.1998	1582	977579.48	4.23	34.3	-106.61
65	0.9315	36.1933	1361	977631.67	2.67	18.3	-103.91
57	0.9600	36.1968	1062	977699.85	1.05	-5.8	-102.22
53	0.9489	36.1272	901	977733.07	0.55	-22.2	-104.36
35	0.9361	36.1163	904	977728.33	0.45	-26.0	-108.51
28	0.9675	36.1910	1011	977712.17	0.87	-9.3	-101.17
19	0.9754	36.1796	957	977724.52	0.75	-13.6	-100.66
18	0.9814	36.1593	887	977741.88	0.62	-17.8	-98.61
17	0.9728	36.1429	876	977742.87	0.55	-20.2	-100.06
36	0.9604	36.1365	887	977737.79	0.59	-21.9	-102.67
7	0.9970	36.1808	857	977745.25	0.66	-23.8	-101.75
8	0.9876	36.2004	935	977727.61	0.68	-17.3	-102.44
72	0.9323	36.1233	919	977725.92	0.50	-23.8	-107.62
82	0.9246	36.1284	932	977721.64	0.55	-24.0	-109.00
83b	0.9218	36.1426	978	977715.97	0.84	-15.5	-104.42
74b	0.9261	36.1468	1001	977712.59	0.97	-11.8	-102.69
63	0.9320	36.1358	948	977721.68	0.64	-19.1	-105.43
120	0.8820	36.2878	1217	977644.32	0.62	-13.3	-124.37
119	0.8894	36.2730	1210	977648.30	0.59	-11.5	-121.96
107	0.8957	36.2565	1201	977652.67	0.63	-9.9	-119.51
98	0.9087	36.2603	1222	977647.66	0.73	-8.5	-119.92
81	0.9193	36.2920	1309	977625.90	0.70	-3.5	-122.89
100	0.9155	36.2836	1314	977626.21	0.83	-1.6	-121.34
44	0.9549	36.2944	1310	977625.98	0.75	-3.2	-122.64
25	0.9736	36.2920	1307	977628.86	1.24	-1.3	-119.98
175	0.8163	36.2210	1189	977657.81	0.54	-8.3	-116.85
176	0.8233	36.2227	1162	977665.16	0.54	-9.3	-115.38
165	0.8359	36.2115	1188	977663.53	0.78	-2.9	-111.16
145	0.8441	36.2127	1152	977669.63	0.76	-8.0	-112.90
166	0.8411	36.2373	1161	977660.86	0.47	-13.9	-120.01
177	0.8286	36.2318	1159	977663.09	0.46	-12.3	-118.19
128	0.8842	36.0699	877	977724.12	0.33	-38.4	-118.55
108	0.8794	36.0567	873	977721.71	0.32	-42.0	-121.81
32	0.9534	36.0405	858	977733.26	0.28	-35.3	-113.77
33	0.9529	36.0556	856	977737.20	0.28	-32.0	-110.27
34	0.9523	36.0726	858	977738.70	0.29	-29.9	-108.31
52	0.9424	36.1199	896	977730.72	0.46	-26.1	-107.87

Gravity station	Latitude	Longitude	Elevation	Gravity value	Terrain correction	FAA	Bouguer
71	0.9254	36.1083	900	977725.37	0.69	-30.2	-112.08
181	0.8773	36.1598	982	977709.04	1.37	-21.1	-109.82
103	0.8881	36.1680	1179	977671.61	1.58	2.2	-104.38
102	0.8919	36.1522	1019	977706.85	1.01	-11.9	-104.38
113	0.8858	36.1546	996	977709.04	1.17	-16.8	-107.01
150	0.8493	36.1091	889	977727.29	0.50	-31.4	-112.51
149	0.8446	36.0902	886	977723.52	0.48	-36.1	-116.93
151	0.8530	36.1216	887	977728.69	0.54	-30.7	-111.51
141	0.8567	36.1344	883	977732.30	0.71	-28.3	-108.61
152	0.8509	36.1461	918	977723.89	0.76	-25.9	-109.38
142	0.8599	36.1495	956	977716.32	0.80	-21.8	-108.69
132	0.8697	36.1406	943	977721.74	0.66	-20.4	-106.25
131	0.8646	36.1260	897	977729.46	0.55	-26.8	-108.60
170	0.8271	36.1086	922	977720.59	0.60	-27.9	-111.90
171	0.8265	36.1260	926	977722.06	0.76	-25.2	-109.41
172	0.8267	36.1448	957	977716.01	0.61	-21.7	-108.88
162	0.8296	36.1509	965	977714.65	0.57	-20.6	-108.56
153	0.8452	36.1620	1007	977704.86	0.65	-17.5	-109.21
135	0.8675	36.1958	1145	977672.62	1.32	-7.2	-110.93
125b	0.8772	36.2023	1119	977677.37	1.15	-10.5	-112.02
116a	0.8811	36.2091	1243	977651.45	1.20	1.8	-111.03
116	0.8837	36.2112	1292	977640.85	1.70	6.3	-110.51
115a	0.8841	36.2054	1250	977651.05	1.37	3.6	-109.75
115	0.8835	36.2013	1186	977664.99	1.17	-2.2	-109.88
115c	0.8806	36.1940	1209	977660.43	1.09	0.3	-109.52
95a	0.8906	36.1914	1272	977648.64	1.37	7.9	-107.40
75	0.9192	36.1790	1489	977600.52	3.99	26.7	-105.96
75a	0.9185	36.1835	1527	977589.90	4.04	27.8	-108.30
95b	0.9082	36.2001	1616	977568.47	5.18	33.8	-109.28
95	0.9024	36.1995	1502	977594.42	3.97	24.6	-109.22
105a	0.8986	36.2019	1382	977621.71	2.27	14.9	-109.63
105	0.8938	36.2064	1357	977626.80	1.68	12.3	-110.53
96	0.9014	36.2111	1458	977604.46	2.69	21.1	-110.00
86	0.9078	36.2017	1613	977568.89	5.01	33.3	-109.68
84a	0.9126	36.1768	1438	977608.66	3.86	19.1	-108.99
64a	0.9222	36.1959	1481	977605.41	2.61	29.1	-104.20
56a	0.9362	36.1899	1259	977654.77	2.17	9.9	-103.42
56b	0.9374	36.1936	1258	977654.04	1.91	8.9	-104.64
29	0.9591	36.2058	1058	977698.84	0.97	-8.1	-104.19
40	0.9590	36.2141	1026	977704.12	1.07	-12.7	-105.74
30	0.9658	36.2211	978	977711.01	0.96	-20.6	-109.38
21	0.9717	36.2172	962	977715.38	0.87	-21.2	-108.58
20a	0.9758	36.2089	953	977719.31	0.94	-20.0	-106.54

Gravity station	Latitude	Longitude	Elevation	Gravity value	Terrain correction	FAA	Bouguer
20	0.9744	36.1997	976	977716.76	0.85	-15.5	-104.19
64b	0.9316	36.1832	1438	977613.81	3.59	24.2	-104.17
64c	0.9342	36.1779	1393	977626.66	4.47	23.2	-100.20
55a	0.9416	36.1781	1285	977651.28	3.35	14.4	-100.12
55	0.9410	36.1694	1147	977683.72	1.90	4.3	-99.04
46	0.9478	36.1722	1079	977698.44	1.72	-2.0	-99.25
38a	0.9511	36.1801	1159	977678.43	2.09	2.7	-101.56
38	0.9561	36.1835	1120	977688.67	2.06	0.9	-99.82
39b	0.9599	36.1890	1033	977706.73	1.18	-7.9	-101.51
92	0.9002	36.1438	994	977711.54	0.83	-14.9	-105.32
92a	0.8952	36.1443	983	977713.81	0.81	-16.1	-105.44
91	0.9052	36.1232	909	977723.55	0.55	-29.2	-112.02
90	0.9050	36.1029	886	977727.29	0.39	-32.5	-113.42
54a	0.9201	36.1387	960	977716.81	0.77	-20.2	-107.53
54b	0.9288	36.1421	973	977716.86	0.76	-16.2	-104.70
54	0.9368	36.1440	977	977717.66	0.76	-14.2	-103.06
45a	0.9415	36.1487	990	977715.75	0.85	-12.1	-102.08
45	0.9458	36.1530	990	977717.18	0.95	-10.7	-100.56
37a	0.9511	36.1573	985	977718.11	1.12	-11.3	-100.56
37	0.9566	36.1644	969	977722.03	0.98	-12.3	-100.26
27a	0.9606	36.1701	988	977719.08	0.96	-9.4	-99.12
27	0.9638	36.1754	956	977725.41	1.09	-13.0	-99.62
27b	0.9729	36.1729	940	977728.29	0.78	-15.1	-100.53
69y	0.9225	36.0519	873	977727.76	0.30	-36.1	-115.92
51y	0.9343	36.0663	866	977733.15	0.29	-32.9	-112.08
33y	0.9308	36.0832	868	977733.76	0.34	-31.7	-110.98
34y	0.9491	36.1060	878	977734.86	0.37	-27.5	-107.74
52y	0.9371	36.1077	889	977730.20	0.39	-28.8	-109.96
48a	0.9523	36.2001	1091	977692.09	1.49	-4.6	-103.24
48	0.9484	36.2047	1135	977683.03	1.59	-0.1	-102.65
49a	0.9473	36.2122	1089	977691.72	1.58	-5.6	-103.94
49	0.9469	36.2215	1080	977691.42	1.38	-8.7	-106.38
58	0.9368	36.2134	1292	977645.87	2.52	11.2	-104.83
66	0.9292	36.2067	1471	977603.04	3.54	23.6	-107.82
123a	0.8777	36.1755	1140	977677.59	0.79	-3.8	-107.61
112a	0.8862	36.1445	956	977718.55	0.80	-19.6	-106.53
87a	0.9092	36.2026	1688	977551.20	8.10	38.8	-108.03
87b	0.9086	36.2094	1616	977570.71	4.80	36.1	-107.41
87	0.9111	36.2234	1530	977589.25	3.98	28.1	-108.34
78a	0.9115	36.2265	1445	977608.75	2.35	21.4	-108.89
78	0.9148	36.2336	1397	977618.53	2.10	16.3	-109.77
68a	0.9192	36.2398	1312	977637.71	1.06	9.3	-110.07
68	0.9243	36.2420	1237	977652.87	1.80	1.3	-110.44

Gravity station	Latitude	Longitude	Elevation	Gravity value	Terrain correction	FAA	Bouguer
59	0.9315	36.2354	1238	977652.13	1.75	0.8	-111.02
67	0.9271	36.2277	1247	977653.01	2.00	4.5	-107.93
77	0.9208	36.2187	1441	977610.47	2.34	21.8	-108.08
22a	0.9993	36.2464	881	977726.97	1.03	-34.7	-114.47
22b	0.9841	36.2408	936	977717.17	0.92	-27.5	-112.42
22	0.9762	36.2341	952	977715.64	0.87	-24.0	-110.50
31	0.9636	36.2397	979	977707.60	1.06	-23.7	-112.47
41	0.9551	36.2338	1002	977704.97	1.13	-19.2	-110.02
97b	0.9052	36.2235	1441	977610.56	2.33	22.0	-107.95
97	0.9010	36.2336	1302	977639.55	1.02	8.1	-110.37
107a	0.8978	36.2405	1260	977645.05	0.79	0.6	-114.20
107b	0.8926	36.2459	1227	977649.77	0.65	-4.8	-116.75
117a	0.8861	36.2404	1206	977654.35	0.74	-6.7	-116.61
117	0.8819	36.2328	1241	977649.69	0.74	-0.6	-113.69
136	0.8655	36.2148	1133	977673.68	0.61	-9.8	-113.18
145a	0.8594	36.2101	1109	977680.17	0.61	-10.7	-111.87
144	0.8556	36.1946	1035	977696.45	0.85	-17.3	-111.38
155	0.8491	36.1971	1053	977694.10	0.84	-14.0	-109.83
164a	0.8458	36.1936	1040	977696.93	1.00	-15.2	-109.64
154	0.8456	36.1816	996	977708.58	0.79	-17.1	-107.74
143a	0.8518	36.1788	1003	977705.15	1.01	-18.4	-109.44
143	0.8562	36.1760	1058	977695.53	0.74	-11.1	-107.44
134	0.8629	36.1778	1094	977688.15	0.69	-7.4	-107.08
146	0.8579	36.2179	1128	977674.09	0.57	-10.9	-113.87
157	0.8449	36.2293	1158	977665.49	0.48	-10.3	-116.03
147	0.8554	36.2396	1159	977662.86	0.49	-12.6	-118.46
138	0.8634	36.2540	1178	977655.06	0.51	-14.6	-122.14
118	0.8797	36.2555	1190	977655.53	0.53	-10.4	-119.10
127	0.8737	36.2443	1182	977659.20	0.56	-9.2	-117.11
137	0.8643	36.2334	1167	977664.39	0.56	-8.6	-115.15
146a	0.8575	36.2287	1162	977665.84	0.55	-8.7	-114.78
84b	0.9034	36.1579	1092	977690.77	1.30	-5.5	-104.40
84c	0.9105	36.1620	1178	977673.00	2.01	3.3	-102.84
74a	0.9155	36.1656	1225	977662.32	2.35	7.1	-103.00
74	0.9212	36.1634	1156	977678.88	2.13	2.3	-101.63
83a	0.9143	36.1598	1129	977683.85	1.57	-1.0	-103.05
83	0.9089	36.1602	1166	977675.36	1.78	1.9	-103.30
61	0.7545	36.1797	1037	977687.06	0.54	-25.8	-120.40
62	0.7631	36.1949	1050	977683.07	0.66	-25.8	-121.46
42	0.7713	36.2032	1080	977676.68	0.62	-22.9	-121.42
43	0.7841	36.2084	1112	977670.80	0.73	-19.0	-120.28
33	0.7917	36.2160	1148	977662.58	0.52	-16.1	-120.93
34	0.7936	36.2239	1144	977662.71	0.51	-17.2	-121.69

Gravity station	Latitude	Longitude	Elevation	Gravity value	Terrain correction	FAA	Bouguer
6	0.8128	36.2244	1169	977661.07	0.51	-11.2	-117.96
5	0.8078	36.2246	1154	977663.04	0.51	-13.8	-119.22
255	0.8054	36.2316	1144	977661.97	0.51	-18.0	-122.44
19	0.8126	36.2552	1169	977652.05	0.58	-20.2	-126.90
20	0.8021	36.2761	1198	977642.10	0.83	-21.2	-130.29
118c	0.8115	36.2315	1148	977662.60	0.50	-16.1	-120.97
69	0.7725	36.1813	1036	977689.91	0.53	-23.3	-117.81
38	0.7707	36.1886	1038	977688.59	0.59	-24.0	-118.63
40	0.7834	36.1849	1049	977687.73	0.57	-21.5	-117.16
301	0.7882	36.1858	1081	977682.76	0.68	-16.6	-115.10
17	0.8261	36.2258	1153	977666.07	0.50	-11.2	-116.46
16	0.8293	36.2134	1197	977660.67	1.25	-3.0	-111.58
15	0.8304	36.2006	1208	977659.76	1.49	-0.5	-109.87
14	0.8317	36.1915	1120	977679.92	1.38	-7.5	-108.90
13	0.8305	36.1804	992	977708.70	0.95	-18.2	-108.28
121	0.8380	36.1715	985	977711.48	0.66	-17.6	-107.33
24	0.8467	36.1709	991	977709.47	0.68	-17.8	-108.04
259	0.8399	36.1780	997	977708.20	0.71	-17.2	-107.96
261	0.8448	36.1865	1001	977705.57	0.94	-18.6	-109.52
27	0.8466	36.2002	1058	977692.12	0.93	-14.5	-110.63
7	0.8166	36.2134	1233	977651.91	0.78	-0.6	-112.98
253	0.8129	36.2069	1240	977651.22	0.83	0.9	-112.09
4	0.8068	36.2123	1226	977651.47	0.89	-3.2	-114.81
3	0.8064	36.2018	1217	977654.48	0.84	-3.0	-113.79
32	0.7930	36.2029	1146	977667.78	0.60	-11.5	-116.09
39	0.7840	36.1993	1151	977665.44	1.29	-12.3	-116.62
2	0.8063	36.1904	1169	977666.57	1.03	-5.7	-111.92
1	0.8068	36.1793	1014	977700.98	1.73	-19.1	-110.40
1a	0.8075	36.1725	1019	977700.45	0.69	-18.1	-110.88
11	0.8160	36.1738	1020	977700.70	0.95	-17.5	-110.18
10	0.8176	36.1794	1018	977701.81	0.98	-17.0	-109.47
91	0.8212	36.1894	1163	977670.18	1.97	-4.0	-108.70
251	0.8175	36.1892	1211	977658.65	1.97	-0.7	-109.82
252	0.8154	36.1969	1183	977664.65	1.57	-3.3	-110.28
28	0.8471	36.2137	1143	977671.86	0.75	-8.5	-112.64
47	0.8777	36.1587	983	977710.81	1.12	-19.0	-108.08
48	0.8726	36.1884	1169	977670.92	0.74	-1.5	-108.03
S560	1.0275	36.2398	881	977730.99	0.63	-30.7	-110.95
S601	1.0320	36.2246	871	977738.29	0.56	-26.5	-105.90
S563	1.0179	36.2776	1061	977677.62	0.98	-28.6	-124.93
S562	1.0218	36.2650	879	977718.37	2.07	-43.9	-122.53
S561	1.0242	36.2531	892	977722.48	0.75	-35.8	-116.94
S600	1.0338	36.2113	861	977744.35	0.53	-23.6	-102.04

Gravity station	Latitude	Longitude	Elevation	Gravity value	Terrain correction	FAA	Bouguer
S559	1.0375	36.1995	852	977749.39	0.51	-21.3	-98.98
S558	1.0402	36.1888	850	977752.96	0.49	-18.4	-95.87
S557	1.0448	36.1706	846	977755.30	0.44	-17.3	-94.46
S556	1.0537	36.1527	820	977760.87	0.38	-19.8	-94.61
S555	1.0574	36.1286	786	977762.41	0.41	-28.7	-100.43
S637	1.0434	36.1237	794	977763.00	0.41	-25.6	-98.05
S630	1.0239	36.1431	808	977762.17	0.47	-22.1	-95.73
S636	1.0258	36.1709	832	977756.86	0.48	-20.0	-95.83
S639	1.0150	36.2001	853	977747.83	0.57	-22.5	-100.19
S623	1.0449	36.2699	936	977706.13	0.62	-38.7	-123.95
S631	1.0540	36.2318	905	977727.48	0.51	-26.9	-109.46
S603	1.0772	36.0630	781	977752.59	0.55	-40.1	-111.25
S602	1.0723	36.0767	777	977755.86	0.47	-38.1	-108.92
S552	1.0681	36.0897	776	977758.67	0.44	-35.6	-106.34
S553	1.0637	36.1077	783	977760.49	0.45	-31.6	-102.98
S700	1.1128	36.0789	768	977753.94	0.67	-42.9	-112.73
S629	1.0426	36.1238	792	977762.87	0.40	-26.4	-98.62
S628	1.0102	36.0838	796	977758.43	0.40	-29.5	-102.09
S635	1.1005	36.0963	771	977756.15	0.51	-39.8	-109.98
S626	1.0993	36.1249	787	977756.34	0.51	-34.6	-106.32
S618	1.0913	36.1503	845	977752.37	0.46	-20.7	-97.74
S621	1.0908	36.2156	983	977719.23	0.53	-11.2	-100.91
S620	1.0743	36.1930	909	977738.99	0.52	-14.3	-97.14
S640	1.1144	36.2159	1143	977685.37	1.09	4.2	-99.62
S622	1.1092	36.2380	1092	977690.05	0.76	-6.9	-106.29
S632	1.0870	36.2306	980	977714.47	0.53	-16.9	-106.31

Appendix C: MT Phase tensor

Phase tensor maps of MT data for a selected volcanic area at Paka geothermal area. Phase tensor ellipses are shown for frequencies 10, 1, 0.1 and 0.01 Hz.

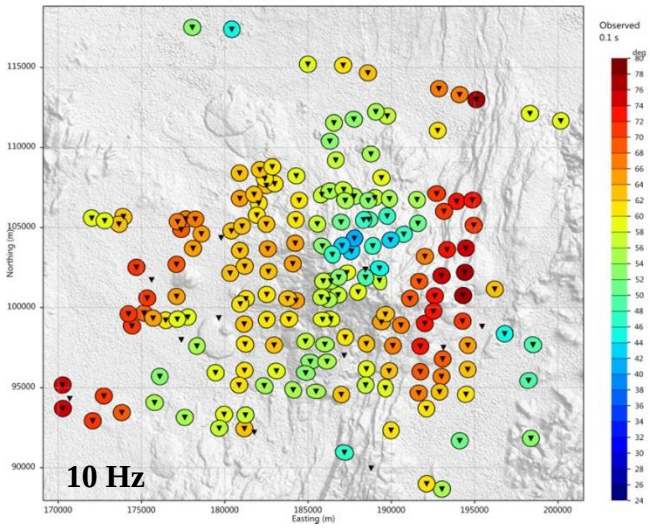

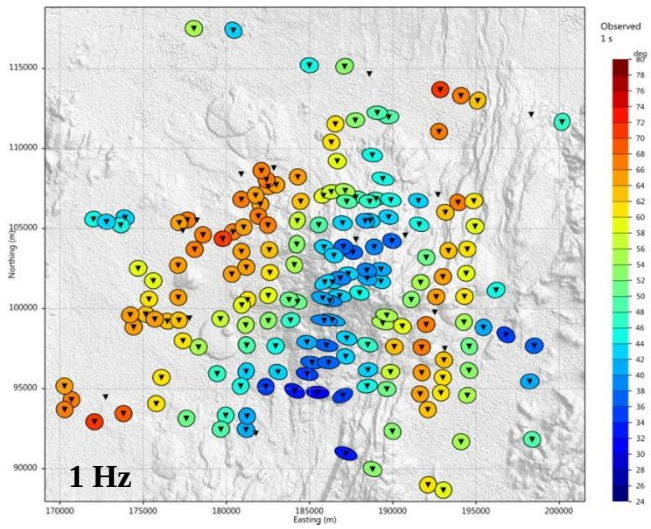

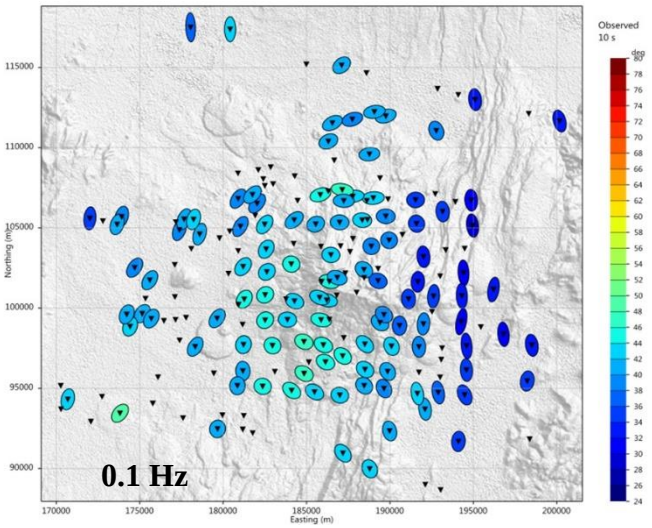

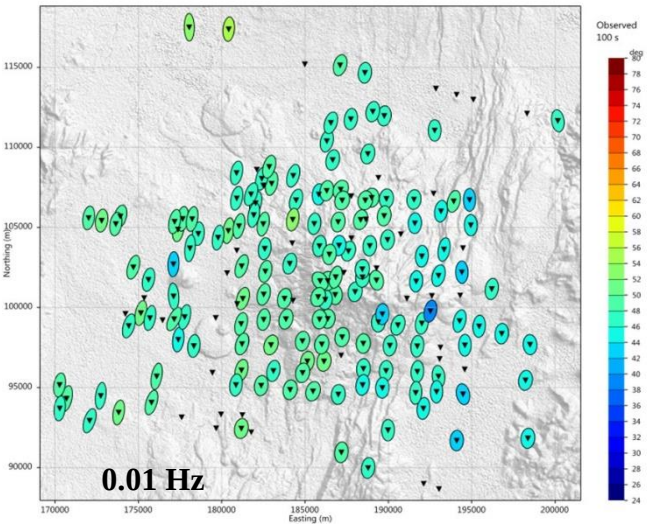

Appendix D: 2D Synthetic modelling of MT data

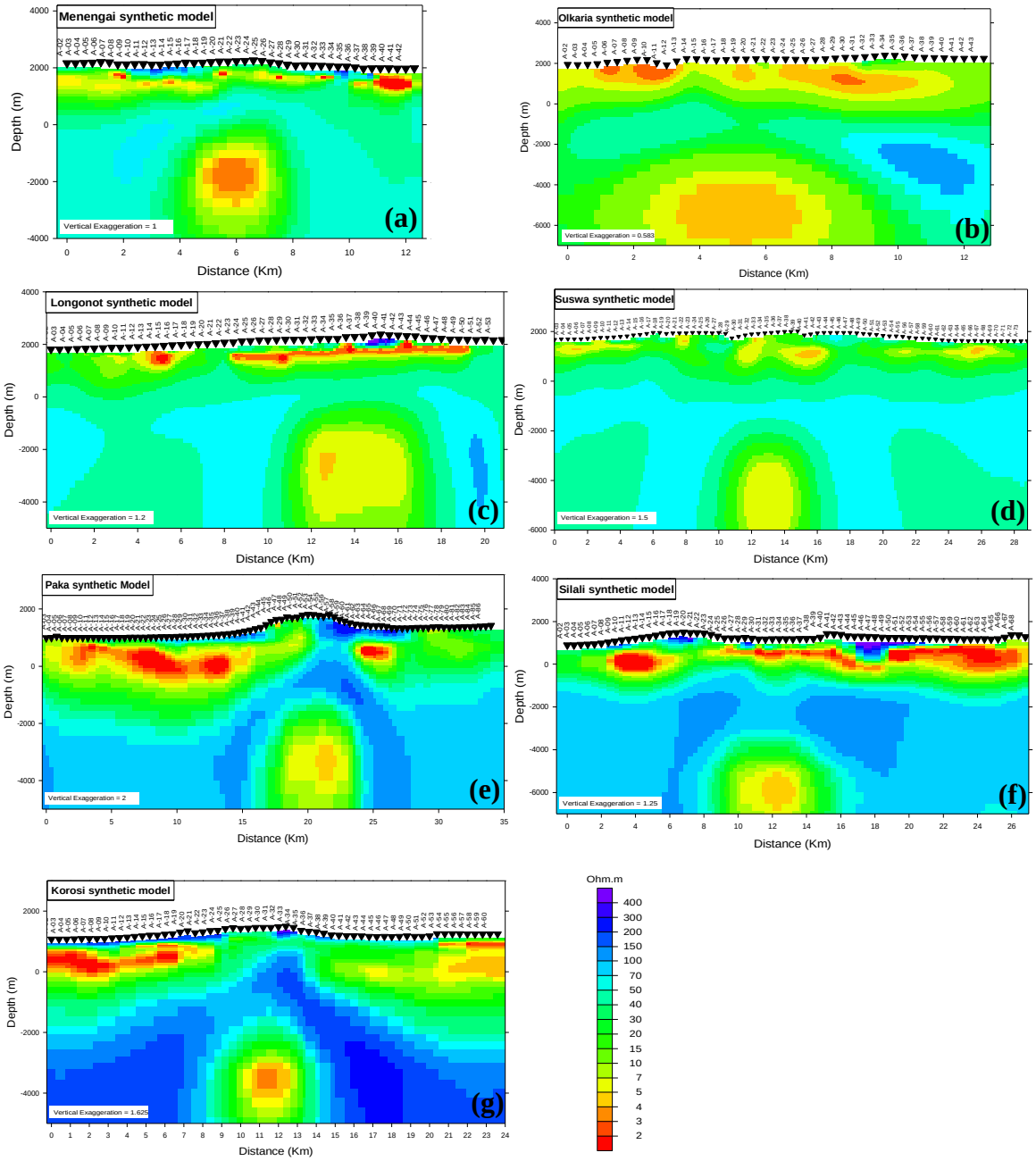

Synthetic models to speculate on probable magma chambers at (a) Menengai (b) Olkaria (c) Longonot (d) Suswa (e) Paka (f) Silali (g) Korosi.

Appendix E1: Resistivity maps of southern Kenya Rift

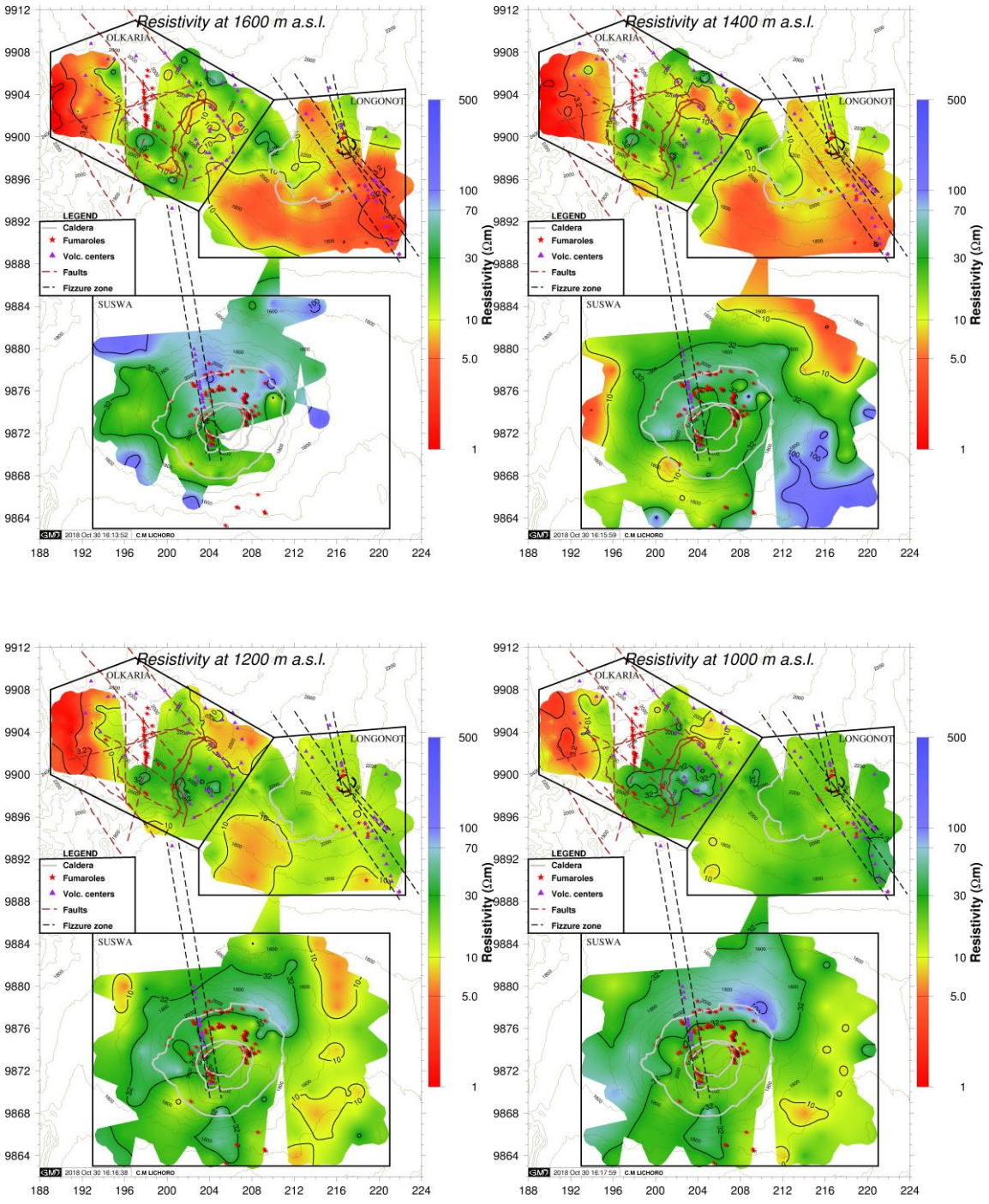

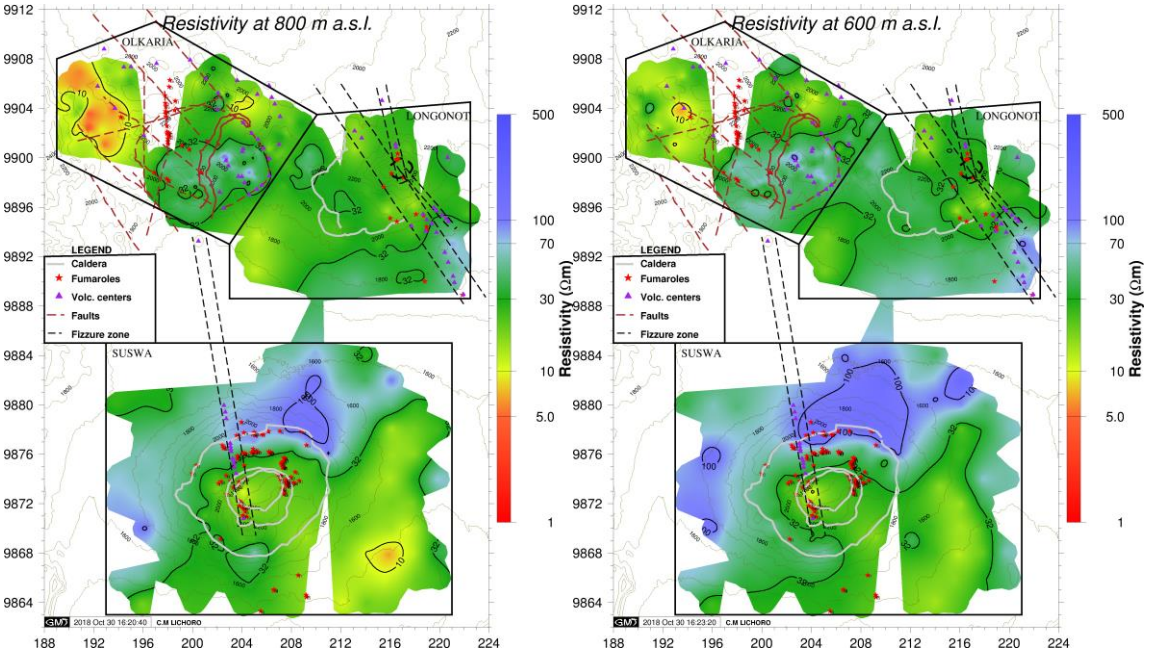
Resistivity at 800 m a.s.l.
OLKARIA
LONGONOT
SUSWA
LEGEND
Caldera
Fumaroles
Volc. centers
Faults
Fizzure zone
Resistivity (Ωm)
500
100
70
30
10
5.0
1
9912
9908
9904
9900
9896
9892
9888
9884
9880
9876
9872
9868
9864
188
192
196
200
204
208
212
216
220
224
2018 Oct 30 16:20:40
C.M LICHORO

Resistivity at 600 m a.s.l.
OLKARIA
LONGONOT
SUSWA
LEGEND
Caldera
Fumaroles
Volc. centers
Faults
Fizzure zone
Resistivity (Ωm)
500
100
70
30
10
5.0
1
9912
9908
9904
9900
9896
9892
9888
9884
9880
9876
9872
9868
9864
188
192
196
200
204
208
212
216
220
224
2018 Oct 30 16:23:20
C.M LICHORO

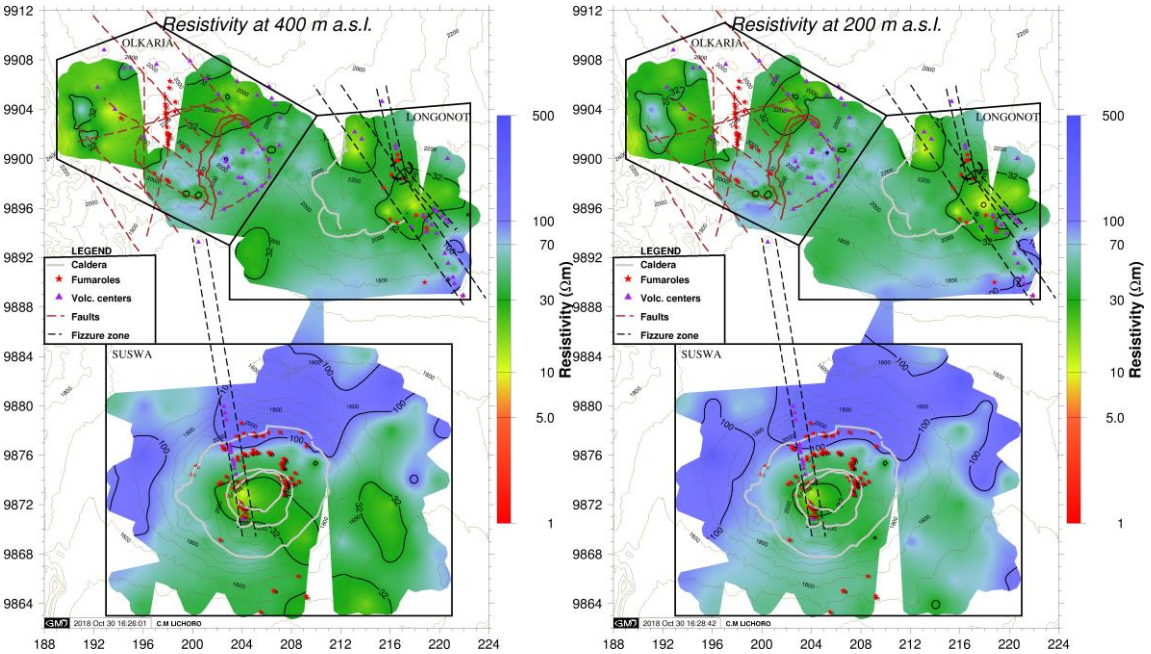
Resistivity at 400 m a.s.l.
OLKARIA
LONGONOT
SUSWA
LEGEND
Caldera
Fumaroles
Volc. centers
Faults
Fizzure zone
Resistivity (Ωm)
500
100
70
30
10
5.0
1
9912
9908
9904
9900
9896
9892
9888
9884
9880
9876
9872
9868
9864
188
192
196
200
204
208
212
216
220
224
2018 Oct 30 16:26:01
C.M LICHORO

Resistivity at 200 m a.s.l.
OLKARIA
LONGONOT
SUSWA
LEGEND
Caldera
Fumaroles
Volc. centers
Faults
Fizzure zone
Resistivity (Ωm)
500
100
70
30
10
5.0
1
9912
9908
9904
9900
9896
9892
9888
9884
9880
9876
9872
9868
9864
188
192
196
200
204
208
212
216
220
224
2018 Oct 30 16:28:42
C.M LICHORO

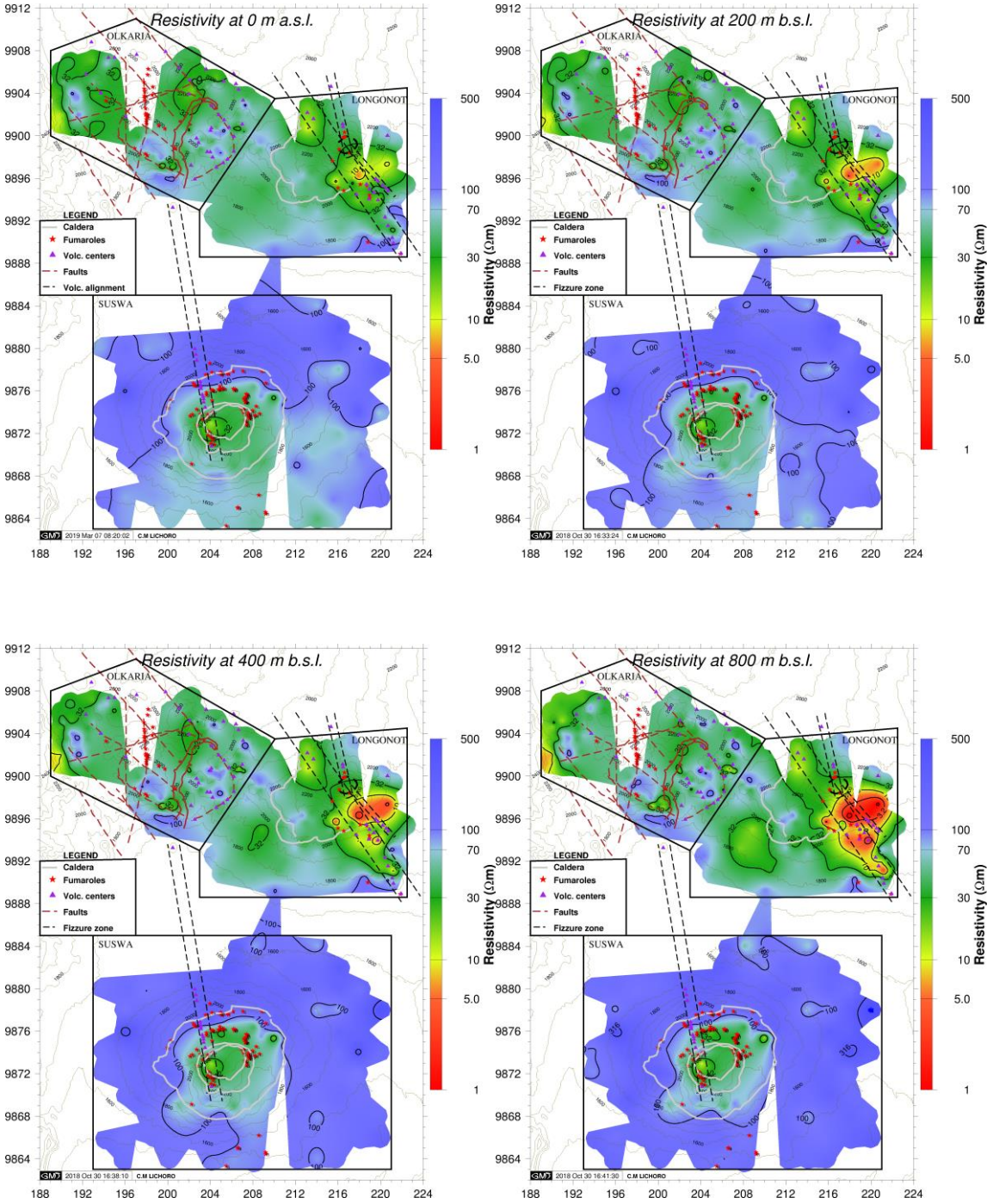
Resistivity at 0 m a.s.l.
Resistivity at 200 m b.s.l.
Resistivity at 400 m b.s.l.
Resistivity at 800 m b.s.l.
OLKARIA
LONGONOT
SUSWA
LEGEND
Caldera
Fumaroles
Volc. centers
Faults
Volc. alignment
Fizzure zone
Resistivity (Ωm)
500
100
70
30
10
5.0
1
9912
9908
9904
9900
9896
9892
9888
9884
9880
9876
9872
9868
9864
188
192
196
200
204
208
212
216
220
224

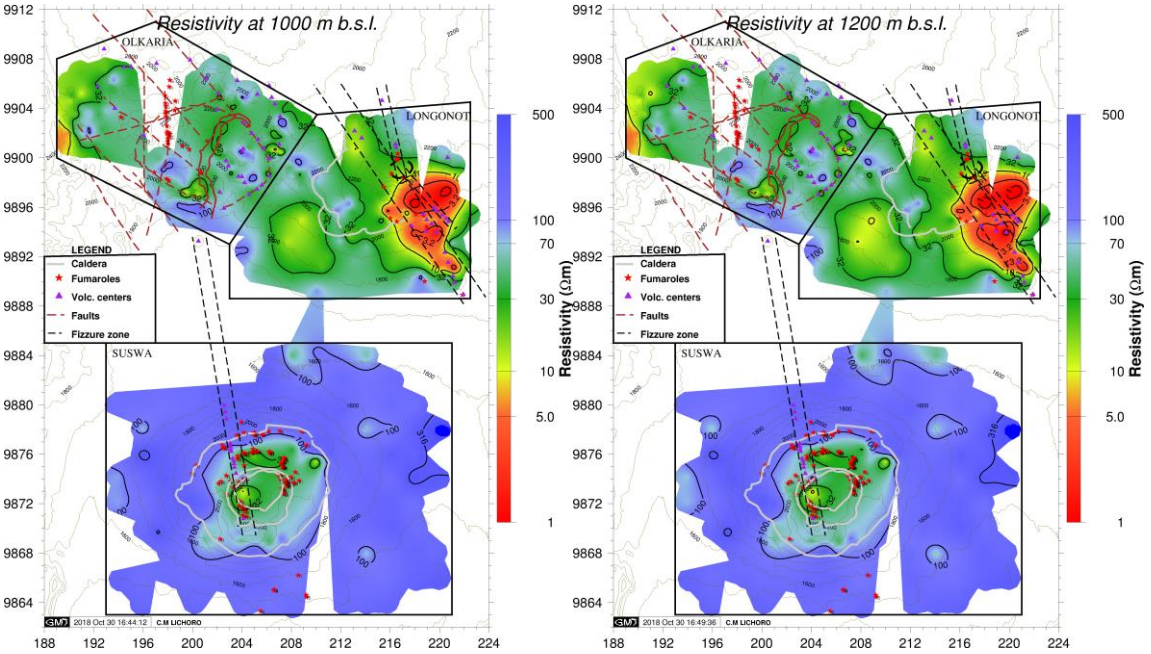
Resistivity at 1000 m b.s.l.
OLKARIA
LONGONOT
SUSWA
LEGEND
Caldera
Fumaroles
Volc. centers
Faults
Fizzure zone
Resistivity (Ωm)
500
100
70
30
10
5.0
1
9912
9908
9904
9900
9896
9892
9888
9884
9880
9876
9872
9868
9864
188
192
196
200
204
208
212
216
220
224
2018 Oct 30 16:44:12 C.M LICHORO

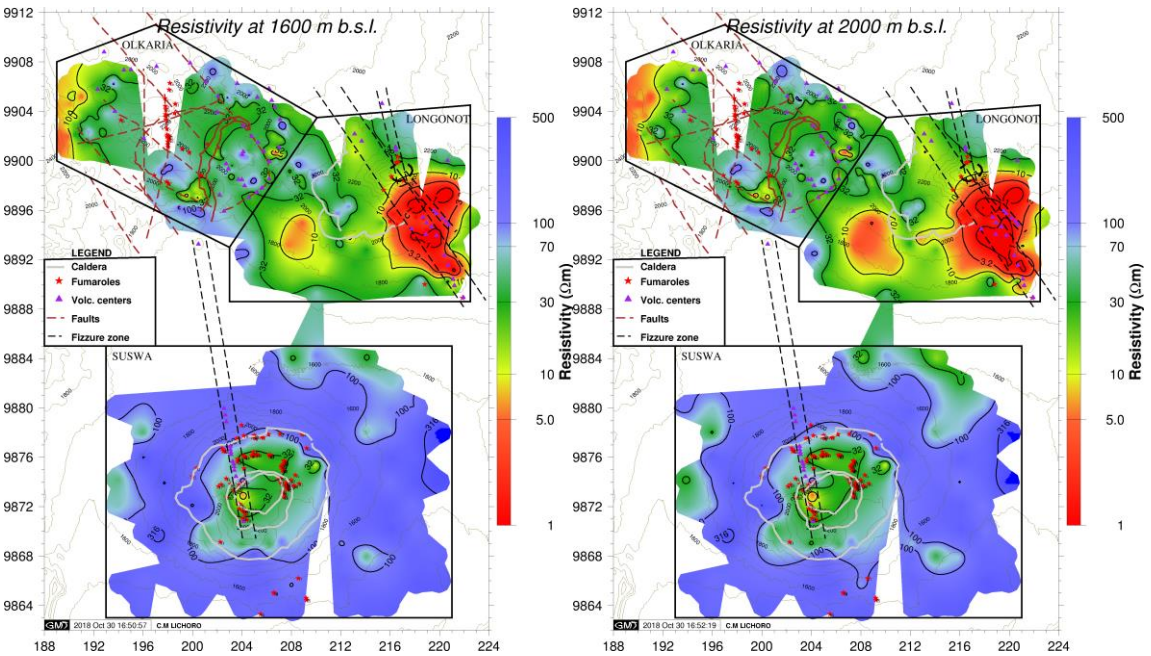
Resistivity at 1600 m b.s.l.
OLKARIA
LONGONOT
SUSWA
LEGEND
Caldera
Fumaroles
Volc. centers
Faults
Fizzure zone
Resistivity (Ωm)
500
100
70
30
10
5.0
1
9912
9908
9904
9900
9896
9892
9888
9884
9880
9876
9872
9868
9864
188
192
196
200
204
208
212
216
220
224
2018 Oct 30 16:50:57 C.M LICHORO

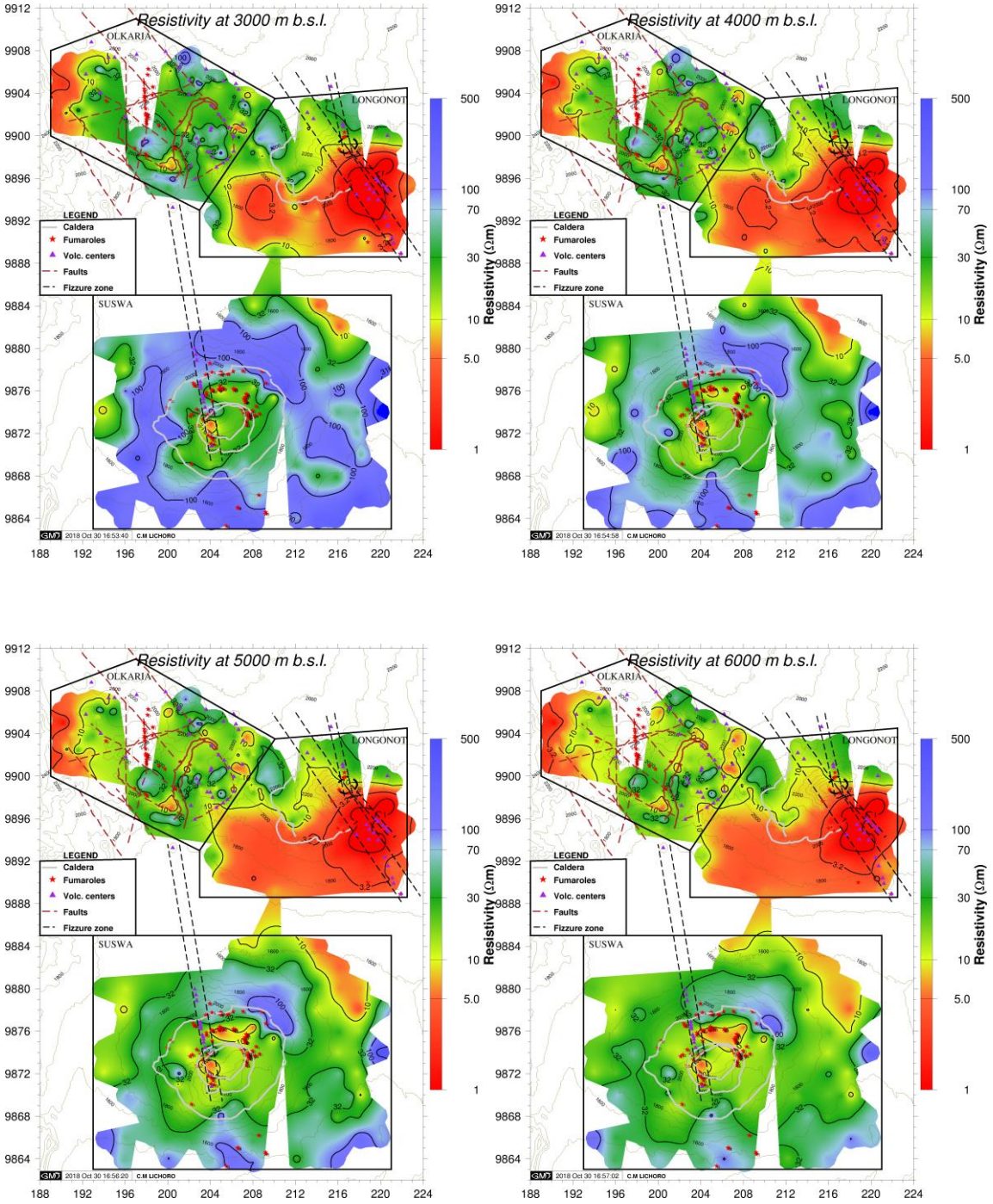
Resistivity at 3000 m b.s.l.
Resistivity at 4000 m b.s.l.
Resistivity at 5000 m b.s.l.
Resistivity at 6000 m b.s.l.
OLKARIA
LONGONOT
SUSWA
LEGEND
Caldera
Fumaroles
Volc. centers
Faults
Fizzure zone
Resistivity (Ωm)
500
100
70
30
10
5.0
1
9912
9908
9904
9900
9896
9892
9888
9884
9880
9876
9872
9868
9864
188
192
196
200
204
208
212
216
220
224

Appendix E2: Resistivity maps of northern Kenya Rift

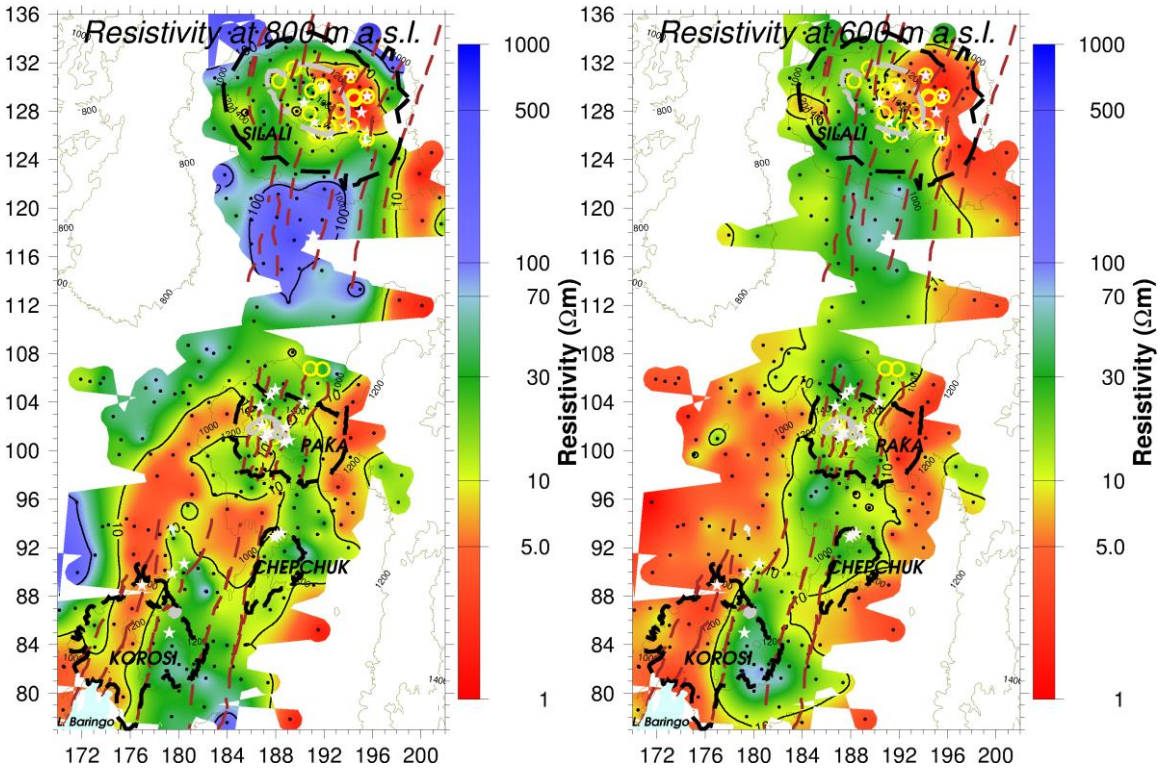

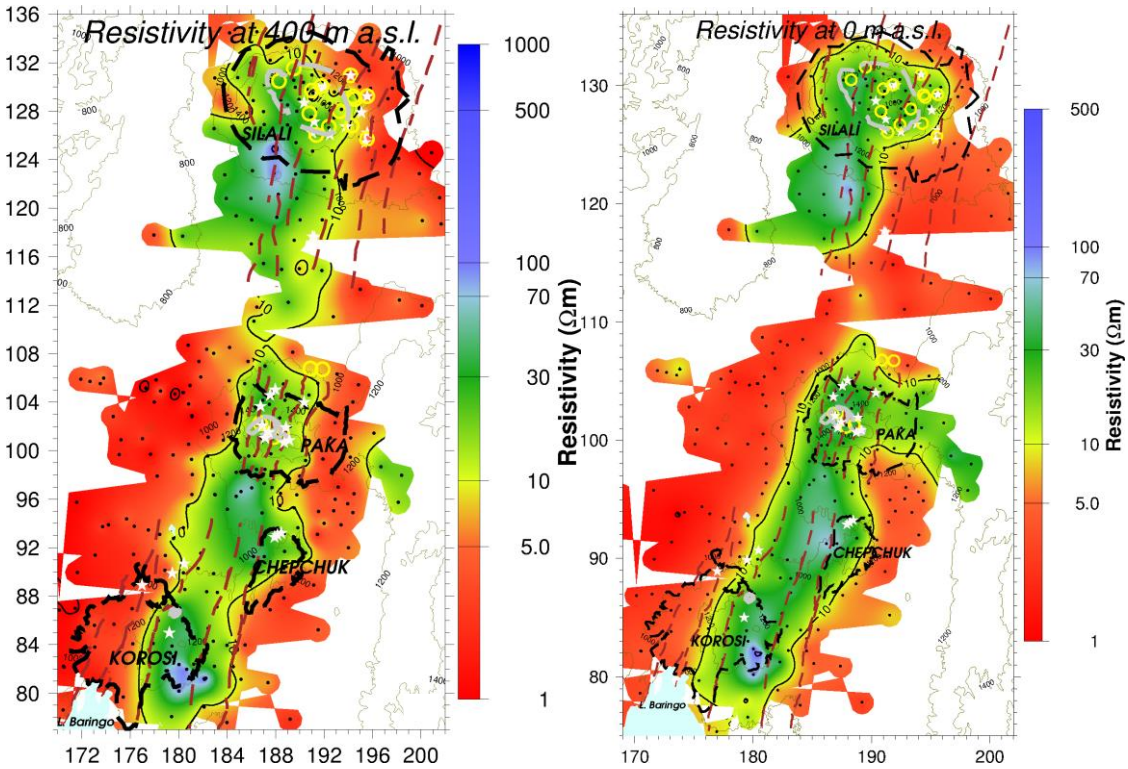

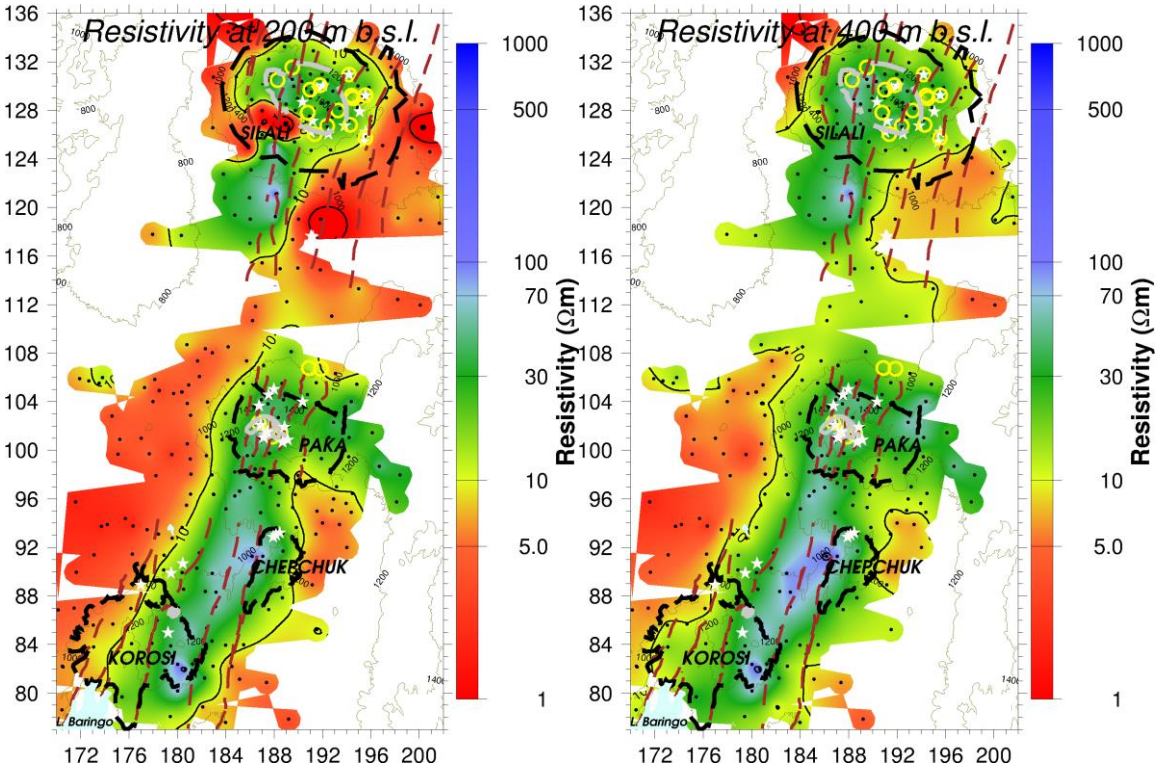
Resistivity at 200 m b.s.l.
Resistivity at 400 m b.s.l.
SILALI
PAKA
CHEPCHUK
KOROSI
L. Baringo
Resistivity (Ωm)
1000
500
100
70
30
10
5.0
1
136
132
128
124
120
116
112
108
104
100
96
92
88
84
80
172 176 180 184 188 192 196 200

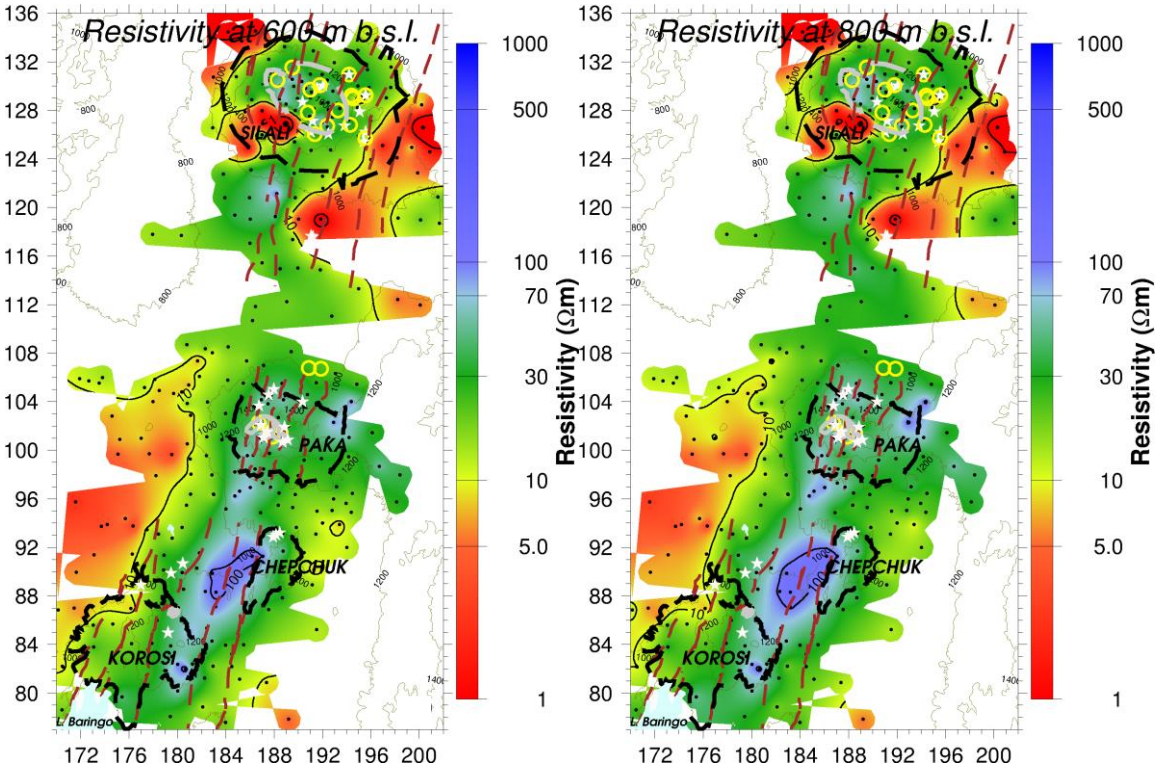
Resistivity at 600 m b.s.l.
Resistivity at 800 m b.s.l.
SILALI
PAKA
CHEPCHUK
KOROSI
L. Baringo
Resistivity (Ωm)
1000
500
100
70
30
10
5.0
1
136
132
128
124
120
116
112
108
104
100
96
92
88
84
80
172 176 180 184 188 192 196 200

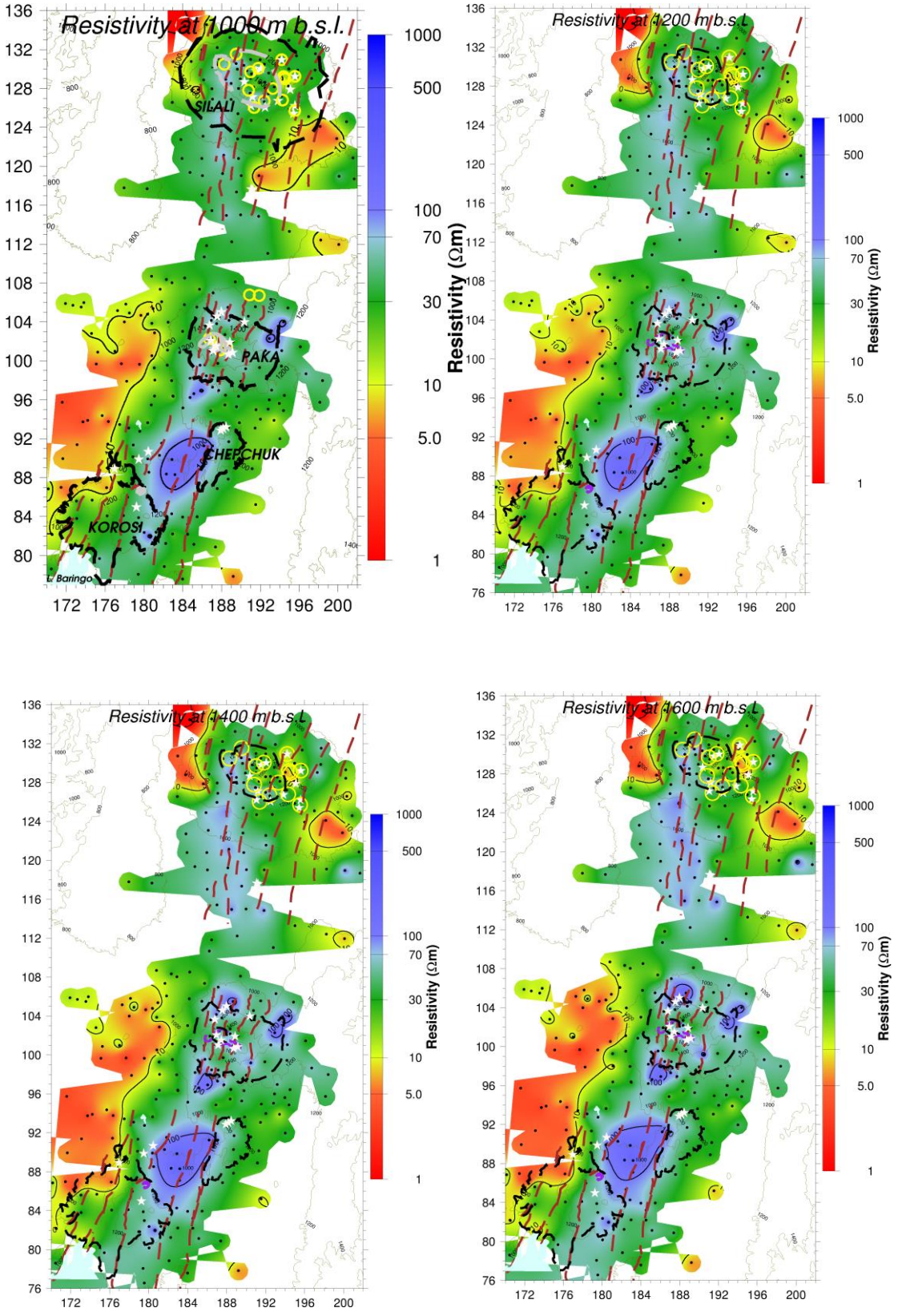
Resistivity at 1000m b.s.l.
Resistivity at 1200 m b.s.l
Resistivity at 1400 m b.s.l
Resistivity at 1600 m b.s.l
SILALI
PAKA
CHEPCHUK
KOROSI
L. Baringo
Resistivity (Ωm)
1000
500
100
70
30
10
5.0
1

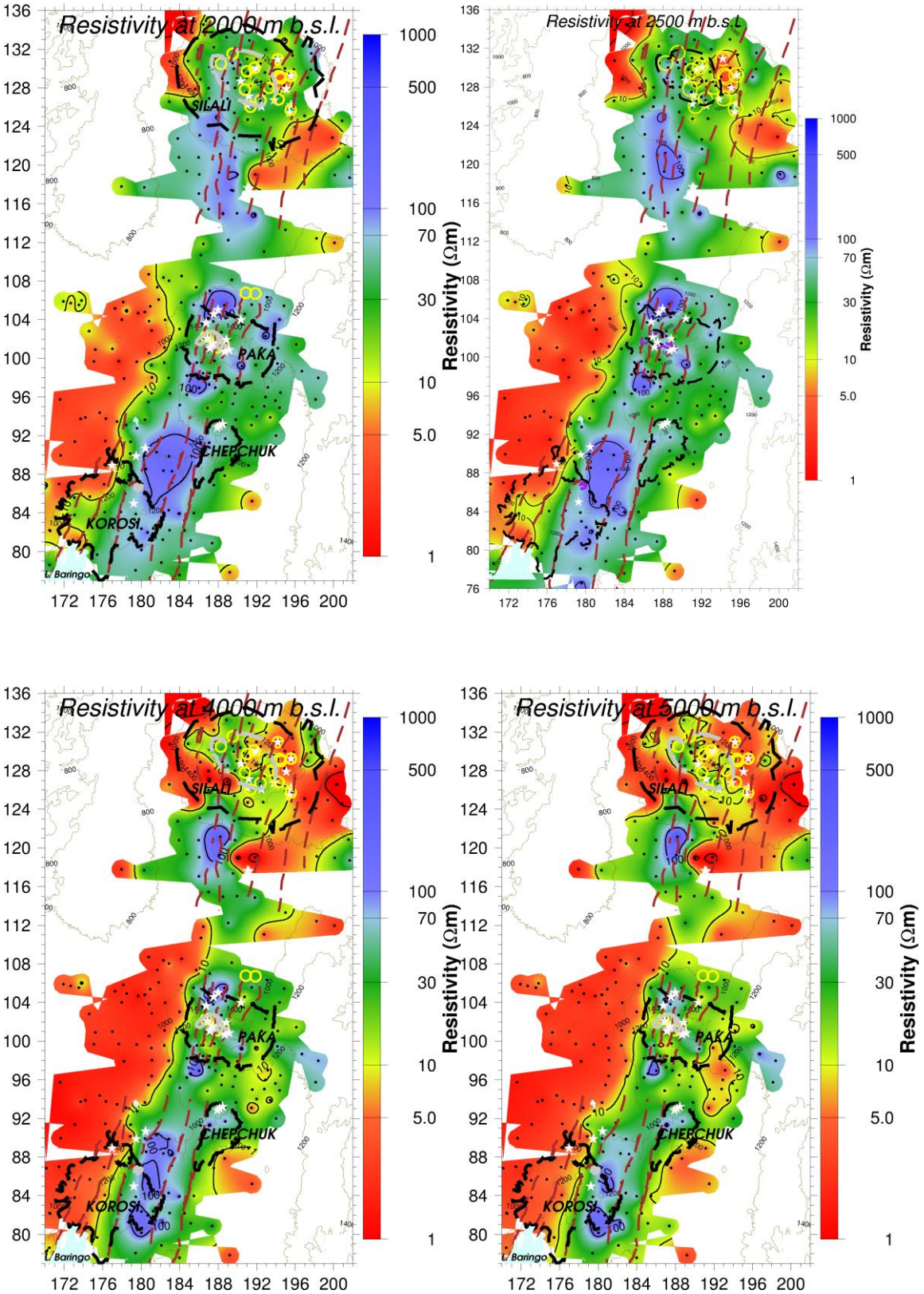
Resistivity at 2000m b.s.l.
Resistivity at 2500 m b.s.l.
Resistivity at 4000m b.s.l.
Resistivity at 5000m b.s.l.
SILALI
PAKA
CHEPCHUK
KOROSI
L. Baringo
Resistivity (Ωm)
1000
500
100
70
30
10
5.0
1
172 176 180 184 188 192 196 200

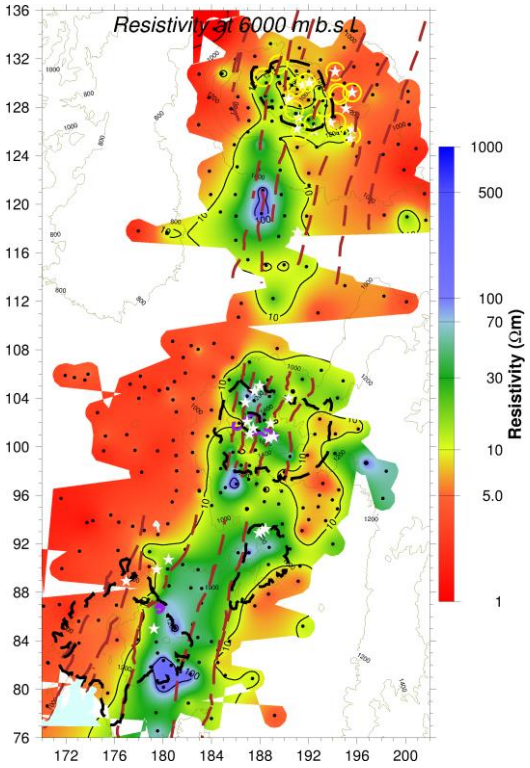
Resistivity at 6000 m b.s.l.
136
132
128
124
120
116
112
108
104
100
96
92
88
84
80
76
172
176
180
184
188
192
196
200
1000
500
100
70
30
10
5.0
1
Resistivity (Ωm)